INVESTIGATION OF HYPERLOOP SKELETON TUBE DESIGN

Luka Ekart
MSc. Thesis

TUDelft

Iv-Groep
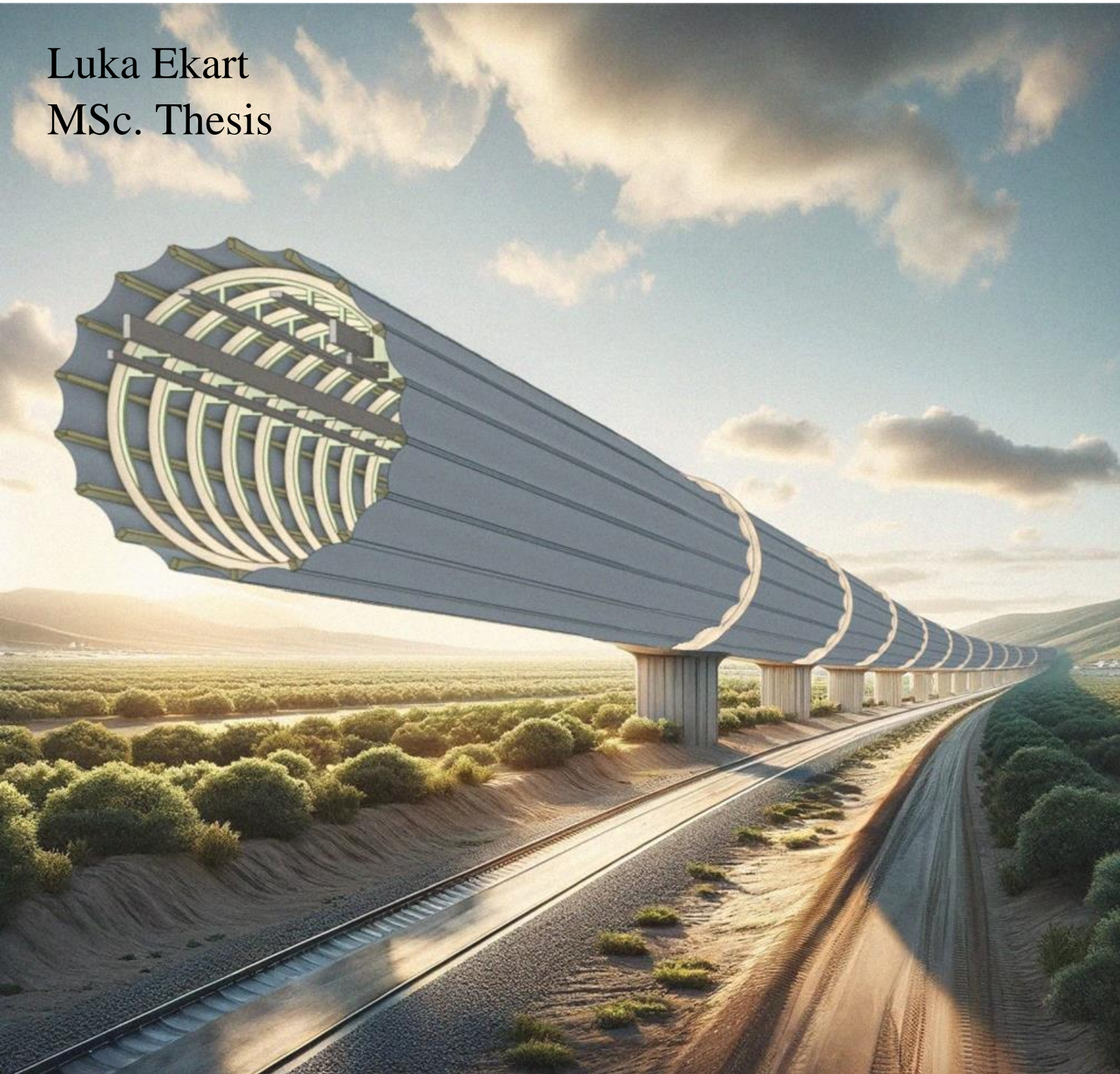
INVESTIGATION OF HYPERLOOP SKELETON TUBE DESIGN

by

Luka Ekart

to obtain the degree of Master of Science
at the Delft University of Technology
in Civil Engineering.

Student number: 5595746
Project duration: May, 2023 – March, 2024
Thesis committee: Prof. Dr. M. Veljkovic – TU Delft, Steel and composite structures (chair)
Dr. F. Kavoura – TU Delft, Steel and composite structures (daily supervisor)
Dr. ir. K. N. van Dalen – TU Delft, Dynamics of Solids & Structures
T. Cristutiu – Iv-Groep
J. Koeken – Iv-Groep (daily supervisor)
Faculty: Civil Engineering and Geosciences, Delft
Company: Iv-Groep

An electronic version of this thesis is available at http://repository.tudelft.nl/.

Preface

This thesis symbolizes the culmination of my academic journey in obtaining the Master of Science degree in Civil Engineering from Delft University of Technology. Engaging with the topic of Hyperloop has been instrumental in deepening my understanding of this cutting-edge technology. This research voyage has also expanded my expertise in the domain of slender steel structures, stimulated innovative ambitions and provided a solid foundation of knowledge.

I would like to express my gratitude to the assessment committee. Firstly to Prof. Dr. Milan Veljkovic, the chair of the committee, for intriguing discussions and encouragements regarding the innovative aspects of my work. To my daily supervisor Dr. Florentia Kavoura, for the continuous support and guidance throughout my thesis. I am particularly thankful for your enthusiasm and positivity. To Dr. ir. Karel van Dalen for your valuable input and establishing a connection between me and the hyperloop industry. I am grateful to Teodora Cristutiu for giving me the opportunity to work on this topic, as well as for the given freedom on the direction of this thesis. And finally, a special thanks to Jeroen Koeken for continuous support, engaging discussions and attentive oversight of my progress. Thank you for your practical approach and comprehensive guidance.

A special appreciation to the Iv-Groep for providing me with the topic in this rapidly evolving field, and to the engineers of the structural department for insightful discussions and valuable support.

Last but not least, I would like to thank my family, friends and girlfriend. I am deeply grateful for your support, motivation, and love; it means a lot to me.

Abstract

The objective of the European Green Deal is to reduce net greenhouse gas emissions by at least 55% by 2030 and to achieve climate neutrality by 2050 [1]. Due to a growing global population and increased needs for travelling on the one hand, and progressive bans of short-haul flights by the governments on the other, the need for a more sustainable and fast means of transportation comes in high demand.

The Hyperloop transportation system has emerged as the fifth mode of transportation, offering an energy-efficient, fast alternative for freight and passenger transportation. However, to successfully establish the Hyperloop network, an extensive tube infrastructure would need to be constructed with requirements of being safe, sustainable, and cost-effective. At the time of this project, various tube designs and materials have already been examined and evaluated; given its preliminary stage of development, new design ideas are rapidly emerging. Engineers are faced with two fundamental challenges: firstly, defining safety limits, and secondly, establishing the balance between the safety, environmental footprint, and operational efficiency of hyperloop infrastructure.

The Hyperloop Skeleton tube design is the latest addition to the integral designs that holds great potential in terms of weight efficiency. The aim of this research is to determine the applicability and efficiency of the newly proposed tube design and to evaluate structural performance to imposed loads. For the design evaluation, the study uses a numerical approach. Skeleton tube design is initially disassembled into individual components, which are analysed separately to identify potential weaknesses of the design as well as to predict their behaviour within the assembly. After that, the study conducts the analysis of the assembly. The initial design lacked rail support design; thus, a design is proposed and implemented in the model for the global analysis. Within the assembly, the research identifies critical sections and design weaknesses. In accordance with this, it proposes and analyses a new ring-to-stringer connection design. Additionally, a comparison study has been conducted with the conventional (plain) tube design, currently used at the European Hyperloop Centre (EHC) [2].

Based on numerical results, the skeleton tube design is conditionally satisfactory in terms of ultimate and serviceability limit states. The design can resist the main load case – vacuum pressure. Nevertheless, the slender components and thin plates make the tube susceptible to plate rupture or penetration if exposed to environmental actions; thus, making the hyperloop system vulnerable to accidental and impact loads. Moreover, the elastic strength capacity of rings, which are primarily in compression and are therefore critical components, is nearly reached. An initiation of local plastic response is observed, yet due to integral design, the stresses distribute among components; thus, it does not progress into a fully plastic response. Based on these findings and considering that dynamic loads are yet to be assessed, it can be projected that a strength capacity will be exceeded in further research.

The proposed steel bracket design for ring-to-stringer connection provides an alternative to welded connections. It improves stress concentrations within the ring, and considering that it is a bolted connection, further contributes to the ease of assembly, maintenance and the demountability aspect. However, the requirement for 288 such connections per 16-meter-long tube section might significantly increase the total cost of skeleton tube design.

Based on the comparison study, it is proven that the conventional tube design performs better in terms of structural performance under the considered loading conditions. However, in a controlled environment with the absence of external actions, the skeleton tube design could efficiently operate. In this case, a material efficiency of up to 28% can be achieved if the structure also supports the rails and the pod, and up to 37.8% if the tube is solely used for vacuum pressure retention.

Emerging technologies, currently in the process of development and yet to demonstrate their contribution to a more sustainable future significantly depend on the performance and success of their initial prototypes and real-world applications. Skeleton design offers a cutting-edge design, which is on the *safety – sustainability* spectrum drastically leaning to the latter. A secondary protective structure is

required for consideration of the skeleton design in the hyperloop application. The design can nonetheless be viable for other applications, which operate in a safe and controlled environment, with the absence of external loads. This research lays a foundation for any further research on the skeleton tube design.

Symbols and abbreviations

Symbol	Definition
A	Area [mm^2]
A_{ref}	Reference area of the structure [mm^2]
A_{total}	Total contact area at ring to stringer connection [mm^2]
A_{strip}	Strip area of the stringer segment [mm^2]
α_b	Function of end distance (e1) and pitch parallel (p1) [-]
b	Distance between stringers [mm]
C_e	Exposure factor
c_f	Force coefficient
$c_{f,0}$	Force coefficient of cylinders without free-end flow
D	Ring diameter [mm]
D	Bolt diameter [mm]
δ_v	Vertical deflection [mm]
δ_0	Deflection at mid span due to permanent actions [mm]
H	Horizontal force [kN]
E	Young's modulus [MPa]
F_f	Frictional force [kN]
F_n	Force normal to the plane [kN]
$F_{V,Rd}$	Bolt resistance to shear [kN]
$F_{b,Rd}$	Bearing resistance of the plate [kN]
F_w	External force acting on the tube [kN]
f_{ub}	Ultimate tensile strength of the bolt [N/mm2]
f_u	Ultimate tensile strength [N/mm2]
I_y	Second moment of Area [mm^4]
k	Safety factor [-]
k_l	Function of edge distance (e2) and pitch perpendicular (p2) [-]
L	Length of the tube [mm]
l	Distance between cable supports [mm]
L	Critical buckling length [mm]
ΔL	Cable elongation [mm]
M	Design bending moment [kN/m]
$M_{pl,Rd,y}$	Design resistance for bending
μ	Static (μ_s) or kinetic (μ_k) frictional coefficient
μ_4	Snow load shape coefficient
σ_n	Stress due to axial force [MPa]
N_{cr}	Critical buckling load [kN]
$n_{stringers}$	Number of stringers
n_{rings}	Number of rings
n_0	First natural bending frequency
v	Kinematic viscosity of the air
P	Point load [kN]
q_{atm}	Atmospheric pressure [MPa]
q_{Ed}	Imposed design load [MPa]
q_{tube}	Pressure in the tube [MPa]
q_{self}	Self-weight
q_{vac}	Vacuum pressure [MPa]

q_r	Rails load [kN]	
q_w	Wind load [kN/m^2]	
q_s	Snow load [kN/m^2]	
$q_{s.pod}$	Static pod load [kN]	
q_{br}	Breaking of the pod [kN]	
$q_p(z_e)$	Peak velocity pressure at reference height z_e [kN/m^2]	
R_e	Reynolds numbers	
s_b	Balanced snow load [kN/m^2]	
s_{ub}	Unbalanced snow load [kN/m^2]	
T	Cable tensile force [kN]	
t	Thickness [mm]	
UC	Unity check	
V	Design shear force [kN]	
$V_{pl,Rd,y}$	Design resistance for shear force [kN]	
$v(z_e)$	Peak wind velocity [m/s]	
w	Vertical displacement [mm]	
z_e	Reference height	
γ_M	Material factor	
γf	Partial factor for actions	

Contents

1   Introduction

This chapter includes an introduction to the hyperloop technology and outlines the background of this research. Furthermore, the problem statement, research objectives and questions, and report structure are described.

1.1. About hyperloop

Hyperloop is a new proposed means of transportation for cargo and people, capable of high-speed and driverless driving in a capsule-like vehicle travelling through a depressurised tube. Due to the levitation of the pods, the resistance forces are drastically reduced, and therefore, the hyperloop can theoretically travel at 1000 km/h, consuming minimal energy [3]. By utilising clean energy sources like solar, wind, or hydroelectric power, the environmental impact of the hyperloop can be significantly reduced. It holds the prospect of replacing short-haul flights and establishing an emission-free network due to being supplied by renewable energy sources producing zero operational emissions [4]. In short, the hyperloop concept offers a fast and sustainable method of transportation, combining the best of two worlds.

The sustainability aspect of the hyperloop system is closely linked to the tube design, which is the dominant factor in the determination of the total amount of material used. Since the technology is still in the early developmental stage, many hyperloop companies and research groups work on their own unique tube designs. These designs are being closely researched and analysed, especially due to safety being one of the main design factors. One of the new tube concepts is the hyperloop skeleton tube design, which, based on the preliminary assessment, proves to be exceptionally weight efficient.

As the Hyperloop concept evolves and progresses towards implementation, tube designs will continue to be refined based on engineering feasibility, cost-effectiveness, safety considerations and environmental footprint. By making thoughtful decisions from the start, the hyperloop system has the potential to overhaul the world's sustainable transportation needs.

1.2. Problem statement

Hyperloop technology has been actively developed by many companies since the publishing of the White Paper [5] by Elon Musk. Although many feasibility studies were completed at the request of the national governments, and promising advances were seen in the development of hyperloop components, the need for large investments is one of the main drawbacks for large-scale implementation. As the hyperloop is still under development, and the infrastructure has yet to exist, it gives the opportunity to research, optimise, and develop hyperloop concepts thoroughly. The tube design is of great importance for safety and for ensuring a flawless operation. It also has a significant environmental impact, considering the predicted total length of the infrastructure. By use of known materials and simplistic design concepts, the safety aspect can be met.

However, new designs are constantly being developed, and based on detailed and thorough risk analysis, it may become feasible to lower the safety margin. This could lead to material weight savings and, subsequently, a decreased environmental impact. Passenger and structure safety are two of the main conditions in hyperloop tube performance assessment; therefore, two main objectives need to be addressed by engineers: i) identifying acceptable safety limits and ii) establishing the balance between the safety, environmental impact and operational efficiency of hyperloop infrastructure.

1.3. Research objectives and questions

The main objective of this research is to assess a new hyperloop tube design in terms of ultimate and serviceability limit states. Moreover, to identify weaknesses and modify the design appropriately to mitigate potential failure modes. Additionally, the design performance is evaluated in a comparative study with the existing plain tube design, which serves as the benchmark design.

To accomplish these research objectives, the following research questions were formulated:

Main research question:

What is the structural performance of the hyperloop Skeleton tube design, exposed to external and internal actions associated to the general, vehicle and environmental load classes?

The main question is then divided into five sub-questions:

1. How do the hyperloop Skeleton tube design additions (rail supports) and improvements (connection design) affect the structural performance?
2. How does the skeleton tube design compare to the plain tube design in terms of structural performance and sustainability?
3. Which failure modes is the hyperloop skeleton tube experiencing under considered actions, and what is the structural response to them?
4. Which imperfections have the most significant effect on the structural performance of the hyperloop skeleton tube design?
5. How can structural safety be researched and implemented in the hyperloop skeleton design?

1.4. Simplifications and clarifications of this research

The total length of the tube section is 16m, which can be computationally demanding for a detailed FEA model. Due to the complexity of the design, some details were removed from the model, such as edge radiuses at stringers, rings and plates; bolt holes on the flanges were removed as well, and the slot holes in the shims and flanges were modified for a precise fit with the stringers. These changes were implemented to streamline the model, ease the meshing process, and speed up the computational time. In the analysis of shorter tube sections, more details are included, while in the analysis of individual components, all details are retained to ensure an accurate model response under imposed loading. All connections are modelled as bonded connections, which means that no sliding or separation between faces or edges is allowed. This modelling decision was made with the understanding that accurate connection modelling is less critical at the preliminary design analysis. As the analysis progresses further into details, the connections can be modelled accordingly to reflect specifics. This research does not investigate structural response to dynamic loadings. Additionally, it does not include the interaction between the tube and the foundation, although a design solution in the plain tube design is presented.

1.5. Thesis structure

This report assesses and evaluates the new hyperloop Skeleton tube design and thereafter compares it to the benchmark tube design. Initially, a literature review has been conducted to gather general information about the hyperloop technology, infrastructure, and existing designs. After that, the plain tube and skeleton tube design are introduced and described. First, an analytical approach was conducted to verify the design choices. Following this, Finite Element (FE) models were made and analysed. Based on FEA results, several issues have been addressed, such as stress concentrations at connections and initiation of plastic response. Moreover, the report includes a proposed solution for the rails supports and a ring-to-stringer connection design for the skeleton tube design. Lastly, a comparison study is conducted between the two designs.
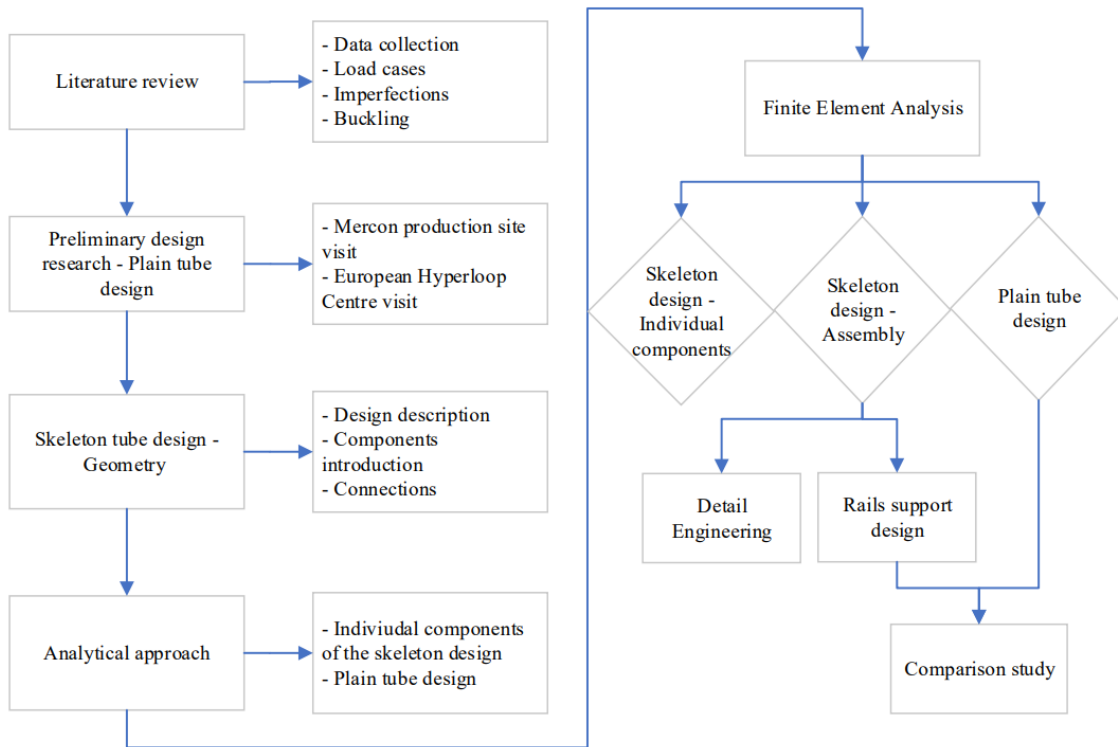
Figure 1: Workflow diagram

2   Literature review

In this chapter, general information about the hyperloop infrastructure is gathered and presented. This includes codes and standards that are applicable to the hyperloop tube structure, the existing designs and considerations by other research parties, imperfections affecting the structural performance of the infrastructure, and the safety and sustainability aspects of the hyperloop.

2.1   Codes and standards

No norms or standards exist for the design of the hyperloop infrastructure, but the structure is in principle an underpressurized steel tube. Therefore, Eurocodes can be used for the plain tube design, which represents a cylindrical steel structure exposed to the inner pressure. As of January 2023, a technical report named 'NPR-CEN-CLC/TR 17912: Hyperloop systems - Standards Inventory and Roadmap [6]' has been published, which presents a set of standards created for different transportation modes and industries. This report can serve as valuable guidelines for the future development of standards in the hyperloop sector. The codes and standards used for each load case individually are presented in Table 1. For the non-linear FEM analysis methods, DNV [7] standards were used.

Table 1: Load cases and corresponding standards

Load case	Load type	Codes and standards
Self-weight	General	EN 1991 - Eurocode 1 – Actions on Structures - Part 1-1
Vacuum pressure	General	/
Snow load	Environmental	EN 1991 – Eurocode 1 – Actions on Structures – Part 1-3
Wind load	Environmental	EN 1991 – Eurocode 1 – Actions on Structures – Part 1-4
Rails load	General	/
Static pod load	Pod	/
Moving pod load	Pod	EN 1991 – Eurocode 1 – Actions on Structures – Part 2 – Traffic loads on bridges
Breaking pod load	Pod	
Thermal expansion	General	EN 1991 - Eurocode 1 – Actions on Structures - Part 1-5
Accidental loads	General	EN 1991 – Eurocode 1 – Actions on Structures – Part 1-7

2.2   Hyperloop infrastructure

The hyperloop concept is evolving rapidly, and many big parties are involved, making advances in all hyperloop aspects. Due to the size of the potential hyperloop network, the tube design, size, and properties are important for future implementation. The tube has two main objectives: i) maintaining a low-pressure environment and ii) protecting the pods from external conditions [3].

In 2020, an agreement was signed between TATA Steel [8] and Posco [9] for the hyperloop tube production. Additionally, they will join their efforts in researching and designing new innovative tube designs [10], which would prove to be safe and weight/cost efficient. Different designs using various materials have been considered, with many yet to be revealed. All of them have a common objective, to decrease the total weight, in consideration of producibility and transportability.

The main components of the hyperloop system are the vacuum structures, known as the tubes, from which almost all the air is removed by vacuum pumps; the pods, designed to carry passengers or freight; the levitation and guidance system installed within the tube; and the propulsion system [11]. The main hyperloop systems and components are presented in the following figure:
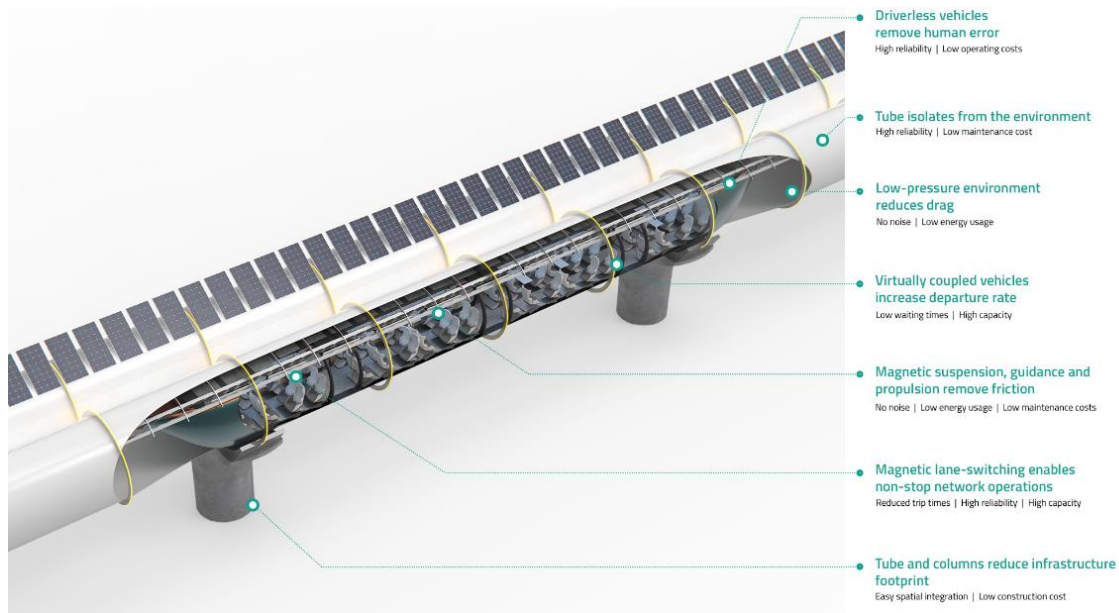
Figure 2: Main hyperloop system components based on Hardt Hyperloop [12]

The infrastructure design also consists of support bearings, which may be fixed or moveable. These bearings should resist potentially significant lateral loads imposed by seismic actions or unbalanced pressure loads, e.g., wind gusts. Thermal expansion of the tube is another major factor when designing the connection between adjacent tube segments. The expansion joints allow for longitudinal thermal expansion of the tube. They are considered weak points due to their decreased thickness and excessive non-linear deformation. Additionally, these are susceptible to fatigue [11]. Ongoing research on this matter is performed by many parties, from engineering firms, material manufacturers to universities and start-ups.

2.3   Designs & materials

The skeleton tube is designed to be made from structural steel. Knowing that the plain tube design is made from specialized hot-rolled steel PosLoop355 steel, which has 1.7 times better vibration absorption than general steel, according to Posco [13], the same steel type could be used for the skeleton design. However, due to its slender design, a higher steel grade could be used as well, such as S460. Increasing the steel quality will negatively affect the cost but might significantly improve the structural integrity of the design. Both options, S355 and S460, were considered in this research.

2.4   Imperfections

The hyperloop tube is a slender steel structure that is susceptible to various imperfections. These are categorised into material, geometrical, and structural imperfections. Material imperfections refer to the various flaws that can occur during the manufacturing process or over the course of the material use. These imperfections are incorporated in the material curve.

Geometrical imperfections of members are determined by geometrical tolerances found in product standards, and according to EN1993-1-1 [14], and these include:

1. *Lack of verticality* – In the skeleton tube design, the rings, flanges and shims can potentially be influenced by lack of verticality. Consequently, this can lead to gaps between components and impact connections. The ring to stringer connection is very sensitive, as it is a critical point in the load path. A lack of vertical alignment in the rings can result in a lack of fit and generate eccentricities in the connections.
2. *Lack of straightness* – This geometric imperfection primarily impacts stringers and plates, potentially leading to a lack of fit of components. Lack of straightness can cause misalignments

5

and complications during construction. Forcefully positioning them in place can induce unwanted internal stresses. These can negatively influence the structure's ability to withstand the anticipated loads.

3. *Lack of flatness* – This imperfection can be seen locally in the skeleton tube design, as for example at the webs and flanges of the rings and stringers. It can be particularly noticeable at rings, where the production process involves material bending, leading to bent or curved surfaces. Components that experience compressive stresses will be sensitive to those imperfections.

4. *Lack of fit* – These imperfections are common for complex structures with many connections. The skeleton tube is an example, featuring 288 ring-to-stringer connections per 16m tube section. This means that a single lack of fit can cause a cascading effect on the subsequent connections.

Structural imperfections are introduced due to the fabrication assembly of the structure. Due to the many connections being present in the skeleton tube design, small imperfections can accumulate and affect the overall structural integrity of the design. These imperfections are addressed with the help of DNV [7] standards when evaluating the buckling of the structure. More on that in section 7.2.8.

2.5 Buckling

Since the hyperloop structure is still in an early design stage, not all forces acting on it are identified or determined. Thus, certain strength and deflection restrictions can be pre-set, but the tube cannot be solely designed and optimised based on the allowable deflection. Nonetheless, the plain tube can be designed based on another structural aspect, which is one of the governing failure modes, vacuum buckling.

In essence, the hyperloop technology works on the principle of vacuum pressure, which causes compressive forces on the tube wall or, in the case of the Skeleton tube design, on the rings. Once the compressive stress overcomes the critical buckling load, the component buckles. Critical buckling load governs the plain tube design; therefore, knowing the vacuum pressure, the design is optimised based on the out-of-plane buckling resistance. The proposed pressure in the tubes p_{tube} is 100 Pa, which lowers the drag force of the air on the pod [5]. The vacuum pressure action on the shell of the tube is the difference between the atmospheric pressure and the pressure within the tube. The critical tube pressure is calculated using the following equation [15]:

$$P_{cr} = \frac{E}{4 \cdot (1 - \nu^2)} \cdot \left(\frac{t}{R}\right)^3 \tag{2.1}$$

Where t is the thickness of the tube, and R is the radius. This formula for the critical buckling pressure is valid for an endless plain traditional tube. Hardt has previously designed a spirally welded tube design with a wall thickness of 25 mm in order to prevent vacuum buckling, considering the radius of 1.75 m and a safety factor of 1.2 [16]. The latest design has a radius of 1.25m and a wall thickness of 16mm.

This approach of determining critical buckling pressure cannot be applied to the skeleton tube design since it is an integral design as opposed to a cylindrical design. Therefore, each component needs to be verified as an individual element within the assembly. Skeleton tube design is prone to local buckling due to its thin elements. Local buckling is often characterized by distortions or wrinkles. Local buckling is particularly relevant in thin-walled elements or sections with geometric irregularities. This buckling mode is expected in skeleton tube design since the components are well integrated, forming a complex assembly which could not buckle globally with ease. Another reason is that components are made out of thin walls; thus, local buckling will be the governing mode.

A buckling of build-up elements can be a potential failure mode as well, considering the connection between stringers and plates. The interaction between those two components can influence overall buckling behaviours. Interactive buckling occurs when different modes of buckling interact with each other, and it can only be present in the skeleton tube design, although the possibility is rather small.

Due to the high speed of the pod, dynamic instabilities are very likely to appear, leading to buckling. Dynamic loadings, such as wind or seismic forces, can also induce dynamic instabilities. Dynamic effects may amplify the susceptibility of steel members to buckling, and their consideration is crucial in certain structural designs.

2.6 Safety

Ensuring the safety of a hyperloop system is a complex and multifaceted task that involves addressing various technical, operational, and regulatory aspects. The guideway and infrastructure matter includes the tube structural integrity, track design, tube supports and alignment and connectivity between segments and components. Regular inspections, maintenance, and monitoring are essential to identify and address potential issues during the operation. On the other hand, to ensure safety in the design phase, many scenarios need to be considered and weaknesses identified. This is done in FE analysis, in which geometrical defects are considered and structural response to them evaluated. Due to the slender

design of the integral design, the operational performance of the design might be proportionally more affected than the plain tube design.

Therefore, rigorous testing and certification processes are required to validate the safety and reliability of the design advances from the preliminary stage. Prototypes should undergo extensive testing, both in controlled environments and atmospheric conditions, to identify and address potential design flaws and safety concerns. Hyperloop developers and operators should also work closely with regulatory authorities, engineering experts, and other stakeholders to create safety measures that encompass all possible considerations and scenarios.

2.7   Fatigue

Fatigue loading is induced by the travelling pod inside of the tube, by thermal expansion and contraction, by vacuum pressure fluctuations and, to a lesser extent, by external factors. Moving pod is the main source of fatigue since it also generates vibrations in the structure. The steel plain tube and a pod with a weight of 100kN is not prone to fatigue, as concluded by Museros et al. [17]. That research was done on the plain tube design, while other designs, such as an integral design, will have a different fatigue performance. Engineering details, such as bolted connections used for the rail supports, might prove to be critical and should be checked separately. Fatigue can be mitigated by material selection and treatment, research and testing, and by optimising the structure design in a way to minimise stress concentrations. The latter is done during the preliminary design stage, where the stress concentrations are identified by performing a FE analysis of the assembly. Thereafter, the design can be revisited to mitigate structural weaknesses.

2.8   Sustainability

The European Green Deal aims to cut net greenhouse gas emissions by at least 55% by 2030 and achieving climate neutrality by 2050. This is achievable by reforming European policies on climate, energy and transport, among other [1].

The hyperloop system is designed to be highly energy-efficient compared to other transportation modes. Utilising the low-pressure environment in the tube severely reduces air resistance and, consequently, the needed energy for transporting pods at high speeds. Nonetheless, achieving sustainability requires careful planning, design, and operation.

The proposed propulsion concept can be powered by renewable energy sources such as solar, wind, or hydroelectric power [3]. Using clean energy for hyperloop operations reduces the carbon footprint associated with the transportation system. It also proves to be efficient in land use, especially in the case of an elevated tube infrastructure built along the pre-existing highway or railway infrastructures [5].

Minimising noise pollution is a crucial aspect of sustainability, especially in urban and suburban areas. Hyperloop systems, with their enclosed tubes and streamlined design, have the potential to reduce noise levels compared to traditional transportation modes. Conducting life cycle assessments of materials used in hyperloop construction is important for evaluating the overall environmental impact. This can influence the material and design choices in the preliminary stage. The economic sustainability of hyperloop systems is essential for their long-term success. Factors such as construction costs, operational efficiency, and ticket pricing impact the system's affordability and accessibility, ensuring it remains economically viable. Designing a hyperloop infrastructure which can be easily maintained and repaired if needed also contributes to sustainability in the long run. E.g., modular construction can offer cost-effective replacements of damaged components, such as in the skeleton tube design.

However, it is important to note that the hyperloop is still a concept, and large-scale implementation and real-world performance are yet to be fully realised. The actual sustainability of hyperloop systems will depend on various factors, including the energy sources used, the materials and manufacturing processes employed, and the overall environmental lifecycle assessment of the infrastructure and

vehicles. Nonetheless, the core principles of energy efficiency, reduced emissions, and land use efficiency make the hyperloop a viable option with great potential to reduce global emissions. Additionally, collaboration between stakeholders, adherence to best practices, and continuous innovation will contribute to making hyperloop systems more sustainable and environmentally friendly.

3 Preliminary design research – Plain tube design

To understand the main features of hyperloop tube designs, research on already existing designs was done. Since the hyperloop technology is still in its early stages of development, companies tend to keep design information confidential, and there are no universal design standards available yet. Therefore, most of the information gathered in preliminary research is from online published articles, from meetings and site visits. The European Hyperloop Centre (EHC) [2], located in Groningen, NL, has a 420m long test site with a spirally welded plain tube design. The tubes were manufactured by Mercon [18] company in Gorinchem and transported to Groningen, NL. The photographs featured in this chapter were either captured at the Mercon production site or at the EHC.

Figure 3: Plain Tube design assembled for the EHC

Figure 4: Plain tube production at Noksel España [19]

The following information and measurements were gathered from the production site visit. EHC tube design is an above-ground plain tube design, measuring 2.5m in diameter and supported at every 16m. Posco steel [9] manufacturer supplied PosLoop355 steel for the tube production [13]. The tube thickness is governed by the critical buckling pressure and measures 16mm. The tube has a stiffening ring of 20mm thick at a span of 8m to improve the buckling behaviour of the tube. Tube flanges positioned at the ends of the tube sections serve as the tube supports and as a connection between the tube sections. The connection between flanges must be sealed to retain vacuum pressure; thus, rubber rings are attached to the flanges and compressed once the bolts connecting the flanges together are pre-tensioned. Rail supports are spaced by 1m in the longitudinal direction, with the exception of the first and last, which are spaced 0.5m from the tube flange. All rail supports are bolted to the tube itself, as it can be seen in Figure 5, and the inner components are presented in Figure 6.

Figure 5: Rail support and holes for bolted connections

Figure 6: Inner components, where:
1. Levitation rails; 2. Propulsion rig
3. Guidance rails; 4. Safety rails

The weight of all rails per 16m tube section is approximately 6 tonnes. With the assumption that all rails are of the same weight, one rail imposes a 0.625 kN/m load on the tube. Flanges have two cut-outs (Figure 7) at the bottom, which slide onto the foundation. A sliding support design is used, as seen in Figure 8, to allow sliding in the longitudinal direction. The same design is supposed to be used for the Skeleton tube design.

Figure 7: Close-up of the support
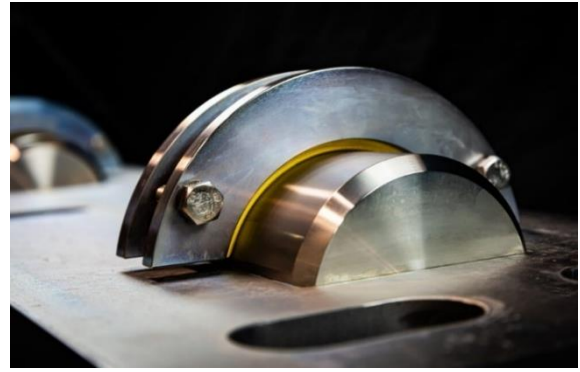
Figure 8: Sliding compact support by DRIE-D [20]

Another hyperloop tube aspect which needs to be addressed is the material expansion and contraction. Since the tube is made out of steel, it is prone to thermal fluctuations. This is accommodated using expansion joints, which are positioned at every four tube sections. As seen in Figure 9, the expansion joint looks like a wrinkled steel plate, which enables the tube to expand freely in the longitudinal direction.

Figure 9: Expansion joint from the outside of the tube

Figure 10: Expansion joint from the inside of the tube

4 Skeleton tube design

The skeleton tube design has been showcased by TATA Steel [8] in a video that outlines their involvement in the development of the hyperloop. The prototype displayed in the video clearly revealed the shape and the number of components. As seen in Figure 11, the plates are curved inwards, and the connections are welded. At the kick-off event of the European Hyperloop Centre, TATA Steel presented the lightweight, integral design, and a small-scale model was placed adjacent to the model of a spirally welded tube design (Figure 12). This provided a direct comparison of the two designs, from which the general global dimensions could be extracted.

Figure 11: Front view of the integral tube design [21]

Figure 12: Integral design presentation at European Hyperloop Center kick-off event [22]

Furthermore, it is observed that the edge flanges are the same in both designs and that the rings in the integral design are spaced the same as the rail supports in the plain tube design. The reinforcing skeleton of the integral design is similar to the aircraft fuselage or the structure of the submarine, which supports the pressure hull. By making certain assumptions about dimensions and by basic extrapolation of these, namely the ring, stringer and plate cross-sections, a model was constructed in Ansys. The following two figures show the assembly and its components.
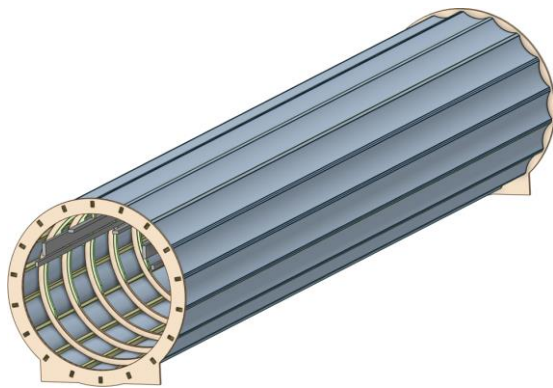
Figure 13: Model of the skeleton tube design modelled in Ansys
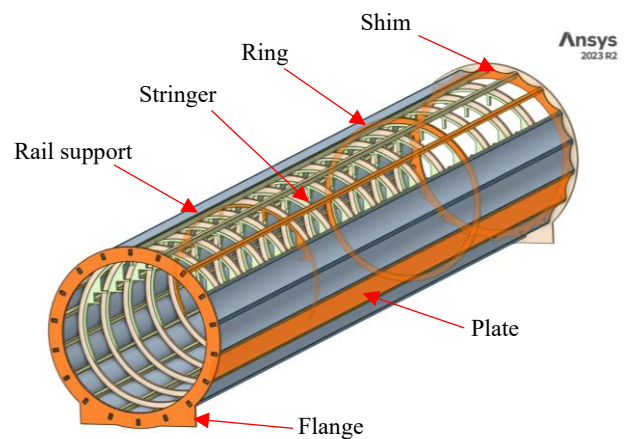
Figure 14: Components of the Skeleton tube design

The cross-section of the skeleton tube design resembles the buckling failure mode of the plain tube design. Figure 15 represents the cross-section of the first buckling mode of the circular tube exposed to the inner pressure. Looking at the curved shape of plates in Figure 16, it is noticeable that it follows the shape of the inward buckling of the plain tube design. With this design decision, the tube skin buckling failure mode is eliminated.
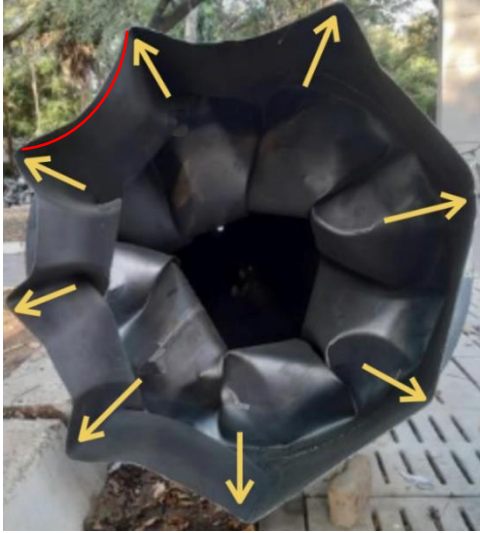
Figure 15: Buckling shape of the plain tube design – Destructive testing performed by Avishkar Hyperloop [23]
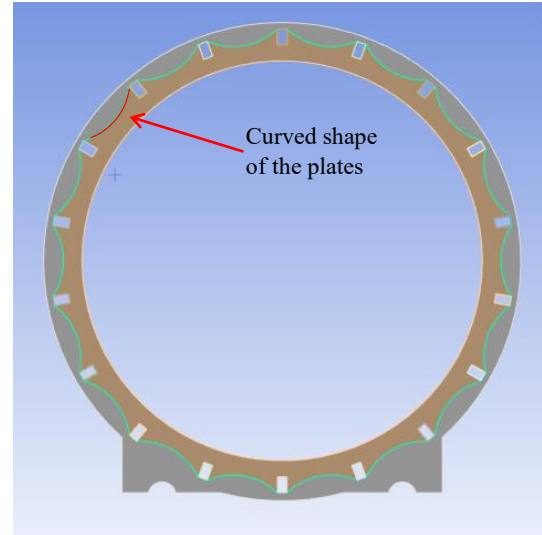
Figure 16: Cross-section of the skeleton tube design

Each component is presented in detail in the next subsections; additionally, technical drawings are given in Appendix. B.

4.1 Plates

The Shell of the Skeleton design consists of curved plates and flanges. There are 18 plates in total, positioned in a circular pattern. The plate bends inwards by roughly 85mm, therefore the spacing between the plate and ring flange is 15mm. This spacing is also the deflection limit of the curved plates.
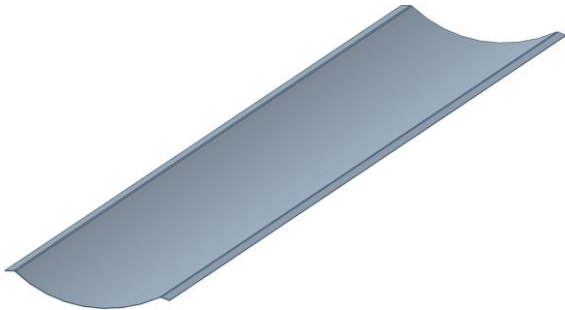
Figure 17: Single plate of the skeleton tube design.
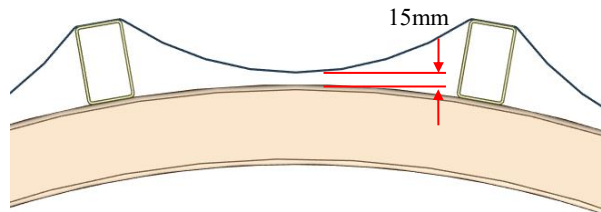
Figure 18: Side view. The gap between the plate and the ring represents the deflection limit.

Plates are loaded by vacuum pressure, which acts from the inside of the tube, and external loads, such as wind and snow load, if the tube is to be constructed without the secondary protective structure. Considering the thickness of the plates, which is only 1 mm, a conclusion is made that they do not contribute to the structural rigidity of the whole structure. Thus, all loads act normal to the surface of the plates, directed towards the centre of the tube.

Connections

Plates are connected with flanges to the stringers in the longitudinal direction. The type and execution of those connections are of great importance since they also influence the plate's behaviour. In this research, an assumption is made that components are rigidly connected, meaning that the flanges would be either welded or glued to the stringers using structural adhesives.
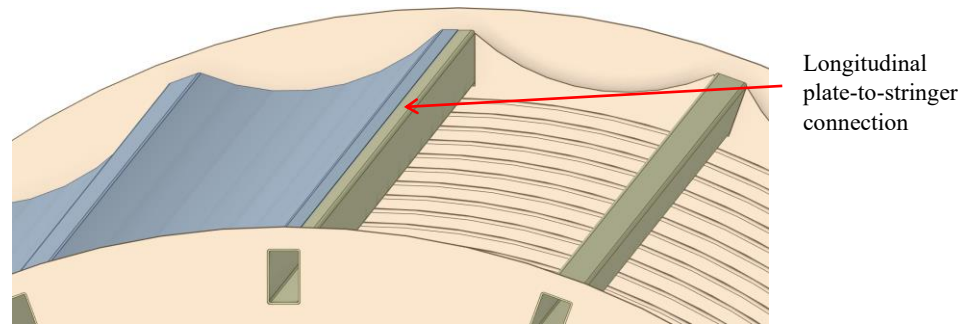
Figure 19: Plates are connected via plate flanges to the stringers

Considering the plate thickness, welds might prove to be unsuitable, while structural adhesives might not perform as welds in the actual application. This opens the door to another research topic analysing the performance of different structural adhesives in hyperloop skeleton tube design applications. In this research, the connections are set to fully fixed, meaning that connected plate flanges cannot move nor rotate with respect to stringers. The shims offer a contact surface for the plates in transverse direction. This connection can be crucial in case of thermal expansion and present a weakness to transverse loadings. The width of the saddle is 20mm, which presents the threat of detachment. If the edge of the plate slides off, this creates a gap in the structure and can cause an instant release of vacuum pressure. Plates serve as a skin of the tube, which needs to be vacuum proof as well. This can be achieved with structural adhesives, although a certain amount of vacuum loss is expected. Separate research could be done on the vacuum loss limit, for which the tube can still operate efficiently.

Number and continuity of plates

The plates also need to be connected to each other in the longitudinal direction; therefore, another design consideration is the number of plates to be used. The design consists of 18 plates in a circular pattern, which offers different design options, such as two halves of the shell (9 + 9 plates), a shell with a 1-2-1 running order of the plates or even 18 individual plates. One of the factors is the type of connection to be used; another is the fabrication, transportation and assembly of the structure. Designing and constructing two halves of the tube shell increases the fabrication speed, where a single sheet of steel can be bent to form the required shape of one half of the tube shell. In case of a plate failure, replacing half of the tube shell might will prove to be cost-inefficient; thus, the production of individual plates presents the best option.

In conclusion, initial savings can be made by producing two halves of the shell, but in the long term, it could drastically increase the maintenance and repair costs. So, the decision was made to design and analyse the tube with individual plates.

Response to loading

Looking at the shape of the plate and the direction of the loading, it is evident that the whole component will be in tension and that plates will deform in the direction of the initially curved shape (Figure 20). Theoretically speaking, the plate should have some amount of bending resistance along the flange, but due to its thickness, this is dismissible.
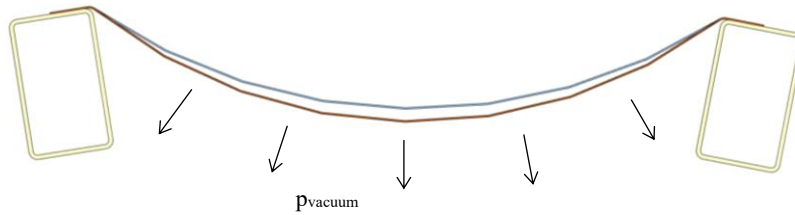
Figure 20: Expected plate deformation due to vacuum loading

If the boundary conditions are fixed, and the plate does not take any bending due to 1mm thickness and it acts as a membrane. In this case, a simplification can be made that the plate is simply supported along the edge in the longitudinal direction. Looking at a cross-section of the plate, using boundary conditions as stated before and assigning vacuum pressure loads, the plate can be modelled as a cable structure with a uniform load along the cable.

4.2   Stringers

Stringers are the longitudinal members, which support plates and connect the rings. The top flanges of the stringers serve as the longitudinal supports for plates, while the bottom flanges are connected to the top flanges of the rings. At the ends they are slotted into the shim and flange of the tube.
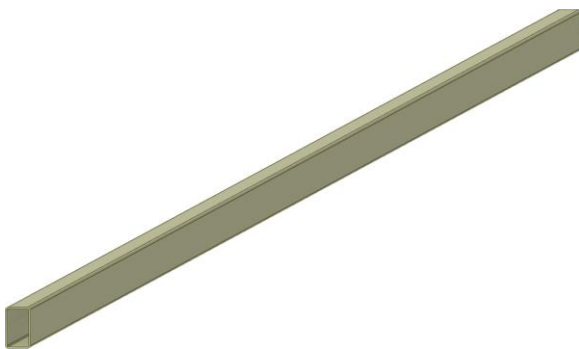
Figure 21: Single stringer of the skeleton tube design
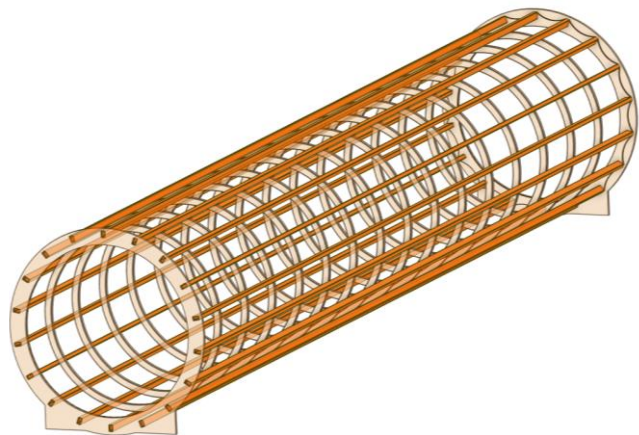
Figure 22: Location of the stringers within the Assembly.

The cross-section of the stringer is RHS ▮▮▮▮▮▮▮. The vacuum pressure load is transferred from the plate flanges to the top flange of the stringer and thereafter through the webs of the stringer to the rings. Stringers also offer most of the resistance to the longitudinal loads. The shell takes some amount of the force, but due to its thickness, it is dismissible. A load pattern in the longitudinal direction of the tube appears due to the pod acceleration and deceleration, due to thermal expansion and due to wind load in the longitudinal direction.

4.3   Rings

Rings are positioned between the stringers, and it is the only component group which is predominately in compression. They are crucial members for generating vacuum pressure resistance, which is the critical load case for the design. The cross-section is the same as that of the stringers, RHS ▮▮▮▮▮▮, and the diameter of the ring is 2.5m. The rings offer support to the stringers, and they are the final component in the load path. 16 rings are positioned in a 16m long tube segment, with the first and last rings spaced 0.5m from the tube flange, while all rings are spaced 1m between each other.
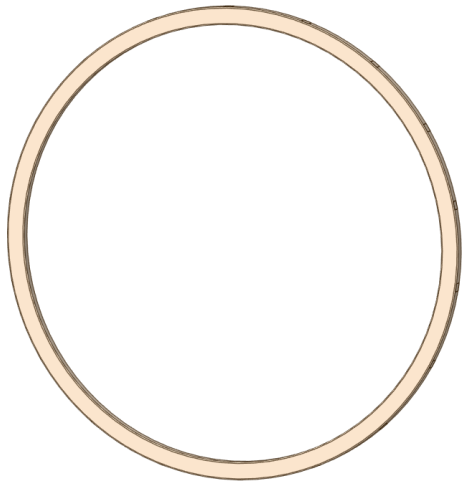
Figure 23: Single ring of the skeleton tube design
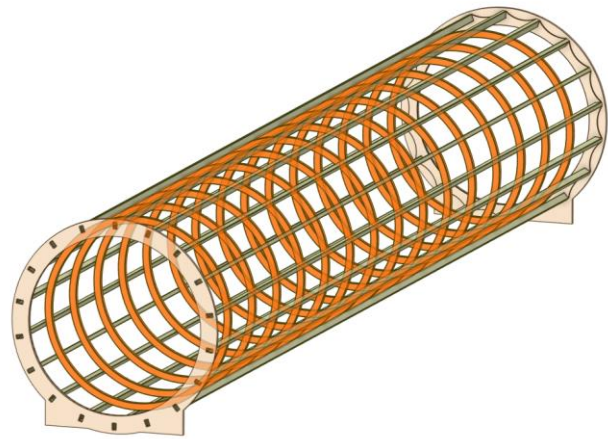
Figure 24: Location of the rings within the Assembly. Spacing between the rings is 1m, while spacing between the ring and flange is 0.5m

The ring-to-stringer connections can prove to be problematic since the connection surface on the ring has a radius, while the stringer's flange is flat. Additionally, due to the bending process during the ring production, the flanges and webs tend to buckle inwards. This creates a gap between connecting components and can cause structural and assembly issues. Several workarounds have been done to mitigate this problem, as well as a proposal for a new connection. More on that in chapter 8.

4.4 Shim

Shims serve as a saddle for the plates, i.e., they offer a transversal support to the curved plate. The inner diameter of the shim is 2.5m, the thickness is 20mm, and curved saddles have the same arch as curved plates (Figure 26). They also have 18 slotted rectangular holes for stringers to be fixed. Shims are then bolted to the flanges of the tube.
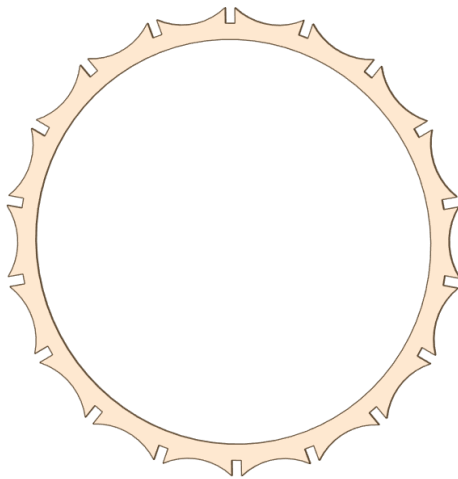
Figure 25: Shim of the skeleton tube design
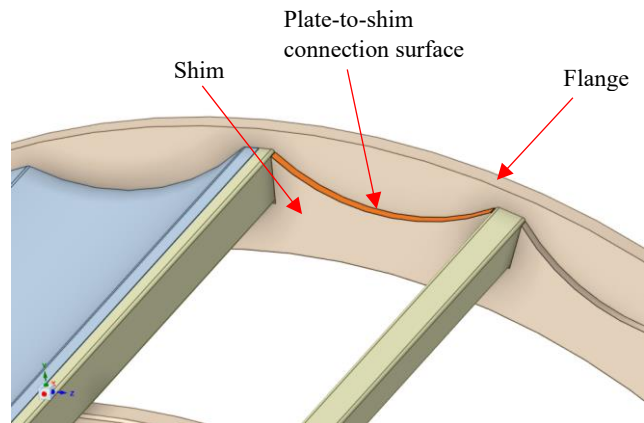
Figure 26: Curved surface for plate-to-shim connection.

4.5 Flange

The tube flange is the last component, marking the end of the tube segment. The inner diameter measures 2.5m, and the thickness is 40mm. It has 36 bolt holes, which serve to connect shim on one side and to connect to another tube segment on the other. Flanges are also connected to the foundation on the bottom edge, following the same principle as the flanges of the plain tube design constructed at European Hyperloop centre.
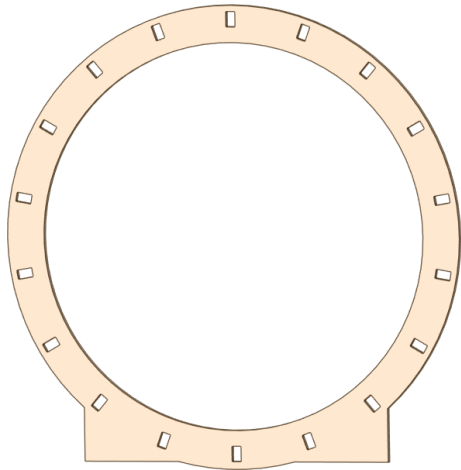
Figure 27: Flange of the skeleton tube design
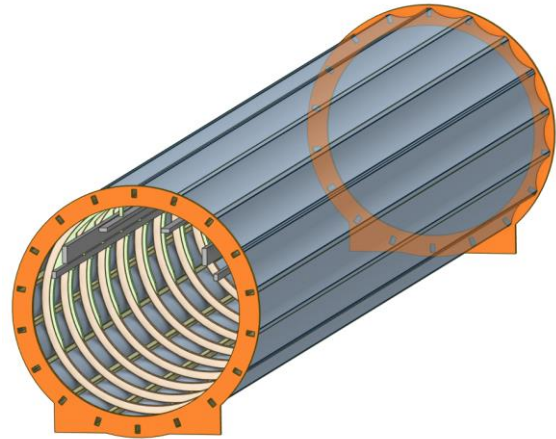
Figure 28: Flanges within the assembly

4.6   Rails support

Rail supports are located on the inside of the rings, offering support for the rails and inner components. In the plain tube design, rail supports are bolted to the tube, which can be seen as pinned connections, and therefore present dead load only to the structure. On the contrary, in the skeleton tube design, they also reinforce the structure due to being rigidly connected to the rings.

This design decision has been made after several options were considered. Skeleton tube design is lightweight, and the thicknesses of components are between 1 and 3mm; thus, bolted connections cannot be considered. The initial idea for this tube design was to serve only one purpose, and it is to retain vacuum pressure. Inner components would then be supported by a beam spanning between the pylons. This idea was scrapped after considering the weight of the rails and the additional weight due to the pod. Research could be conducted on the minimum required span between pylons to make this approach feasible, e.g., 8m instead of a 16m span between supports.

Another design factor for rail supports was buckling failure mode. Rings are in compression, and the webs of the rings can experience local buckling. Resistance of the rings also governs the design since the load path from the vacuum pressure, as well as from external actions, ends at the rings. With this consideration, the idea of rigidly connecting supports to the rings emerged. The design process is showcased in the following figures:
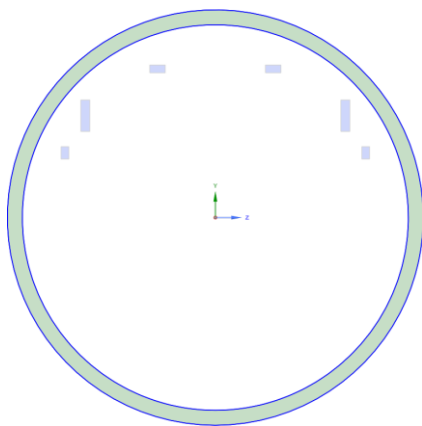
Figure 29: Position of the inner components
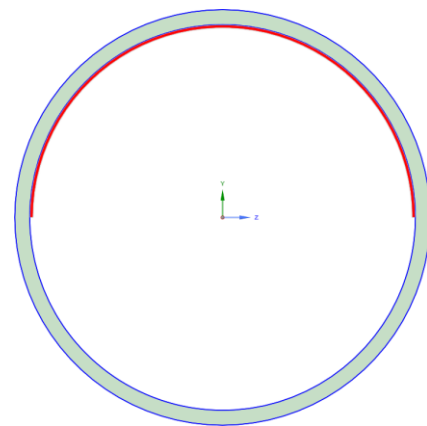
Figure 30: First version of the ring reinforcement with flat edges
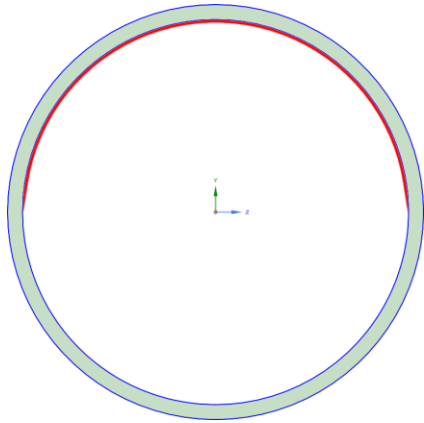
Figure 31: Tapered edges to reduce stress concentration in the ring
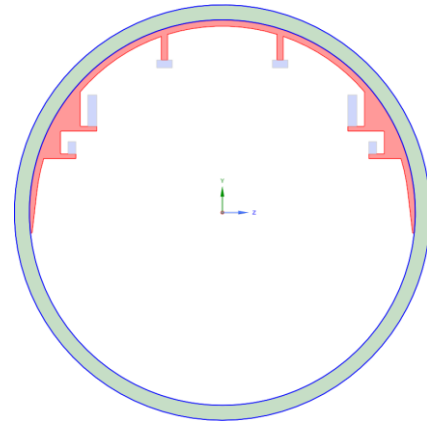
Figure 32: Rail support design based on the location of the rails
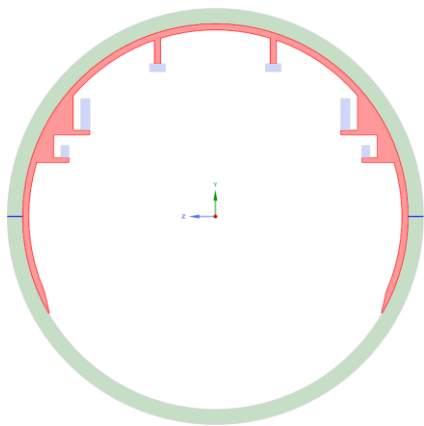

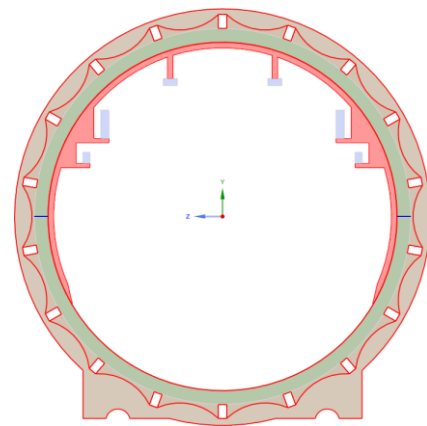*Figure 33: Extended edges to reduce stresses and additionally reinforce rings*

Figure 34: Front view of the Skeleton tube design with the final version of the support

The rail supports are not optimised in terms of weight. The design was governed by the location of the rails within the tube and by stresses in the rings. This justifies the tapered edges and increased length, which not only additionally reinforces the structure but also reduces stresses in the rings at the location where the supports end.
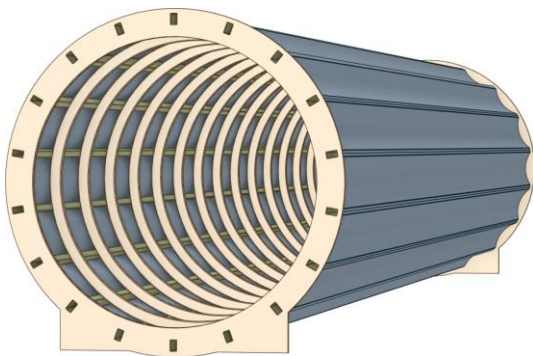
Figure 35: Skeleton tube design without rail supports
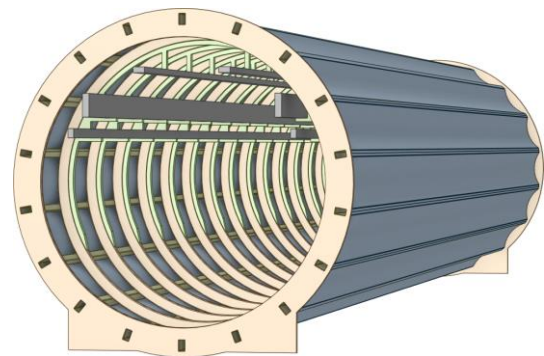
Figure 36: Skeleton tube design with rail supports

Fixed rail supports could also have a positive influence on the fatigue resistance of the structure, but this aspect necessitates a further researched. Following the assessment and verification of the supports' impact on the structure, the design optimisation can be conducted. This would be done by reducing the material at locations which are underutilised.

5 FEM model

In this chapter, the FEM approach is introduced. Modelling and analysis have been conducted in Ansys software, and the nonlinear material data was taken from DNV [7] standards. Additionally, this chapter provides an overview of all load cases acting on the hyperloop tube, as well as ultimate limit states and serviceability limit states combinations.

5.1 FE analysis type material properties data

Static structural analysis is performed in Ansys software [24], which determines the effect of static loads acting on the structure. From static analysis, it is possible to extract stresses, strains, deformations and internal forces/moments in the model. For the stability analysis, to determine the susceptibility to buckling, the eigenvalue buckling analysis is used. The static structural analysis can be performed using a linear or nonlinear analysis. The background for nonlinear analysis is that the stiffness of the system is not constant and changes with the deformation of the element. Therefore, the force vs displacement relation takes a nonlinear form. In the FEA model, these nonlinearities are introduced with:

Geometrical nonlinearity – The initial deformation of the tube might be linear, but as the deformation progresses, the cross-section of the component decreases, and the stiffness consequently reduces. In the skeleton tube design, this is expected to be expressed more vividly at thin plates onto which the vacuum pressure is acting.

Material nonlinearity – It involves the nonlinear behaviour of a material, which is captured in the material curve. It depends on the component deformation, rate of deformation, temperature, etc. In Ansys software, the material nonlinearity is defined with either bilinear or multilinear material data model. Two steel grades were considered in this research, S355 and S460. Corresponding multilinear isotropic hardening data is shown in Figure 37 and Figure 38, where true stress is plotted against plastic strain. This data also defines the transition from elastic to plastic behaviour. In Ansys, initially, the linear material curve is followed until the stress in the material reaches the first point, which deviates from the linear curve, as defined in the graphs. Thereafter, the nonlinear material curve is triggered, and the stress follows the predefined nonlinear stress-strain relationship.
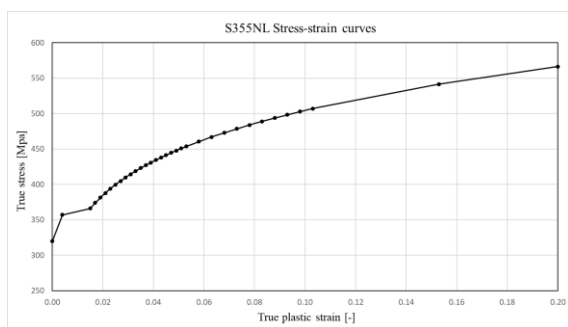

Figure 37: True stress - Plastic strain material curve for S355NL
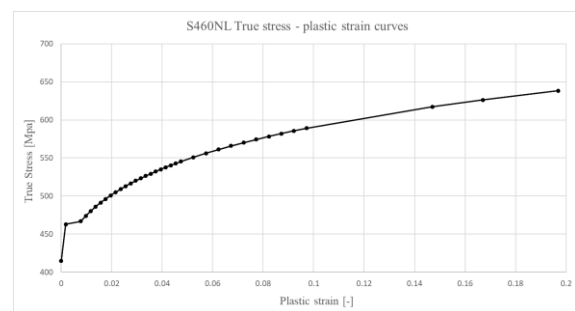
Figure 38: True stress - Plastic strain material curve for S460NL

Both material curves provide data beyond the ultimate strength of the material. This does not, however, affect the analysis since the ultimate strength of the material is known, and the results are only read until that point ($f_{u,S355}$ = 490MPa; $f_{u,S460}$ = 540MPa).

Contact nonlinearity – The initial applied force needs to be equal to the frictional force to allow for relative displacement between two surfaces. Following this, an increase in initial displacement occurs due to the applied force. This is not applicable in the preliminary design of the skeleton tube design since the plate-to-stringer connection type is not yet determined. If structural adhesive is considered as one of the connection options, then this nonlinearity would become relevant.

5.2 Newton-Raphson solver

A nonlinear problem is solved using a Newton-Raphson solver. This solver can be used in any nonlinear problem in structural mechanics and Ansys [24] uses this method by default. The solver starts with a zero initial displacement and an initial estimate of the stiffness, then it applies a force called F_a and calculates the resultant displacement u_1. This displacement is then imposed on the system and calculates the sum of all internal forces generated in the system called F_1. This is one iteration, and if this system is in equilibrium, then F_a equals F_1. If this is not the case, then the second iteration starts, where the initial displacement is u_1, and the estimate of stiffness is recalculated. The same steps are repeated, and the force F_2 is compared to F_a once again. This iteration process is repeated until this condition is met, and that is known as the force-converged solution. In theory, the number of iterations is infinite because to obtain a zero difference between F_a and F_n is almost impossible. Therefore, tolerance is defined as the difference between the forces.

The method is clearly presented in the following steps, given by Ansys guidebook [25].

Step 1: Initial displacement $\{u_0\}$ is assumed, which is either zero or from previous step

Step 2: Stiffness matrix [K] is linearized and evaluated based on the current displacement $\{u\}$ and other variable factors such as nonlinear material land contract status.

Step 3: The internal force F_{int}^n is computed from the element stresses.

Step 4: The displacement increment is calculated: $\Delta u^n = \frac{(F_{ext} - F_{int}^n)}{K^n}$

Step 5: Add Δu to $\{u_n\}$ to obtain the next approximation.

Step 6: Then the residual force is calculated: $F_{res}^n = F_{ext} - F_{int}^n$

Step 7: If $F_{res}^n \leq convergance\ criteria$ then the solution converged.

Step 8: Else, repeat step 1 through 7.

5.3 Mesh and Element type

The choice of the appropriate element type in the finite element method strongly depends on the problem being addressed. Hyperloop tube is a long and slender structure with a small height over length (h/L) ratio; therefore, transverse shear deformation does not significantly affect the structure. Thus, the 2D shell elements are recommended to use. They are generally used for thin-walled structures, membranes, or plate-like elements. Thin components of the tube indicate that large deformations can be anticipated once the loads are applied. Consequently, the use of higher-order elements is preferred for accurate stress estimations [7]. Thin shells do not consider stresses perpendicular to the surface, so for detail engineering, 3D elements were used to obtain accurate results.

Mesh density varies based on the model being analysed. Stress is expected to change rapidly at connections, and large elements are likely to lose some of the stress distribution. The mesh has been selectively refinement until the results did not change significantly. In larger models, such as 16m and 5m long tube section models, a coarser mesh was used to decrease the analysis time. Mesh at contact points and surfaces in a 5m model is sufficiently dense to correctly represent the stresses and potential failure modes. When modelling the detail, special consideration has been taken in transitioning mesh density and in the generation of mesh along the edges and corners, as these locations are susceptible to singularities. Mesh type and size is given in the corresponding table of each result section.

5.4   Contacts

Skeleton tube design consists of mostly thin-walled components, for which welds might not be the most optimum solution. However, since this is the early evaluation of the design, an assumption has been made that all components are perfectly bonded. This means that the two surfaces, which are in contact, can neither slide nor separate from each other. All normal and tangential forces are being transferred between the surfaces. This decision contributed to the ease of modelling and analysis.

In case if the connections would have been done using structural adhesives instead of welds, then a small translation would be expected between bodies in contact. This could be modelled with a different contact type, such as a spring connection, where a translational stiffness can be determined. The results would not differ significantly in the analysis of the preliminary design, but if the research was solely focused on the comparison between welded connections and connections using structural adhesives, then the differences could be potentially identified.

5.5   Load cases

In the design of the hyperloop tube, many load cases need to be considered. The system does not have unified rules for the infrastructure design yet. Thus, recent reports do not consider the same load magnitudes or load cases. Structural demands are taken from the methods of Eurocode in order to comply with the European safety standards. Since the tube is planned to be supported on the piers, the main anticipated failure mode is buckling. Environmental load cases are region-specific, and for this research, Groningen, Netherlands, was chosen since that is where the European Hyperloop centre is located.

5.5.1   Self-weight

Self-weight is classified as a permanent fixed action [26]. It represents the dead load acting on the structure due to its own mass and is dependent on the material and the cross-section of the components. The self-weight of the tube components is considered in all assembly analyses and disregarded in detail analysis. The self-weight of rails is assigned as the area load at the locations of attachment, where the weight was given at the production site visit. In Ansys, it is calculated using the standard earth gravity of 9.81 m/s^2 and material density of 7800 kg/m^3 for steel. The self-weight of the cabling is not considered due to the dismissible effect on the structure, while the propulsion system load is embedded in the pod load itself [3].

5.5.2   Vacuum pressure

The defining characteristic of the hyperloop system is the near-perfect vacuum environment within the tube. Vacuum pressure is the critical design parameter which affects the system's efficiency, safety and energy consumption. The load magnitude exhibited by this pressure is the difference between the atmospheric pressure and the pressure within the tube. The proposed pressure by Elon Musk's Hyperloop white paper [5] is 100 Pa inside the tubes. Considering the circular shape of the tube, the distributed force acts inwards, perpendicular to the tube's surface.

$$q_{atm} = 101\,325 \text{ Pa } = \text{ atmospheric pressure}$$
$$q_{tube} = 100 \text{ Pa } = \text{ tube pressure}$$

The imposed pressure on the plates is therefore:

$$q_{Ed} = q_{atm} - q_{tube} = 0.1 \text{MPa} \tag{5.1}$$

The plain steel tube that is currently being produced has a thickness of 16mm. Knowing that radius measures 1250mm, and Young's modulus is taken as 210GPa:

$$P_{cr} = \frac{E}{4 \cdot (1 - v^2)} \cdot \left(\frac{t}{R}\right)^3 = 0.12 MPa \qquad (5.2)$$

Therefore, in this research the vacuum pressure of $p = 0.12 MPa$ is used for ULS checks, and 0.1MPa for SLS.
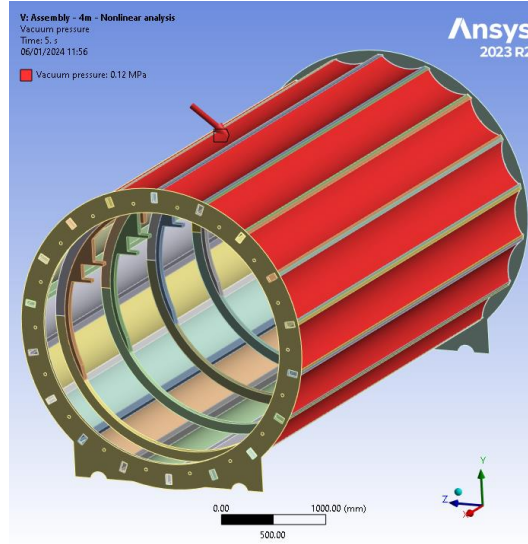

Figure 39: Vacuum pressure acting normal to the curved surfaces of the plates - 5m model with rail supports.

5.5.3 Snow load

Hyperloop tube structure has a cylindrical shape, and according to NEN EN1991-1-3 [27], it is considered as a cylindrical roof. The snow load is determined using the following formula for the fundamental design situation:

$$s = \mu_i \cdot C_t \cdot s_k \qquad (5.3)$$

By taking s_k as 0.7 kN/m² for the Netherlands, C_k as 1 and μ4 as 2 (see section C of Appendices for derivation), a balanced snow load s_b is obtained as 0.56 kN/m². The load is assigned to the top plates of the tube, as seen in Figure 40.
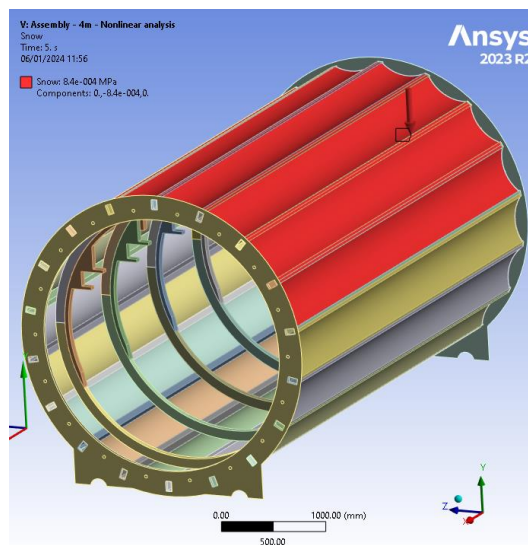
Figure 40: Snow load acting on the top plates in – Y-axis (ULS).

5.5.4 Wind load

The hyperloop tube is intended to be supported by piers at the edges of 16m long sections. Wind load calculation is dependent on the type of hyperloop system, i.e., whether it is constructed on the ground or above ground. In case it is on the ground, then the wind actions can be calculated with the assumption that the tube is a longitudinal circular cylinder. According to EN1991-1-4 [28], the wind force acting on the external surfaces is calculated with the following expression:

$$F_w = c_s c_c \cdot c_f \cdot q_p(z_e) \cdot A_{ref}$$ (5.4)

Reference area is calculated as 40m², $c_s c_c$ can be taken as 1, and air density is taken as 1.20kg/m³ [0.0012 kN/m³] and c_f resulted in 0.42 (see section C of Appendices for detail calculations). Therefore, the external force acting on the 16m long tube section is:

$$F_w = 10.04 \ kN$$

This results in an area pressure of:

$$q_w = 0.251 \frac{kN}{m^2} = 0.00025 \ MPa$$ (5.5)
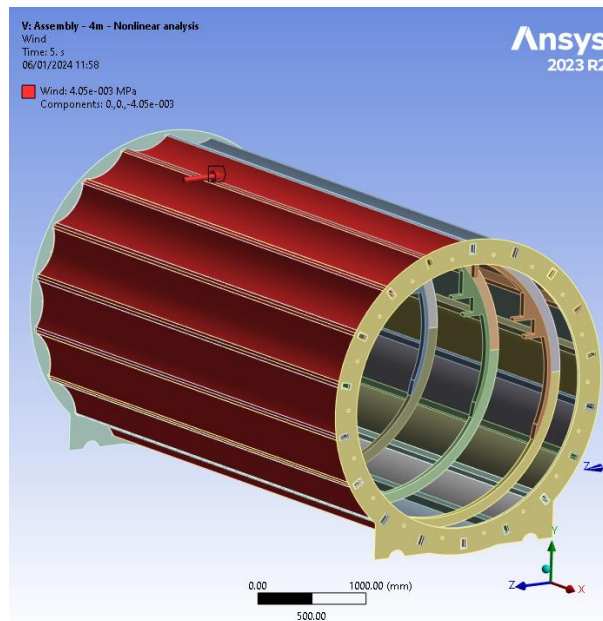
Figure 41: Wind load acting on the plates in – Z-axis (ULS).

5.5.5 Rails load

Rails are attached to the rail supports and introduce a dead load to the structure. Along the pod rails, the load consists of the levitation and propulsion rails. The load from the rails is concentrated at the points where they connect to the rail supports, meaning that the design of these supports affects how the load is distributed. By knowing the general location of the inner rails, the supports are designed (see Chapter 4.6), and the loads are assigned, as seen in Figure 42.
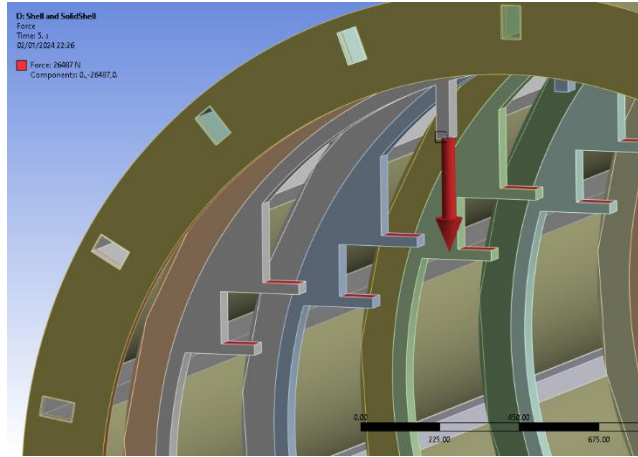
Figure 42: Rails load assigned at connection locations on the rail supports

5.5.6 Static load of the pod

The pod is attached to the rails and represents a vertical load to the rail supports. The magnitude depends on the size and length of the pod, as well as the weight of the cargo. In this study, it is assumed that the pod weight is 20 tons, with a length of 16 meters. Pod load is taken from the work of Muserues et al. [17], who investigated pod weights ranging from 10 to 20 tons and determined that fatigue is not a design concern for plain tube design. The assumption regarding length is made for the purpose of simplifying the application of load to the ring supports, ensuring even distribution among all rings in a single tube section. Therefore, the total pod weight is 196.2kN, which imposes a load of 12.26kN per ring support.

5.5.7 Moving pod

The pod is attached to the rails, and the rails are supported by the rail supports. As the pod moves along the rails, that imposes a moving load, which is transferred through the rail supports to the structure. According to NEN EN1991-1-2 [29], dynamic effects should be taken into account. This consideration is due to several factors: rapid rate of loading due to the speed of the pod; the passage of successive loads with approximately uniform spacing, which can excite the structure and, under certain circumstances, create resonance; and due to the potential wheel load variations resulting from either track or wheels [29]. Due to the lack of hyperloop infrastructure standards, the NEN EN1991-1-2 [29] is adopted for this load case. Based on these general design rules, the results from static analysis should be multiplied by the dynamic factor Φ.

Additionally, it is determined that dynamic analysis is required for this structure (See section C of Appendices). But, since dynamic analysis of the structure is outside the scope of this research, only the static analysis is performed with the use of dynamic factor, which resulted in:

$$\Phi_2 = 1.15$$

The total pod load is therefore:

$$F_{pod} = 196.2kN \cdot \Phi_2 = 225.63 \ kN \tag{5.6}$$

5.5.8 Breaking of the pod

Pod deceleration imposes a longitudinal force on the rails and from the rails to the rail supports. This force can cause instability of the rings and stringers. In the model, the longitudinal force is applied to the surfaces to which the rails are attached.

A maximum suggested permissible deceleration for trains provided by J.P. Powell et al. [30] is set at 2.45 m/s^2 for forward-faced passengers, which is approximately 0.25g. Considering the pod weight to be 20000 kg, this imposes the following longitudinal breaking force:

$$F_b = m \cdot a = 20000 \cdot 0.25 \cdot 9.81 = 49 \, kN \qquad (5.7)$$

The force is transferred from the rails to the ring supports. For simplicity, an assumption is made that the pod measures 16m; thus, since 16 ring supports are present per 16m tube segment, this imposes the following longitudinal load per ring support:

$$F_{l,ring} = \frac{F_b}{16} = 3062.5 \, N \qquad (5.8)$$

5.5.9 Thermal expansion

The temperature of the hyperloop tube structure may increase due to environmental conditions, leading to the expansion of the material. Considering the potential extensive length of the hyperloop network, this thermal expansion could result in large stresses in the tube. Therefore, the temperature variation needs to be determined, after which an assessment can be done on the tube expansion. Currently, the thermal expansion of the structure is mitigated with expansion joints. In this research, the temperature ranges from 20°C to 80°C is considered. The temperature deviation is otherwise based on extreme scenarios, where the maximum temperature is taken as 70°C, and -30°C as the minimum temperature. This Temperature range is in line with the range which was considered for the tube design currently used at the European Hyperloop Centre.

5.5.10 Foundation settlement

Foundation settlement is another concern which needs to be addressed. Sudden settlement can cause loss of contact between the tube and support, and consequently, the tube stays elevated above the foundation. This doubles the bending length of the tube and could have adverse effects on the passing pod inside the tube. The tube would also have increased compressive stress on the top and tension stress on the bottom. This scenario could be checked by either doubling the length of the tube and assigning the same loads or by assigning displacement support and allowing initial displacement that represents the foundation settlement. To foresee such occurrences, a monitoring system could be implemented at the supports, detecting any settlements at any part of the infrastructure.

5.5.11 Accidental loads

Hyperloop structure should be checked for accidental loads, such as vehicle impact, hyperloop pod impact, explosion etc. Considering the pod velocity and high safety measures required for the operation of the hyperloop system, it is important that the structure can withstand loads by accidental occurrences. It is a low-probability event, but the system needs to be well isolated from external factors to operate without disturbances. This load case was not considered in this research; however, the approach is provided in section Impact load analysis recommendation of Appendices.

5.6 Load combinations

Load combination is defined based on NEN-EN1990, Actions on Structures [26]. Structure consequence class 2 (CC2) is chosen in case the hyperloop tube is to be used only for cargo transportation and CC3 in case of passenger transportation. Since this is still preliminary research of the design, an assumption is made that only cargo will be transported in the initial phases of hyperloop applications. Therefore, for this structure, CC2 is determined. Load factors are taken from Table NB.4 – A1.2 (B) from NEN-EN1990 [31], where an unfavourable condition was chosen for permanent actions.

Table 2: Load cases and load magnitudes

Load case	Load magnitude
q_{self} - Self-weight	/
q_{vac} - Vacuum pressure	0.1 MPa
q_r - Rails load	58.860 kN
q_w - Wind load	0.375 kN/m^2
q_s - Snow load	0.56 kN/m^2
$q_{s.pod}$ - Static pod load	196.2 kN
q_{br} - Breaking of the pod	3.06 kN

General combination formula:

$$1.2q_{self} + 1.2\psi_0 q_{vac} + 1.2\psi_0 q_r + 1.5\psi_0 q_w + 1.5\psi_0 q_{br} + 1.5\psi_0 q_s + 1.5\psi_0 q_{st.p.}$$

Ten load combinations were formed, but only three most probable and critical are presented in this research. This is Load Combination 1, which is a scenario of the operating tube but without any external or internal actions. Load Combination 2 includes the snow load case, and load combination 10 is the critical combination, in which all load cases are present. All combinations, along with combination factors and corresponding load magnitudes, are given in section D of Appendices.

ULS combinations

LC1: Vacuum pressure only: $1.2q_{self} + 1.2\psi_0 q_{vac.} + 1.2\psi_0 q_r$

LC2: Snow: $1.2q_{self} + 1.2\psi_0 q_{vac} + 1.2\psi_0 q_r + 1.5\psi_0 q_s$

LC10: Critical combination: $1.2q_{self} + 1.2\psi_0 q_{vac} + 1.2\psi_0 q_r + 1.5\psi_0 q_w + 1.5\psi_0 q_s + 1.5\psi_0 q_{st.p.}$

SLS combinations

LC1: Vacuum pressure only: $q_{self} + \psi_0 q_{vac.} + \psi_0 q_r$

LC2: Snow: $q_{self} + \psi_0 q_{vac} + \psi_0 q_r + \psi_0 q_s$

LC10: Critical combination: $q_{self} + \psi_0 q_{vac} + \psi_0 q_r + \psi_0 q_w + \psi_0 q_s + \psi_0 q_{st.p.}$

6   Analytical approach

Initially, an analytical approach has been used to verify the components of the skeleton tube design. The model was simplified down to simple cases of beams and plates. Only the critical load case was considered, which is the vacuum pressure. Initial analytical checks gave an indication of whether the structure has the capacity to withstand the assigned loads.

6.1   Skeleton tube design

Preliminary analytical checks were performed on the components of the skeleton design. The initial load path has been identified, and each component has been modelled as a statically determinate structure. One of the known critical load cases on the tube is the vacuum pressure, which is the difference between the atmospheric pressure outside the tube and the pressure inside the tube. Taking the inner pressure as 100Pa, the imposed pressure on the plates is therefore 0.1MPa.

Considering the calculated area load, all components were checked in regards to either their strength, stability or deflection. To obtain the load distribution, the model can be simplified as two simply supported beams offering support to a longitudinal plate. The *a* and *b* in Figure 44 represent the spacing between two rings and spacing between two stringers, respectively.
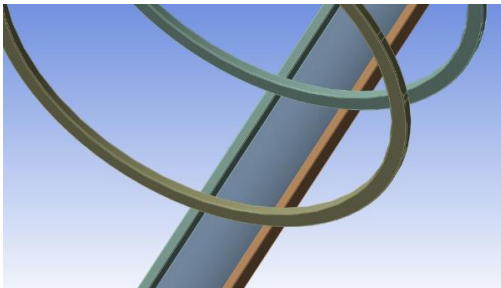
Figure 43: Isometric view of two stringer, two rings and a plate within the assembly
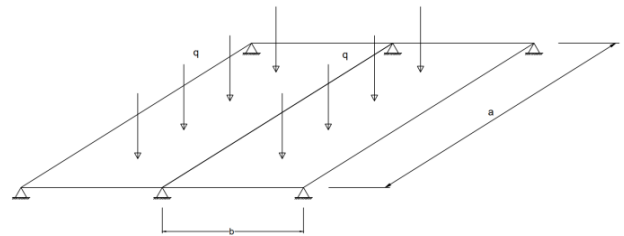
Figure 44: Simplification of the rings and stringers assembly

An assumption is made that the load is distributed as if the plates were flat, and not curved. The area load is evenly distributed across the plate, where each stringer takes half the area load. Given the plate thickness, tube length, ring diameter and number of rings and stringers, the area load per plate can be estimated. A safety factor of $k = 1.2$ is used.

$$q_{Ed} = (q_{atm} - q_{tube}) \cdot k = 121 \frac{kN}{m^2} \tag{6.1}$$

$$\text{Line load: } q = q_{Ed} \cdot b = 53.4 \frac{kN}{m} \tag{6.2}$$

The following verifications are related to strength, stability and serviceability. For detailed calculations see Appendices E.

6.1.1 Stringer verification

The stringers are simplified as the beams loaded by a uniformly distributed load along the length.
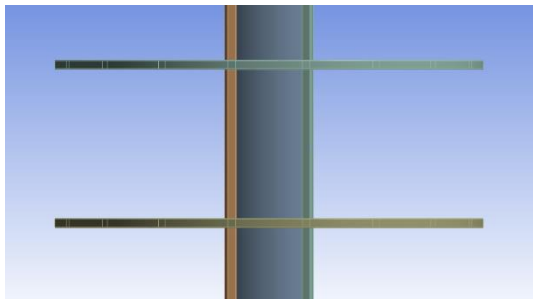
Figure 45: Top view of the stringers within the assembly
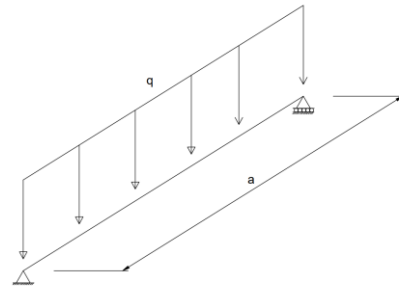
Figure 46: Stringer simplification

Bending moment resistance, shear force resistance and a combination of both have been verified. Lateral torsional buckling is not expected to take place since a rectangular cross-section is assigned, and moreover, the length of the elements is short. Deflection does not play a vital role when considering only 1m spacing between the rings; nonetheless, the verification was done. With the assumption of pinned boundary conditions, it resulted in 3.57mm, whereas the deflection limit is 4mm (see section E of Appendices for detail calculations).

6.1.2 Ring verification

The load path goes from the plates to the stringers, and from the stringers to the rings. Load on the ring can be expressed as point loads at the location of the stringers, as presented in the following figures.
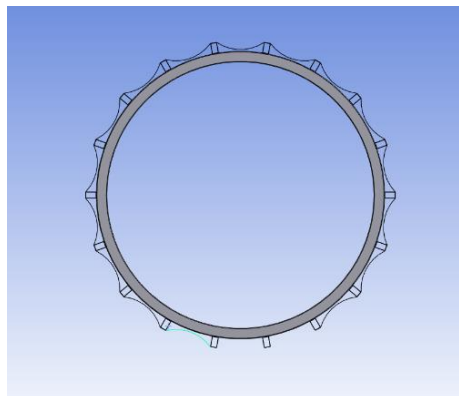
Figure 47: Cross-section of the Skeleton tube design
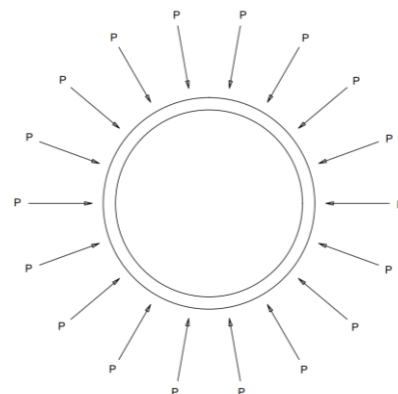
Figure 48: Simplification of the ring model

Point loads from the stringers represent the shear force to the rings, therefore the check is identical to the shear resistance check of the stringer. For the stability check, the ring is simplified as a column laterally supported at the location of the stringers. The applied load in this case is only from the vacuum pressure, but in a later stage, the critical load affecting the ring stability will be the non-uniform loading, such as wind or snow load.

Initially the critical buckling length is taken as the distance between two point supports, represented by stringers, as seen in Figure 49. To recreate a critical situation, an assumption is made that ring-to-stringer connections in the middle fail, so the supports in the middle are removed. This increases the critical buckling length to 2.5m.
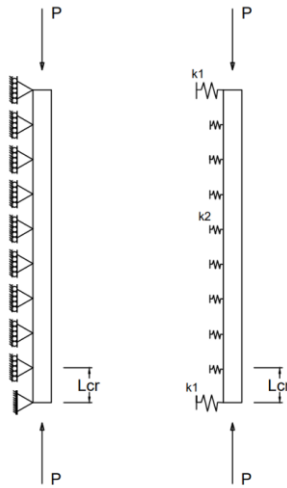
Figure 49: Simplification of the ring for the stability verification

For more realistic simplification of the model, the supports could be expressed as springs since the tube itself experiences global buckling. Ring-to-stringer connections would determine the stiffness of these springs. But the global instability of the rings is not significant, therefore the initial assumption can be used. The verification proved that the global stability of the rings is not satisfactory.

6.1.3 Plate verification

Curved plate has been modelled as a cable structure with the uniform load along the cable.
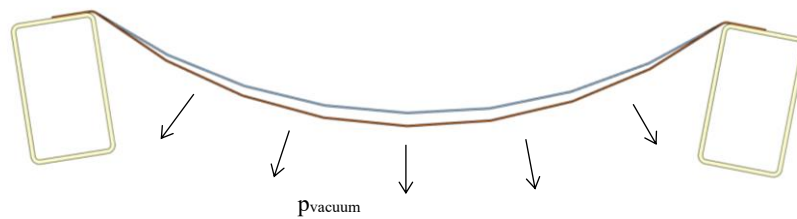
Figure 50: Plate cross-section
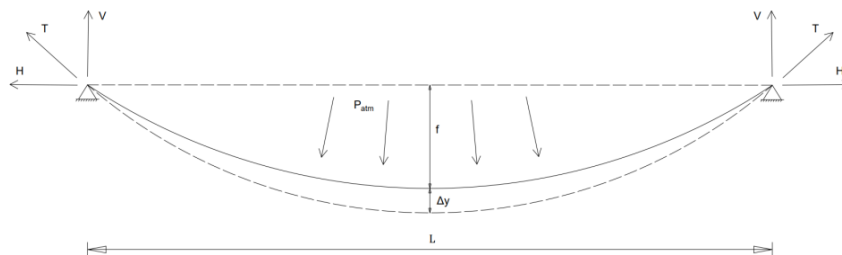
Figure 51: Plate simplification as a cable structure

In order to calculate the deflection of the plate, axial cable deformation (strain) needs to be calculated. An assumption is made for the pinned supports, and in order to calculate the deflection of the plate, axial cable deformation was calculated. The total vertical deflection due to vacuum pressure resulted in only 0.6mm, which meets the allowable deflection of 15mm. Detail calculations are given in section E of Appendices.

6.1.4 Ring-to-stringer connection verification

The load path travels through the webs of the stringer to the webs of the ring. Since components lay perpendicular to each other, the area through which the load is transferred is concentrated on four strips. One of the issues is that the ring has a curved flange, while the stringer has a flat flange. This geometrical discrepancy leads to a gap between the two surfaces which are in contact. Although a single gap alone is unlikely to cause unforeseen structural behaviour once the tube operates, it can nonetheless affect the construction process, especially if the geometrical imperfections would accumulate throughout the whole length of the tube section. One of the potential issues is a non-uniform load transfer to the ring, which could cause increased stresses on one side, and consequently, local buckling of the webs.

Vacuum pressure load path

If only the vacuum pressure load is considered, since it is a critical load case, then the stress in the webs can be calculated. A vacuum pressure of 0.12 MPa is considered in this research, and the vacuum is retained by the plates of the skeleton tube design. The load is then transferred from the plates to the stringers, and subsequently to the rings. For clarification, Figure 52 represents forces in previously described load path.
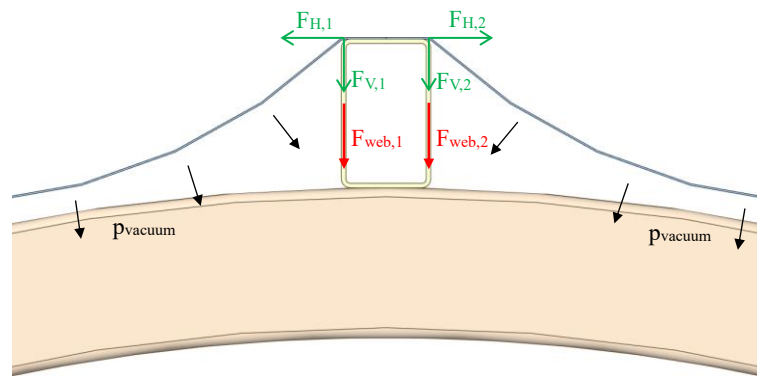
Figure 52: Visualisation of the load path due to vacuum pressure. Initially, the vacuum exerts its pressure on the curved plates. The force from the plate is then divided into horizontal and vertical force component. The force is then transferred via stringer webs to the rings. The bending moment in the plates is neglected due to their thickness.

For the analytical calculation, a simplification of curved plates is made and assumed as if they are flat. Another assumption is made that the radius will not affect the load path, i.e., the radius is small enough to transfer the load as if it wasn't present. The spacing between stringers is 400mm, the width of the stringer flange is 60mm, and the spacing between rings is 1000mm. The load per ring is therefore calculated as follows:

$$A_{total} = 460000 \ mm^2$$
$$F_n = p \cdot A = 55.2 \ kN \tag{6.3}$$

Two loaded strips are applicable if the stringer does not deform significantly, i.e., if the ring flanges do not buckle upwards once the load is applied. In case of a larger deformation, then the flanges are less utilised, and the load transfer into four smaller areas becomes evident. The normal stress in the case of two strips is therefore calculated as:

$$A_{strip,2} = \ 3 \cdot 60 \ = 180 \ mm^2$$

$$\sigma_n = \frac{F_n}{2A_{strip,2}} = 153.33 \frac{N}{mm^2} \tag{6.4}$$

$$UC = \frac{\sigma_n}{f_y} = 0.44 \ \ O.K.$$

In case of large deformation, the load would be distributed to four strips. In the analytical method, it is difficult to predict the length of a single strip since it depends on the steel grade, load magnitude and total deformation. An inverse engineering approach can be used to calculate the minimum required area strip for which the yield stress will not be reached. Therefore:

$$\sigma_n = \frac{F}{A} \quad \rightarrow \quad A = \frac{F}{\sigma_n} = 155.5 \; mm^2$$

$$A_{strip,4} = \frac{A}{4} = 38.87 \; mm^2 \tag{6.5}$$

$$A_{strip,4} = w \cdot l \quad \rightarrow \quad l = \frac{A_{strip,4}}{w} = 13 \; mm$$

The minimum length is, therefore, 13 mm. It should be noted that the analytical approach was performed considering vacuum pressure only. Due to the slenderness of the structure, it is expected to be sensitive when exposed to non-uniform loadings, and its structural response might prove to be difficult to predict and verify analytically.

In the following table, all analytical results are summarised.

Table 3: Summary of analytical results

Unity check	$\dfrac{M_{Ed}[kNm]}{M_{pl,Rd,y}\,[kNm]}$	$\dfrac{V_{Ed}[kN]}{V_{pl,Rd,y}\,[kN]}$	$\dfrac{\sigma\,[MPa]}{\sigma_y\,[MPa]}$	$\dfrac{\delta[mm]}{\delta_{allowed}\,[mm]}$	$\dfrac{P}{N_{cr}[kN]}$
Stringer	0.6	0.37	/	0.89	/
Ring		0.37	/	/	0.08
Plate	/	/	0.2	0.04	/
Connection	/	/	0.44	/	/

6.2   Plain tube design

As mentioned in Chapter 2.5, the buckling resistance of the tube can be verified using the critical buckling formula. Knowing that the radius of the tube is 1.25m, and that the thickness determined by the designers is t = 16mm, the critical pressure can be calculated.

$$P_{cr} = \frac{E}{4 \cdot (1 - v^2)} \cdot \left(\frac{t}{R}\right)^3 = 0.121 \; MPa \tag{6.6}$$

The anticipated vacuum pressure for efficient use of the hyperloop system is 1 bar, which imposes 0.1MPa surface pressure. The unity check it therefore:

$$UC = \frac{0.1}{0.121} = 0.826 \quad O.K. \tag{6.7}$$

7 FEM Approach - Skeleton tube design

Skeleton tube design is initially decomposed into single components, which are analysed separately. Appropriate boundary conditions are assigned at the locations where they are connected to adjacent components in the assembly. FEM analysis of individual components is conducted to identify potential weaknesses of the design and to predict their behaviour within the assembly. Thereafter, the whole skeleton tube design assembly is analysed. For the comparison study, the plain tube design, which is used at the test site at the European Hyperloop Centre has been modelled using the information gathered from the production site and test site visit. Additionally, based on identified weaknesses in the assembly, design modifications are suggested. The proposed ring-to-stringer connection design is also modelled and analysed.

7.1 Individual components

Skeleton design consists of three unique components: plate, stringer, and ring. For the simplicity of comparison with the analytical approach, only the vacuum pressure load case has been considered in all models.

7.1.1 Plate analysis

Initially, a single plate was analysed to determine whether the 1 mm thickness can withstand vacuum pressure load. Boundary conditions are set as fully fixed at the surfaces, which are in contact with the stringers and shims, and pressure load is assigned normal to the surface. The setup is presented in Figure 53.
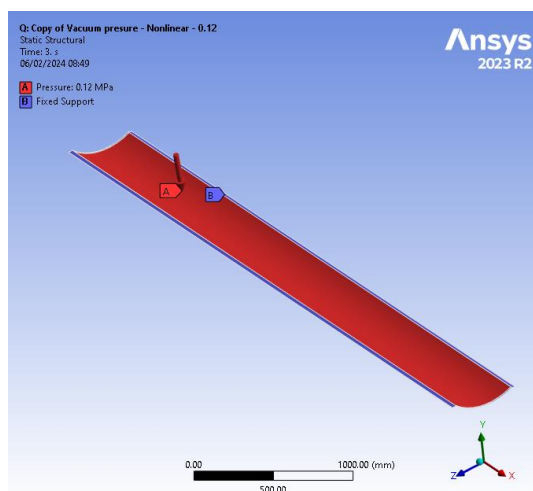
Figure 53: Single plate model setup. Fully fixed boundary conditions are assigned at the flanges and edges of the curved surface.
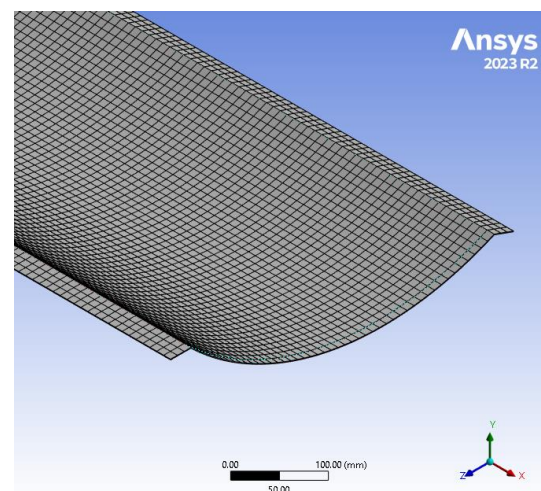
Figure 54: Single plate - mesh [10 mm]

Due to the small thickness of the plates, large deformation were expected once the loads are assigned. The choice of steel grade can affect the structural response of the plates in terms of deflection. Therefore, structural steel S355 and S460 have been considered in the analysis. The boundary conditions in the model of a single plate are not the exact representation of the stringers. Due to forces passing from the plate to the top flanges of the stringers, the stringer webs tend to buckle. Therefore, the stringers' support to the plate flanges represents more of a spring support. The stringer web deformation is dismissably small on the global scale but contributes to the plate deformation shape. This is showcased in more detail in Chapter 7.2.

The model details are presented in the following table:

Table 4: Single plate - model settings

Material	Structural steel S355
Model type	Shell
Mesh	Quadratic
Element size	10mm
Analysis type	Linear and nonlinear
Loads	Vacuum pressure

Equivalent stress and total deformation were obtained from the linear analysis. The highest stress occurs along the edges where the plate bends, as illustrated in Figure 55. The deformation is of the anticipated shape, with the maximum deflection in the middle of the plate, Figure 56.
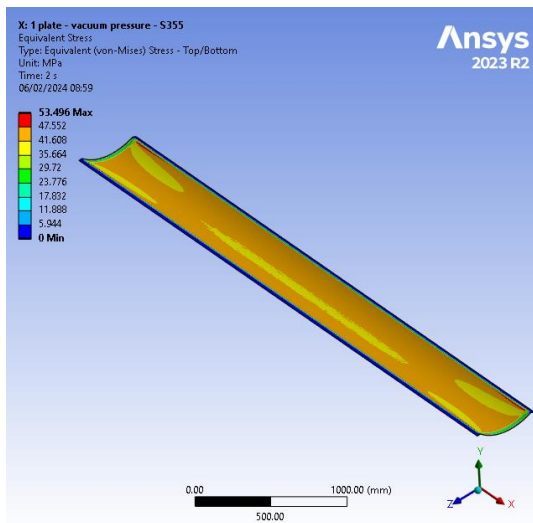
Figure 55: Equivalent Von-Mises Stress [MPa] – Linear analysis
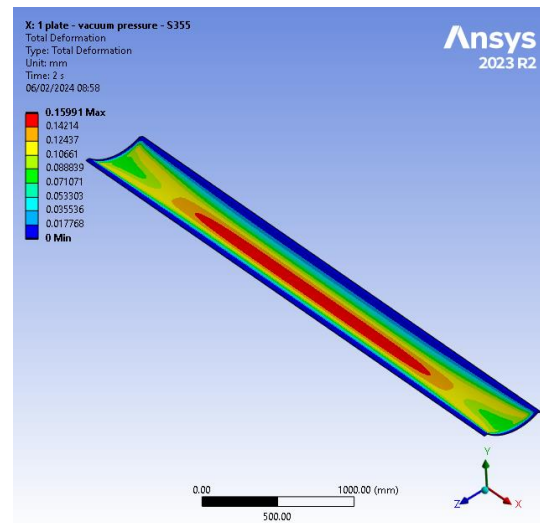
Figure 56: Total deformation [mm] – Linear analysis

Subsequently, a nonlinear analysis was conducted, and the same results were extracted. It was expected that the deformation will be slightly larger and more uniform, while stresses almost identical since it exhibits an elastic response.
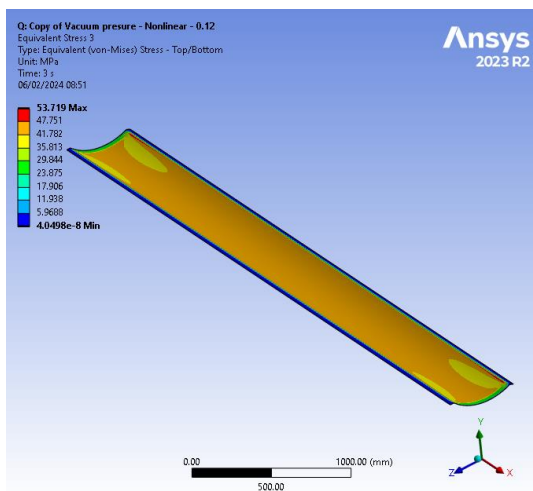
Figure 57: Equivalent Von-Mises Stress [MPa] – Nonlinear analysis
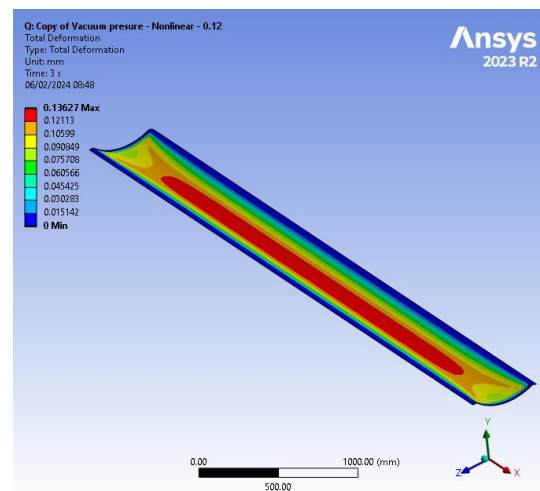
Figure 58: Total deformation [mm] – Nonlinear analysis

The linear analysis exhibits larger maximum deformation, while the deformation in the nonlinear analysis is more uniform along the entire plate. Comparing Figure 56 and Figure 58, it is visible that the plate begins deforming towards the edges, while in the linear model, the maximum deformation is concentrated in the centre area of the plate. Stress is increased along the plate edges, which is partially due to modelling and due to the design as well. Moreover, the comparison of stress levels between both types of analysis and both steel grades did not differ since the plate was not loaded to its yield point.

The difference in deformation between the linear and nonlinear analysis is 15% and 12.5% for S355 and S460 steel, as seen in Graph 1 to Graph 4. This is an indication that a nonlinear analysis is required, and an even larger discrepancy between the two types of analysis is anticipated in the assembly model.
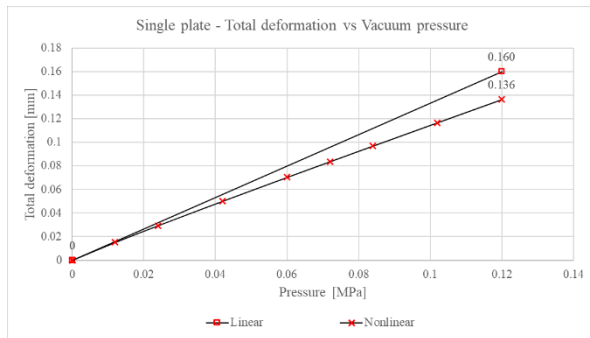
Graph 1: Deformation difference between linear and nonlinear analysis of the single plate – S355
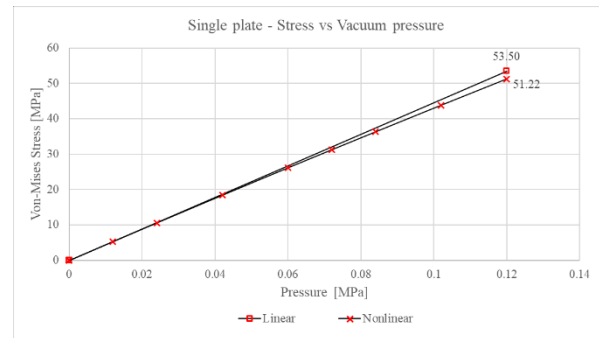
Graph 2: Stress difference between linear and nonlinear analysis of the single plate – S355
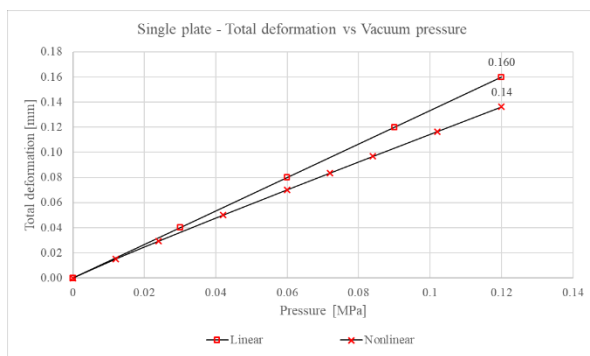
Graph 3: Deformation difference between linear and nonlinear analysis of the single plate – S460
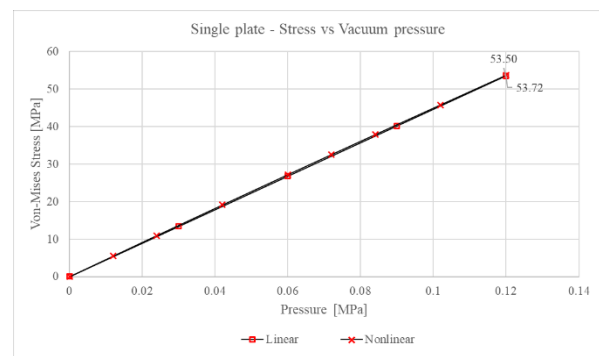
Graph 4: Stress difference between linear and nonlinear analysis of the single plate – S460

7.1.2 Gradually increased point load analysis

The skin of the skeleton tube design measures 1mm in thickness, and it does not offer significant resistance to any external actions. An analysis was conducted to determine its resistance to the point load. A circular area of roughly 3000mm² has been gradually loaded until failure. This encompasses a scenario in which a heavy object is laid on top of the plate. Vacuum pressure is present as well to consider an unfavourable situation. The setup is identical to the previous analysis, with boundary conditions set as fully fixed at the surfaces which are connected to the stringers and shims. The load was gradually increased from 0 to 20 MPa, or until failure. The aim was to identify the load at which the yield point and ultimate strength is reached.
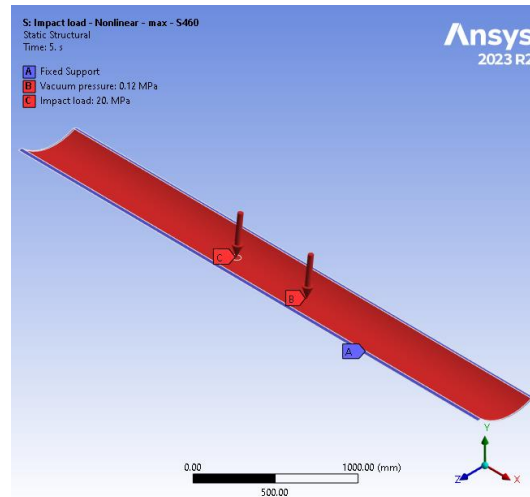
Figure 59: Setup of the impact load analysis. Vacuum pressure is assigned to the curved surface (B) and additional circular area load (C)

The yield strength was reached at area pressure of 1.87MPa (Figure 60), which is approximately a load of 5.61kN. The plate deforms vertically by 4.85mm, as seen in Figure 61. This deformation is satisfactory, since it ensures that the plate will not make contact with the ring, given the 15mm spacing between them.
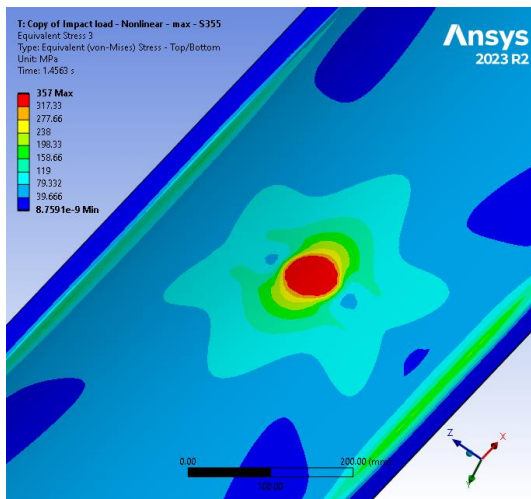
Figure 60: Yield strength at p = 1.87 MPa – S355
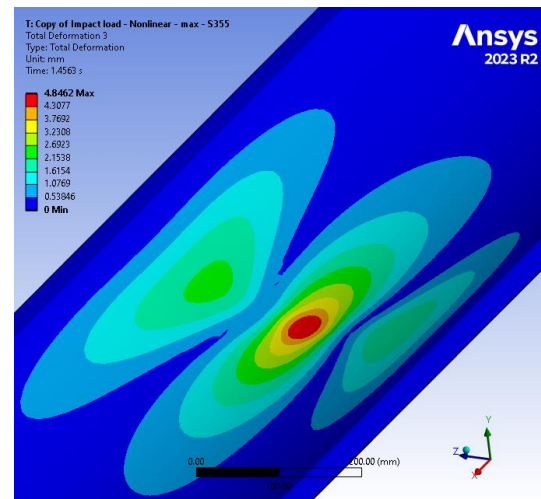
Figure 61: Total deformation at p = 1.87 MPa – S355

Ultimate strength is reached at 8.9MPa of area pressure, or a point load of 26.7kN (Figure 62). The deformation at this stage is 15.5mm, which is 0.5mm more than the maximum allowed deformation.

This indicates that if the point load would have been assigned directly above the ring, contact could occur in an unfavourable situation, and potentially causing the plate to rupture prematurely.
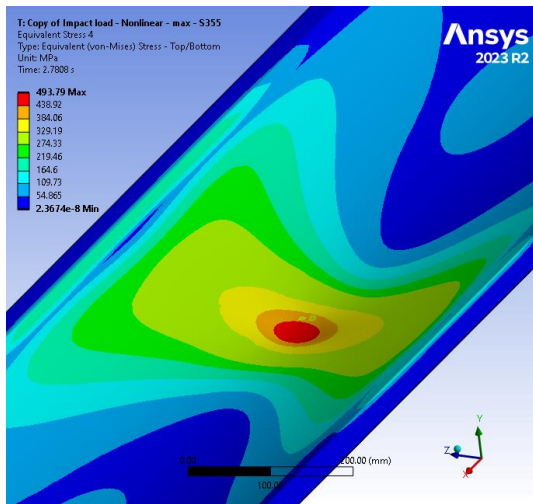
Figure 62: Fracture at p = 8.9 MPa S355
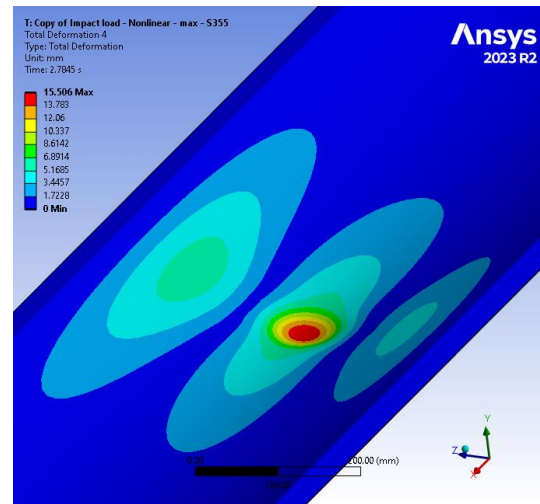
*Figure 63: Total deformation at p = 8.9 MPa – S355*

By increasing the steel grade from S355 to S460, the area pressure at which the yield point is reached is increased by 8.5%, and the total deformation at that point is 4.36mm. That is 11% less than for S355. The failure point is reached at the area pressure of 7.93MPa, which translates to 23.79kN. The total deformation at that point is 11.14mm.

All results are compiled in the following graphs, demonstrating the gradually increasing circular area pressure, and plate's corresponding stress (Graph 5) and total deformation (Graph 6). As expected, the S355 steel grade is more ductile, and therefore the material reaches the yield point sooner, but it is able to deform plastically more than the S460.
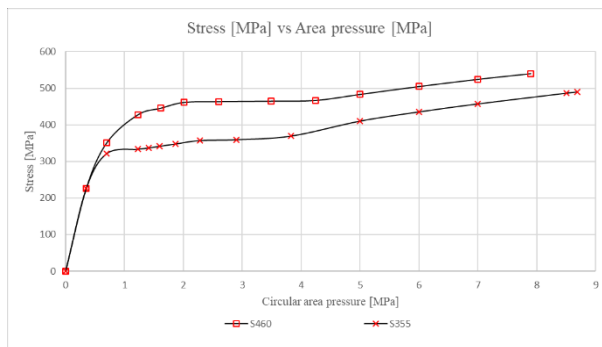
Graph 5: Point load analysis - Stress [MPa] in the plate
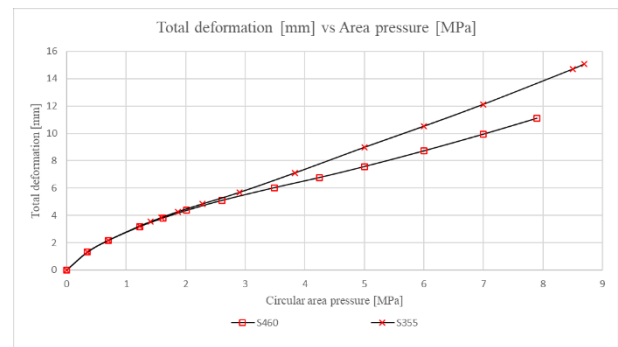
Graph 6: Point load analysis - Total deformation [mm] of the plate

7.1.3 Thermal effects

If the tube is exposed to the sunlight, or if the internal components heat up while operating, this imposes a thermal action on the structure. In the case of the skeleton tube design, where many components are interconnected, thermal expansion can cause many unwanted or unforeseen stresses in individual components. This can consequently negatively affect connections, cause residual stresses and ultimately weaken the structure. Linear expansion formula will be used in this application. Thermal expansion is governed by change in temperature and change in temperature cause a change in the rate of expansion. Linear expansion formula is given as:

$$\Delta L = \alpha \cdot L_0 \cdot \Delta T \qquad (7.1)$$

Coefficient of thermal expansion for Structural steel is 0.000012 C^{-1}. This coefficient of thermal expansion is defined by default in Ansys software as well. The length of the single plate model is 4m, and the temperature increase is from the ambient temperature of 22°C to 80°C. Therefore, the temperature change is 58 °C. This results in thermal expansion of 2.78 mm.

As seen in Figure 64, in order to obtain directional deformation due to thermal condition, the roller support had to be assigned at the location of the stringers and on one side of the plate, where the plate is connected to the shim. The other side of the plate is fully fixed.
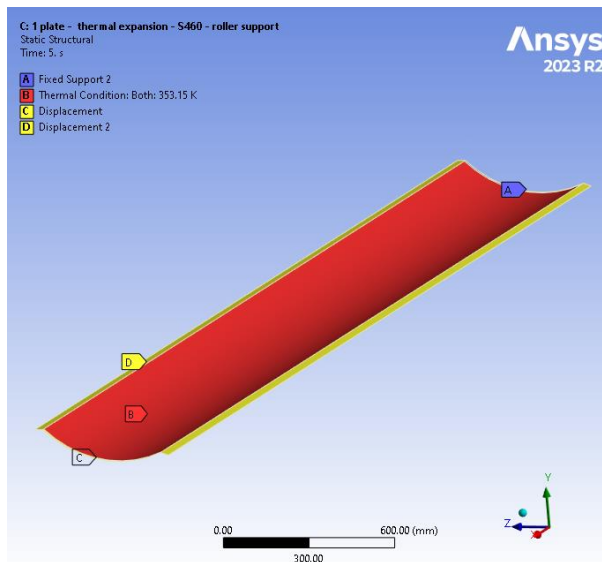
Figure 64: Thermal expansion analysis - Setup
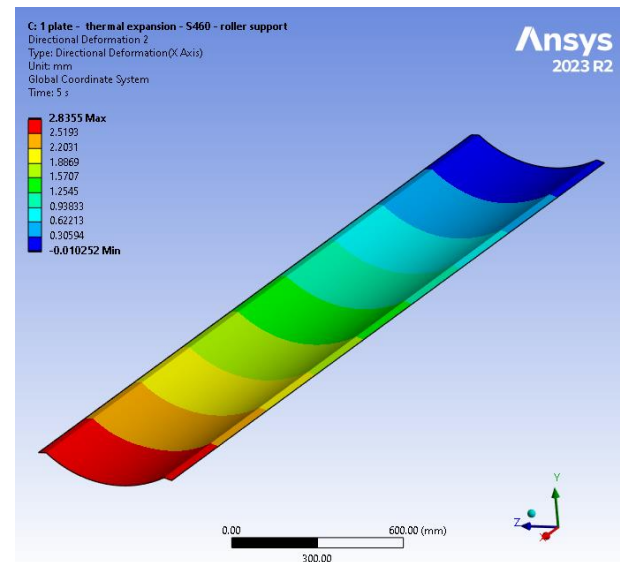
Figure 65: Thermal expansion - directional deformation [δx = 2.83mm]

Ansys analysis output an almost identical result, with the directional deformation of 2.83mm per 4m long plate section. The difference between analytically calculated expansion and FEM result is 0.076mm or 1.65%. This is due to the boundary conditions assigned in the model, where the fixed side is not an edge, but a strip of the plate, which is connected to the shim. Considering that the length for the tube section is 16m, the longitudinal tube expansion in the critical scenario will result in ~11.1mm, meaning that there is a need for expansion joints.

7.1.4 Ring analysis

The FE analysis of the ring only is done by applying two line loads, as seen in Figure 66. That is the area where the stringer due to bending transfers the load to the ring webs, and the load magnitude is governed by the vacuum pressure load case. The setup is done in a way that is comparable to the simplified analytical approach.
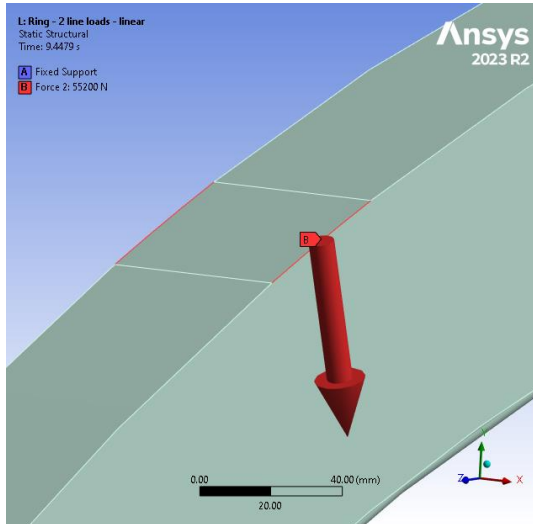

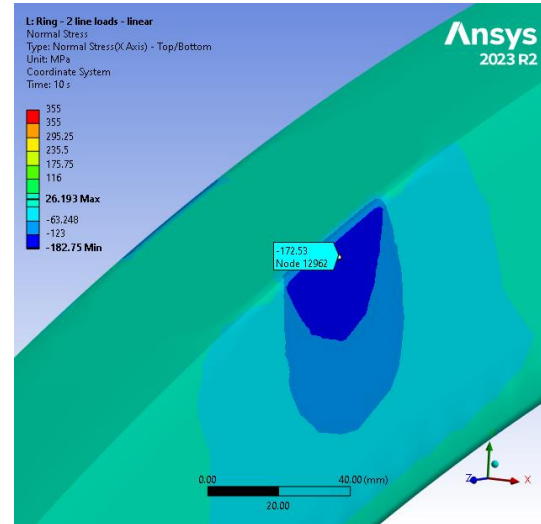*Figure 66: Setup of the ring analysis.*   *Figure 67: Normal stress [MPa] at the loaded strip.*

Maximum stress is at the location of the support. This stress reading can be dismissed, since it is not of the essence. Probe is used to read the stress at the relevant location, which is slightly under the applied load. The normal stress σ_n results in 172.53 MPa, which is 11% higher than the result obtained from the analytical approach. The difference can be explained by considering the deformation, which is present in the FEA model. As the ring web under the load deforms, there will be forces acting in the opposite direction since the material tends to resist the deformation.

7.2 Assembly

A single tube section measures 16m in length, but due to the model's size, a shorter 5m long model has also been analysed. Limitations of each model are stated before the section with results. The three most probable load combinations are considered and presented. These are LC1, LC2 and LC10, which are also described in section 5.6. LC1 is applicable when the tube is under vacuum pressure, but exposed to environmental actions, nor the pod loads. LC2 is a scenario in which the snow load is the dominant load case, and LC10 is the critical load combination, which includes all considered load cases.

7.2.1 Linear vs nonlinear analysis

Initially, it had to be determined whether linear analysis is suitable for this model. It is anticipated that many components of the design will deform when the model is loaded, and these deformations will affect the global structural response of the assembly. Identical model was analysed first using a linear material and without large deformations, and thereafter using a nonlinear material and with large deformations turned on. Assembly stresses are given in Figure 68 and Figure 69, where the stress in the linear analysis reaches 517MPa. This is beyond the 490MPa ultimate strength of S355 steel. On the contrary, the nonlinear analysis resulted in maximum stress of 336 MPa, which is below the yield strength. One of the conditions for linear analysis is to stay within the elastic limit, and if the material in the model experiences a nonlinear stress-strain behaviour, then the nonlinear analysis must be used. As the structure deforms, the component's stiffness decreases. Consequently, the stresses decrease as well, and generally the model deformation increases.
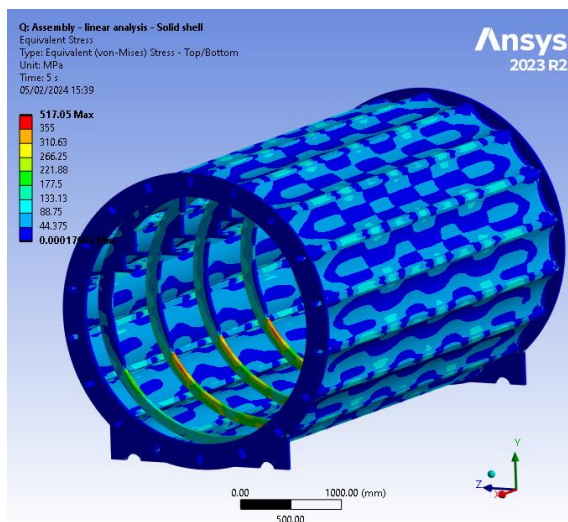
Figure 68: Equivalent von Mises stress [MPa] of the assembly due to LC10 – linear analysis
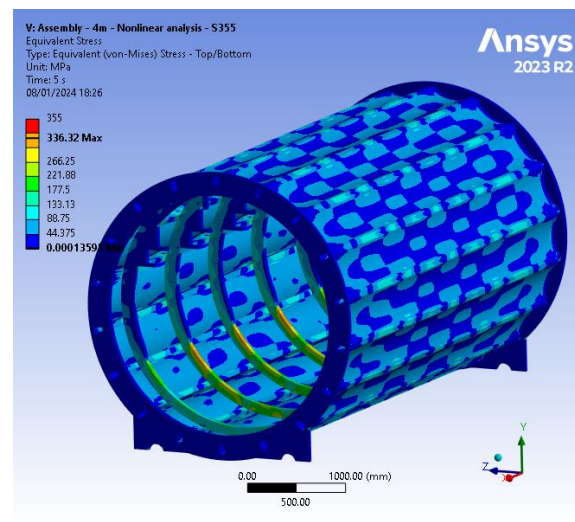
Figure 69: Equivalent von Mises stress [MPa] of the assembly due to LC10 – nonlinear analysis

As mentioned in the individual component analysis, the nonlinear response usually leads to a larger deformation. Looking at Figure 70, the legend shows larger total deformation compared to deformation in Figure 71. But after observation of the components, it is noticeable that this is only valid for the plate, which has a similar response as in the analysis of individual components (see Chapter 7.1). The nonlinear deformation of the assembly is more uniform compared to the linear response, and besides the plates, other components exhibit larger deformation.
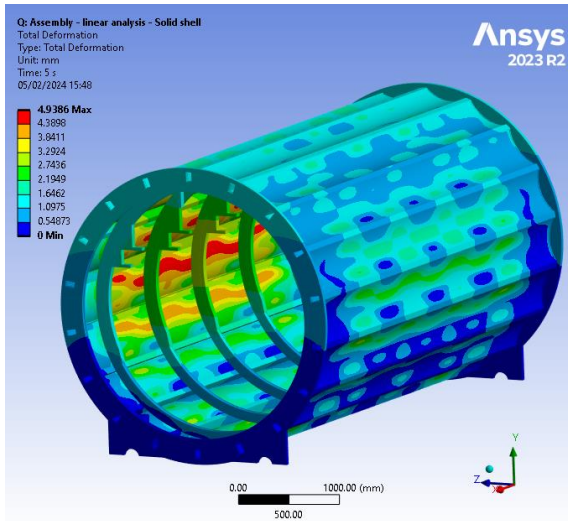
Figure 70: Linear analysis: Total deformation [mm] of the Assembly due to LC10.
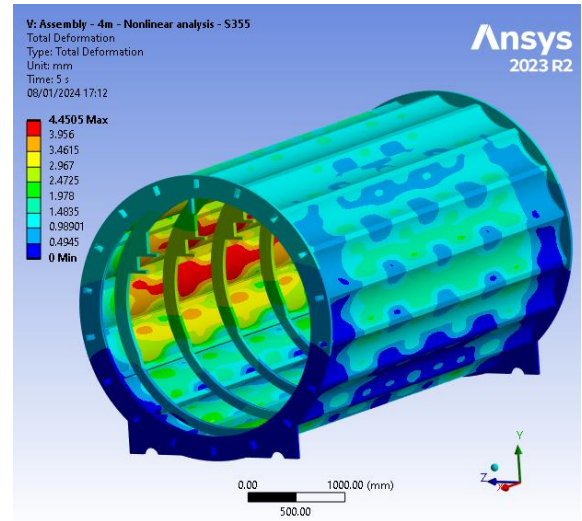

Figure 71: Nonlinear analysis: Total deformation [mm] of the Assembly due to LC10.

In conclusion, the linear model does not result in correct stresses; additionally, structure is made out of thin elements which undergo larger deformations under loading. Thus, a nonlinear analysis is needed for this research.

7.2.2   Skeleton design - 16m - SLS

The 16m long section is modelled and analysed to determine the vertical deflection. Since only the global deflection of the tube is verified in this analysis, a linear analysis is performed. A small influence on the global vertical deformation might have the longitudinal stiffness of the plates, which, due to linear analysis, might contribute to less accurate and more conservative results. In the linear analysis, the plates will not additionally deform due to loss of stiffness, and therefore, they might take additional forces. It should be noted that due to a coarse mesh and linear analysis, the stresses are not verified; instead, a 5m long tube section is modelled and analysed for this purpose.

Table 5: Analysis settings – 16m model without rail supports

Settings	
Material	Structural steel S355 - linear
Model type	Shell
Mesh type	Quadratic
Analysis type	Linear

Table 6: Component mesh sizes – 16m model without rail supports

Component	Mesh size [mm]
Plates	80
Stringers	80
Rings	60
Edge flanges	40
Shims	40

Table 7: SLS combination – 16m model without rail supports

Load case	Magnitude
Self-weight	~
Vacuum pressure	0.1 MPa
Snow load	0.00056 MPa
Wind load	0.00025 MPa

This design does not have rail supports and has the sole purpose of retaining vacuum pressure and resisting environmental actions. The general idea for this design is that the rails would be supported only at pylons and reinforced by a beam on the inside of the tube. Therefore, the structure is not affected by the moving pod load, but simultaneously, the tube structure does not provide support to the rails. Consequently, the rails should be sufficiently reinforced at the supports (pylons) to meet strength and deflection limits.

When determining the total vertical deformation, it is important to consider that each set of components behaves differently under different loads. Plates will primarily deform due to the vacuum pressure, and their deformation will not have a significant influence on any other components. Stringers, on the other hand, will have maximum deformation at the midspan between rings, and their bending will cause global deformation of the plates. On the contrary, rings will not experience large deformations locally but will have evident global displacement. This means that due to self-weight, snow load and wind load, the ring centre axis will move and indicate the global deflection of the tube. Another important ring behaviour is that they will not have a symmetric deformation due to non-uniform loading. Vacuum pressure load case induces a symmetric ring deformation, while wind and snow load will induce an ellipsoidal ring shape.

Vertical deformation limit can be determined based on EN1990 [31], which states that the total vertical deflection measured along any track due to rail traffic should not exceed L/600. To determine the maximum permissible vertical deflection for railway bridges with 3 or more simply supported spans, the following figure should be used [31]:
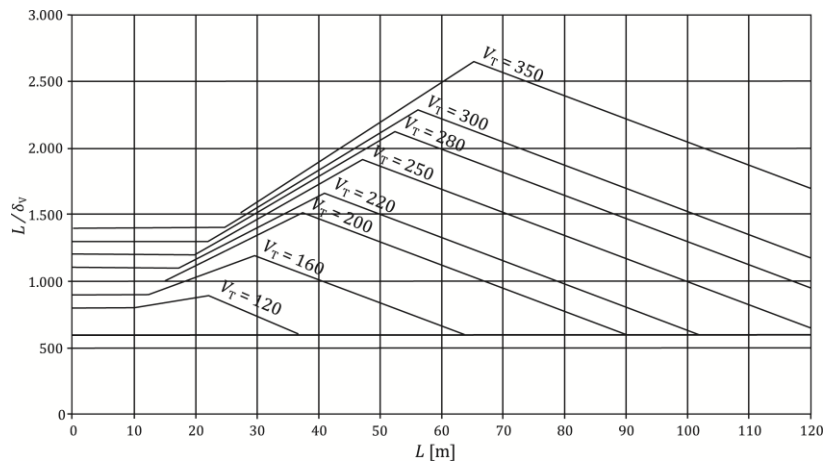

Figure 72: Maximum permissible vertical deflection δ_v for railway bridges with 3 or more successive simply supported spans [31]

Taking the speed V_T as 350km/h, which is the highest available from this graph, the deflection limit results in:

$$\frac{\frac{L}{\delta_v}}{600} = \frac{1500}{600} = 2.5mm \tag{7.2}$$

The level of comfort can be decreased from very good to either good or acceptable, as per Table 8.

Table 8: Levels of comfort and associated vertical acceleration limits [31].

Level of comfort	Limiting value of vertical acceleration b_v m/s²
Very good	1,0
Good	1,3
Acceptable	2,0

The vertical deflection limits increase to 3.25mm for a *good* level of comfort and up to 5mm for *acceptable*. The hyperloop rails have an additional deflection limit based on the vertical misalignment between the 1m long rail segments. The allowable vertical displacement is 1.5mm per rail segment for operational conditions. Since the rails are hanging from the top of the tube, it is possible to mitigate structure deflection by calibrating the heights of rail segments.

SLS verification

In the serviceability analysis of the 16m long tube section, the critical SLS load combination was used. Vertical deflection is read from the side of the eight ring, as seen in Figure 74.
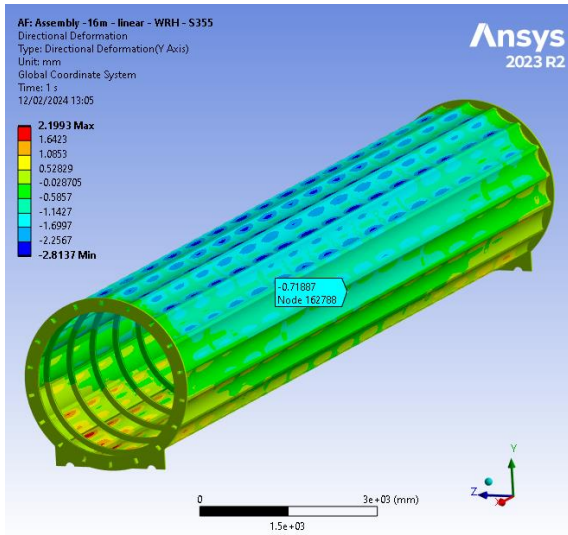
Figure 73: Total vertical deformation [mm] – LC10 - SLS
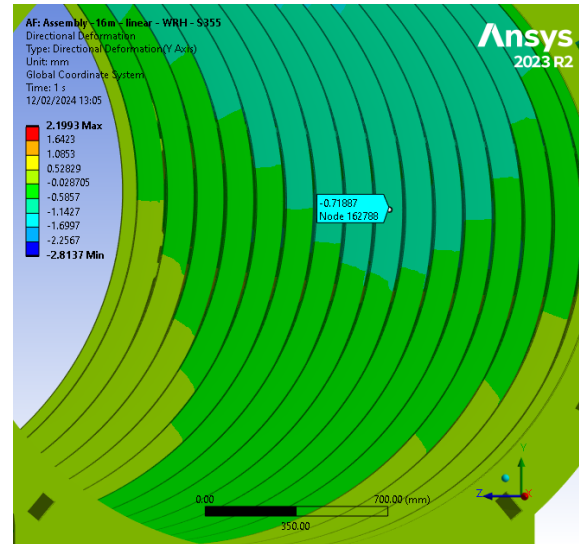
Figure 74: Vertical deformation [mm] - middle ring

Figure 75 represents the vertical deformation of the rings. Observing the dark blue colour scheme of the top side of the middle rings, it shows a vertical downwards deformation of up to 1.29mm, while the bottom side of the edge rings experience a vertical upwards deformation of up to 0.47mm.
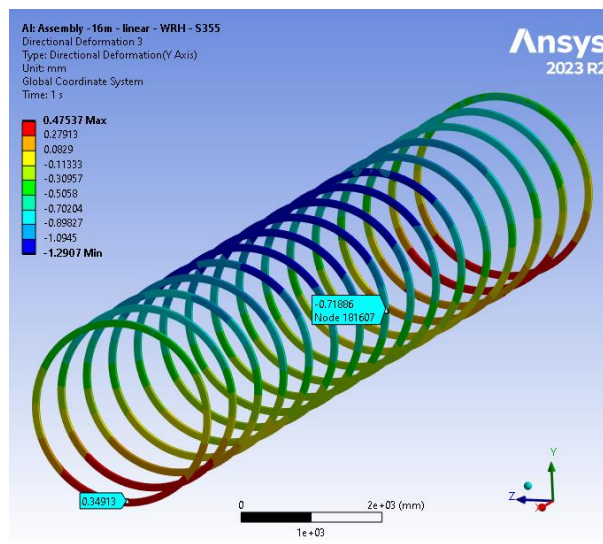

Figure 75: Vertical deformation of the rings [mm]

This analysis provided the general global deformation of the 16m long tube section. The vertical deflection of the entire tube is 0.72mm (Figure 73). Additionally, the rings deform into an ellipsoid shape, but this deformation is localised to an individual ring, and it does not influence global deflection.

7.2.3 Skeleton design - 5m – ULS

The following model is a 5m long variant of the skeleton tube design without rail supports. The purpose of this model is to verify the strength and stability of the design and to identify weaknesses. A nonlinear analysis is performed since the plastic response is predicted. A finer mesh compared to a 16m long model is generated to output more accurate results. A critical ULS load combination (LC10) is used, as described in Chapter 5.6.

Table 9: Analysis settings – 5m model without rail supports

Settings	
Material	Structural steel S355 - Nonlinear
Model type	Shell
Mesh type	Quadratic
Analysis type	Nonlinear

Table 10: Mesh size - 5m model without rail supports

Component	Mesh size [mm]
Plates	50
Stringers	50
Rings	20
Edge flanges	40
Shims	40

Table 11: ULS combination – 5m model without rail supports

Load case	Magnitude
Self-weight	~
Vacuum pressure	0.12 MPa
Snow load	0.00084 MPa
Wind load	0.000375 MPa
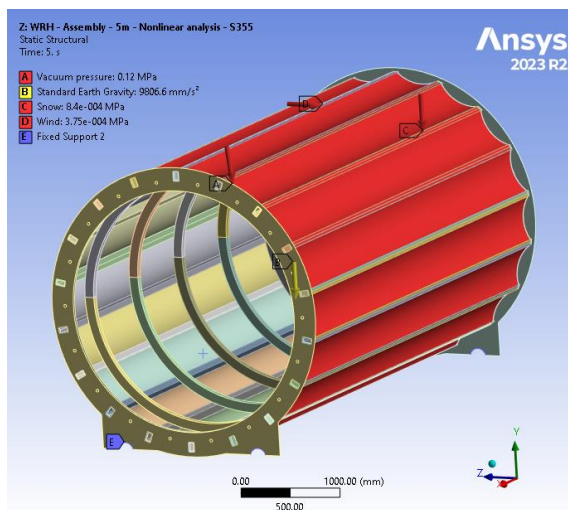
Figure 76: Setup of ULS analysis of the assembly with LC10
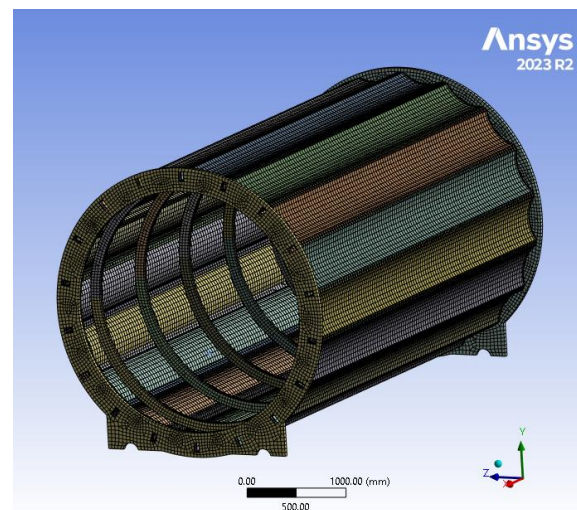
Figure 77: Meshed assembly with mesh sizes as given in Table 10

Figure 78 illustrates the total deformation contour of the assembly under Load case 1, and Figure 79 displays deformation resulting from Load case 10. Plates positioned at the top of the tube exhibit larger deformation due to self-weight for LC1, while for LC10 the deformation is more prominent at the top left of the model due to the wind and snow load. Observing increased deformation of the plates at the edges of the tube, this is due to the first ring being spaced only 0.5m from the flange and consequently being more reinforced.
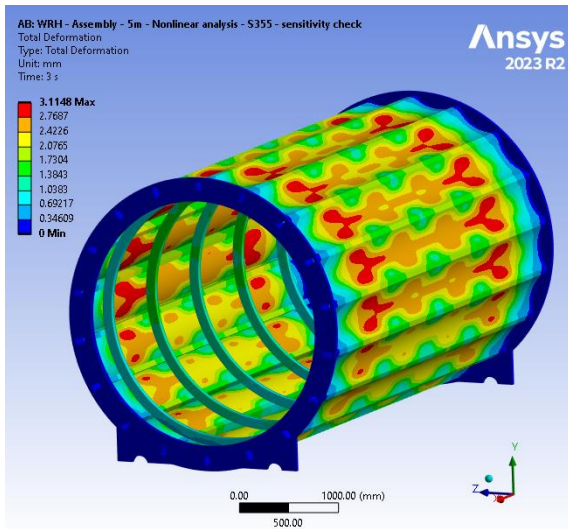
Figure 78: Total deformation [mm] of the assembly without rail supports due to LC1.
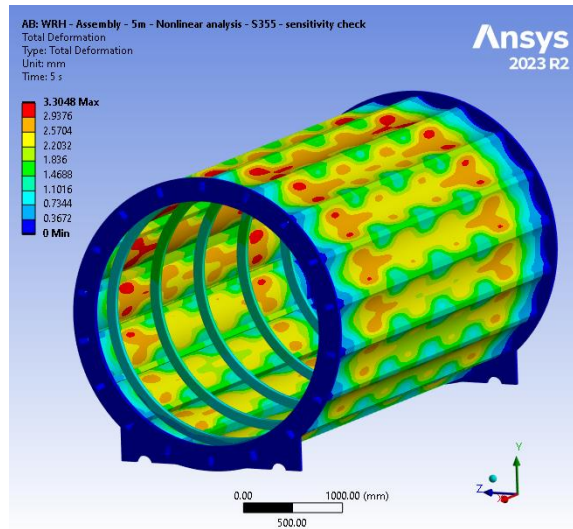
Figure 79: Total deformation [mm] of the assembly without rail supports due to LC10.

Graph 7 shows deformations of the critical components within the assembly. Three load combinations are considered: LC1 ($0 < t \leq 3$), LC2 ($3 < t \leq 4$) and LC10 ($4 < t \leq 5$). The load cases are gradually applied, and the final time step of each load combination represents the final deformation due to that specific combination. A linear deformation increase is seen for all components in LC1. Afte that, a deformation decrease is seen for the plate and stringer, while ring deformation increases as the LC2 is reached.
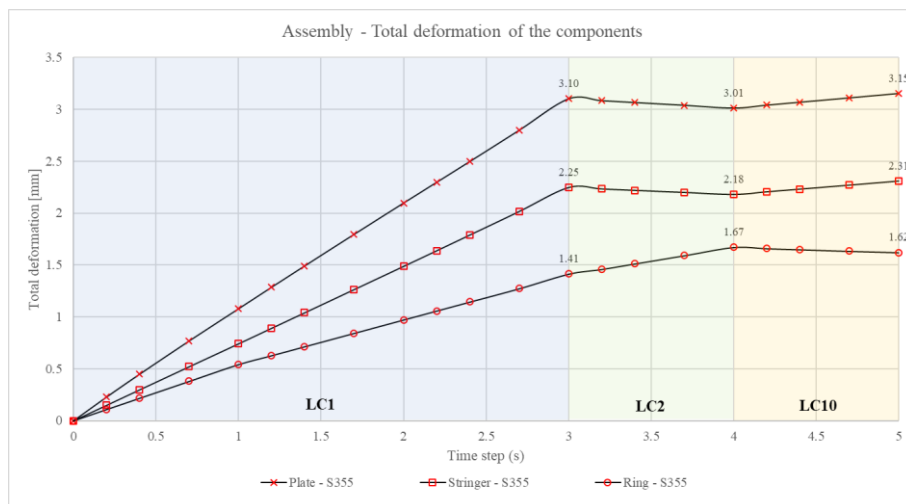
Graph 7: Total deformation [mm] vs Time step [s] of the individual components in the assembly without rail supports. The time steps indicate load combinations, also marked with colours.

The snow load is gradually assigned at $t = 3s$, causing the ring to become non-uniformly stressed and to change from a circular to an ellipsoidal shape. The analysis with S460 steel grade resulted in marginal deformation differences. The reason for this is explained in the stress assessment in the next section.

45

Strength verification

Equivalent von Mises stresses due to LC10 are presented in Figure 80. Stresses in the ring hoover between 40MPa and 260MPa (see Chapter 7.2.6 for the stress range in the ring), with stress concentrations at connections and an increase in compressive stresses spanning from the connection to the inner flange. The maximum stress of 339 MPa is at the ring to stringer connection, as seen in Figure 81.
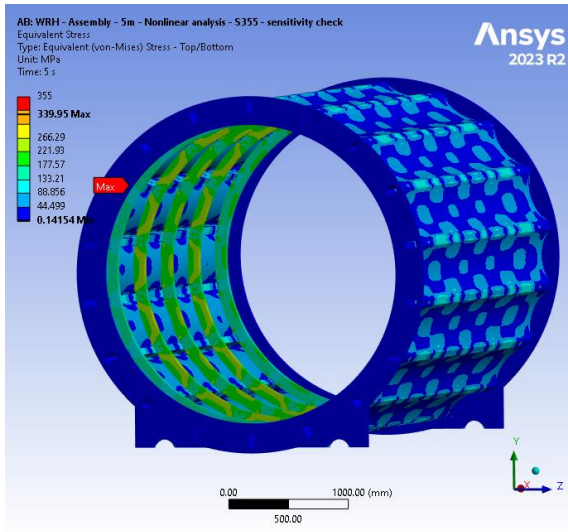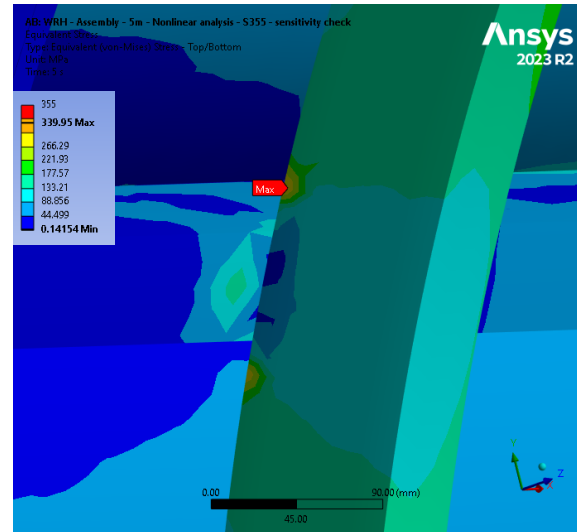

Figure 80: Stress [MPa] of the assembly without rail supports due to LC10

Figure 81: Maximum stress [MPa] at the stringer to ring connection. Four stress concentrations are expressed in the ring at each connection because of the load path through the webs of components (UC = 0.96)

The same approach of presenting load combinations 1, 2 and 10 is used for stresses. It should be noted that Graph 8 represents the stresses of the centre ring, side stringer and side plate. The central ring is chosen because it has no influence on increased stiffness from either edge of the tube.
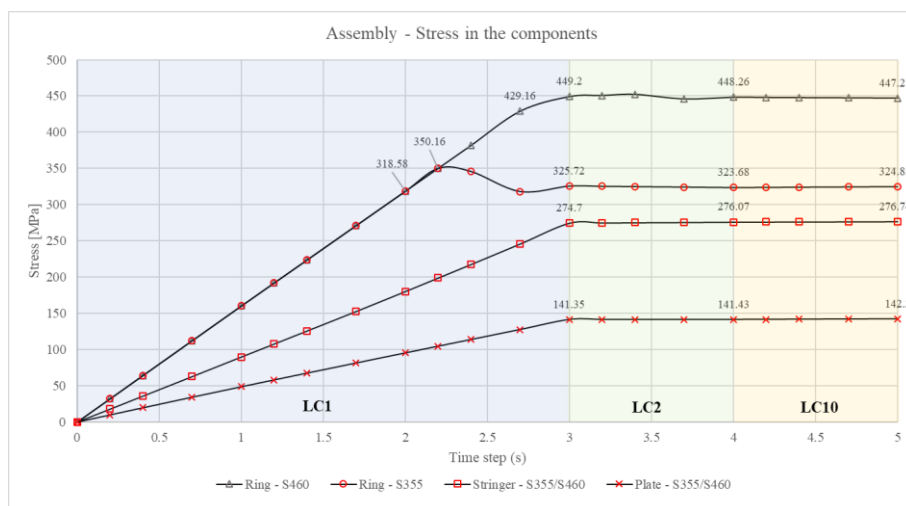
Graph 8: Maximum stress [MPa] vs Time step [s] of the individual components in the assembly. The time steps indicate load combinations.

Observing the ring stress curve, the peak is at t = 2.2s, where the stress reaches σ_{VM} = 350MPa. After this point, the stress decreases. This is because a plastic response was triggered at that load, and the ring began to deform plastically. This initiation of plastic deformation caused the ring to deform locally and distribute the concentrated stresses. Compression stress concentrations can be seen in Figure 82, and

46

the contact area with the stringer is in tension since this area of the ring flange is being stretched. When S460 steel is assigned as the material, the stress in the ring increases up to σ = 449.2MPa at LC1. Stress does not significantly change after t = 3s, which signifies the severity of the vacuum pressure load case.
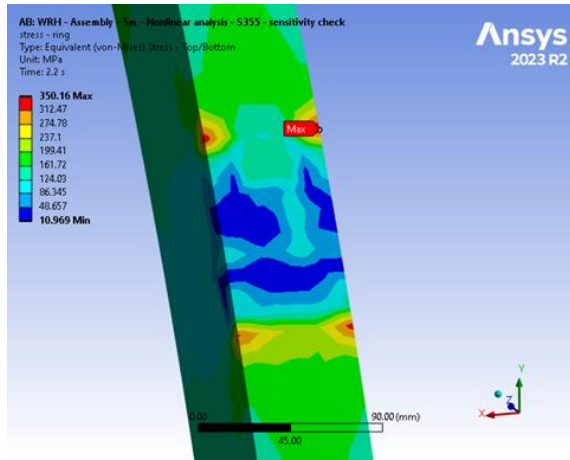

Figure 82: Maximum stress [MPa] in the ring at t = 2.2s. Four concentration points can be seen due to compression stress.
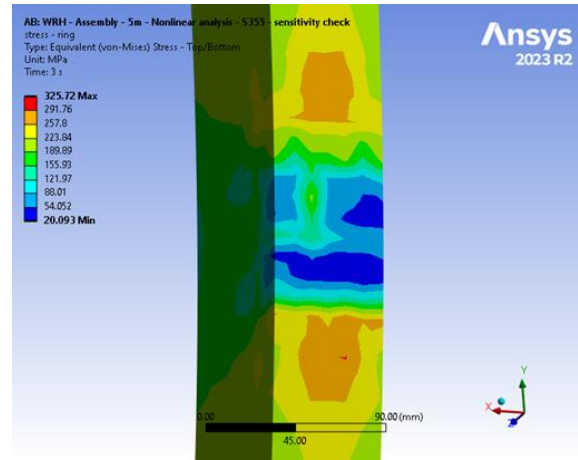
Figure 83: Decreased stress [MPa] at t = 3s due to previous initiation of plastic deformation.

Although the stresses were beyond the yield strength in the linear analysis, the yield point was not fully reached in the nonlinear analysis. A nonlinear response is initiated, local plastic deformation initiates and the stress gets dispersed to other components.

Plate deformation

The plate deformation was expected to be uniform across the cross-section of the plate, with maximum total deformation in the middle, since the vacuum pressure acts normal to the surface. Nonlinear FEM analysis proved differently, where the plate deformed in a sinusoidal shape. This shape of the plate is achieved due to combination of the following factors: deformation of the stringers, plate to stringer connection type and lateral tensile forces due to plate curvature. The latter is the main reason, and the following figures describe the structural behaviour. One plate is isolated for the verification (Figure 84) and the total deformation of a short plate strip is expressed, as seen in Figure 85. Based on the deformation contour and node results, it can be seen that the total deformation in the middle of the plate is smaller than at the sides.
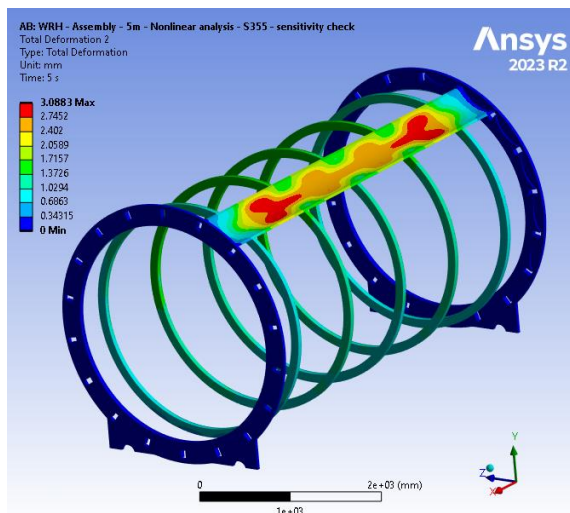

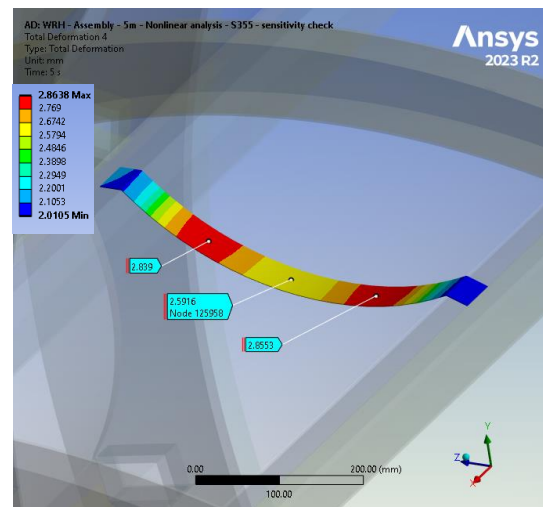*Figure 84: Total deformation [mm] of the single plate and adjacent components.*

Figure 85: Strip of the plate deformation [mm] located between two rings. This is a true scale deformation.

The side view and scaled-up deformation clearly showcase the deformation shape (Figure 86). This deformation can be explained by deconstructing forces in the plate. The vacuum pressure acts normal to the surface, meaning that the force is acting perpendicular to the plate in its local coordinate system. In the global coordinate system, the central part of the plate only has the vertical force component, while force acting at the side of the plate is decomposed into vertical and horizontal force component. Figure 87 clearly shows force components, where due to horizontal force F_H, the central part of the plate is tensioned and subsequently the vertical deformation u_1 is decreased.
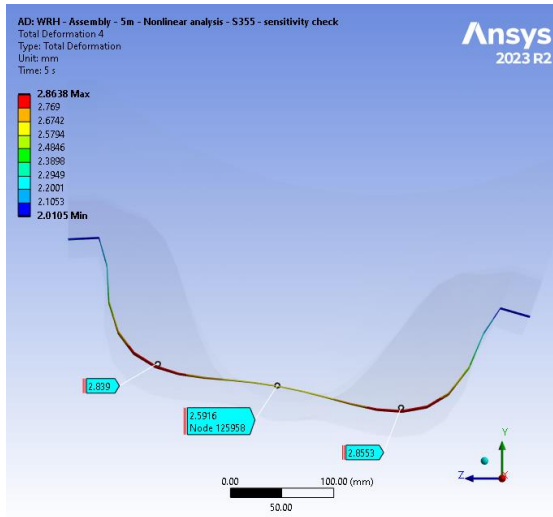
Figure 86: Side view of the plate strip with scaled-up (x78) deformation. The middle of the plate deforms less than the sides, creating a sinusoidal shape response.
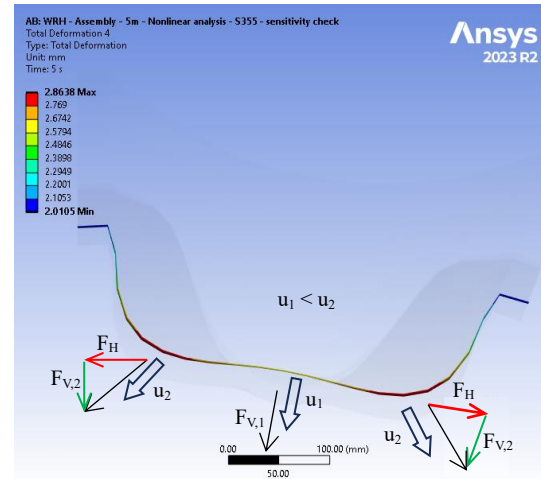
Figure 87: Horizontal and vertical force components due to vacuum pressure. F_H forces tension the middle part of the plate, causing it to deform vertically less, therefore $u_1 < u_2$.

7.2.4 Skeleton design - 16m with rail supports - SLS

The same analysis is repeated for the 16m long model with rail supports. As stated before, the 16m long model is analysed solely for the purpose of verifying vertical deflection. The reading is taken at the side of the ring, just as at the skeleton tube design without rail supports.

Table 12: Analysis settings – 16m model with rail supports

Settings	
Material	Structural steel S355 - Nonlinear
Model type	Shell AND solid-shell
Mesh type	Quadratic
Analysis type	Nonlinear

Table 13: Mesh size - 16m model with rail supports

Component	Mesh size [mm]
Plates	80
Stringers	80
Rings	60
Edge flanges	40
Shims	40
Rail supports	40

Table 14: SLS combination – 16m model with rail supports

Load case	Magnitude
Self-weight	
Vacuum pressure	0.1 MPa
Rails load	58.86 kN
Snow load	0.00056 MPa
Wind load	0.00025 MPa
Static pod load	196.2 kN

This model includes rail supports, and therefore, rails and static pod load cases are additionally assigned. Vertical deflection is taken from the side of the eight ring (Figure 89), which resulted in δ = -3.33mm.
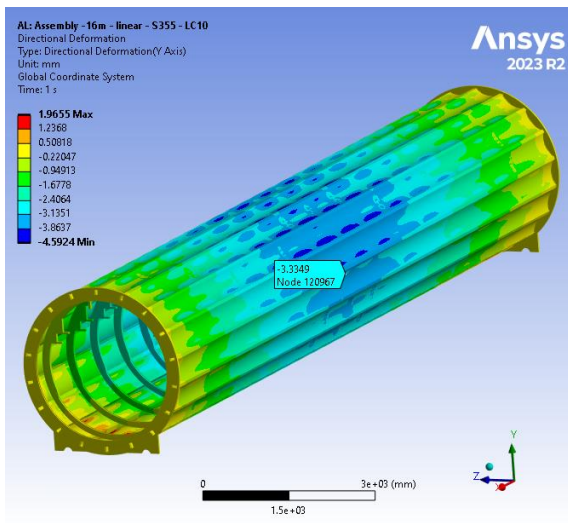

Figure 88: Vertical deflection [mm] of the assembly due to SLS LC10- 16m model with rail supports.
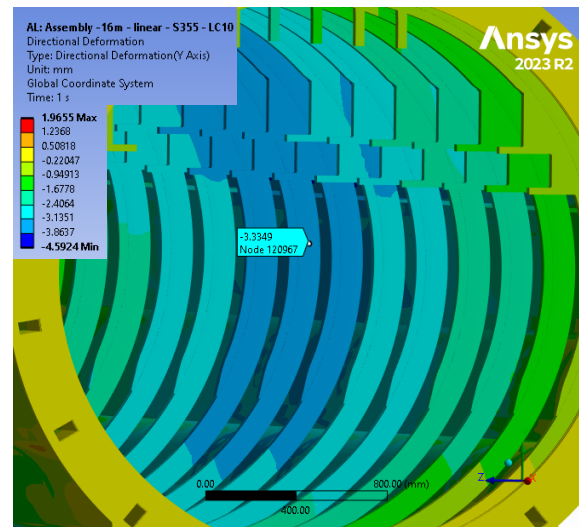
Figure 89: Vertical deflection of the eight ring [mm] due to SLS LC10

Rings indicate the global tube behaviour. It can be seen in Figure 90 that the central rings deflect downwards while the rings located at the edges of the tube deform upwards. This is due to fixed boundary conditions and the global bending moment in the tube. The structural response of the ring is discussed in detail in section 7.2.5.
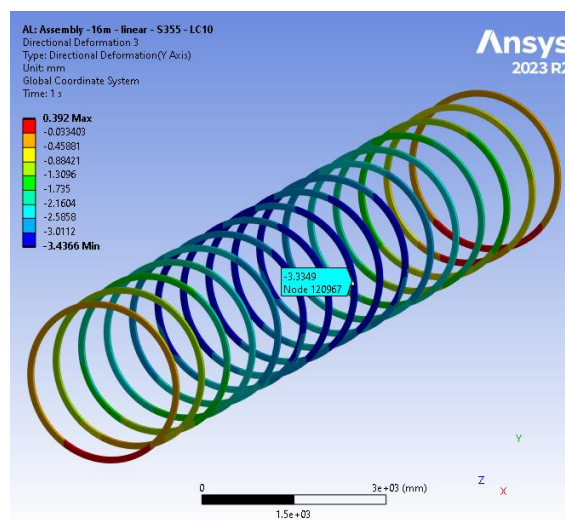

Figure 90: Vertical deformation of the rings [mm]

The results cannot be directly compared to the model without rail supports since this model has an additional objective, which is to support rails and the pod. Rail supports act as a reinforcement of the rings and not only as a dead load on the tube. This design decision drastically improved the performance of the structure, especially since rings are the critical components of the assembly. Moreover, the pod is hanging from the top of the tube, which means that reinforcing rings in the upper part increases their compression capacity.

7.2.5   Skeleton design - 5m with rail supports - ULS

Thereafter, a 5m long model with rail supports is analysed for strength. The ULS load combination 10 (LC10) is used in this analysis. The thickness of rail supports is 60mm, and the use of shell elements proved to cause large stress concentrations at the connections. Therefore, solid-shell elements are used for these components.

Table 15: Analysis settings – 5m model with rail supports

Settings	
Material	Structural steel S355
Model type	Shell AND solid-shell
Mesh type	Quadratic AND linear
Analysis type	Nonlinear

Table 16: Mesh size - 5m model with rail supports

Component	Mesh size [mm]
Plates	50
Stringers	40
Rings	20
Edge flanges	40
Shims	40
Rail supports	20

Table 17: ULS combination – 5m model with rail supports

Load case	Magnitude
Self-weight	
Vacuum pressure	0.12 MPa
Rails load	26.487 kN
Snow load	0.00084 MPa
Wind load	0.000375 MPa
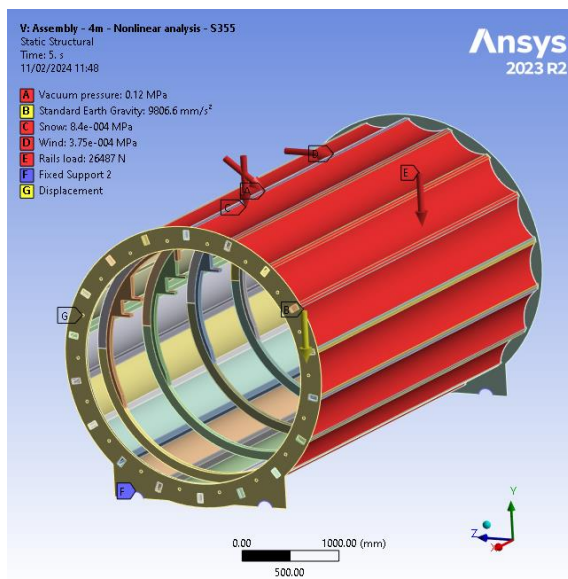
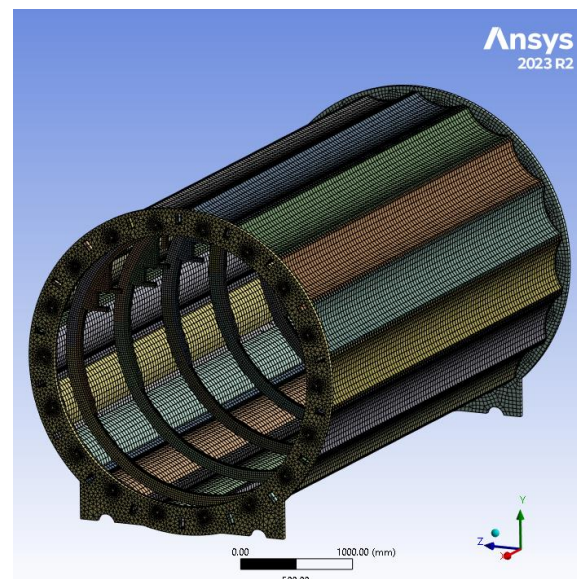*Figure 91: Setup of ULS analysis of the assembly with LC10*

Figure 92: Meshed assembly with mesh sizes as given in Table 16

51

Figure 93 and Figure 94 showcase the total deformation of the assembly due to LC1 and LC10. Larger deformation is expressed at the sides of the tube, which is also indicated by the deformation contours. This structural response is due to the rail supports reinforcing the rings at the top and the sides. Thus, the ring is reinforced against horizontal ovalisation on both sides, while only at the top against vertical ovalisation.
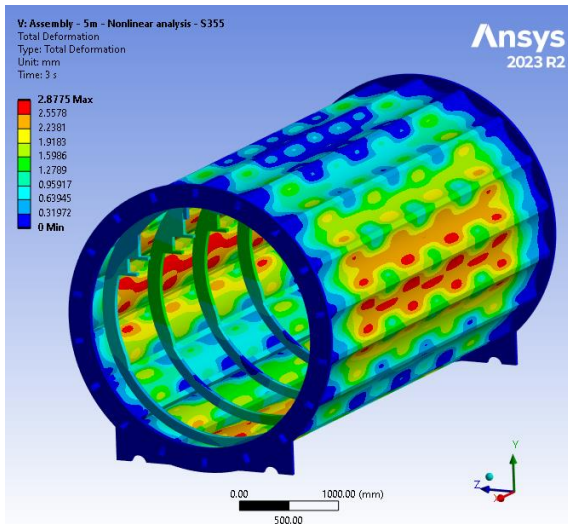

Figure 93: Total deformation [mm] of the assembly with rail supports due to LC1
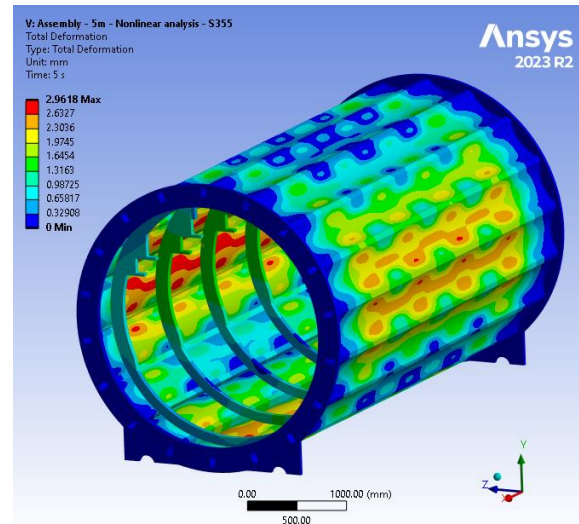
Figure 94: Total deformation [mm] of the assembly with rail supports due to LC10

Graph 9 shows the total deformation of the critical components in the assembly. The deformation is primarily influenced by the ring's behaviour. A linear deformation increase is seen for all components in the LC1 region of the graph. At this stage the rings vertically ovalise. In LC2, the snow load is added to the top of the tube, which counteracts the vertical ovalisation; thus, the total deformation decreases. With the inclusion of wind load in LC10, which represents a horizontal force, the ring tends to vertically ovalise once again. This observation is further explained in the following paragraph.
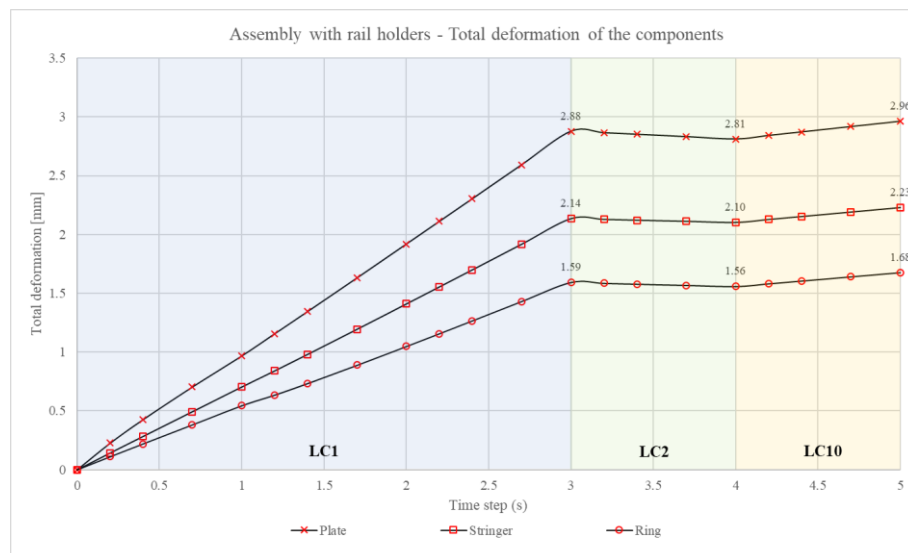
Graph 9: Total deformation [mm] vs Time step [s] of the individual components in the assembly with rail supports. The time steps indicate load combinations, also marked with colours.

Ring deformation

The rail supports are fully fixed to the rings, thus, they behave as a reinforcement of the ring. Due to them, the ring's stiffness is drastically increased at the side and at the top. Figure 95 showcases the

loading of the rings due to vacuum pressure, and the stiffness difference in the ring, due to which the vertical ovalisation happens.
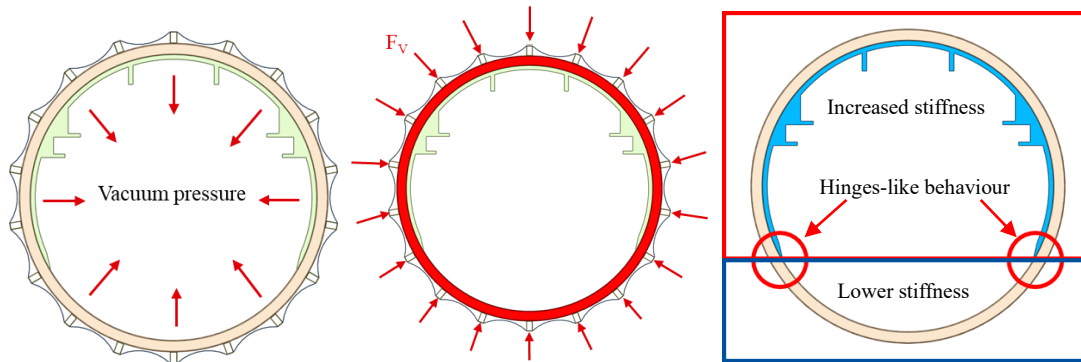

Figure 95: Left: Vacuum pressure load case. Middle: Forces acting on the ring through the stringers. Right: Representation of increased stiffness due to rail support and the locations of sudden change in stiffness, where the hinge like behaviour is observed.

Consequently, a large deformation discrepancy is observed between the top/bottom and the sides of the ring. As seen in Figure 96, the deformation is mirrored across the centreline. For visualisation, Figure 96 and Figure 97 represent a scaled-up deformation for LC1 and LC2, showcasing both the rigid movement and the bending part of the ring distinctly. Undeformed wireframe indicates the direction of ring deformation. At the ends of the rail support, where the stiffness decreases, these two locations act as a hinge. At these locations the ring bends and consequently the bottom side of the ring vertically deforms.
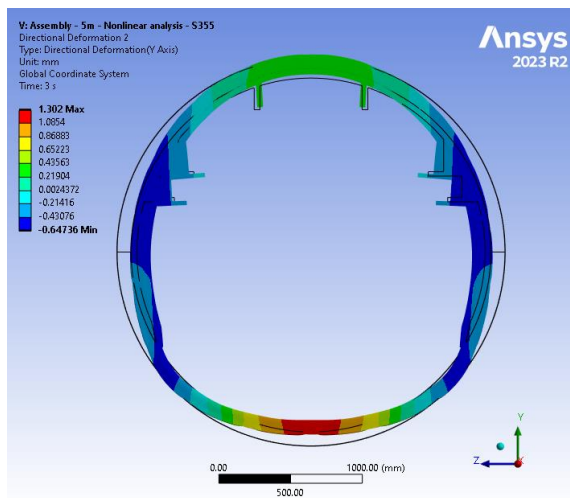

Figure 96: Vertical scaled-up deformation of the ring due to LC1. Wireframe shows the undeformed shape of the ring.
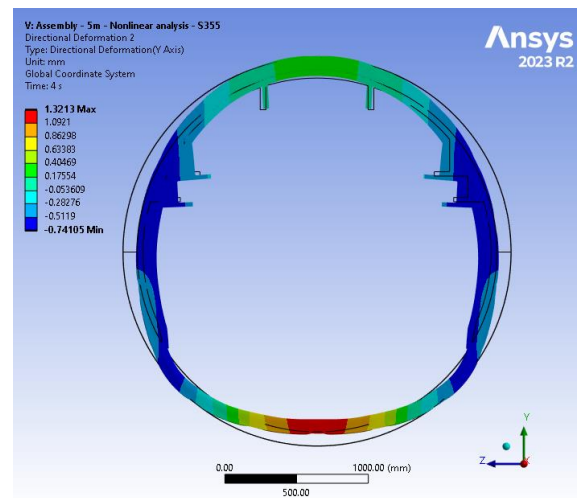

Figure 97: Vertical scaled-up deformation of the ring due to LC2. Wireframe shows the undeformed shape of the ring.

The following two figures show the scaled-up horizontal deformation of the ring due to LC1 and LC2. It is observed that the total horizontal deformation decreases after the snow load is assigned.
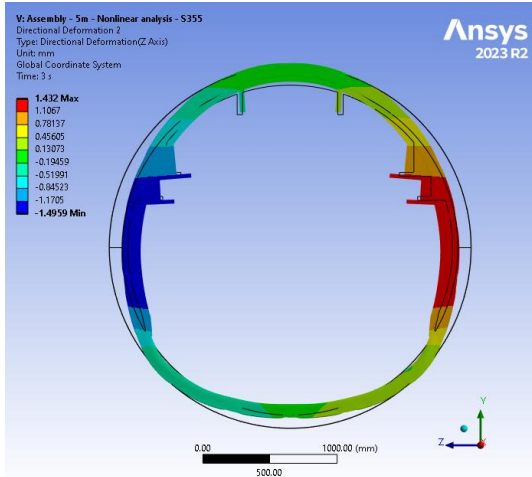
Figure 98: Horizontal scaled-up deformation due to LC1.
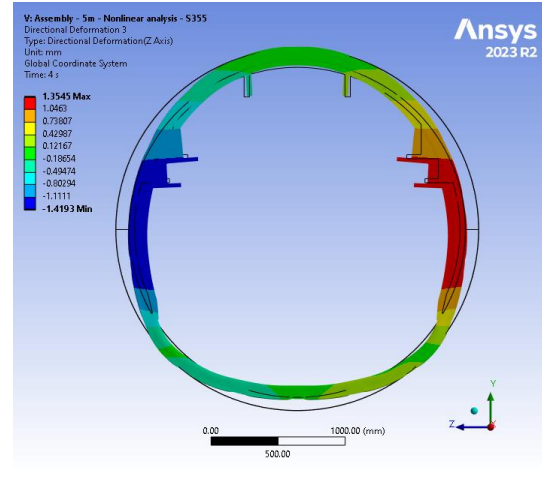Wireframe shows the undeformed shape of the ring.

Figure 99: Horizontal scaled-up deformation due to LC2.
Wireframe shows the undeformed shape of the ring.

In order to understand better the ring behaviour, four control points were chosen on the middle ring from which the deformation data is taken (Figure 100). Each control point is a node located the outer flange of the ring and has its own local coordinates, as shown in Figure 101.
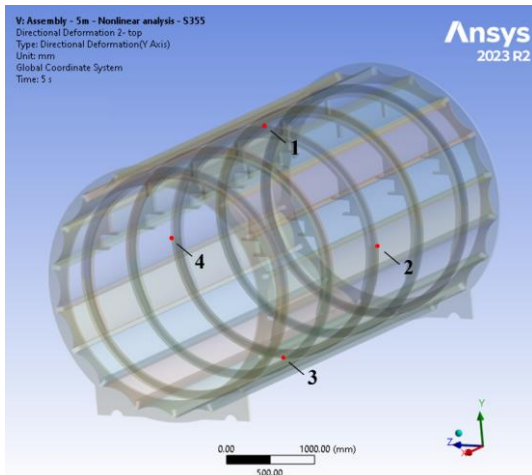

Figure 100: Nodes locations on the middle ring from which the deformation data is extracted.
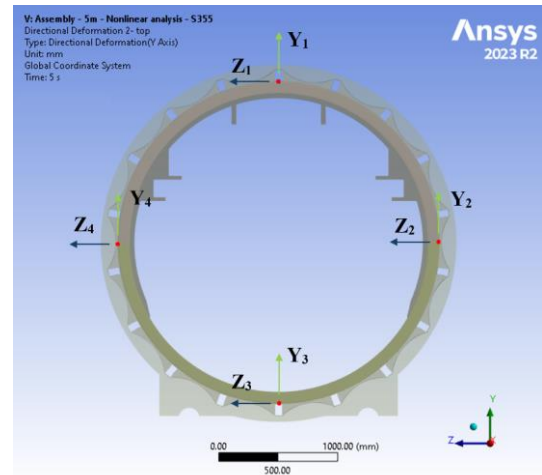

Figure 101: Ring nodes and corresponding local axis.

Displacement data of those control points is presented in Table 18. LC1 includes the vacuum pressure, LC2 adds the snow load and LC10 adds the wind load from the Z direction. An observation is made at Z_2 and Z_4 (control point 2 and 4), where the node displacement decreases from LC1 to LC2. This is due to the snow load counter acting the vertical ovalisation. The wind load thereafter increases vertical ovalisation and the displacement increases again.

Table 18: Node displacement [mm] per load combination – design with rail support

Axis	$\delta_{LC1}[mm]$	$\delta_{LC2}[mm]$	$\delta_{LC10}[mm]$
Y_1	0.38	0.2	0.24
Z_1	~0	~0	-0.17
Y_2	-0.45	-0.55	-0.58
Z_2	1.38	1.29	1.23
Y_3	1.27	1.29	1.25
Z_3	~0	~0	~0
Y_4	-0.45	-0.55	-0.51
Z_4	-1.45	-1.36	-1.5

Strength verification

The strength evaluation of the model resulted in the maximum von Mises stress of 342.56MPa at t = 2.2s. This translates to UC = 0.96; therefore, the structure still exhibits an elastic response. The stress concentrations are identified at the ring to stringer connections, as shown in Figure 103.
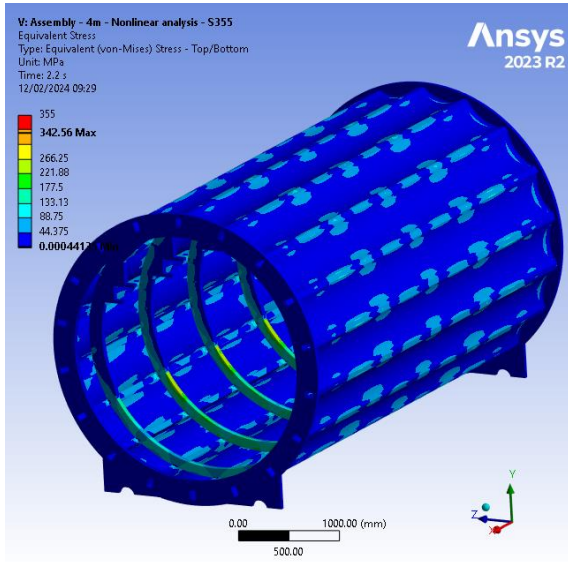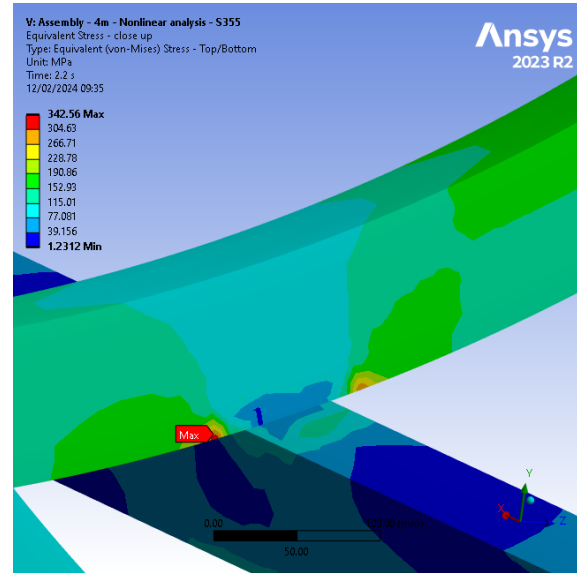

Figure 102: Maximum stress [MPa] for S355 model

Figure 103: Maximum stress in the ring at the ring-to-stringer connection. (UC = 0.96)

At t = 2.2s the structure is still being gradually loaded by LC1 (0 < t ≤ 3s). Graph 10 gives information on stresses in individual components in regard to load combinations. Looking at the Ring S355 curve, as previously stated, the peak is reached at t – 2.2s and then a small dip seen until it increases again up to 340MPa. For the stress decline, the same explanation can be given as for the design without rail supports. As the stress approaches the yield point, the nonlinear material data is triggered. This initiates a nonlinear response, in which the element stiffness falls and the local deformation increases. The increase in deformation cannot be seen in Graph 9, because the global deformation of components is more prominent, while this affects the local deformation (at the ring-to-stringer connection in this case). Stress data also proves the magnitude and severance of the vacuum pressure load case, while snow and wind load only have a marginal effect on the structure in terms of strength.
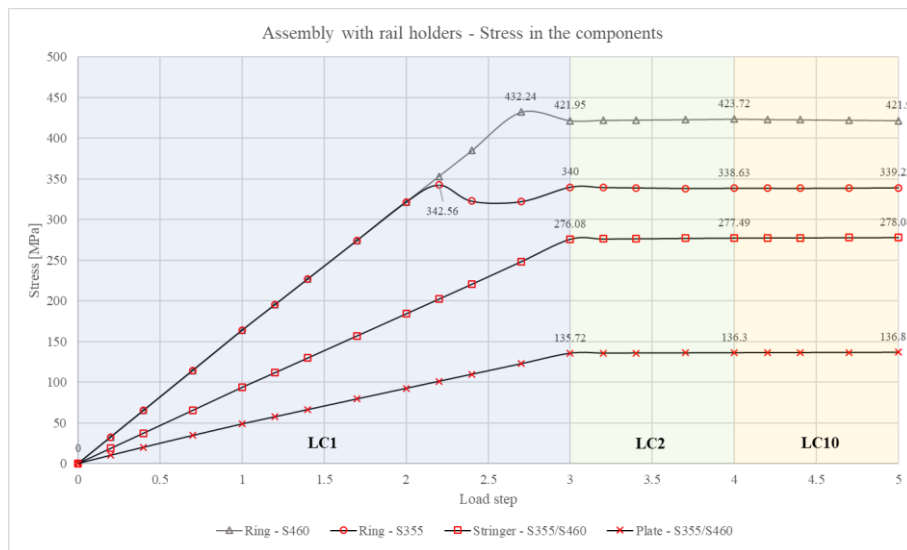
Graph 10: Maximum Stress [MPa] versus Time step [s] for critical components. The time steps indicate load combinations.

The stress rise after t = 2.6s is due to the ring bending at the location of rail support edges. At this location, the ring's stiffness is significantly decreased; thus, it acts as a pivot. Figure 104 and more specifically Figure 105 illustrate the described stress concentration. This response was mitigated to some extent by increasing the length of the rail supports, as well as with the addition of tapered edges.
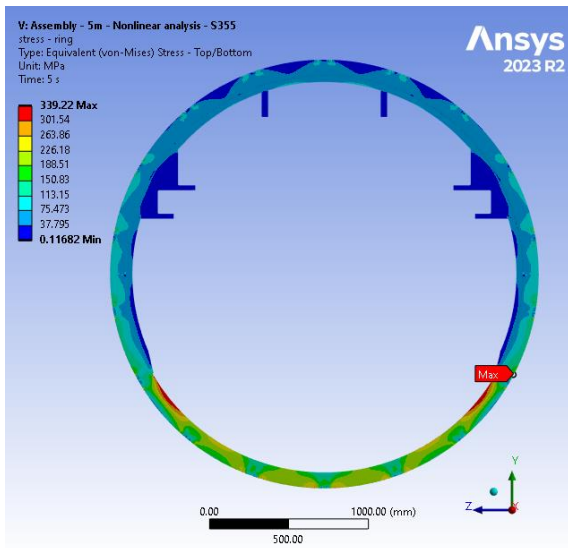

Figure 104: Stress [MPa] in the ring at t = 5s. The maximum stress is on the outer flange, at the connection with the stringer. Inner flange exhibits stress of up to 313MPa
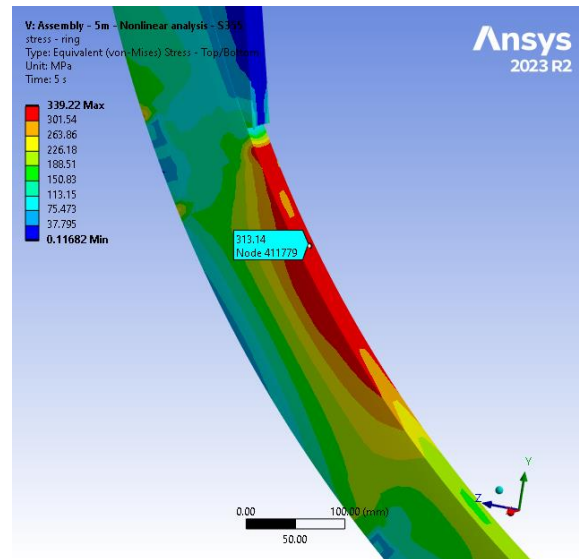

Figure 105: Stress concentration in the inner flange of the ring next to the tapered end of the rail support for LC10 with UC = 0.88

Looking back at Graph 10, it represents stresses of the critical components, and not at specific nodes of critical location Two stress concentrations were identified in the ring (see Figure 103 and Figure 105). Therefore, each critical location needs to be assessed separately, to understand the stress behaviour. The control points were chosen at the stress concentrations, as presented in Figure 106 and Figure 107.
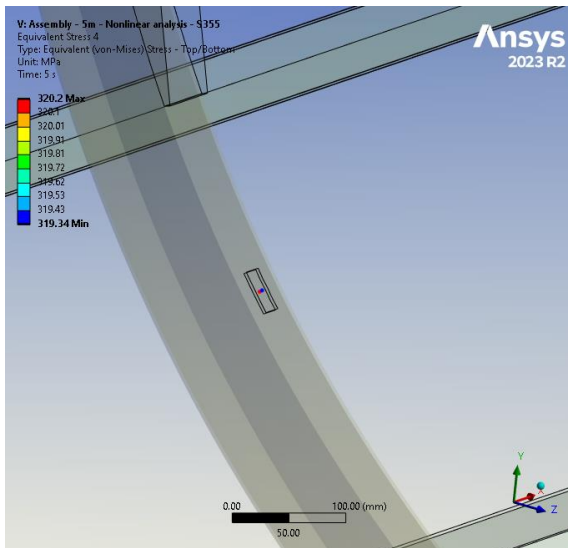

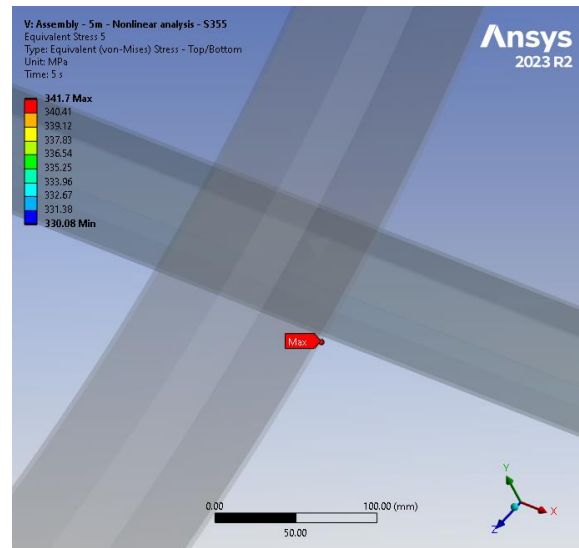Figure 106: Control point at the ring flange

Figure 107: Control point at the ring-to-stringer connection

Stress build-up at both points due to load combinations is given in Figure 108. It is seen that ring flange location exhibits a maximum stress of 321MPa at t = 3s, while stress at ring-to-stringer connection increases up to 340.8MPa.

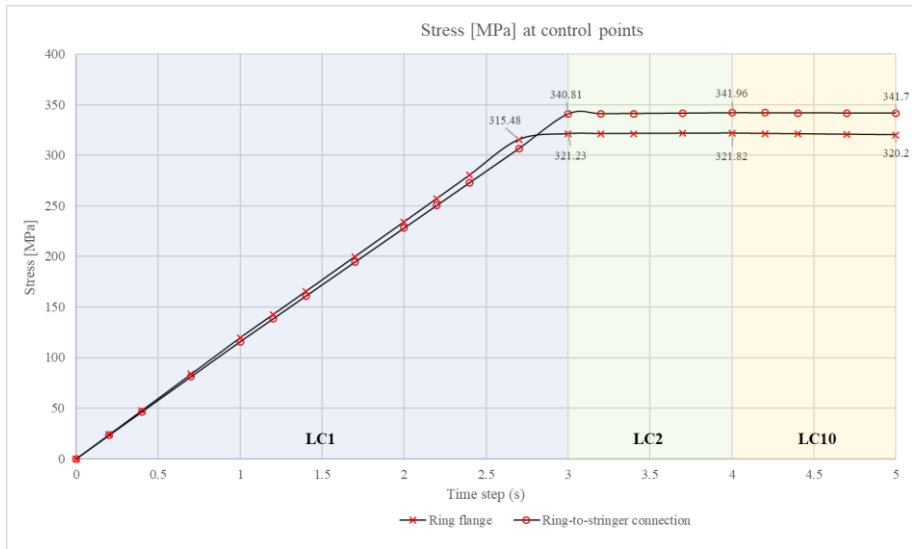*Figure 108: Von Mises stress [MPa] at the control points due to different load combinations*

Each ring-to-stringer connection represents a critical location in the assembly. For the given loading conditions, the assembly still deforms elastically; although, at critical locations a nonlinear response is initiated and a full plastic response is anticipated in case of a sudden unforeseen load increase.

7.2.6 Stress in the ring

With the addition of the rail supports, the stress in the ring webs has reduced. The following figures showcase the von Mises stress of the central ring's web. Figure 109 represents the stress in the design without rail supports. An increase can be seen towards the inner flange in the centre between the stringers, where the stress reaches 263MPa. Looking at Figure 110, the stress pattern is different, because the rail support mostly resists the compressive forces. In both designs local stress concentrations are seen at the contact location with the stringer.
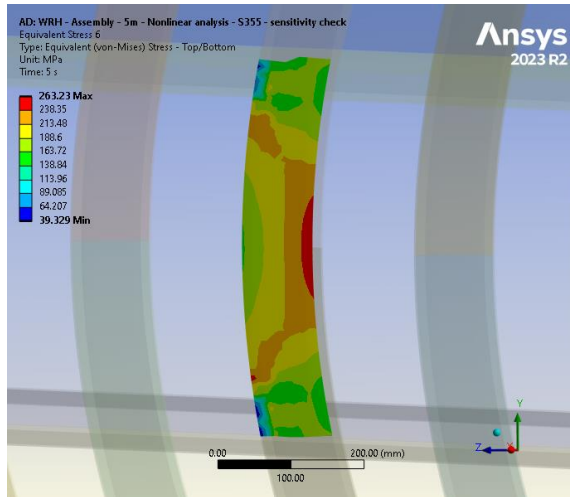

Figure 109: Equivalent von Mises stress [MPa] in the design without rail supports.
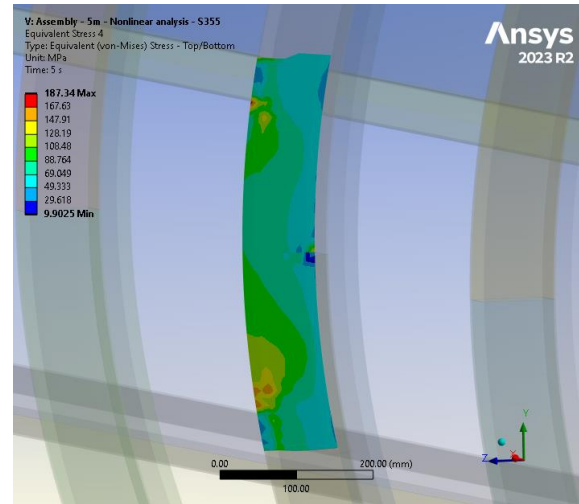

Figure 110: Equivalent von Mises stress [MPa] in the design with rail supports.

Stress at those locations needs to be verified by identifying the largest absolute principal stress. Since the rings are in compression, the minimum principal stress is extracted at the contact location. The minimum principal stress in the design without rail supports results in 386MPa (Figure 111), and with the addition of rail supports in 355MPa (Figure 112). The minimum principal stress is larger than the von Mises stress, and it proves that yielding will be initiated in the design without rail supports.

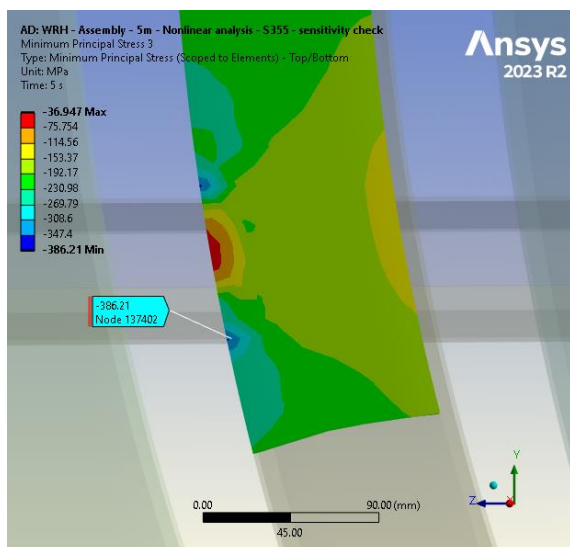*Figure 111: Minimum principal stress [MPa] at the ring-to-stringer connection of design without rail supports.*
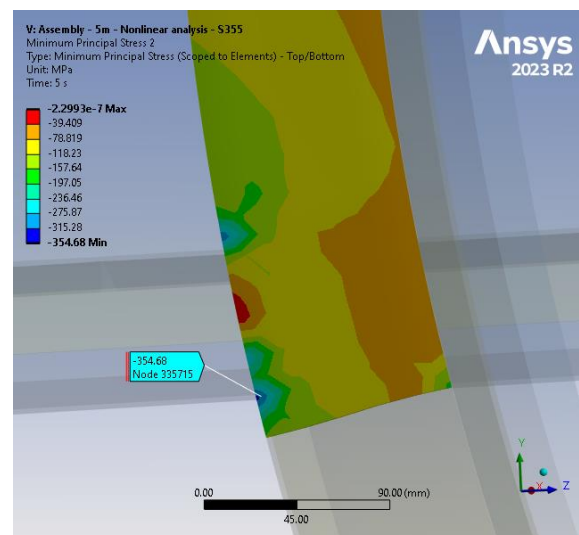
Figure 112: Minimum principal stress [MPa] at the ring-to-stringer connection of design with rail supports.

Since the minimum principal stress exceeds the yield point, the equivalent plastic strain needs to be verified and compared to the maximum gross yielding strain. Knowing from the calibration model that

58

the principal plastic strain is roughly $\varepsilon_{shell} \sim 0.05$, while the maximum plastic strain in the model is roughly $\varepsilon_{plastic} \sim 0.01$ (Figure 117), it is safe to conclude that the design is structurally within the ULS conditions.

Figure 113: Maximum equivalent plastic strain [mm/mm] at ring-to-stringer connection

Figure 114: Maximum equivalent plastic strain [mm/mm] in the ring flange at the end of the rail support

7.2.7 Fatigue verification due to vacuum pressure fluctuations

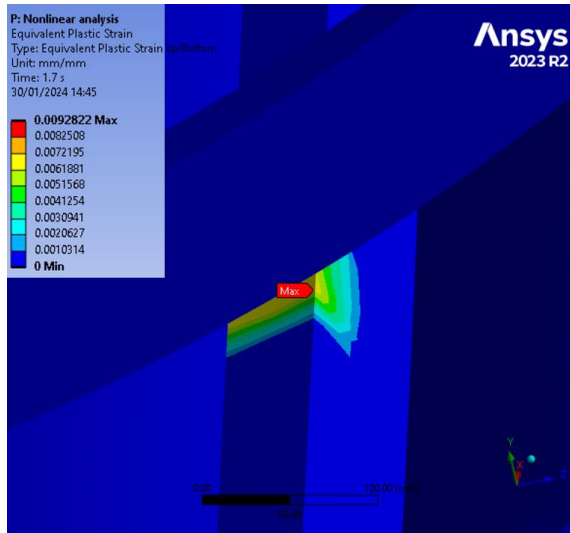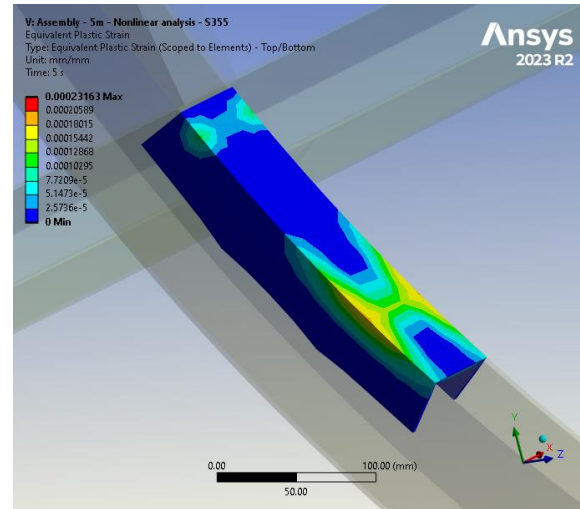High stresses are primarily caused by the vacuum pressure load case. Therefore, a cyclic loading appears whenever the tube depressurises. Upon pressurization of the tube, the stresses increase as presented in the previous chapter. Given the extensive length of the potential hyperloop system, the closing valves would need to be incorporated. These valves would serve to isolate tube segments that are pressurized and in use from those that are depressurised and not in use. Whenever the tube depressurises and subsequently pressurises again, it imposes a load cycle. While it is not anticipated to pose a fatigue issue, due to the relatively high stress levels, the detail is nevertheless verified.

To conduct linear elastic fatigue verification, the principal stresses are extracted from the location of the stress concentration at the edge of the rail support. For accurate stress range $\Delta\sigma$, the results are taken from the same node in the mesh. As seen in Figure 102 and Figure 115, the maximum and minimum principal stress results in 99.6MPa and -359MPa, respectively. Both figures show the same ring detail, where compressive stress is exhibited at the top of the flange, while tensile stress at the bottom.
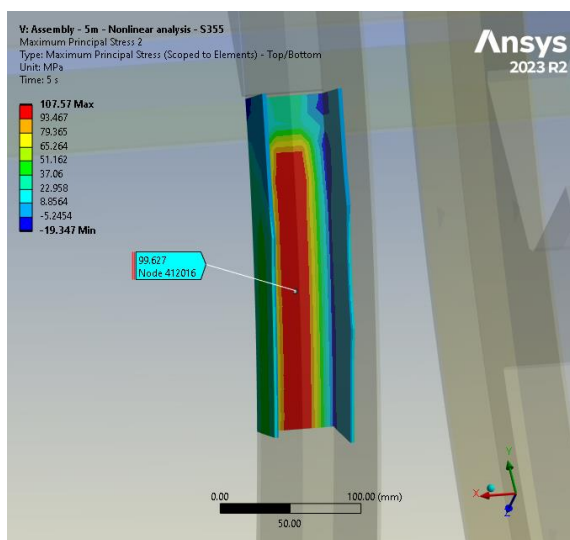

Figure 102: Maximum principal stress [MPa] in the inner flange of the ring next to the tapered end of the rail support for LC10 (σ_{max} = 99.6MPa)
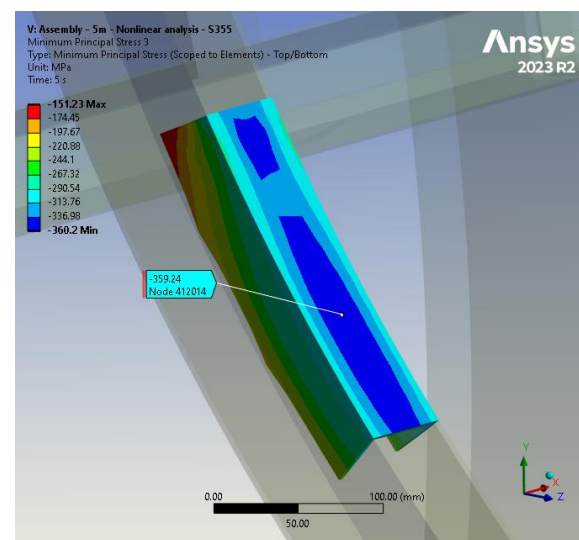
Figure 115: Minimum principal stress [MPa] in the inner flange of the ring next to the tapered end of the rail support for LC10 (σ_{min} = -359.24MPa)

The stress range $\Delta\sigma$ is therefore 458.8MPa. This detail represents the failure of the base material, given the detail category 160 (construction detail 3 in Table 8.1 of EN1993-1-9 [32]). With the given stress range, the detail's fatigue life results in $34.5 \cdot 10^3$ cycles. The projected fatigue life may appear suboptimal initially; it is noteworthy that if the tube becomes depressurised twice per day, the fatigue lifetime would still be 47 years.

Additionally, according to DNV [7] the low cycle fatigue of base material is verified. This is done because the stress is just below the yield point, and the nonlinear response was initiated. The maximum principal strain at the location of the stress concentration is presented in Figure 116.
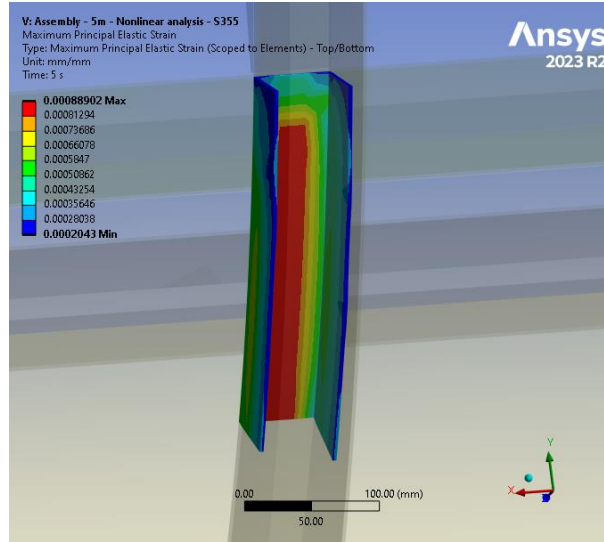
Figure 116: Maximum principal elastic strain [MPa] in the inner flange of the ring next to the tapered end of the rail support for LC10

The number of cycles to failure is calculated using the following equation given in DNV [7] standards:

$$\frac{\Delta\varepsilon_l}{2} = \frac{\sigma_f'}{E}(2N)^{-0.1} + \varepsilon_f'(2N)^{-0.43} \tag{7.3}$$

Where:

$\Delta\varepsilon_l$ is the fully reversible local maximum principal strain range
E   is the modulus of elasticity (material constant)
σ_f' is the fatigue strength coefficient (material constant)
ε_{hs}' is the fatigue ductility coefficient (material constant)

Taking σ_f' and ε_{hs}' as 175MPa and 0.091 ('*air*' environment), as per Table 5-6 of DNV [7], the number of cycles to failure results in 515000. Whenever the tube becomes depressurised, it counts for one cycle. Therefore, it is safe to conclude that this detail is prone to low cycle fatigue.

On the contrary, the low cycle fatigue of welded joints requires data of fully reversible maximum principal hot spot strain range. A mesh with element size of *t x t* is recommended by DNV [7]. Since fatigue verification of connections is outside the scope of this research, only a recommendation is given on the procedure. The connection should be localised, preferably modelled with solids instead of shell elements with mid side nodes, such as 20-noded brick elements. The fully reversible maximum principal hot spot strain range should thereafter be determined and used in verification of the low cycle fatigue of welded joints. The verification steps are provided in DNV [7], chapter 5.2.5.

7.2.8 Eigenvalue-buckling analysis

Structure buckling involves sudden loss of stiffness and a deformation change. Local buckling usually appears in an isolated region, and the structure can still support all the loads. Eigenbuckling analysis is a linear method that predicts theoretical buckling strength. It is a computationally efficient way of determining buckling shapes and buckling loads, but it can yield unconservative results since it does not include any nonlinearity in the analysis. It uses a linear perturbation method, a type of analysis designed to solve a linear problem based on its prior linear or nonlinear preloaded status. The prior analysis is the base analysis, and the perturbated analysis uses the effects of the base analysis for future analysis.

Three different methods are proposed by DNV standards [7] for buckling resistance analysis:

1. Linearized approach: apply the FE method for assessing the buckling eigenvalues (linear bifurcation analysis) and determine the ultimate capacity using empirical formulas
2. Full non-linear analysis using standard defined equivalent tolerances and/or residual stresses
3. Non-linear analysis that is calibrated against standard formulations or tests.

The first two named approaches are used and compared in this research.

Initially, a linear eigenvalue buckling analysis of the model was performed. Observing the load cases and the load path in the skeleton tube design, it is evident that rings will be in pure compression. Therefore, it is expected that buckling will appear in the rings. As seen in Figure 117, local buckling appeared in the webs of the rings.
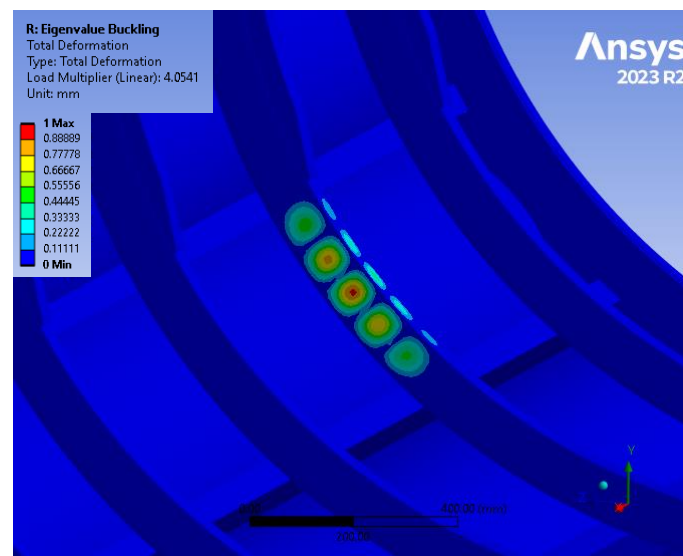

Figure 117: First buckling mode of the Skeleton tube design with rail supports

First ten buckling modes were extracted, and all of them expressed local buckling in the webs of the rings. The first ten buckling modes are presented in Table 19, with their buckling factors. Figures of all buckling modes are given in section FEM results of Appendices.

Buckling shape	Eigenvalue - λ
1	4.054
2	4.061
3	4.077
4	4.085
5	4.196
6	4.201
7	4.220
8	4.224
9	4.238
10	4.243

Determination of buckling resistance by use of linearized buckling values

According to DNV, in order to establish the buckling resistance of the structure using linearized buckling values, a linear analysis should be performed, and maximum compressive and von Mises stresses expressed. Then, the eigenvalue buckling analysis should be run, to determine eigenvalues and eigenmodes. The governing buckling mode is then chosen, and the von Mises stress is taken from the point in the model where the stress will reach the yield stress first.

Then, the critical buckling stress, σ_{ki}, needs to be determined. This is done by multiplying the representative stress, σ_{Rep}, with the eigenvalue, k_g, of the governing buckling mode:

$$\sigma_{ki} = k_g \cdot \sigma_{Rep} \tag{7.4}$$

Representative stress is the stress in the centre of the buckled web of the ring, as seen in Figure 118 and Figure 119.
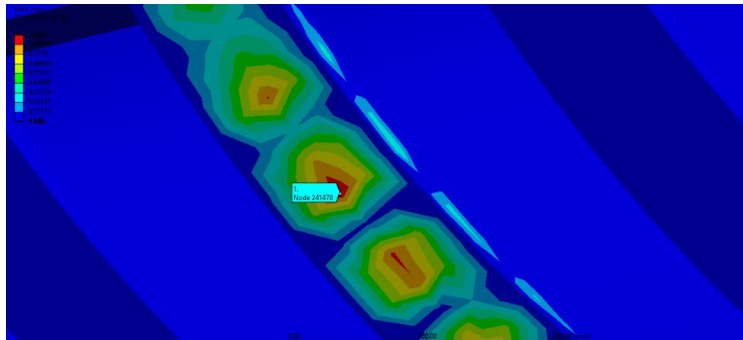

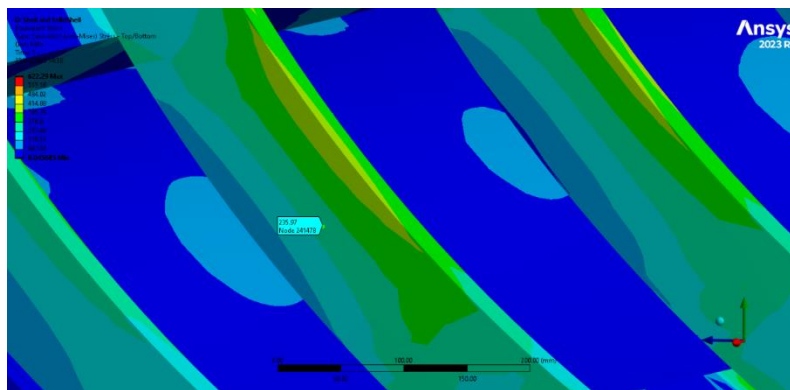*Figure 118: Node in the model with the highest von Mises stress*

Figure 119: Representative stress [σ_{Rep} = 236 MPa]

So:

$$\sigma_{ki} = 1054 \ MPa$$

The reduced slenderness is calculated as:

$$\bar{\lambda} = \sqrt{\frac{f_y}{\sigma_{ki}}} = \sqrt{\frac{355}{1054}} = 0.58 \tag{7.5}$$

Then, the κ factor needs to be determined. Web buckling of the ring can be considered as the buckling of the stiffened plate, where the flanges act as stiffeners. Therefore, the following equation can be used from DNV Table 5-7 Buckling curves [7]:

$$\kappa = \frac{1}{\varphi + \sqrt{\varphi^2 - \lambda^{-2}}} \leq 1.0 \tag{7.6}$$

Where:

$$\varphi = 0.5\left[1 + \alpha\left(\bar{\lambda} - 0.2\right) + \bar{\bar{\lambda}}^2\right] \tag{7.7}$$

And $\alpha = 0.3$ for strict tolerances and moderate residual stresses. So, this gives factor $\varphi = 0.73$ and factor $\kappa = 0.86$. After obtaining all the factors, the buckling resistance R_d can be determined, where the material factor is taken as 1.15:

$$\frac{R_d}{S_{Rep}} = \frac{\kappa f_y}{\gamma_M \sigma_{Rep}} = \frac{0.86 \cdot 355}{1.15 \cdot 236} = 1.13 \tag{7.8}$$

Unity check:

$$UC = \frac{1}{1.13} = 0.89 \leq 1$$

Buckling resistance from non-linear analysis using standard defined equivalent tolerances

The buckling resistance of the model can be assessed through a nonlinear analysis, where the initial imperfections, residual stresses and material non-linearity are taken into account [7]. The determined equivalent geometrical imperfections are assigned to the nonlinear model, inducing buckling in the wanted part of the model.

The Ansys workflow is also showcased in Figure 88, where initially, a linear static analysis was performed, meaning that the linear material has been assigned, and large deflections in the model were deactivated. Subsequently, eigenvalue buckling analysis was performed, providing buckling modes and their corresponding eigenvalues. A separate Ansys project was then created for post-buckling analysis. The model is transferred with a critical buckling shape assigned. To induce the desired buckling shape, a scaling factor had to be defined for the initially perturbed shape, which was done according to DNV standards [7].
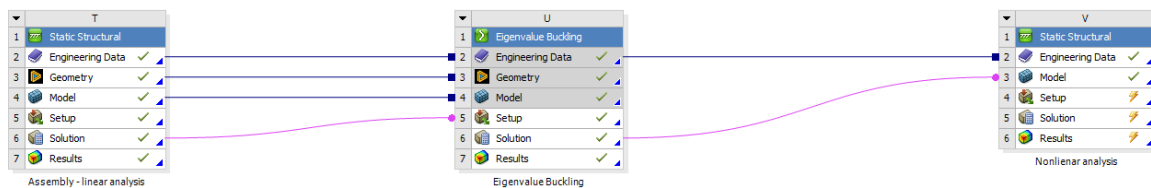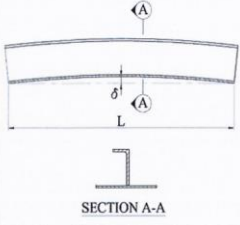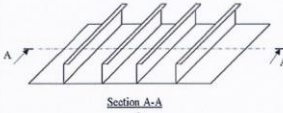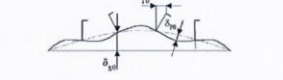

Figure 120: Workflow of buckling analysis in Ansys

In the nonlinear analysis of the model, the magnitude of the initial geometrical imperfection is determined using Table 20. The web can be seen as a plane plate between two stiffeners, presented by the ring flanges.

Table 20: Equivalent imperfections based on DNV [7]

Component	Shape	Magnitude	
Longitudinal stiffener girder webs	bow	L/400	SECTION A-A
Plane plate between stiffeners	buckling eigenmode	s/200	Section A-A
Longitudinal stiffener or flange outstand	bow twist	0.02 rad	

Therefore, the *s* from Table 20 represents the height of the web, which is 100mm. This interpretation is also visualised in Figure 121.
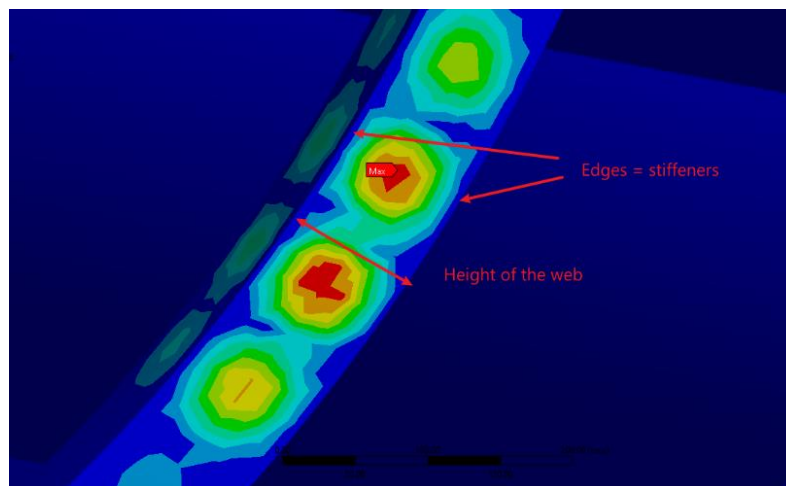
Figure 121: Interpretation of the ring web as the plane plate between stiffeners

This yields a scaling factor of 0.5. Given that the total deformation of the web from the linear analysis is 1mm, the initial geometrical imperfection of the web before the nonlinear analysis is 0.5mm. The load magnitudes in the nonlinear post-buckling analysis were gradually increased until the failure. By increasing the load magnitude, it is possible to determine the load factor at which failure happens in the model with an initial geometric imperfection.

The ring experienced failure at vacuum pressure of 0.17MPa. Wind and snow loads were increased as well, but have minimal influence compared to the vacuum pressure. In the next two figures, the final deformation of the ring is showcased before the failure. For visualisation of the ring behaviour, Figure 123 shows the scaled-up (x36) deformation. The maximum deformation of the ring is seen above the buckling point. This is due to global ring deformation, where the buckled point act as a hinge.

Figure 122: Total deformation [mm] of the buckled ring at the failure point
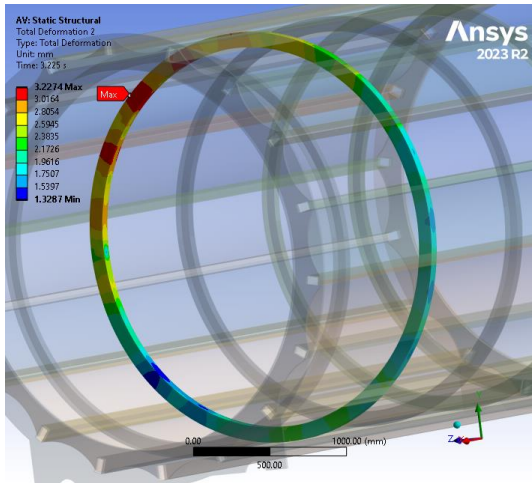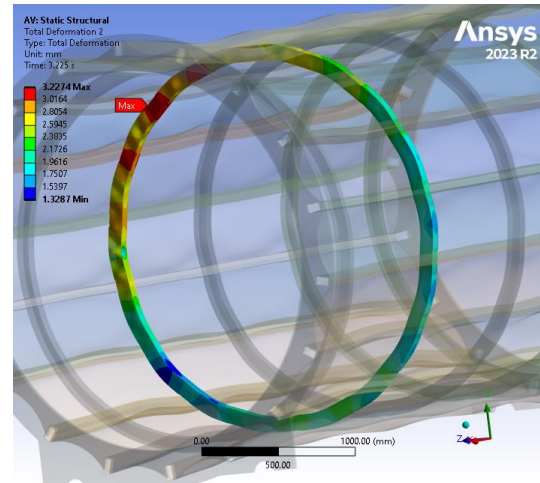
Figure 123: Scaled-up deformation [mm] of the buckled ring at the failure point for visualisation

Looking at the scaled-up deformation of the ring at the failure point in Figure 124, it is evident that the webs buckle outwards for 2.55mm, while the flange buckles inwards for 1.7mm. This is the last data set before the failure. Figure 125 shows the stress in the ring at the failure point.
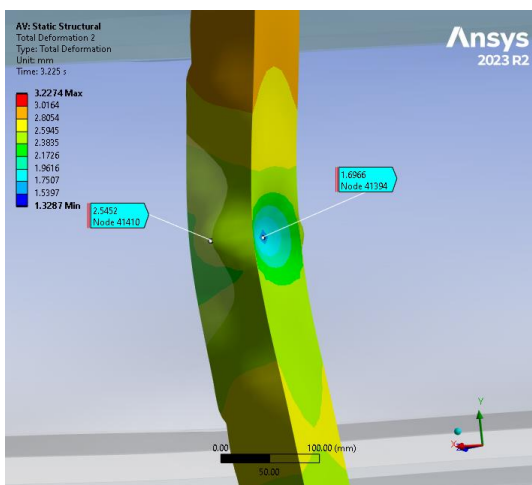
Figure 124: Close-up of the ring deformation (scaled-up) at the buckled location.
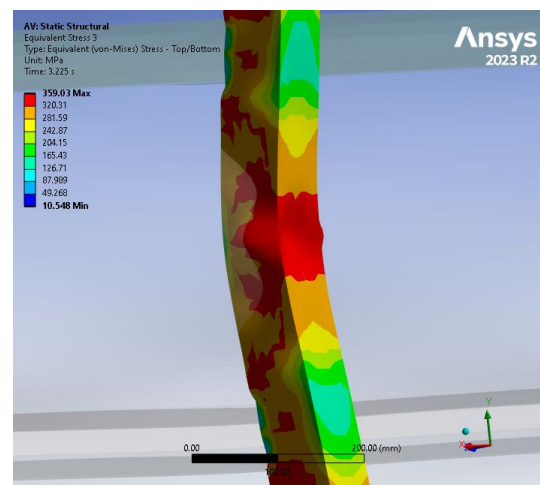
Figure 125: Stress [MPa] at the buckled location

Figure 126 and Figure 127 represent the stress and total deformation of the buckled ring as the vacuum pressure gradually increases. The yield strength is reached at vacuum pressure of 0.082MPa (Figure 126), then a plastic plateau is seen from p = 0.143MPa until failure at p = 0.17MPa. The stress curve slightly ascends before the failure, indicating the beginning of material's strain hardening. Although the ultimate strength of S355 steel is 490MPa, the ring failed at 359MPa. This is due to multiple factors: i) Initial geometrical imperfection which initiated the buckling, ii) slender components reach yield and ultimate strength sooner, and iii) a multilinear nonlinear material data has been used instead of bilinear. This can cause a preliminary failure in the post-buckling analysis; thus, DNV [7] standards suggest assigning a bilinear material.
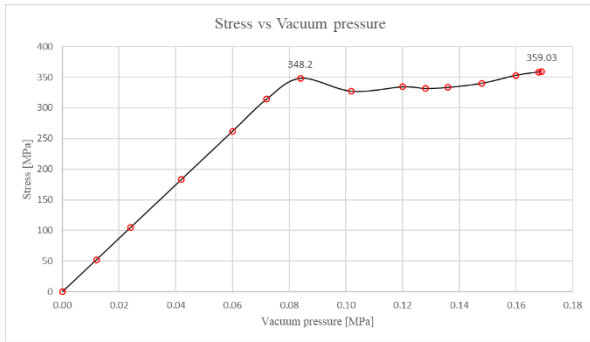
Figure 126: Stress [MPa] vs vacuum pressure [MPa] of the buckled ring.
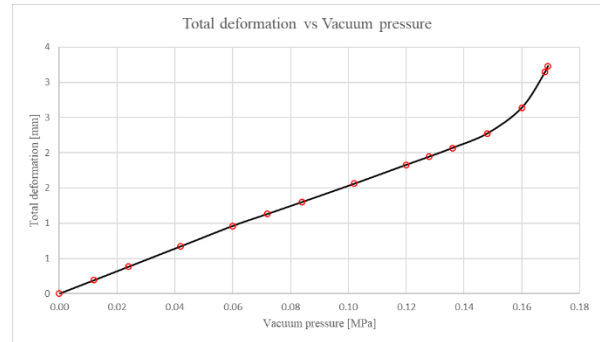
Figure 127: Total deformation [mm] vs vacuum pressure [MPa] of the buckled ring

Looking at Figure 38 in section 5.1, the nonlinear material data triggers at 320MPa, while the bilinear isotropic hardening material data has a linear stress-strain curve until the yield strength of 355MPa (Figure 128).
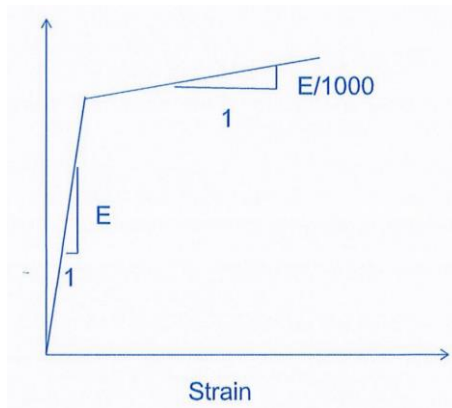
Figure 128: Bilinear material model to be used for the post-buckling nonlinear analysis as given in DNV [7]

Using the bilinear material data, it is observed that the stress reached 370MPa before the nonlinear response.
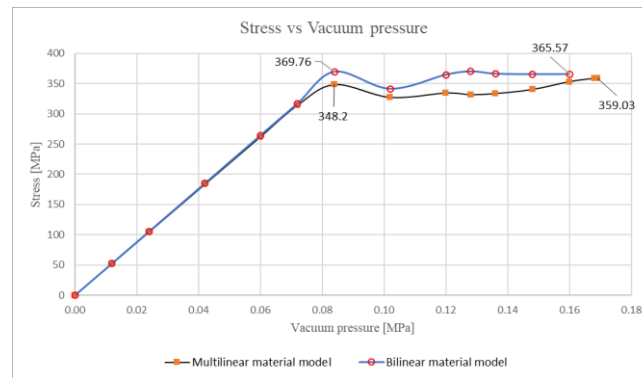
Figure 129: Comparison of stress data using bilinear and multilinear material model. The stress in the model with bilinear data overshoots beyond the yield point.

This is a computational error due to stress extrapolation from the integration points to the nodes. Stress and strain values are read at the nodes. As explained in Ansys innovation course [33], in case of the elastic response, the values at integration points (points between the nodes) are extrapolated to the nodes. In case of a plastic response at the integration points, these are simply copied to the nodes, as seen in Figure 130.

67
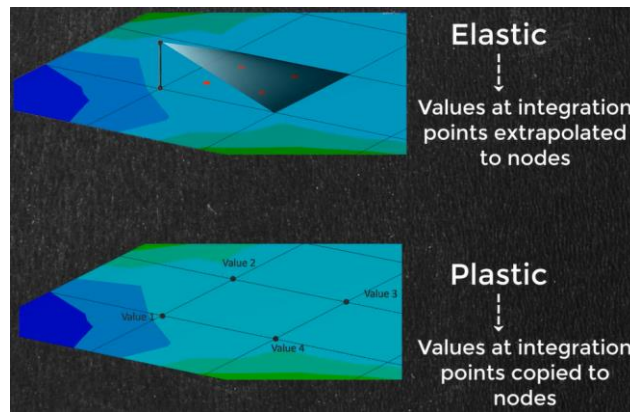
Figure 130: Values projected to the nodes in case of an elastic and plastic response [33]

The problem appears when the stress is just below the yield point. In this case, the extrapolation of values is permitted, but the extrapolated stress at the node exceeds the yield stress. This can be mitigated by increasing the mesh density or by using a command code in Ansys, which forces the values from the integration points to be copied to the nodes.

Lastly, the equivalent plastic strain is checked at the point of failure. As seen in Figure 131, it results in 0.6%. This indicates that the failure happens without large preceding plastic deformation.
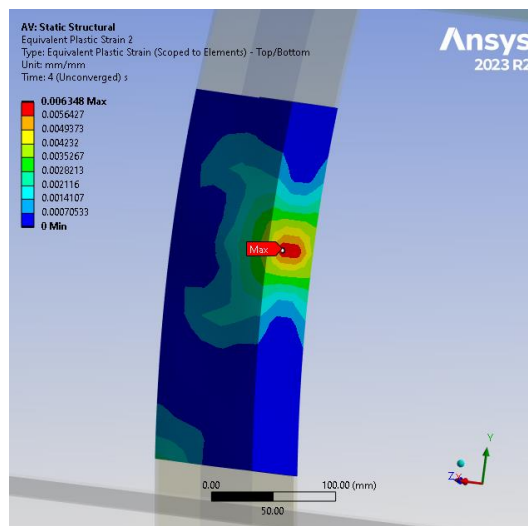
Figure 131: Maximum equivalent plastic strain [mm/mm]

Both approaches satisfy the unity check, where the linearized approach yields unity check of 0.89, while the full non-linear approach results in 0.7. Comparing both approaches, the linearized approach provides conservative results.

8   FEM Approach - Detail Engineering

One of the critical points in the design is the connection between the stringer and the ring. This was identified in the analysis of the assembly, as well as in the assessment of the tube production and construction. In the initial design, the components would be welded together. In a single tube section, there are 16 rings and 18 stringers, which sums up to 288 connections. During the construction, aligning all components and maintaining them in position might prove problematic and result in inaccuracies. Considering that the structure is prone to imperfections and that the straightness of stringers is of great importance, as well as that stress concentrations are present at those locations, the connection type needs to be researched. Initially, a model of welded connection was analysed, and after that, six different connection designs were modelled. They are compared in terms of complexity, efficiency and production.

8.1   Ring-to-stringer connection

One ring and stringer were isolated from the assembly analysis to study the structural behaviour. Assessment of the local stresses is performed to identify reasons for concentrated stresses. A bonded connection is assigned between the ring and the stringer in the assembly. This does not represent the weld, but the stresses in the components are accurate nonetheless since the load path goes through the webs of both components. Figure 132 showcases the stress in the components, and the load path due to the vacuum pressure. The scaled-up deformation of the model in Figure 133 clearly visualises the behaviour of both components. Stress concentrations are attributed to the upward buckling of the ring's top flange. Additionally, the lack of fillets on the components further causes increased stresses.
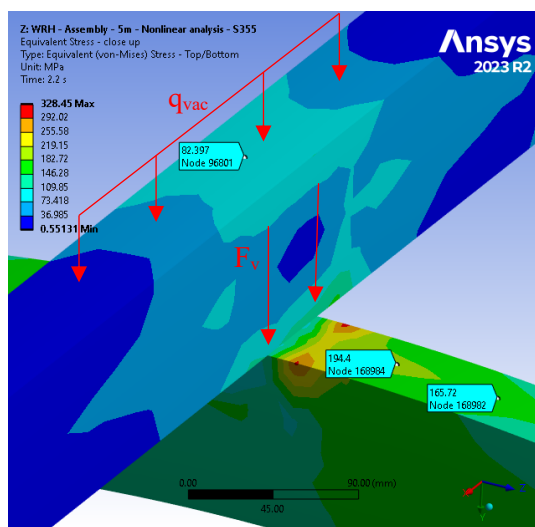
Figure 132: Stress [MPa] of the initial ring to stringer welded connection design. For simplification purposes in the analysis the two surfaces are simply bonded. The arrows represent the load path.
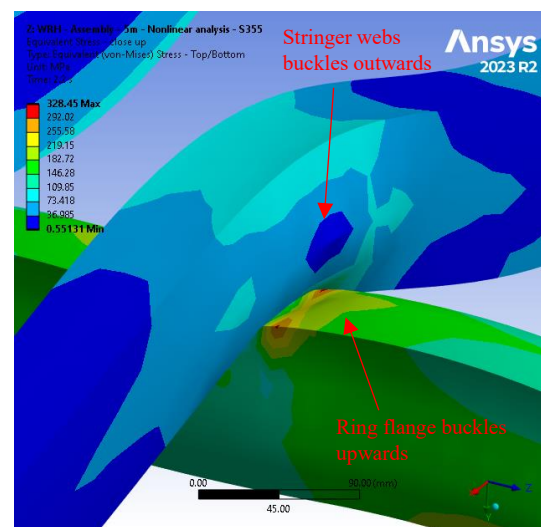
Figure 133: Stress contour with a scaled-up deformation for visualisation of component behaviour.

Based on those results and considering the ease of construction, several connection designs were modelled. The general design idea was to increase the surface through which the load would be transferred and to create a design that also mechanically bonds the two components. The failure should still happen in the ring or stringer, and if that is not the case, it can be guaranteed by either increasing the thickness of the connector (bracket) or assigning a higher steel grade.
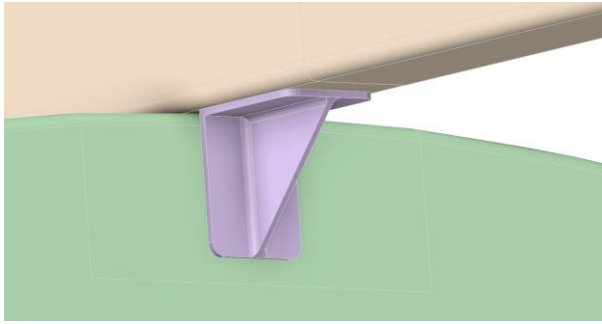
Detail A
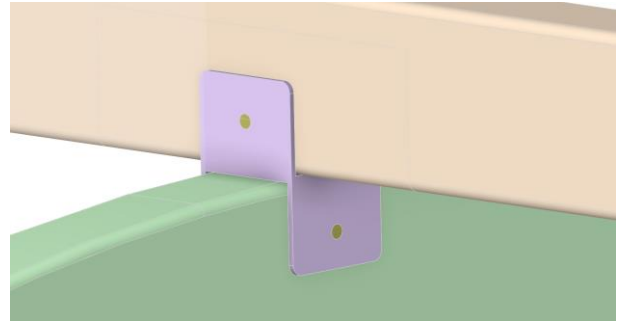
Detail B
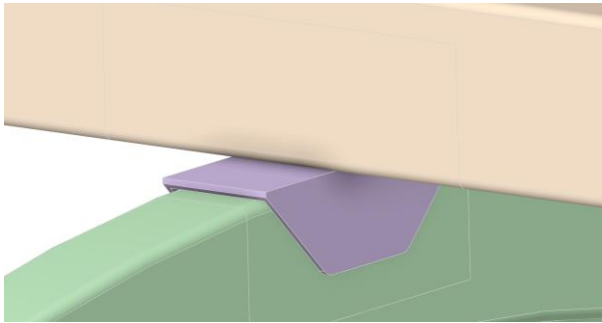
Detail C
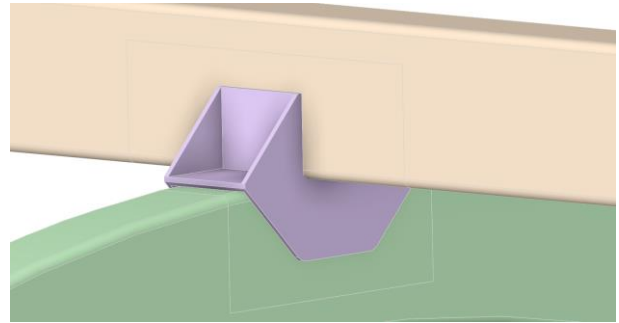
Detail D
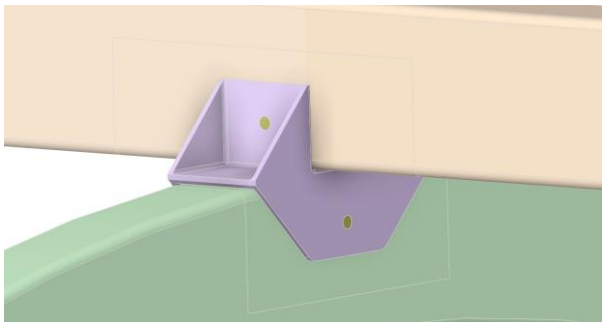
Detail E
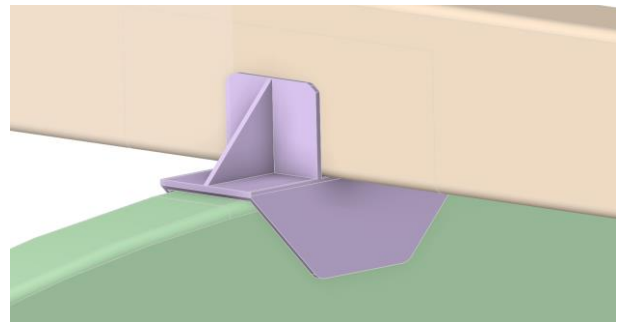
Detail F

Detail A – It improves the bending stresses in the stringer by increasing the longitudinal area through which the load travels. On the downside, it does not resolve the issue of geometrical imperfection between the two contact surfaces. The assembly might prove to be problematic since two individual parts need to be connected.

Detail B – This detail mechanically connects both components, offers limited support for horizontal loads, and can be welded or bolted. Due to its smaller size, it might not perform well in case of accidental loads, and the unreinforced flanges could be weak points.

Detail C – It works like a sleeve for the ring, where the inner surface of the bracket follows the curvature of the ring while the top surface is flat. The steel sleeve could either be welded or bolded to the ring, while the stringer can only be welded to the top surface. It allows some flexibility during assembly and mitigates geometrical imperfections, but the stringer would not be reinforced, and the performance would not outweigh manufacturing costs.

Detail D – This detail is an improvement of Detail C, where two reinforced flanges are added for extra stability of the stringer. It might also ease the assembly process since the components will be mechanically put in place. This bracket would be welded along the edges of both components, which would create a stiff connection but would be an expensive and time-consuming installation.

Detail E – It is identical detail as Detail D, but instead of a welded connection, it is bolted. This change improves the assembly time and cost, and performs equally well, since the bracket is primarily in compression.

Detail F – The last detail is another variant of Detail D, with different flanges. The production aspect was considered in this design, although it does not improve the detail's performance.

After assessing details in terms of efficiency, production, construction method, and durability, Detail E was chosen. All connections can either be welded along the edges to the webs of ring and stringer or bolted. Welds are susceptible to cracks, and considering that component imperfections, such as lack of straightness, can introduce residual stresses in the welds, the focus is on the bolted connection.

Given that the load is assigned to the top flange of the stringer, there is a possibility that the stringer webs to buckle. In such case, the force would be transferred through the bolt. The idea of this detail is that the bolt only serves as a mechanical fixture and not for structural integrity. Due to the slender cross-sections of components, bolts cannot be pretensioned. To prevent such scenario, slotted holes were added to the stringer webs. However, after reassessment of the design, slotted holes were added to the bracket instead. This has been done to not further weaken stringer webs through which the load is transferred. The connection design with slotted holes in the stringer is given section *G* of Appendices.

8.2   Steel bracket connection design

Steel bracket consist of the saddle, which is the curved base plate that is in contact with the upper flange of the ring and bottom flange of the stringer, and two pairs of webs, one parallel to the ring and the other to the stringer. Webs include bolt holes and reassure the mechanical fixture. The slotted hole in the bracket also allows some amount of bolt pretension, and this would also prevent potential uplift of the stringer. However, due to a small bolt size and thin web thickness, pretensioning is not considered in this research. Bolt normal clearance hole should follow the EN1993-1-8 [34] standards, but for FE model simplification, the bolt hole was modelled without clearance.

The goal of this connection design is to mitigate stress concentration and prevent local yielding. Additionally, to ease the installation process and improve maintenance and the component replacement process in case of failure.
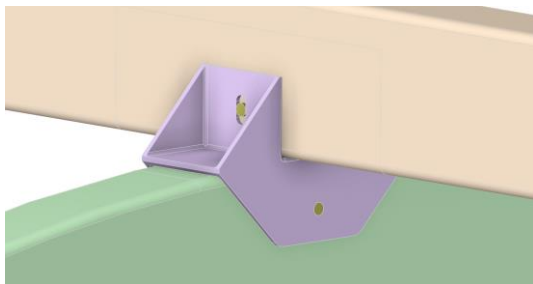
Figure 134: Steel bracket connection design with a slotted hole in the bracket itself.
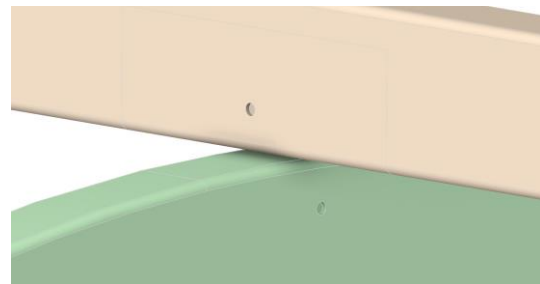
Figure 135: Holes in the ring and stringer, which could be made on site to reassure perfect fit.
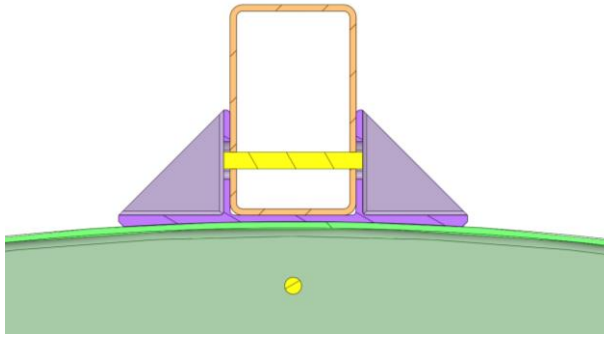
Figure 136: Cross-section of the bracket connection. The inner contact surface follows the radius of the ring.
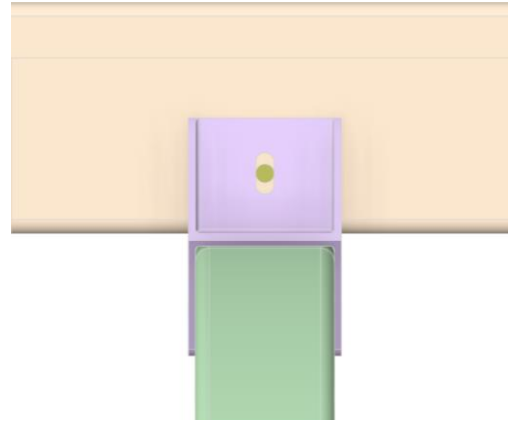
Figure 137: Side view of the steel bracket connection

Although a larger contact area improved overall stress distribution, the four stress concentrations are still visible (Figure 139). Slightly increased stress is also seen in the web of the ring and at the edges, but nonetheless, it is not critical.
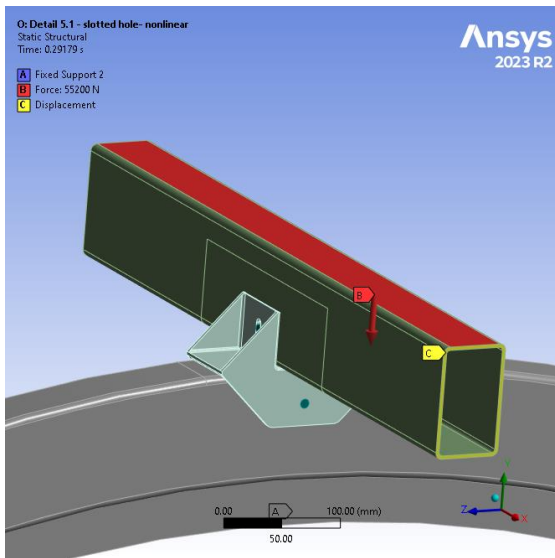
Figure 138: Analysis setup of the bracket connection.
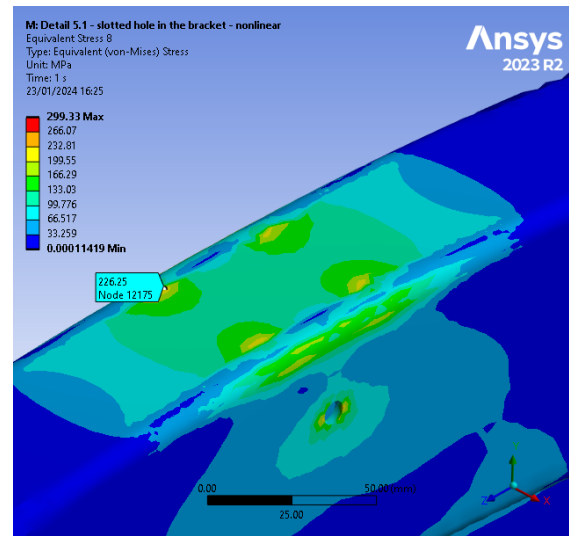
Figure 139: Equivalent von Mises stress [MPa] of 226MPa at the ring contact area. The stress of 299MPa given in stress contour is due to a stress singularity.

Observing the strength performance of the bracket, the critical area is the edge between the bottom webs and the saddle. This is because of multiple reasons, including structural and analysis related. The load travels through the bracket, and an increased resistance and, consequently, increased compressive stress is expected at the edges of components. Additionally, ring webs tend to deform outwards due to compressive load, and this deformation causes bending stress in the bracket webs, as shown in Figure 140. The two components are also in perfect contact along the inner fillet (maximum stress in Figure 141), which means that mesh density influences the results. Maximum stress is localised, signifying that the mesh along the rounded corners is not dense enough. Mesh refinement could decrease these stresses, considering that the total force will be transferred by contact surface.
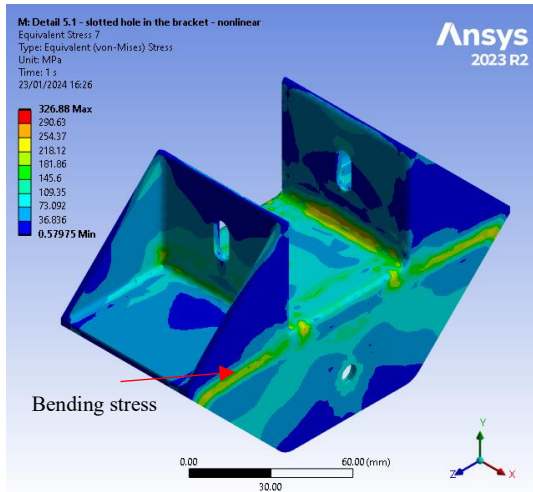
Figure 140: Von Mises stress [MPa] in the bracket - isometric view
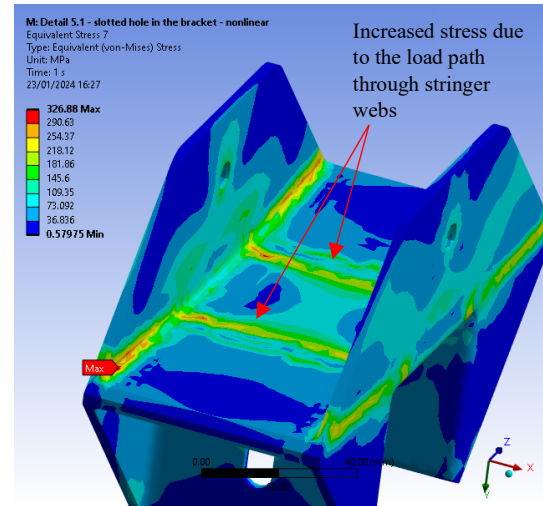
Figure 141: Von Mises stress [MPa] – bottom surface of the bracket

Graph 11 displays the peak stresses in components as the load increases. Stringer data is not included because of the reduced length over which the load is distributed and the boundary conditions that do not fully match actual conditions. The stringer still serves the purpose of transferring the load to the bracket in the analysis, but the results of the stringer itself are not reliable. Yield strength is not reached in any of the components. Moreover, these stresses are attributed to previously discussed stress concentrations.
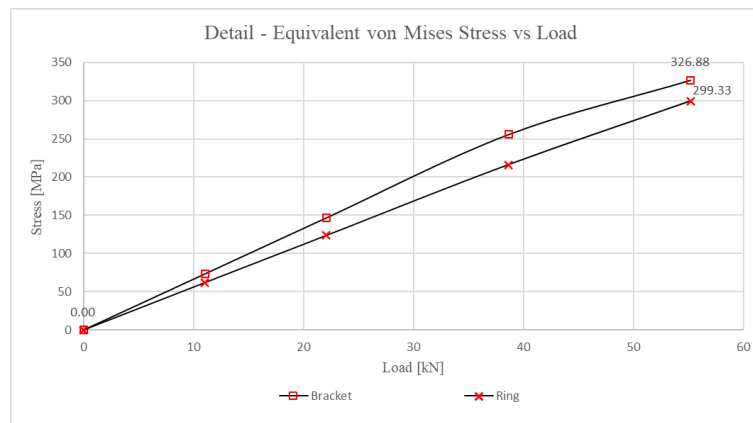
Graph 11: Stress in components in the ring-to-stringer connection design

Observing Figure 142 reveals that the largest deformation occurs in the centre of the bracket. Webs tend to buckle outwards, whereas the area around the bolt hole stays undeformed. In Figure 143, the ring's flange is shown to buckle downwards under the compressive load. The deformations are minor and do not indicate any unexpected behaviour.
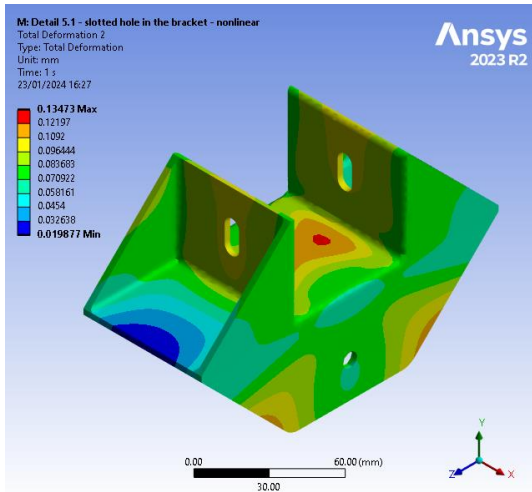
Figure 142: Total deformation [mm] – Steel bracket
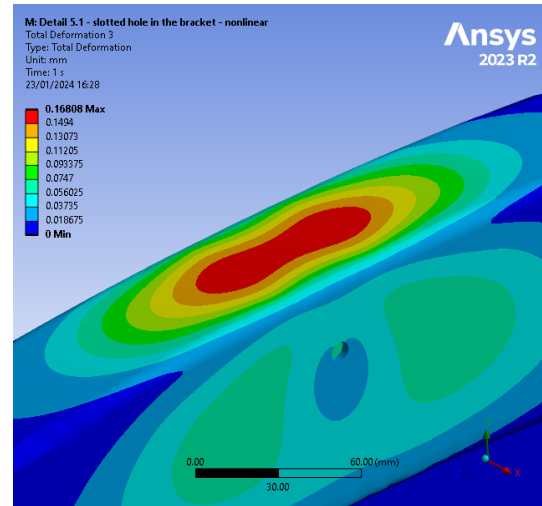
Figure 143: Total deformation [mm] - Ring

Longitudinal load

In case of the stopping pod load, a longitudinal load is assigned through the rail support to the ring. In Chapter 5.5.8, the breaking of the pod load has been determined to be roughly $F = 3000N$. If the load is equally divided among all 18 connectors, then it results in a longitudinal load of $F_l = 170N$ per connection. This load is dismissible small, and it does not affect the design. But considering the shape of the rail support, through which the force is transferred, the load might not be equally divided. An assessment was done, to determine whether the resistance capacity of the bolt and the stringer webs is sufficient in case when only some of the connectors are activated.

The most critical scenario is, if due to lack of ring stiffness, only two bracket connections would have been activated, which are the closest to the rails. This would result in a longitudinal force of $F_l = 1530N$ per connection. In this analysis the vacuum pressure load case is present as well. This does not contribute to the resistance in terms of friction, since a frictionless contact is used, but in terms of mechanical bonding, once the stringer deforms at the edges and clamps the bracket.
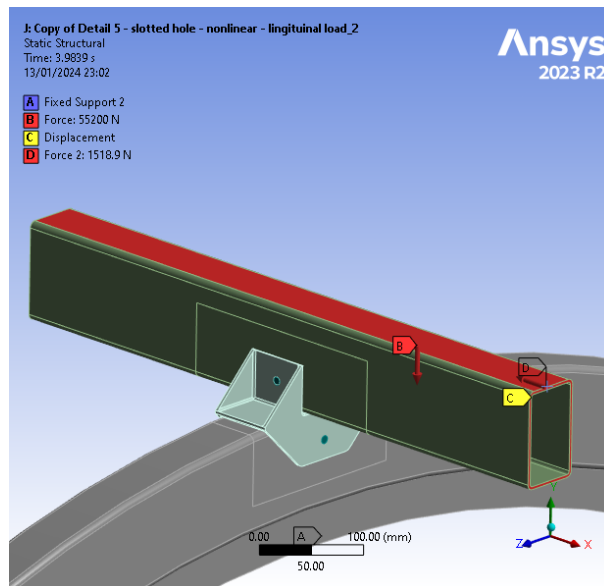
Figure 144: Setup - Breaking of the pod and vacuum pressure

Vacuum pressure load case was considered in the first analysis. Due to compression of stringer against the connector, a frictional connection is expected between the two surfaces. Steel to steel friction coefficient depends on the surface treatment and the amount of contact pressure. Verifying frictional force analytically yields the following:

$$F_f = \mu \cdot N \tag{8.1}$$

Normal force between the surfaces is the point load calculated in chapter 6.1., while the static coefficient of friction is taken as $\mu = 0.14$, which is for coated steel under contact pressure of 20 MPa [35]. Otherwise, the contact pressure between the stringer and the connector is:

$$p = \frac{F}{A} = \frac{55.2kN}{60^2} = 15.33 \ MPa \tag{8.2}$$

But based on the conducted tests, the difference between various contact pressures for the coated steel is minimal.
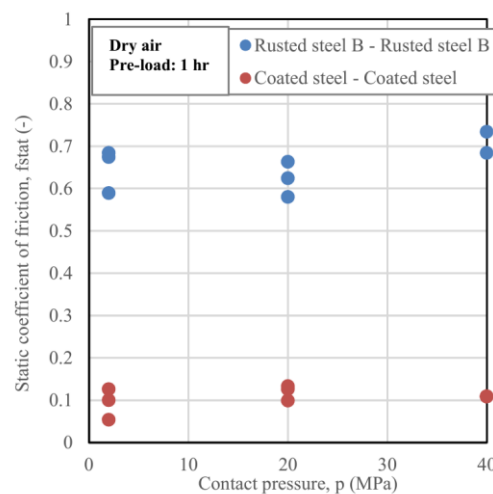
Figure 145: The static coefficient of friction at the first onset of sliding [35]

Therefore:

$$F_f = \mu \cdot N = 0.16 \cdot 55.2kN = 8.83 \ kN \tag{8.3}$$

Which means that in order for the ring to slide out from underneath the stringer while the tube is under vacuum pressure, a longitudinal load of 5.52kN is required per connection. This is in case if bolts would not be present and if no yielding of the stringer is considered. Comparing this value against F_l, which actually exhibits at the connection, it is safe to conclude that the load due to a breaking pod does not destabilise the structure.

The critical scenario is in the case if the pod it is breaking, and the tube instantly depressurises due to e.g., plate failure. Therefore, no compression is present between the stringer and the ring. To increase the severity of the scenario, only two connectors are activated for resistance against the breaking pod load, which gives $F_l = 1531.3N$. The highest stress is expected at the contact point between the stringer webs and the bolt. Expected failure mode, if any, is a bolt shear failure, shearing out of plate part, or hole ovalisation. Figure 147 showcases the maximum von-Mises stress, which is in the web of the stringer. A section plane is used to present stress inside of the stringer.
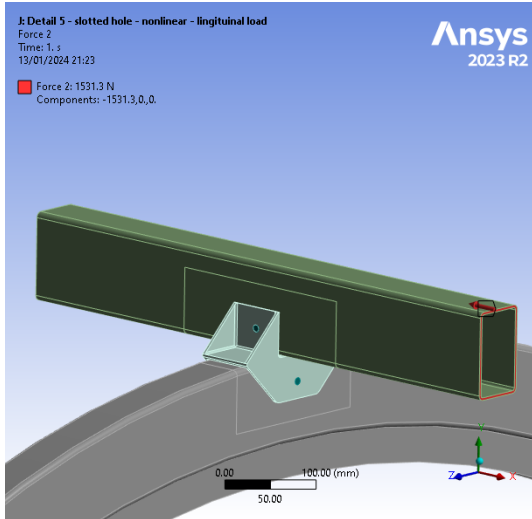
Figure 146: Setup - Breaking of the pod [critical scenario]
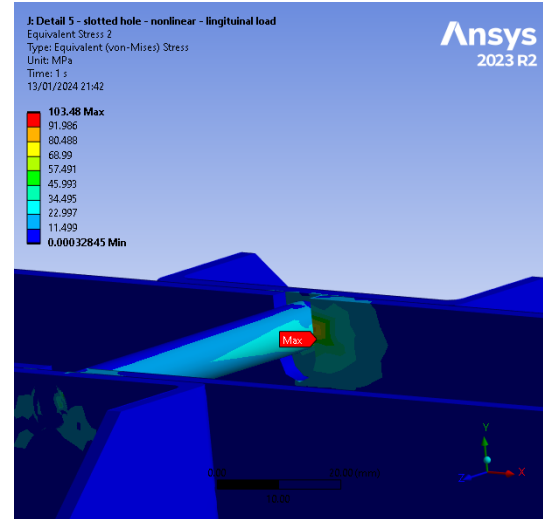
Figure 147: Maximum Equivalent von-Mises stress [σVM = 103.5MPa]

Failure modes are also verified analytically to assess which is the critical failure mode. Bolts are loaded in shear; therefore, the bolt failure is brittle. An assumption is made that the shear face is through the shank and not the thread. Thus, the shear resistance of the bolt is calculated using the following equation:

$$F_{V,Rd} = \frac{0.6 \cdot f_{ub} \cdot A}{\gamma_{M2}} \tag{8.4}$$

A bolt class of 8.8 is chosen, which is the preferred class for non-preloaded bolts. Considering bolt M8, the bolt resistance to shear is:

$$F_{V,Rd} = \frac{0.6 \cdot 800 \cdot 50.265}{1.25} = 19.3kN > F_{l,max} = \frac{1.5}{2} = 0.75kN \tag{8.5}$$

Next check is the bearing resistance, where the general expression is:

$$F_{b,Rd} = \frac{k_1 \cdot \alpha_b \cdot f_u \cdot t \cdot d}{\gamma_{M2}} \tag{8.6}$$

Bearing resistance depends on plate properties (steel grade, thickness), bolt properties (strength class, diameter), the hole diameter and the position of the bolt hole. The factor of 2.5 can be used as a reference value for $k_1 \cdot \alpha_b$, since k_1 needs to be smaller or equal to 2.5, and α_b smaller or equal to 1. $F_{l,max}$ is divided by 2, since the bolt is clamped on both sides. So:

$$F_{b,Rd} = \frac{2.5 \cdot 355 \cdot 3 \cdot 8}{1.25} = 17.04 \ kN > F_{l,max} = \frac{1.5}{2} = 0.75kN \tag{8.7}$$

Judging from the analytical approach, a conclusion could be done that the maximum allowed longitudinal force F_l is roughly 17kN. But it should be noted that the detail has a slotted hole, which weakens the design, and the maximum allowable F_l is therefore less. The bolt and plate resistance are nonetheless sufficient.

Hole misalignment and a gap between the bracket and the ring

If the decision is made that the bolt holes would not be made on site, but rather at the manufacturer, a threat of geometrical misalignments exist. Potential scenario is that the bolt hole in the ring is drilled 5mm above the designated location. This creates a gap between the steel bracket and the ring flange, and consequently the force goes through the bolt, instead of the contact surface. Connection with a 5mm

gap is modelled as seen in Figure 148, and the same load and boundary conditions are assigned as at the previous analysis. The total deformation proves that a minimal deformation can be expected in such case. It also indicates that there is no bolt or plate failure.
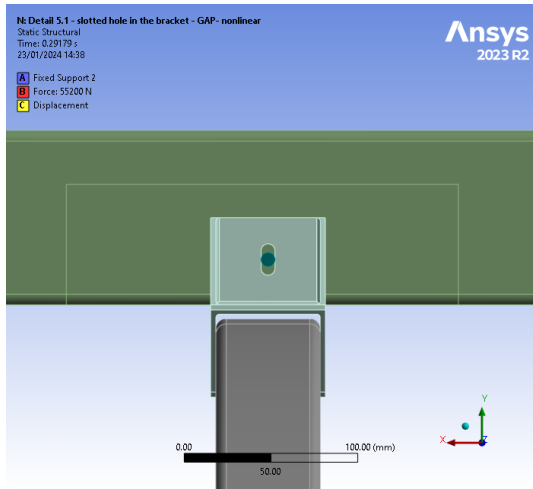
Figure 148: Connection details with a 5mm gap between the bracket and the ring
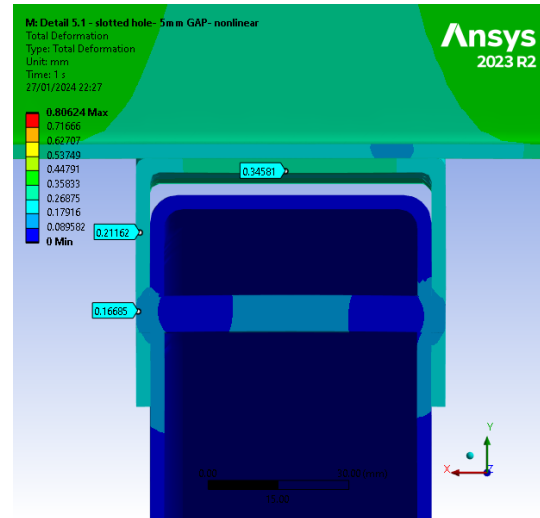
Figure 149: Total deformation [mm] of the detail

Looking at the von Mises stresses in Figure 150, it can be seen that the maximum stress of 638MPa exhibits in the bolt. Since the bolt is non-preloaded, the preferred bolt class is 8.8, with a yield strength of 640 MPa. That means that the bolt does not plastically deform under such conditions; however, in case of impact load, or any other unfavourable situation, which would suddenly increase the load, a plastic response or even failure in the bolt is expected. Observing Figure 151, the increased stress pattern in the bracket web shows a compression above the bolt, but at the same time, the compressive stress is exhibited under the bolt. This is due to the bolt acting as a pivot, around which the plate tends to deform.
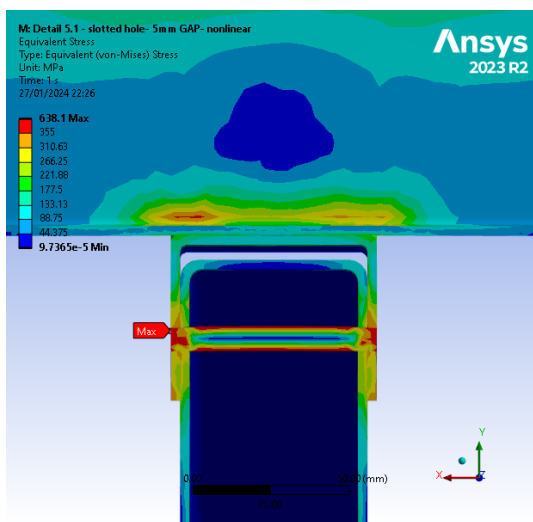
Figure 150: Equivalent von Mises stress [MPa] - cross-section of the detail
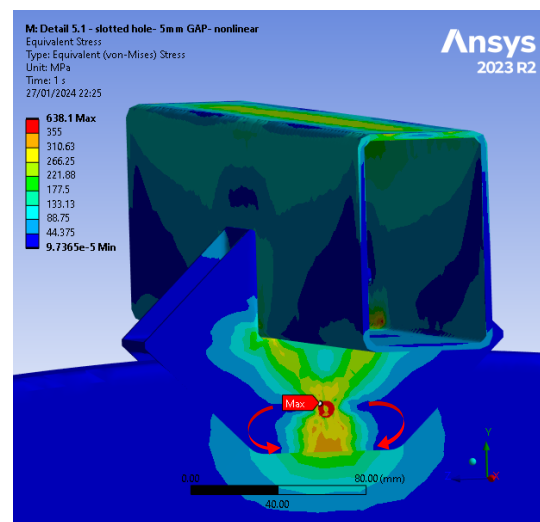
Figure 151: Stress [MPa] in the bracket. Red arrows show the bending of the bracket web around the bolt. This induces compressive stress under the bolt

After that, stresses in the ring and webs of the bracket are assessed. The load path goes from the bracket webs to the bolt. The maximum stress reaches roughly 358MPa at the point of contact and 345MPa in the area adjacent to the contact point. This indicates that the yield strength is reached, and the bracket plastically deforms at the bolt hole. Due to exceeding yield strength, the plastic strain had to be verified

(Figure 153), which resulted in 1.42%. This is still less than the allowable plastic strain of 4.99%, determined with the calibration model.
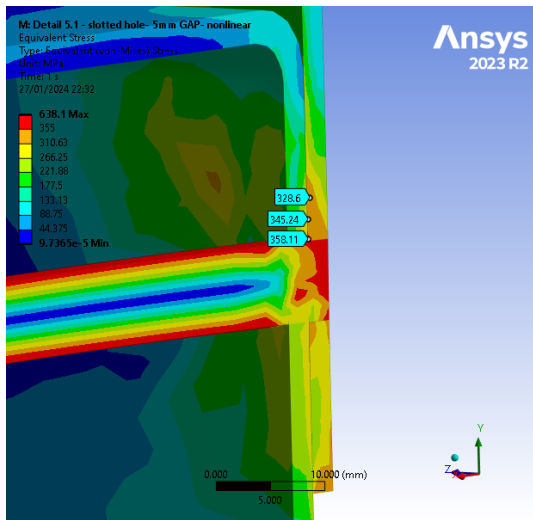
Figure 152: Maximum stress [MPa] in the bracket at the contact with the bolt
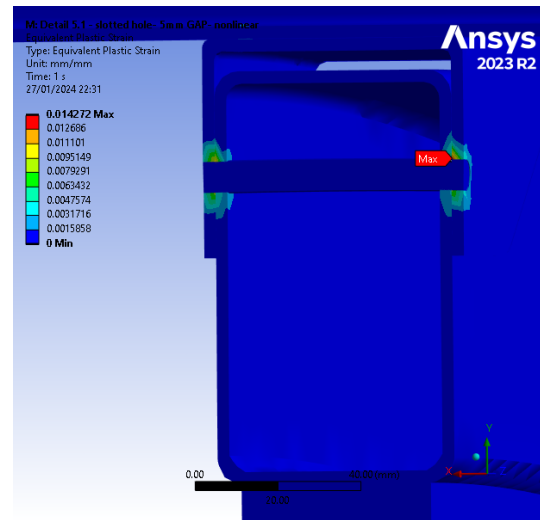
Figure 153: Equivalent plastic strain [mm/mm]

To mitigate the potential gap, the holes could be drilled on-site. If this proves to be a costly process, then a rubber filling could be placed between the bracket and the ring to establish contact between the two surfaces and prevent the force from travelling directly through the bolt. The inclusion of a rubber damper would also require a slight pre-compression of the bracket to the ring, which would ensure that the load passes through the surface contact rather than the bolt. Rubber also absorbs vibrations; therefore, the connection's resistance to fatigue might improve.

Production

The production of brackets might prove to be expensive, especially when considering that the inner surface needs to be milled with a radius to fit perfectly onto the ring surface. Three options are considered for bracket manufacturing: a CNC Milling Process, welding the plates and a precision casting process.

CNC milling is generally used for smaller parts and offers tighter tolerances. A steel block is typically used, from which the model is milled using a CNC machine. This process is especially accurate, and although small corner and geometric errors are possible, as presented in Figure 154, this process is nonetheless more precise compared to casting.
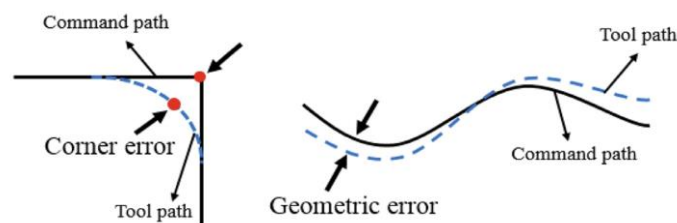
Figure 154: Illustration of corner and geometric error, as presented in the research paper on machining accuracy [36]

The disadvantages of CNC milling include material waste and slower manufacturing speeds. On the contrary, precision casting of steel brackets involves melting the steel and pouring it into a mold. In this case, die casting is the suggested method, which involves inserting the material into the mold under high pressure. This technique improves the surface quality and dimensional accuracy. Additionally,

secondary machining would be required due to the small tolerance requirements of the detail. Casting is a faster process compared to CNC milling, and it produces less material waste. The downsides of casting are unwelcome geometrical imperfections, which could affect the strength integrity [37]. Considering that the steel bracket consists of three plates with details, a welding process can be utilised. This process involves producing the flanges and saddle individually, then welding them into a bracket. Welding can be automated; therefore, it might represent the easiest and most cost-effective production method.

In conclusion, precision casting and welding are the two preferred methods for bracket production, particularly because 288 brackets will be required for a 16m long tube section. Given the hyperloop system's extensive length, mass production of brackets is unavoidable. Casting offers faster and cheaper production, although it comes with the risk of potential geometrical imperfections. Annealing, a heat treatment process, should be considered as well to increase ductility and reduce the possibility of a brittle failure. On the contrary, welding offers a simple and efficient way of producing the brackets. It is advisable to conduct a cost estimation and comparison to determine the most viable production process.

It should be noted that the bracket was designed based on the forces present in this connection. For mass production, the design should be optimised in terms of weight. This optimisation can be achieved by analysing stress results and reducing material in the bracket areas which are underutilised.

Bracket connection at the bottom of the rings

The steel backet connection design has so far been considered to be located at the top of the tube. During the operation of the tube, the brackets are in constant compression due to vacuum pressure. However, should the tube lose its vacuum, there is a concern that the bottom brackets would connect stringers to the rings solely through the bolts. However, this situation is valid only if the detail is considered on a local scale. Globally, plates serve as a shell of the tube, providing some degree of additional stiffness to the stringers, which are continuous and longitudinally connected to the plates.

9   FEM Approach - Plain tube design

The plain tube design is based on the real structure located at the European Hyperloop Centre in Groningen. The global dimensions were obtained from the construction site visit, while locations of rail support connections were determined from the pictures. Global dimensions are identical to the dimensions of the Skeleton tube design. The length of the tube section is 16m, and the tube diameter is 2.5m. The thickness of the tube wall is 16mm, and the thickness of the flanges and reinforcement ring is 20mm.

9.1   ULS and SLS verification

Observing figures from the site visit in section 3, it can be seen that the rail supports are bolted to the tube wall with eight bolts per support. Bolts are then welded onto the tube wall using circular caps. Those caps are modelled as circular areas, as seen in Figure 155. The rails and pod load is, therefore, assigned to those areas.
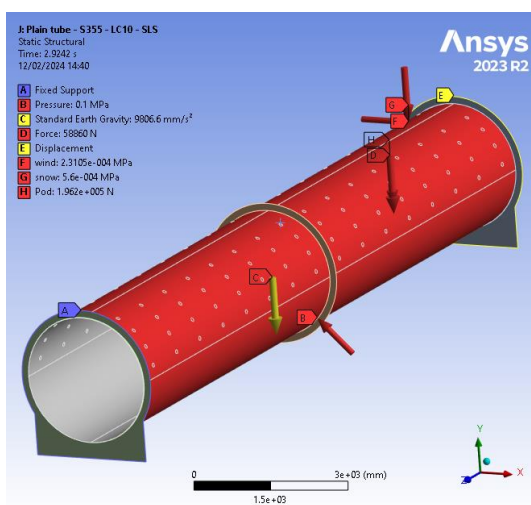
Figure 155: Plain tube analysis setup - SLS
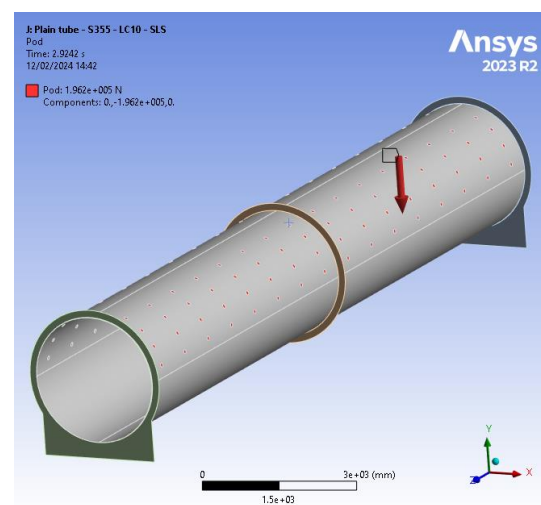
Figure 156: Visualisation of the circular connection areas and its corresponding rail load

The design is governed by the tube buckling and the total vertical deformation. Equivalent von Mises stress does not govern the design since the tube thickness is determined to resist buckling. Pod rails have a small margin of allowable deformation; thus, the total vertical deformation needs to be verified.

Table 21: Analysis settings – Plain tube design

Settings	
Material	Structural steel S355
Model type	Shell
Mesh type	Quadratic
Analysis type	Linear

Table 22: Mesh size - Plain tube design

Component	Mesh size [mm]
Tube	50
Flanges	50
Stiffener	50
Rail support connection	20

Load case	Magnitude
Self-weight	/
Vacuum pressure	0.1 MPa
Rails load	58.86 kN
Snow load	0.00056 MPa
Wind load	0.00025 MPa
Static pod load	196.2 kN

Figure 157 showcases stresses in the tube. An increase can be seen at the location of loaded circular areas, while the peak is at the edge of the flange. This point is a stress singularity, which could be eliminated by remodelling the flange. The strength of the plain tube design is, nonetheless, satisfactory. Maximum vertical deflection is expressed by a blue contour, as seen in Figure 158. This is at the location where the rail supports are attached to the tube itself. The maximum deflection results in 3.4mm. However, to mitigate this issue, the rails can be calibrated to take into account the initial deflection.
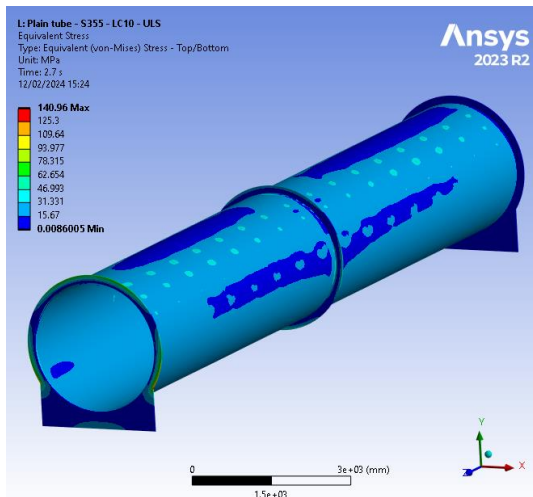
Figure 157: Plain tube S355 - Equivalent von Mises stress [MPa] – ULS – LC10
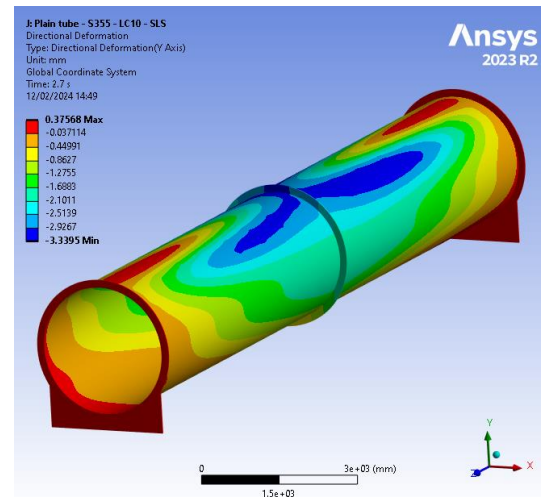
Figure 158: Plain tube S355 - Directional deformation [mm] y-axis – SLS – LC10

9.2   Stability analysis

The plain tube is checked in terms of stability. The vacuum pressure load case has been increased by a safety factor of 1.2. In the analytical verification, the effect of rails and pod load is disregarded. Since those two load cases are present in the FEA model, it is expected to buckle before the vacuum pressure load could reach 0.12 MPa. Therefore, the eigenvalue of the first eigenmode was expected to be less than 1. The first ten buckling modes of the model were extracted, and the results are showcased in Table 24:

Table 24: Buckling shapes and corresponding eigenvalues of the Plain tube design

Eigenmode	Eigenvalue - λ
1	0.831
2	0.831
3	1.055
4	1.055
5	1.065
6	1.065
7	1.128
8	1.129
9	1.410
10	1.417

The eigenvalues of the first two buckling modes are below 1, which is, as previously stated, due to additional load cases. Two buckling sections can be seen in Figure 159, where the stiffening ring in the middle of the tube divides the buckling length.
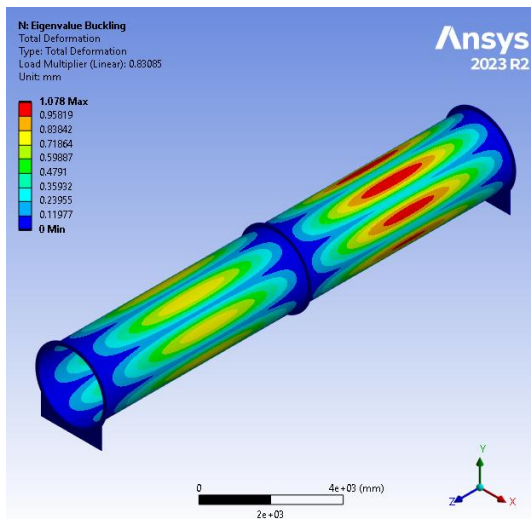
Figure 159: Buckling mode 1 [λ = 0.831] – isometric view
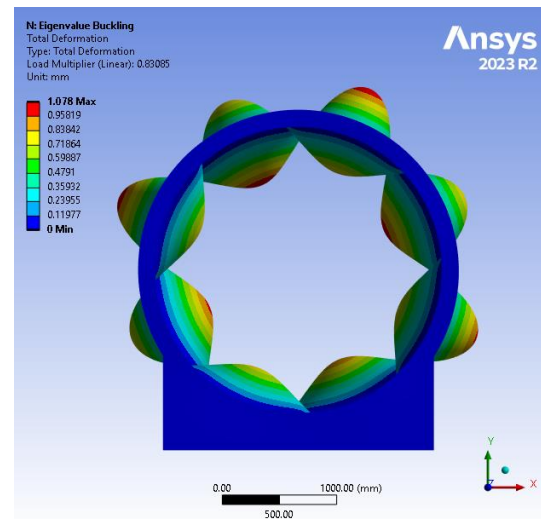
Figure 160: Buckling mode 1 [λ = 0.831] – front view

Steel tube manufacturers provide the tolerances of such deformities, which can be used in the buckling analysis. Given that the buckling factor is below 1, it is necessary to verify the design with a nonlinear analysis incorporating initial geometrical imperfection. However, this theoretical buckling shape does not accurately reflect the real-world geometrical imperfections of the tube. The manufacturer's tube tolerances are provided in terms of out-of-roundness (ovality), eccentricity (wall thickness) and tube straightness reference. A nonlinear analysis with initial geometrical imperfection is nonetheless performed. The initial imperfection scale factor was calculated using Table 20, where *'s'* equals to 8m,

and s/200 results in 40. Vacuum pressure was increased up to 1.2MPa, which is twelve times higher than the anticipated load. As seen in Figure 162, the first buckling shape is initiated.
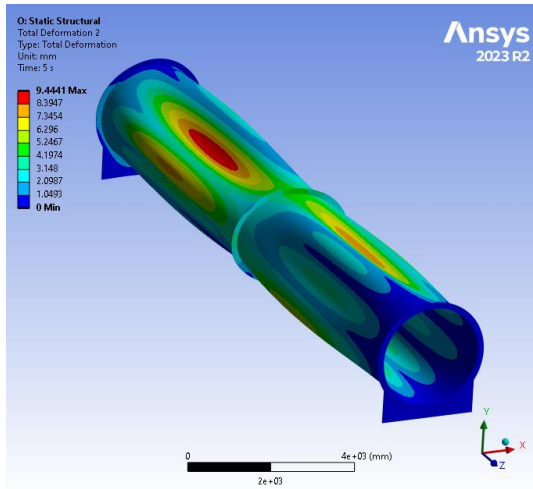
Figure 161: Scaled-up total deformation [mm] of the plain tube design with initial geometrical imperfection at vacuum pressure of 1.2MPa.
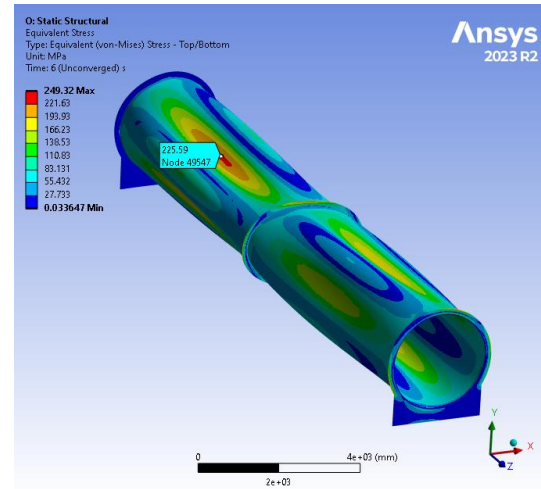
Figure 162: Stress [MPa] at the buckled location of the plain tube design with initial geometrical imperfection at vacuum pressure p = 1.2MPa. The deformation is scaled-up for visualisation of the buckling.

Moreover, in the analytical approach, the codes do not consider global behaviour of the tube. Due to bending, the bottom side of the tube will be in tension, while top in compression. Tensioning of the tube will counteract buckling. This is also indicated with the deformation contour in Figure 161, where the top of the tube which is in compression tends to buckle more than the bottom. In conclusion, the tube design satisfies the buckling requirements.

10 Comparison study

Existing hyperloop test sites opted for the plain tube; thereby, this design can be used as a benchmark design. The comparison study focuses on critical aspects of hyperloop tube design: ultimate limit states, serviceability limit states, thermal expansion, sustainability, and production. The skeleton tube design was analysed for two scenarios, one in which the tube is used solely for retaining the vacuum pressure and the second in which it also supports the pod. Since the plain tube is designed to support rails and the pod, the latter version of the skeleton tube design is used for the comparison study.

Ultimate limit state

The plain tube is not designed based on the ultimate limit state but instead based on the critical buckling pressure. Thus, the plain tube underutilised terms of its strength. Skeleton tube design, on the other hand, is reaching the yield strength limit, with the ULS unity check of 0.96. An initiation of a nonlinear material response was observed at ring-to-stringer connection and in the ring flange.

Fatigue limit state

Fatigue limit state of the assembly has not been fully considered in this research. Due to the number of connections, slenderness of components and potential pod velocity, it is reasonable to anticipate that the dynamic loads imposed by the moving pod will have a significantly impact on the assembly. Connections are critical, and they may also be susceptible to fatigue. Therefore, an assessment of fatigue resistance is recommended for further research on this design.

Serviceability limit state

The hyperloop infrastructure has strict deflection limits. The rails are made out of 1-meter-long segments. These segments have an absolute tolerance of 1.5mm among each other, although a position calibration can be done at installation.

Vertical deflection was extracted from both designs for critical SLS load combination. The plain tube design had a maximum vertical deflection of 3.34mm near the middle of the section at the location of rail supports. However, this deformation is due to local buckling of the tube, and the global vertical deflection resulted in 1.8mm. Global vertical deflection of the skeleton tube design, taken at the side of the central ring, resulted in 3.33mm. As stated before, the effect of initial tube deflection can be mitigated by calibration height of the rails during installation. However, if possible, this should be avoided.

Plain tube does not exhibit any local deformations due to the simplicity of design. On the contrary, skeleton tube design is prone to local deformations. Slender components cause many stress concentrations, and consequently, increased deformations and a plastic response are a threat.

Stability

Structure buckling is divided into local and global buckling. Plain tube design, as according to the standards, experiences global buckling. Skeleton tube design, however, in the first 10 buckling shapes resulted in only local buckling. It is concluded that due to the ring's slender cross-section and since it is in full compression, it will buckle locally first. The ring's web buckling will eventually cause a ring failure, and this may lead to a progressive collapse of the structure.

Thermal response

The infrastructure's operational temperature range is supposed to be between 70°C and -30°C. If the structure's temperature increases uniformly, then the expansion of both designs is expected to be the same due to the same expansion coefficient. In case of a non-uniform temperature increase, then the cross-section of the tube has an influence on the response. In the case of the plain tube design, due to

its thickness, it will take longer to reach the same temperature compared to the skeleton tube design. Therefore, the plain tube outperforms the skeleton tube design at lower temperature ranges.

If we assume that the same temperature is reached in both designs, then the longitudinal force of the plain tube is expected to be higher due to a larger cross-section. Plates of the skeleton tube design would either buckle locally or deflect inwards due to their thickness. The stress increase at the connections is expected to be minor and it not anticipated to affect the global performance. Additionally, the width of the expansion joints for the skeleton tube design could be smaller than for the plain tube.

Impact load resistance

Comparison in impact load resistance heavily favours the plain tube design. The difference in plate thicknesses is 15mm, which means that the plain tube's ability to withstand impact loads is significantly greater. This aspect is one of the determinants of design safety. It is concluded that a skeleton tube design is at a severe disadvantage in resisting environmental and accidental loads. Suggestion on the approach of impact load analysis is provided in section Impact load analysis recommendation of Appendices.

Sustainability

Hyperloop tube designs are compared in terms of material minimization and shadow costs. The total weight of the tube section is calculated by extracting the total volume of the model and multiplying it with the steel density. All components which were modelled are considered, and a comparison of different tube variants are given.

Table 25: Weight comparison of tube designs without rail supports

Design	Tube [m³]	Rail supports [m³]	Brackets [m³]	Total weight [t]	Weight efficiency [%]
Skeleton tube design	0.83	0	0	6.45	37.85
Plain tube design	1.14	0	0	8.90	

Table 26: Weight comparison of tube designs with rail supports

Design	Tube [m³]	Rail supports [m³]	Brackets [m³]	Total weight [t]	Weight efficiency [%]
Skeleton tube design	0.83	0.29	0	8.71	28.07
Plain tube design	1.14	0.29	0	11.15	

Table 27: Weight comparison of tube designs with rail supports and steel brackets in skeleton tube design

Design	Tube [m³]	Rail supports [m³]	Brackets [m³]	Total weight [t]	Weight efficiency [%]
Skeleton tube design	0.83	0.29	0.034	8.97	24.31
Plain tube design	1.14	0.29	0	11.15	

Looking at the weight efficiency to be made with the skeleton tube design, it is evident that the design is significantly more sustainable in terms of material utilisation. Life cycle stage A is considered in the shadow cost estimation. Calculation of the shadow cost *'from cradle to gate'* per kilogram of steel is given in Table 28.

Table 28: Shadow cost of BOF steel (Basic oxygen steelmaking). Values used are proposed by CEG Delft [38].

Impact category	Unit	Monetary value / impact category equivalent in Euro:	Steel BOF [kg]	Shadow cost [€/kg]
Abiotic Depletion	kg Sb eq	0.16	1.67E-02	2.67E-03
Global Warming Potential	kg CO2 eq	0.05	1.94	9.70E-02
Ozone Layer Depletion	kg CFC-11 eq	30	5.66E-08	1.70E-06
Human Toxicity Potential	kg 1,4-DB eq	0.09	5.82E-01	5.24E-02
Ecotoxicity Potential, Fresh water	kg 1,4-DB eq	0.03	3.91E-01	1.17E-02
Ecotoxcity Potential, Marine water	kg 1,4-DB eq	0.0001	3.66E+02	3.66E-02
Ecotoxicity Potential, Terrestrial environment	kg 1,4-DB eq	0.06	4.65E-03	2.79E-04
Photochemical Oxidation Potential	kg C2H4 eq	2	1.17E-03	2.34E-03
Acidification Potential	kg SO2 eq	4	6.53E-03	2.61E-02
Eutrophication Potential	kg PO42- eq	9	1.42E-03	1.28E-02
			Total shadow cost [€/kg]	0.242

Knowing the shadow cost of the steel, a comparison can be done between both designs.

Table 29: Shadow cost calculation of skeleton tube design and plain tube design with rail supports.

Design	Total weight [kg]	Shadow cost [€/kg]	Shadow cost [€]	Shadow cost difference [%]
Skeleton tube design	8707	0.242	2107	21.9
Plain tube design	11151	0.242	2698	

In terms of material use it is shown that the skeleton tube design can save up to 182kg of steel per 16m long tube segment. This is translated to approximately 590eur (21.9%) savings in the shadow costs at the production phase (A1-A3) of steel.

Production

The production process of the plain tube design involves bending and spiral welding of the steel sheet. The welding is performed on the inside and outside. This process offers tight tolerances, is automated and continuous.

The skeleton tube on another hand requires production of six different components. Plates can be easily produced by cutting and bending steel sheets. The same elements can be used for stringers and rings since they have the same profile. Rings would undergo an additional step of bending the hollow profile and welding it into a ring. Tube flange, shim and rail supports need to be laser cut out of the steel plate.

Upon assessment of fabrication processes involved in each design, it is apparent that the plain tube design results in a time and cost-efficient fabrication. Additionally, due to its simple design it is also simpler to achieve strict tolerances.

Maintenance

The maintenance highly depends on the complexity of design. The plain tube is overdesigned in terms of structural strength; therefore, no global nor local failures are anticipated in the infrastructure itself. On the contrary, the skeleton design might require many repairs due to local failures of components. The design has 288 ring-to-stringer connections per 16m tube segment, meaning that a thorough regular inspection should be executed. Detected failures would necessitate immediate repairs, and consequently causing disruptions in operation.

Summary

The comparison study is summarised in Table 30, where the comparison aspects are graded in terms of performance. The performance grading scale starts with (++) for excellent, (+) for good, (o) for neutral, (-) for subpar and (--) for bad performance.

Table 30: Summary of a comparison study between the plain tube design and skeleton tube design

	ULS	SLS	Stability	Impact load	Thermal expansion	Sustainability	Production	Maintenance
Plain tube design	++	++	+	++	-	--	o	+
Skeleton tube design	-	o	+	--	+	++	-	o

Plain tube design showcased a superior performance in terms of Ultimate Limit State (ULS) and Serviceability Limit State (SLS). Additionally, it is expected to outperform skeleton tube design in terms of the impact load resistance. While the skeleton tube design is clearly more sustainable, the overall assessment favours the plain tube design. It is important to highlight that this comparison is conducted in regards of applicability for hyperloop technology. Given its weight efficiency, the skeleton tube design might find applicability in other fields with lower safety requirements.

11 Conclusions and recommendations

This chapter presents the conclusions of this study and answers the research questions accordingly. Furthermore, it provides recommendations for further research.

11.1 Conclusions

The aim of this research is to provide a preliminary analysis and a foundation for further research on skeleton hyperloop tube design. The design was not only structurally verified but also modified and optimised for better structural and operational performance.

A wide range of FEA models were created in Ansys software to answer research questions. Analysis was initially performed on individual components and, after that, on the whole assembly. Critical locations were identified and explained. Additionally, a comparative study was conducted with a spirally welded hyperloop tube, which is currently used at the European Hyperloop Centre in Groningen, Netherlands.

The main research question is as follows:

What is the structural performance of the hyperloop Skeleton tube design, exposed to external and internal actions associated to the general, vehicle and environmental load classes?

Note: This research question is initially related to the Skeleton tube design without rail supports. These were conceptualised to be modelled as dead load, akin to the approach in the plain tube design. The results proved that hinged connections are not feasible in this design. Therefore, rail supports were subsequently added to the design and counted as a design modification.

- Ultimate limit state verification of the skeleton tube design without rail supports on the global scale is conditionally satisfactory. Linear analysis results exceeded the yield point, but nonlinear analysis showcased that due to an integral design, the stresses distribute among all components and subsequently, the design exhibits an elastic response with a unity check of 0.96 (see sections 7.2.1 and 7.2.3).
- Critical locations of the design in regard to ULS analysis are ring-to-stringer connections. The structure nearly reached its maximum stress under load combination 1, before the addition of external loads. This indicates that the magnitude of the vacuum pressure load case overshadows external load cases (see section 7.2.3).
- Individual components, such as rings, did exhibit local deformations due to their slender cross-sections. Plates displayed a sinusoidal deformation response, to which attributed the normal-to-surface load imposed by the vacuum pressure. However, all deformations are within the limits (see section 7.2.3).
- The structural evaluation of the assembly without rail and vehicle loads proved that the design has insufficient structural capacity to bear any additional loads. The unity check of rings resulted in 0.96. Consequently, further analysis was not conducted in which rails and pod loads would be assigned as dead loads. Instead, those findings influenced the design decision to incorporate rail supports as a structural reinforcement.

The following sub-questions were answered considering the skeleton tube design with rail supports.

1. **How do the hyperloop Skeleton tube design additions (rail supports) and improvements (connection design) affect the structural performance?**

Note: Rails support design is designed to be fully fixed to the rings of the skeleton tube design. Therefore, they act as a reinforcement of the assembly and improve its structural performance.

- Stress concentrations appeared in the inner flange of the ring, at the edges of the rail support. The sudden change in cross-section, and subsequently stiffness, initially caused the ring to exhibit a plastic response. This response was mitigated by increasing the length of the rail support, as well as adding a tapered edge (see section 4.6).
- Stress range in the rings, which are critical components, reduced from 150MPa - 250MPa to 60MPa - 150MPa. However, stress concentrations at ring-to-flange connections remained (see section 7.2.6).
- Global tube deflection due to inclusion of rail supports, rails load and pod load increased by 2.615mm compared to the tube design without rail supports (see sections 7.2.2 and 7.2.4.).
- Serviceability limit state verification resulted in an acceptable vertical deformation, especially after considering that the height of the rails within the tube can be calibrated; thus, mitigating tube deformation (see section 7.2.2).
- Static vehicle actions were verified, and the results are satisfactory. The structure can support the rails and the pod; however, the method of attaching rail supports to the tube structure has a large influence on the structural capacity. In this design, the rail supports are fully fixed to the rings and therefore act as structure reinforcement.
- Steel bracket design reduced stress concentrations at the ring-to-stringer connection from 342MPa to 226MPa (see section 8.2). Furthermore, it is a bolted connection, which contributes to the ease of assembly, maintenance, and replacement; and the bracket also mechanically bonds components, so a bolt failure would not necessarily mean a connection failure (considering that the detail is in compression).

2. **How does the skeleton tube design compare to the plain tube design in terms of structural performance and sustainability?**

- The skeleton tube design underperforms in terms of ULS checks. The stresses are close to the yield point, and the design experiences stress concentrations at connections. SLS performance is more aligned with the plain tube design, where the vertical deflection is just slightly larger. The skeleton tube does, however, exhibit many local deformations in the components (see section 7.2).
- Skeleton design offers minimum resistance to impact and accidental loads. Due to the plates being thin, it is susceptible to plate rupture or penetration if the tube is exposed to environmental actions. On the contrary, plain tube design offers sufficient isolation and protection against such loads.
- In terms of thermal expansion, the skeleton design will perform better compared to the plain tube. Thin components will deform locally as the temperature gradient increases; thus, smaller longitudinal forces are expected. Due to that, the width of the expansion joints could be reduced.
- The sustainability aspect is dominated by the skeleton tube design, which proved to have 28% material efficiency with the rail supports, and up to 37.8% weight efficiency if the tube structure is used solely for vacuum pressure retention (see section 10).
- Production of the plain tube design involves a simple spiral welding process. On the contrary, the skeleton tube components involve complex manufacturing processes with strict tolerances.

Therefore, plain tube production is expected to be time and cost efficient compared to the skeleton tube design.

- Due to simplicity and high safety measures, the maintenance of the plain tube design is expected to be minimal. In contrast, the skeleton tube design is likely to demand regular, thorough structural inspections and repairs due to a high component utilisation and many critical locations (connections).

3. Which failure modes is the hyperloop skeleton tube experiencing under considered actions, and what is the structural response to them?

Note: This answer is divided into two parts; first, the anticipated failure modes and second, the potential failure modes.

Anticipated failure modes:

- Initiation of plastic deformation at ring-to-stringer connection was observed, which could result in a connection failure (see section 7.2.5).
- Ring components are in full compression, and a combination of geometrical and construction imperfections as well as unfavourable loading conditions could lead to the local buckling of ring webs or flanges.
- Plate rupture due to impact load: If the impact is between the rings, then the plate failure would only cause a decrease in the vacuum pressure inside of the tube. If the projectile penetrates the plate at the location of the ring, then the impact with the ring could cause a ring failure. In the worst-case scenario, this would lead to a progressive collapse. Such a scenario should be further researched.

Potential failure modes:

- Many connections in the assembly are expected to be welded. The dynamic loads and vibrational effects initiated by the pod during acceleration and deceleration introduce the potential for fatigue failure.
- Longitudinal plate-to-stringer connections can be susceptible to cracking if welded, or delamination in case of the use of structural adhesives.
- Plates need to be connected to the saddles on the shim at the ends of tube segments. The complex connection of a curved plate onto a curved surface introduces a risk of separation and the creation of gaps in the tube.
- During tube operation, plates tend to deflect inwards. This introduces a bending stress along the longitudinal bend between curved surface and plate flanges. This bending stress may lead to the formation of longitudinal cracks.

4. Which imperfections have the most significant effect on the structural performance of the hyperloop skeleton tube design?

Note: The influence of stated imperfections was observed in the results, but it is expected that many other unidentified, and/or unverified imperfections may impact the structure. These are recommended for further research.

- Based on the stability analysis, the local buckling occurs in the webs of the ring. During ring manufacturing, both flanges and webs may experience inward buckling (concave shape) as a result of the bending process. Therefore, this initial geometrical imperfection will worsen the buckling resistance of the rings.

- Due to a complex design with tight tolerances for geometrical imperfections, stringer straightness plays a vital role in the assembly. Stringers are the longitudinal components that bond together all other components into an assembly. Plates are connected to the top flanges, rings to the bottom flanges and edges are slotted into the shim and tube flange. Therefore, any misalignments might cause difficulties during construction, decrease the design integrity and subsequently structural performance.
- Steel bracket detail provided a possible solution to mitigate stress concentrations at the ring-to-stringer connection. However, if the bolt hole in the ring is ill-positioned, it can create a gap between the bracket and the ring. Such lack of fit causes the force to pass through the bolt, which can lead to connection failure.
- The contact surface at the bottom of the steel bracket is designed to match the ring's radius for a perfect fit. If the radiuses differ, either a gap or a four-point contact will be created, both of which will lead to uneven stress distribution.

5. How can structural safety be researched and implemented in the hyperloop skeleton design?

Methods of researching structural safety:

- Innovative technologies introduce new specific load cases and combinations. These need to be thoroughly researched and understood before preliminary designs can be developed and evaluated further. The skeleton tube design is in the current stage overutilized and it is not meeting safety requirements. Similar structural systems can be found and researched in aircraft fuselage or submarine hull design.
- Skeleton design requires a further detailed simulation and verification by means of a finite element approach. Other potential failure modes need to be identified and structural response to initial imperfections should be assessed. Furthermore, design weaknesses should be pinpointed and addressed by design modification and improvement.
- Once the skeleton design proves to be structurally sound and sustainable, it requires extensive testing. This involves recreating operational conditions as well as unpredictable scenarios that lead to a failure (destructive testing).

Methods of implementing structural safety:

- Assigning higher safety factors in the preliminary design stage would result in larger cross-sections and, consequently, higher structural safety.
- Due to the moving pod, the hyperloop infrastructure is exposed to fatigue loading. The skeleton design comprises of up to connections per 16m segment. Therefore, designing fatigue-resistant connections would significantly contribute to the structure's safety.
- Considering that the plates provide minimal protection against accidental and impact loads, a secondary protective structure could be designed to protect the skeleton design against those load cases.

11.2 Recommendations

Based on the research findings presented in this thesis, several recommendations for further design evaluation are proposed:

Design verification:

- Skeleton tube design needs to be verified for dynamic loading due to the moving pod. This could be done by completely modelling the rails and assessing structural response via transient analysis. Additionally, fatigue limit state verification is required due to the moving pod and vibrations exhibited on the structure, as well as the eigenfrequency analysis to identify at which frequencies the system is prone to vibrate.
- Impact load analysis needs to be performed, knowing that the design has a limited resistance against accidental loads. A recommendation on the approach is given in section Impact load analysis recommendation in Appendices.

Design improvement / modification:

- The design could be geometrically optimised, such as in number of stringers, rings and cross-sections. A parametric design approach is advisable.
- The bending section between the plate's curved surface and flanges is critical and could lead to longitudinal cracks. A cross-section modification of the stringer is advisable, where the top flange would be shaped in an arc; thus, eliminating the sudden bending of the plate.

Detail engineering:

- The plate-to-stringer connection might prove problematic in the case of a welded design due to the thickness of the plate. A connection design using structural adhesives is an option, offering some level of vibration absorption and potentially being less susceptible to fatigue. The type of structural adhesive and thickness should be researched. Moreover, the fatigue verification should be performed for each fatigue prone detail in the assembly.

Final remark:

Emerging technologies, such as the hyplerloop, which are still under development and have not yet proven to be a necessity for a more sustainable future, significantly depend on the performance and success of the first prototypes and/or real-world implementations.

Safety is one of the main concerns of hyperloop application, and the infrastructure needs to guarantee a safe and flawless operational environment. At hyperloop applications, safety of two environments needs to be maximised. The internal environment, which is inside of the tube and relates to the passenger safety, and external environment, that encompass tube surrounding. The tube structure divides these two environments, and by increasing the safety of one, it passively increases the safety of the other.

The allowed margins for error are minimal, and the consequences are not only case-specific, but might also negatively affect the progress of emerging technology overall. The societal values and environmental impact are major factors in the implementation of new technologies; however, the emphasis on sustainability aspect cannot overshadow safety, and vice versa.

12   References

[1]   "Delivering the European Green Deal," European Commission, [Online]. Available: https://commission.europa.eu/strategy-and-policy/priorities-2019-2024/european-green-deal/delivering-european-green-deal_en. [Accessed 26 May 2023].

[2]   "European Hyperloop Center," 2024. [Online]. Available: https://europeanhyperloopcenter.com/. [Accessed 28 February 2024].

[3]   M. Kurstjens, J. van Aken, J. van Mil and A. Hirsig, "On the Future Development of Hyperloop Infrastructure," Delft Hyperloop, Delft, 2022.

[4]   A. Dabrowska, . S. de Caluwe, M. Geuze, D. Härtl, R. Roeske and T. Xydianou, "Cargo-Hyperloop Holland, A pre-project feasibility for connecting Noord- and Zuid Holland via hyperloop," Hardt Hyperloop, 2021.

[5]   E. Musk, "Hyperloop Alpha," 2013.

[6]   NPR-CEN-CLC/TR 17912 - Hyperloop systems - Standards Inventory and Roadmap, 2023.

[7]   Determination of structural capacity by non-linear finite element analysis methods, DNV-GL-C208, Edition September 2019.

[8]   "TATA Steel," 2023. [Online]. Available: https://www.tatasteel.com/.

[9]   "POSCO," 2024. [Online]. Available: https://www.posco.co.kr/homepage/docs/eng7/jsp/s91a0000001i.jsp.

[10]   "Agreement signed for hyperloop tube production," Railway Pro, 13 November 2020. [Online]. Available: https://www.railwaypro.com/wp/agreement-signed-for-hyperloop-tube-design/. [Accessed 25 May 2023].

[11]   A. Santangelo, "The infrastructure challenges of hyperloop," *Procedia Structural Integrity,* vol. 44, pp. 626-632, 2023.

[12]   "Hyperloop Progress Paper," Hardt Hyperloop, [Online]. Available: https://docs.hardt.global/what-is-hyperloop. [Accessed 22 February 2024].

[13]   "POSCO Begins Steel Supply for Hyperloop Tubes," POSCO, 18 May 2022. [Online]. Available: https://newsroom.posco.com/en/posco-begins-steel-supply-for-hyperloop-tubes/. [Accessed 29 November 2023].

[14]   NEN-EN 1993 - Eurocode 3: Design of steel structures - Part 1-1: General rules and rules for buildings, 2016.

[15]   C. Hauviller, "Design rules for vacuum chambers," *CAS - CERN Accelerator School : Vacuum in Accelerators,* pp. 31-42, 2007.

[16]   "Designing the Hyperloop tube: geometry and material choice," Hyperloop Connected, [Online]. Available: https://hyperloopconnected.org/2019/11/designing-the-hyperloop-tube-geometry-and-material-choice/. [Accessed 25 May 2023].

[17] P. Museros, C. Lázaro, B. Pinazo and S. Monleón, "Key aspects in the analysis and design of Hyperloop™ infrastructure under static, dynamic and thermal loads," *Engineering Structures,* vol. 239, 2021.

[18] "Mercon," [Online]. Available: https://www.mercon.com/.

[19] "Hardt Hyperloop," Linkedin, December 2023. [Online]. Available: https://www.linkedin.com/company/hardthyperloop/posts/?feedView=all. [Accessed 23 January 2024].

[20] "Hyperloop: The pinnacle of sustainable transport," DRIE-D Mechanical Motion, [Online]. Available: https://drie-d.com/. [Accessed 22 January 2024].

[21] "NOS," 13 July 2022. [Online]. Available: https://nos.nl/regio/noord-holland/artikel/285883-tata-steel-nauw-betrokken-bij-ontwikkeling-van-de-hyperloop-made-in-ijmuiden. [Accessed 12 December 2023].

[22] *European Hyperloop Center kick-off event aftermovie.* [Film]. 2023.

[23] A. H. Middya, A. Ramachandra, S. Goapalan, U. Krishnanunni , P. Sakure, P. Sharma and S. Patole, "Development & Validation of Systematic and Economical Approach to Design Thin Hyperloop Tube," Tamil Nadu, 2023.

[24] "ANSYS, Inc," 2024. [Online]. Available: https://www.ansys.com/.

[25] "Ansys Innovation courses," 2020. [Online]. Available: https://courses.ansys.com/index.php/courses/computational-resource-considerations-recommended/lessons/newton-raphson-method-lesson-3/. [Accessed 22 November 2023].

[26] NEN-EN 1991-1-1+C1+C11 - Eurocode 1: Actions on structures – Part 1-1: General actions – Densities, self-weight, imposed loads for buildings, 2019.

[27] NEN-EN 1991 – Eurocode 1 - Actions on structures - Part 1-3: Snow loads, 2011.

[28] NEN-EN 1991 - Eurocode 1: Actions on structures - Part 1-4: General actions -.

[29] NEN-EN 1991 - Eurocode 1: Actions on structures - Part 2: Traffic loads on bridges and other civil engineering works.

[30] J. P. Powell and R. Palacin, "Passenger Stability Within Moving Railway Vehicles: Limits on Maximum Longitudinal Acceleration," *Urban Rail Transit,* vol. 1, pp. 95-103, 2015.

[31] NEN-EN 1990+A1+A1/C2/NB - National Annex to NEN-EN 1990+A1:2006+A1:2006/C2:2019 Eurocode: Basis of structural design, 2019.

[32] NEN-EN 1993-1-9 - Eurocode 3: Design of steel structures - Part 1-9: Fatigue, 2006.

[33] "How to Evaluate Stress and Yielding in Plasticity — Lesson 2," Ansys Innovation courses, [Online]. Available: https://courses.ansys.com/index.php/courses/topics-in-metal-plasticity/lessons/how-to-evaluate-stress-and-yielding-in-plasticity-lesson-2/How to Evaluate Stress and Yielding in Plasticity — Lesson 2. [Accessed 2 March 2024].

[34] NEN-EN 1993-1-8 - Eurocode 3: Design of steel structures - Part 1-8: Design of joints, 2021.

[35] R. Pijpers and H. Slot, "Friction coefficients for steel to steel contact surfaces in air and seawater," *Journal of Physics: Conference Series,* vol. 1669 , 2020.

[36] C. Hung-Wei and L. Ching-Hung, "Prediction of machining accuracy and surface quality for CNC machine tools using data driven approach," *Advances in Engineering Software,* vol. 114, no. 0965-9978, pp. 246-257.

[37] J. Carlton, "Chapter 20 - Propeller Manufacture," in *Marine Propellers and Propulsion*, 4th ed., 2018, pp. 453-458.

[38] H. Jonkers, "Reader CIE4100 Materials and Ecological Engineering (Q2-2021 ed.).," *Delft Faculty of Civil Engineering & Geosciences,* 2021.

[39] NEN-EN 1991 - Eurocode 1: Actions on structures - Part 1-4: General actions - Wind actions.

[40] NEN-EN 1991-1-5 - Eurocode 1: Actions on structures - Part-1-5: General actions - Thermal actions, 2023.

[41] "NLTIMES," 5 July 2023. [Online]. Available: https://nltimes.nl/2023/07/05/storm-poly-first-ever-severe-summer-storm-netherlands-wind-gust-146-kmh. [Accessed 4 February 2024].

[42] P. Schaumann and C. Keindorf, "A new Tower-Concept with Sandwich-Sections Structural Design of Sandwichtowers for Wind Energy Converters," 2008.

[43] P. Museros, C. Lázaro, B. Pinazo and S. Monleón, "Key aspects in the analysis and design of Hyperloop™ infrastructure under," *Engineering Structures,* vol. 239, 2021.

[44] "EuroTube," [Online]. Available: https://eurotube.org/hyperloop/. [Accessed 29 May 2023].

[45] "European Hyperloop Center kick-off event aftermovie," Hardt Hyperloop, 13 October 2023. [Online]. Available: https://www.youtube.com/watch?v=gY5SWtS1qDo&ab_channel=HardtHyperloop. [Accessed 10 December 2023].

[46] "How to Evaluate Stress and Yielding in Plasticity — Lesson 2," Ansys Innovation course, [Online]. Available: https://courses.ansys.com/index.php/courses/topics-in-metal-plasticity/lessons/how-to-evaluate-stress-and-yielding-in-plasticity-lesson-2/.

13 Appendices

A. Calibration model

A gross yielding check needs to be performed to determine the plastic strain limit. This is done because real structures will include elements of inhomogeneity [7], which will not be precisely captured in the FEM analysis. Gross yielding refers to the occurrence of plastic deformations with strain above 2%, which are expressed over a zone of $I_{yz} > 20t$ in the direction of the maximum plastic strain. The maximum gross yielding strain should be limited to the gross yielding critical strain, which is determined according to DNV-RP-C208 section 5.1.3.2 [7]. The dimensions and boundary conditions of the model are given in Figure 163 and Figure 164.
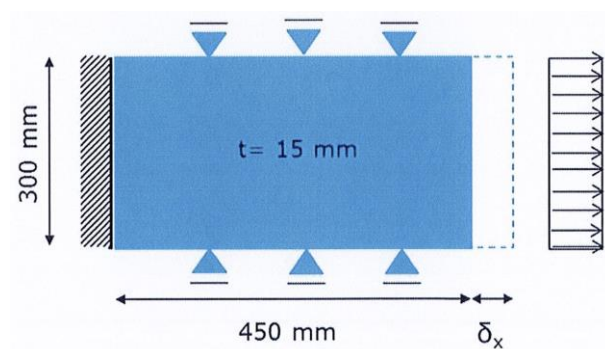
Figure 163: Calibration case CC01, steel plate under uniaxial load plane strain conditions [7]
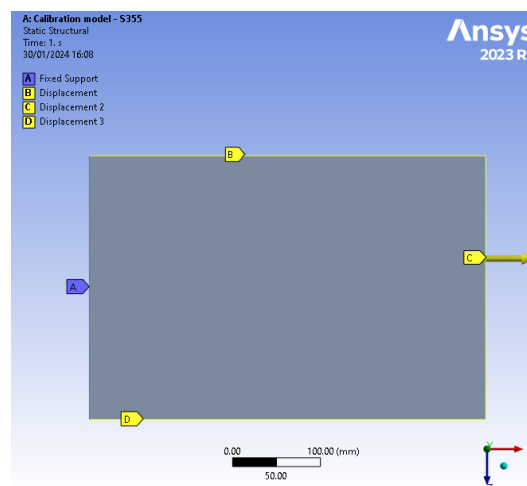
Figure 164: Calibration model setup

The shell model has an element size of 15mm, which is the minimum prescribed mesh size (t x t), while stress – strain curves are given in chapter 5.1. The critical strain is found by the application of a displacement of the edge, which depends on the steel grade given in Table 30.

Table 30: Deformation limits for gross yielding check [7]

	δ_x (mm)				
	S235	S275	S355	S420	S460
CC01	25	24	21	18	18

Two analyses were performed, for steel grades of S355 and S460. Equivalent plastic strain results are presented in Figure 165 and Figure 166 .
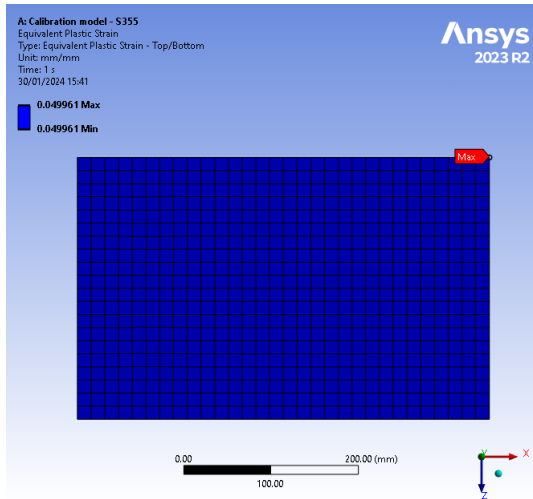
Figure 165: Equivalent plastic strain [mm/mm] - Calibration model [S355]
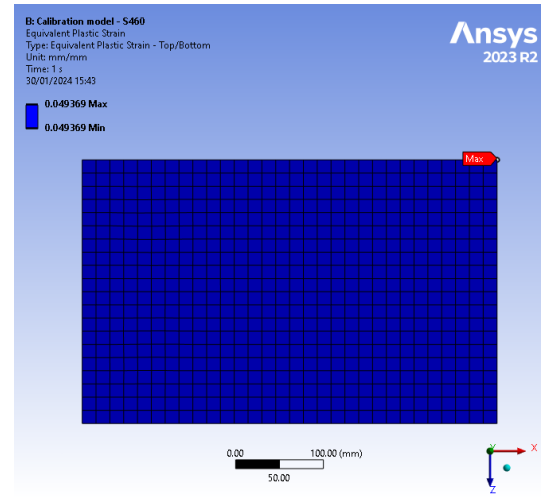
Figure 166: Equivalent plastic strain [mm/mm] - Calibration model [S460]
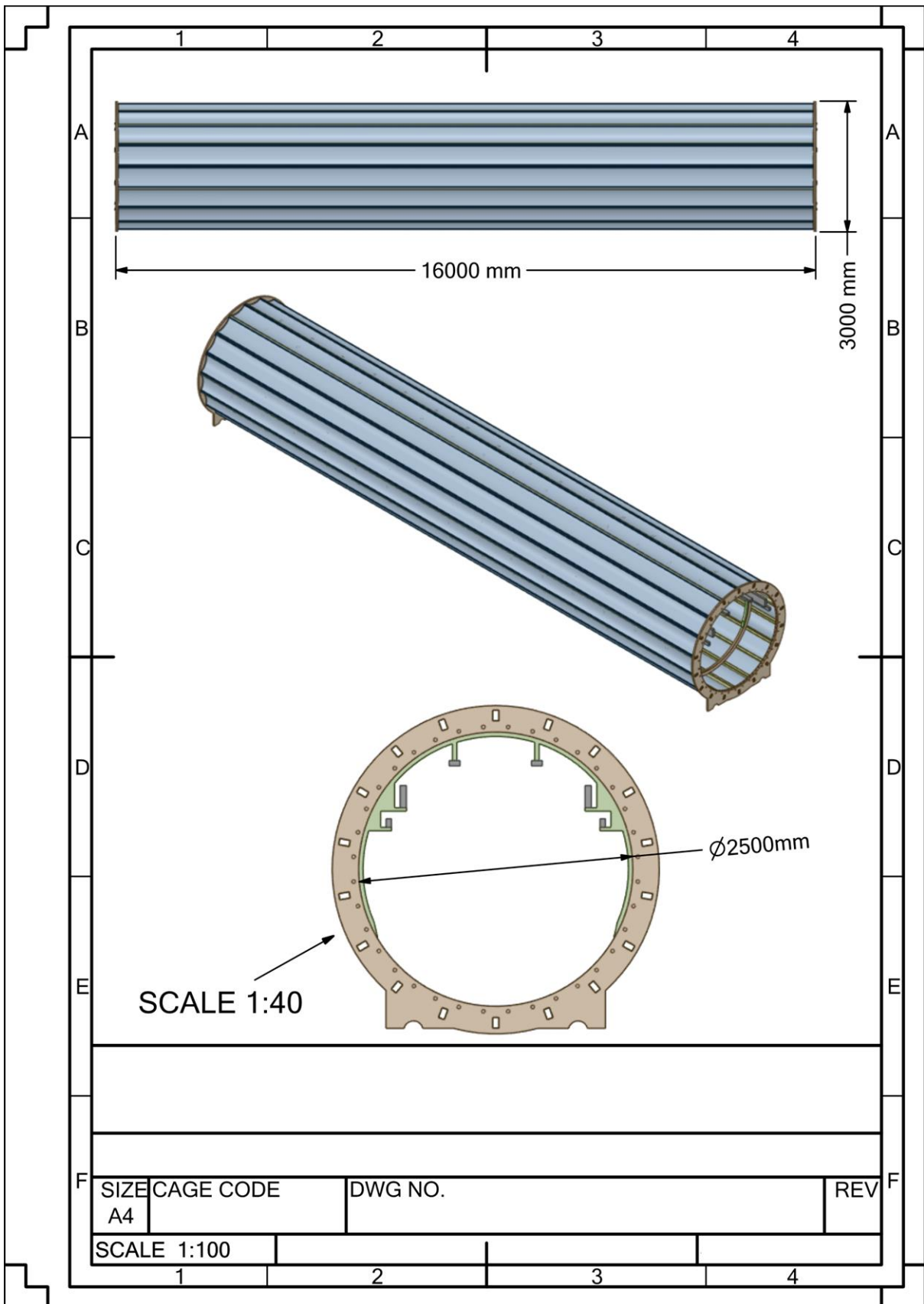
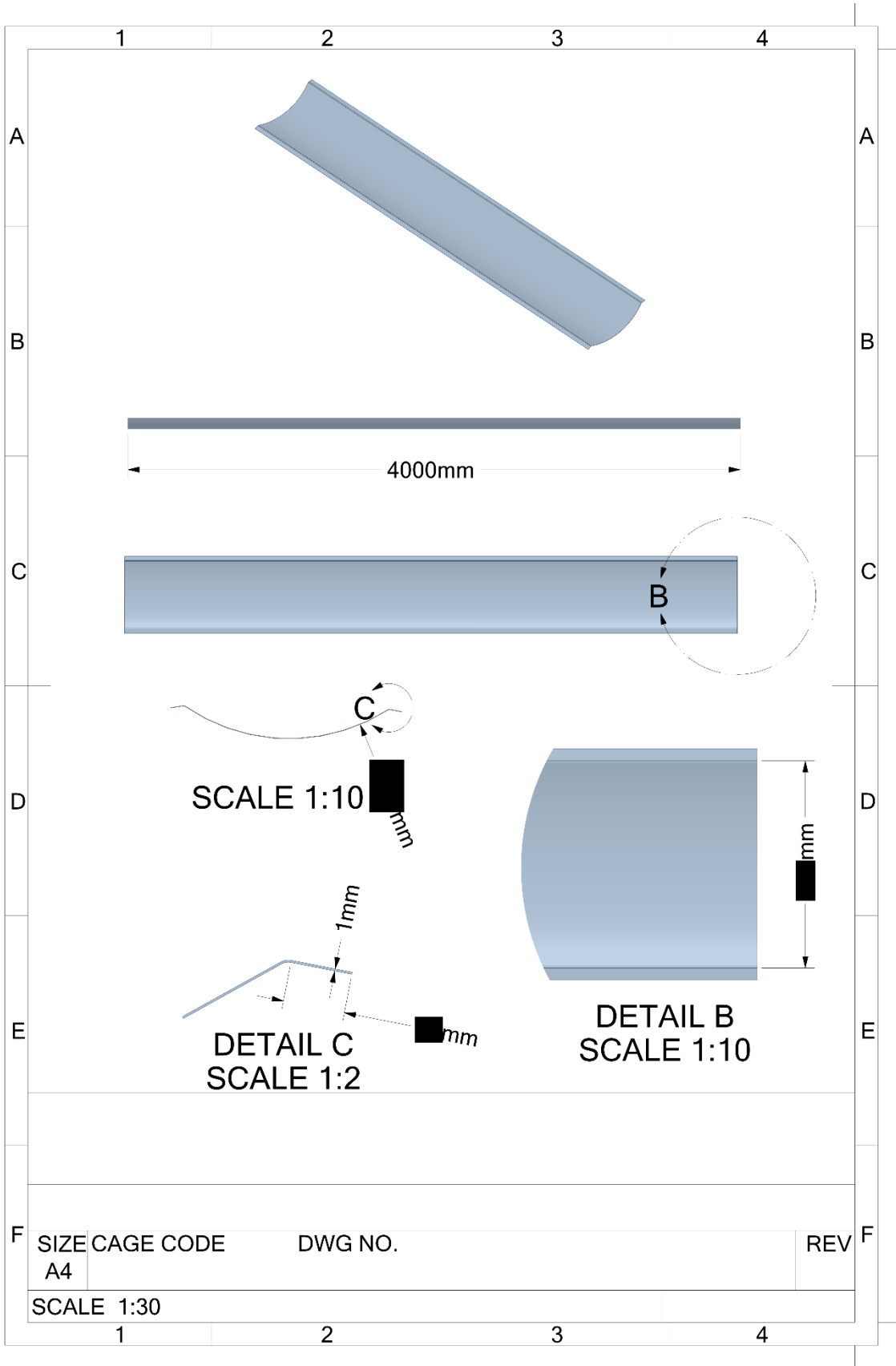Therefore, the principal plastic strains are as follows:
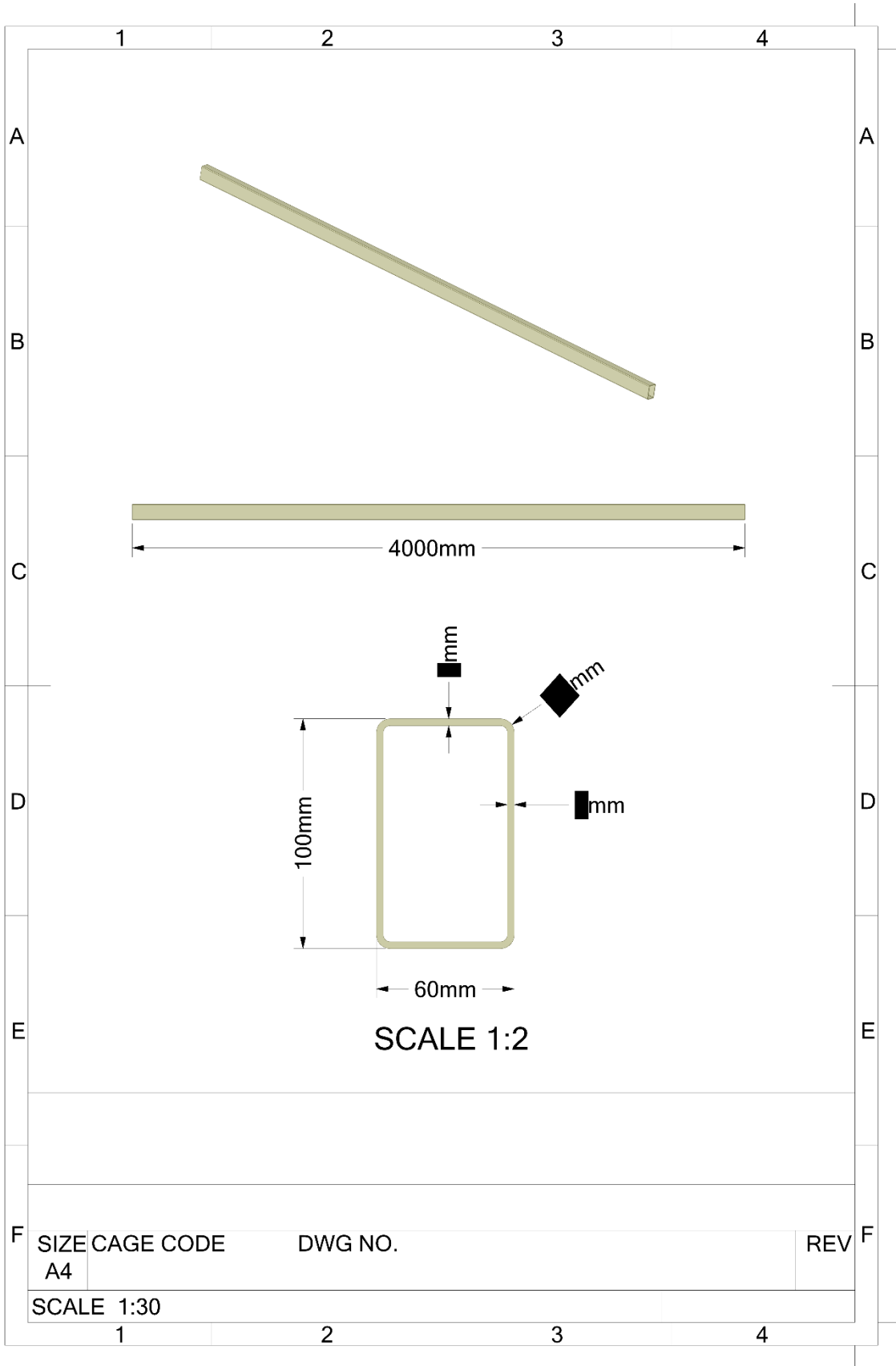
$$\varepsilon_{shell,S355} = 0.049961 = 4.99\ \%$$
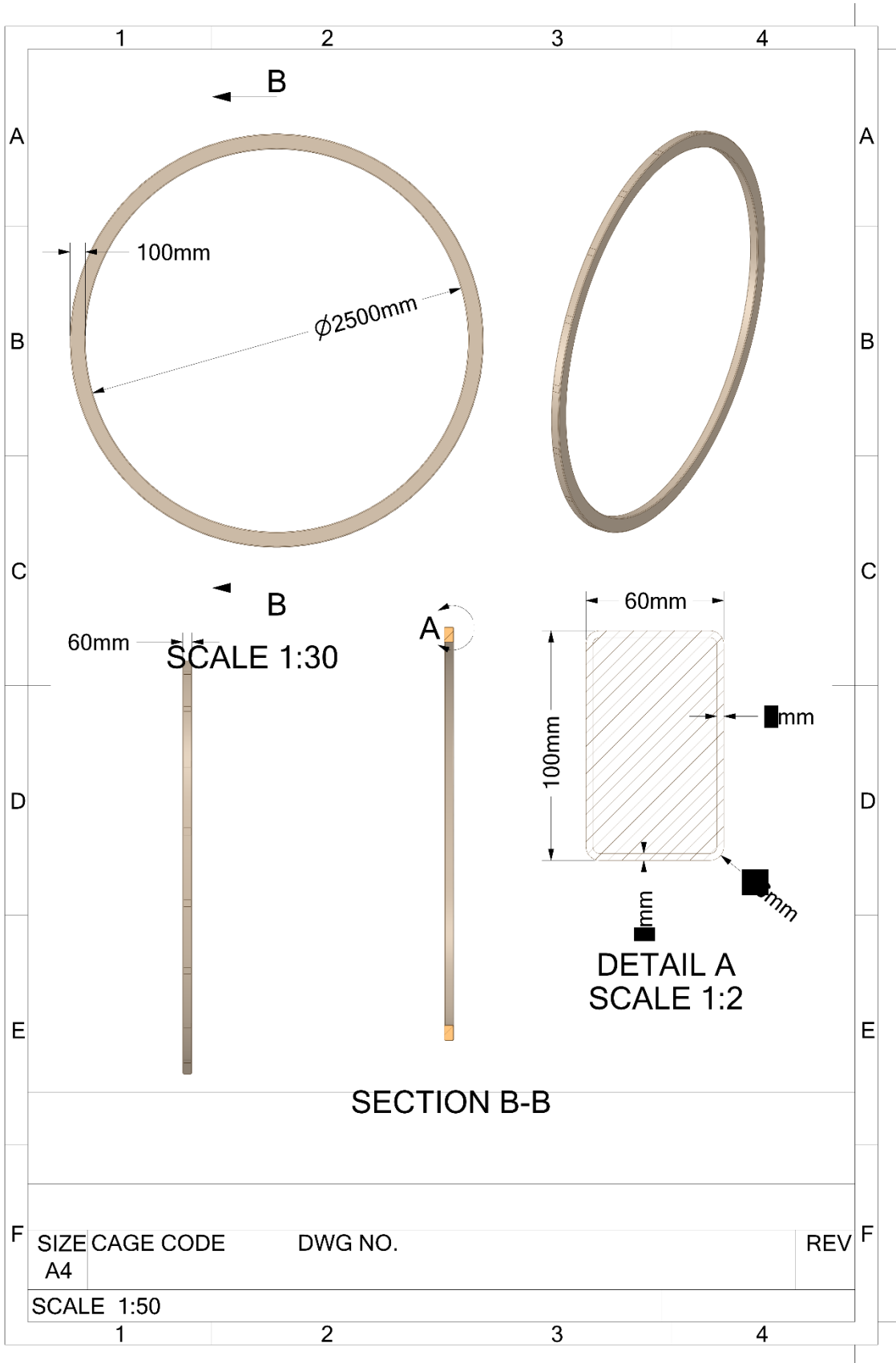
$$\varepsilon_{shell,S460} = 0.049369 = 4.93\ \%$$

According to the calibration model, the gross yielding strain is roughly 5%. However, as stated before, if the area is smaller than 20xt, then the critical strain limit will exceed this value due to local yielding. In simple terms, it means that if the Equivalent von Mises stress surpasses the yield strength in the nonlinear analysis, then the equivalent plastic strain can be compared to the plastic strain limit to determine whether the structure is still within the acceptable limits.
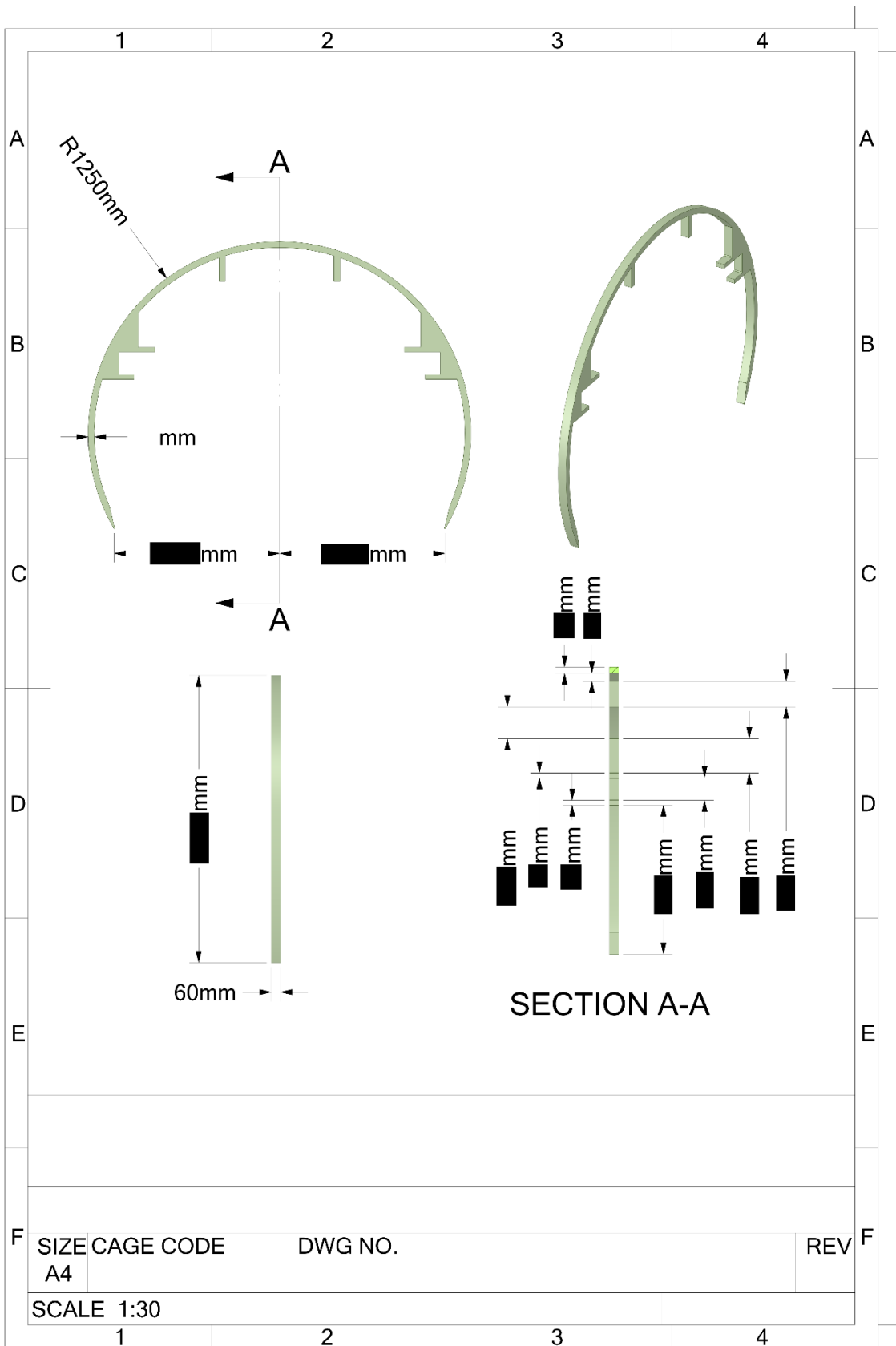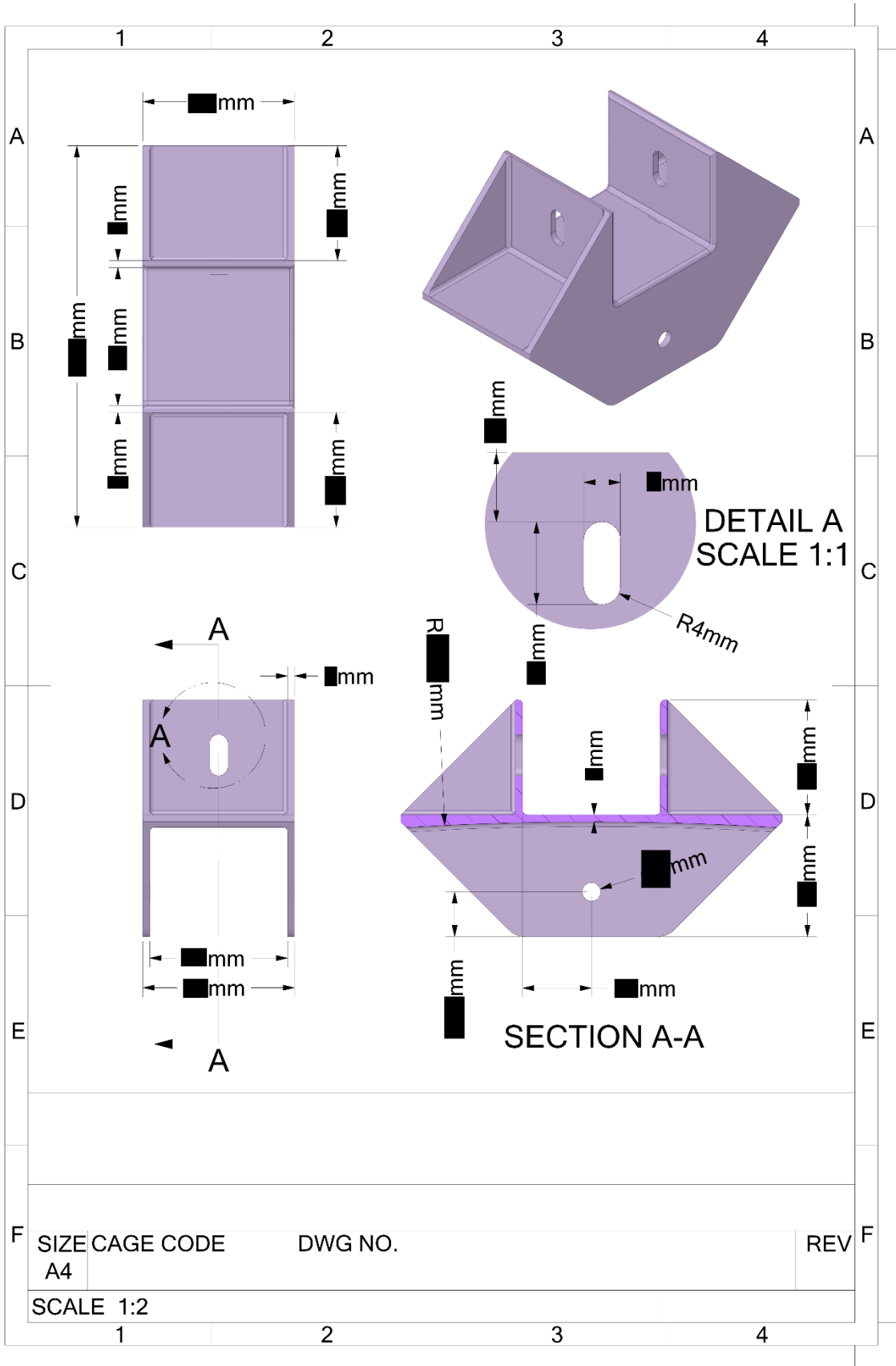
B. Technical drawings

16000 mm

3000 mm

∅2500mm

SCALE 1:40

SIZE A4	CAGE CODE	DWG NO.		REV
SCALE 1:100				

A

4000mm

B

C

SCALE 1:10

DETAIL C
SCALE 1:2

1mm

DETAIL B
SCALE 1:10

SIZE A4	CAGE CODE	DWG NO.	REV
SCALE 1:30			

A

B

4000mm

C

mm

mm

100mm

mm

60mm

D

SCALE 1:2

E

Ø2500mm

100mm

SECTION B-B

60mm

B

SCALE 1:30

60mm

A

100mm

■mm

■mm

■mm

DETAIL A
SCALE 1:2

SIZE A4	CAGE CODE	DWG NO.		REV

SCALE 1:50

E

■mm

⌀2500mm

mm

mm

mm

100mm

DETAIL E
SCALE 1:10

■mm

■mm

SIZE	CAGE CODE	DWG NO.		REV
A4				

SCALE 1:30

R1500mm

∅2500mm

D

60mm

100mm

■mm

■mm

■mm

DETAIL D
SCALE 1:10

■mm

SCALE 1:30

SIZE A4	CAGE CODE	DWG NO.		REV
SCALE 1:30				

103

R1250mm

A

A

mm

mm   mm

60mm

SECTION A-A

mm

mm mm

mm mm mm   mm mm mm mm

SIZE	CAGE CODE	DWG NO.		REV
A4				

SCALE 1:30

■mm
■mm
■mm
■mm
■mm
■mm
■mm
■mm

■mm

DETAIL A
SCALE 1:1

R4mm

■mm

A

A

■mm

A

A

R■mm

■mm

■mm

■mm

■mm

■mm

■mm

■mm
■mm

■mm

■mm

SECTION A-A

105

C. Load cases

Self-weight

Self-weight is classified as a permanent fixed action [26]. It represents the dead load acting on the structure due to its own mass and is dependent on the material and the cross-section of the components. Self-weight of the tube components is considered in all assembly analyses and disregarded in detail analysis. Self-weight of rails is assigned as the area load at the locations of attachment, where the weight was given at the production site visit. In Ansys it is calculated using the standard earth gravity of 9.81 m/s^2 and material density of 7800 kg/m^3 for steel. Self-weight of cabling is not considered due to dismissible effect on the structure, while propulsion system load is embedded in the pod load itself [3].

Vacuum pressure

The defining characteristic of the hyperloop system is the near perfect vacuum environment within the tube. Vacuum pressure is the critical design parameter which affects the system efficiency, safety and energy consumption. The load magnitude exhibited by this pressure is the difference between the atmospheric pressure and the pressure within the tube. The proposed pressure by Elon Musk's Hyperloop white paper [5] is 100 Pa inside the tubes. Considering a circular shape of the tube, the distributed force acts inwards, perpendicular to the tube's surface.

$$q_{atm} = 101\ 325 \text{ Pa } = \text{ atmospheric pressure}$$

$$q_{tube} = 100 \text{ Pa } = \text{ tube pressure}$$

The imposed pressure on the plates is therefore:

$$Area\ load: q_{Ed} = q_{atm} - q_{tube} = 101.225 \frac{kN}{m^2} = 0.1 MPa$$

The plain steel tube that is currently being produced has a thickness of 16mm. Knowing that radius measures 1250mm, and Young's modulus is taken as 210 GPa:

$$P_{cr} = \frac{E}{4 \cdot (1 - v^2)} \cdot \left(\frac{t}{R}\right)^3 =$$

$$= \frac{210000}{4 \cdot (1 - 0.3^2)} \cdot \left(\frac{16}{1250}\right)^3 = 0.12\ MPa$$

Therefore, in this research the vacuum pressure of p = 0.12MPa is used for ULS checks, and 0.1MPa for SLS.
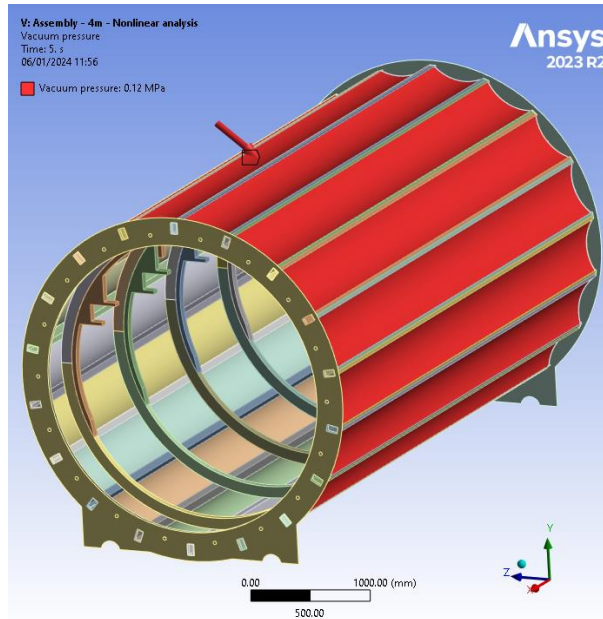
Figure 167: Vacuum pressure - 5m model with rail supports

Snow load

Hyperloop tube structure has a cylindrical shape, and according to Eurocode 1 - Actions on structures - Part 1-3: Snow loads; it is considered as a cylindrical roof.

The snow load is determined using the following formula for fundamental design situation:

$$s = \mu_i \cdot C_t \cdot s_k$$

It has a balanced and unbalanced load arrangement since height over breadth > 0.05. The balanced load arrangement equals to $0.8C_e$, where C_e is the exposure coefficient taken as 1 based on Table 7.1 in EN1991-1-4 [28]. The μ_4 is the snow load shape coefficient, which is a function of the wind exposure of the site and of the geometry of the roof.
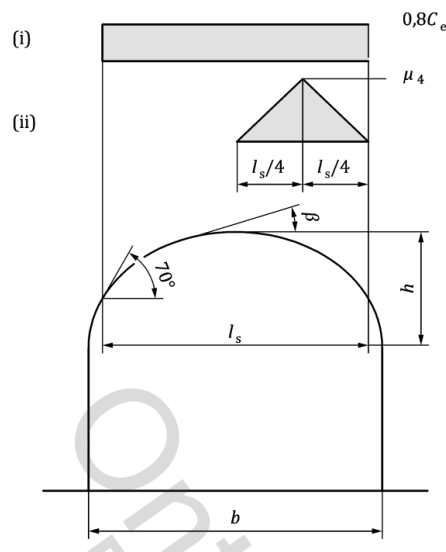
Figure 168: Snow load arrangements for cylindrical roofs where (i) Balanced load arrangement and (ii) Unbalanced load arrangement [27]

Snow load shape coefficient μ_4 is taken from Figure 169, where h/b (height over breadth equals 1) and C_e is 1. So, $\mu_4 = 2$.
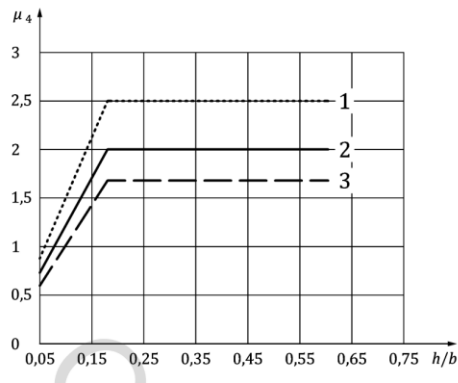
Figure 169: Snow load shape coefficient for cylindrical roofs as a function of h/b (for roof areas with the slope β ≤ 70°) [27]; where 1: (Ce = 0,8)
2: (Ce = 1,0)
3: (Ce = 1,2)

Knowing that the unbalanced load will act only on $l_s/2$ segment of the cross-section, the l_s distance needs to be calculated. The total breadth, b, of the tube is 2.5m, and at this breadth the β angle is 90°. Linearly interpolating for 70° the l_s results in 0.972m, and $l_s/4$ equals to 0.243m. So, using the equation above and taking s_k as 0.7 kN/m² for the Netherlands, we obtain balanced snow load of $s_b = 0.56$ kN/m² and unbalanced snow load of $s_{ub} = 1.12$ kN/m². The unbalanced snow load is 50% higher than the balanced, but for simplicity and considering that it is a preliminary design, only the uniform snow load will be assigned to the model at this stage of the research.

The snow load acting on the tube model is assigned to the top plates, as seen in Figure 170.
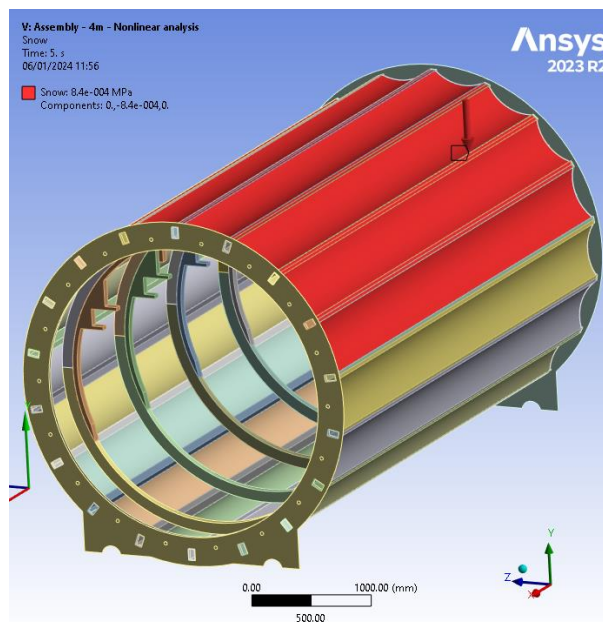
Figure 170: Snow load

Wind load

The hyperloop tube is intended to be supported by piers at the edges of 16m long sections. Wind load calculation is dependent on the type of hyperloop system, i.e., whether it is constructed on ground, or above ground. In case if it is on ground, then the wind actions can be calculated with an assumption that the tube is a longitudinal circular cylinder. According to EN1991-1-4 [28], the wind force acting on the external surfaces is calculated with the following expression:

$$F_w = c_s c_c \cdot c_f \cdot q_p(z_e) \cdot A_{ref}$$

where:

$c_s c_d$ is the structural factor
c_f is the force coefficient for the structure
$q_p(z_e)$ is the peak velocity pressure at reference height z_e
A_{ref} is the reference area of the structure

The Netherlands is divided into three wind zones, and for this research wind zone 2 is chosen.

Figure 171: Wind zones in the Netherlands [39]

The reference height should be taken as $z_e = h + f$, so z_e equals to 2.5m. Terrain category 2 is considered in this research, and the peak wind velocity is taken from Table 31**Error! Reference source not found.**. Basic wind speed for the Netherlands is 27 m/s.

Table 31: Peak velocity pressure [39]

Hoogte	Gebied I			Gebied II			Gebied III	
m	Kust	Onbebouwd	Bebouwd	Kust	Onbebouwd	Bebouwd	Onbebouwd	Bebouwd
1	0,93	0,71	0,69	0,78	0,60	0,58	0,49	0,48
2	1,11	0,71	0,69	0,93	0,60	0,58	0,49	0,48
3	1,22	0,71	0,69	1,02	0,60	0,58	0,49	0,48
4	1,30	0,71	0,69	1,09	0,60	0,58	0,49	0,48
5	1,37	0,78	0,69	1,14	0,66	0,58	0,54	0,48
6	1,42	0,84	0,69	1,19	0,71	0,58	0,58	0,48
7	1,47	0,89	0,69	1,23	0,75	0,58	0,62	0,48
8	1,51	0,94	0,73	1,26	0,79	0,62	0,65	0,51
9	1,55	0,98	0,77	1,29	0,82	0,65	0,68	0,53
10	1,58	1,02	0,81	1,32	0,85	0,68	0,70	0,56
15	1,71	1,16	0,96	1,43	0,98	0,80	0,80	0,66
20	1,80	1,27	1,07	1,51	1,07	0,90	0,88	0,74

So:

$$q_p(z) = 0.6 \text{ kN/m}^2$$

Pressure coefficients of sections depend upon the Reynolds numbers R_e defined:

$$R_e = \frac{b \cdot v(z_e)}{v}$$

where:

b is the diameter
v is the kinematic viscosity of the air ($v = 15 \cdot 10\text{-}6 \text{ m}^2\text{/s}$)
$v(z_e)$ is the peak wind velocity

$$R_e = \frac{2.5 \cdot 27}{15 \cdot 10 - 6} = 4.5 \cdot 10^6$$

The force coefficient c_f for a finite circular cylinder should be determined as follows:

$$c_f = c_{f,0} \cdot \psi_A$$

where:

$c_{f,0}$ is the force coefficient of cylinders without free-end flow
ψ_λ is the end-effect factor

Force coefficient is obtained using **Error! Reference source not found.**, where k/b is the equivalent surface roughness over diameter of the tube.
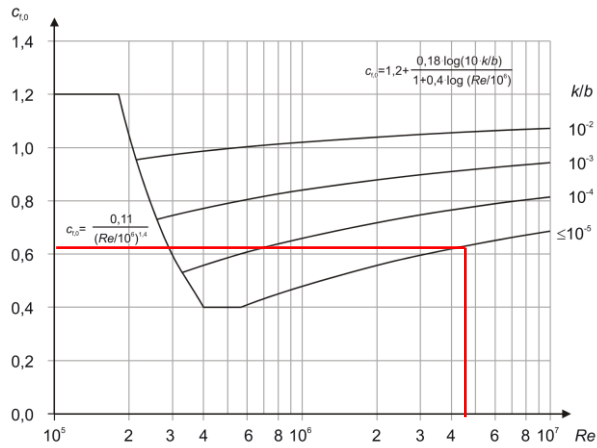
Figure 172: Force coefficient $c_{f,0}$ for circular cylinders without free-end flow and for different equivalent roughness k/b

Knowing Reynolds number from above, and k/b equals to 0.00002 for bright steel, the $c_{f,0}$ equals to 0.62. The solidity ratio φ is calculated as:

$$\varphi = \frac{A}{A_c} = 1$$

where:

A is the sum of the projected areas of the members
A_c is the overall envelope area $A_c = 1 \cdot b$
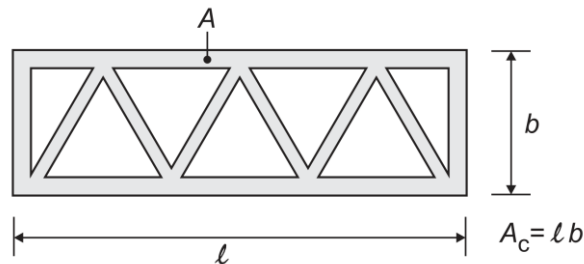
Figure 173: Definition of solidity ratio φ [28]

And the effective slenderness λ for circular cylinder is determined from Table 7.16 [28] as l/b = 6.4. Using φ and λ, the end-effect factor can be read from Figure 174.
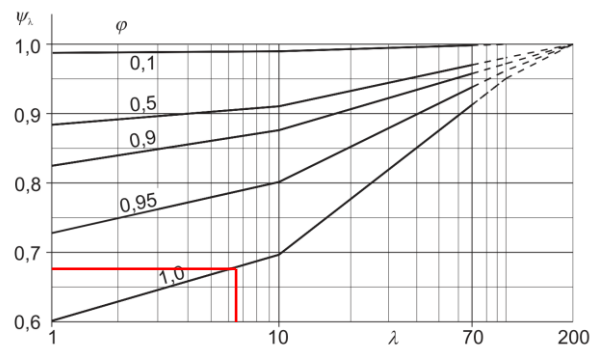
Figure 174: Indicative values of the end-effect factor ψ_λ as a function of solidity ratio φ versus slenderness λ [28]

Therefore, ψ_λ is 0.675 and the force coefficient c_f results in:

111

$$c_f = c_{f,0} \cdot \psi_A = 0.62 \cdot 0.675 = 0.4185$$

Reference area is calculated as $A_{ref,x} = d_{tot}L = 40m^2$, $c_s c_c$ can be taken as 1, and air density is taken as 1.20kg/m^3 [0.0012 kN/m^3]. Therefore, the external force acting on the tube is:

$$F_w = \; 1 \cdot 0.4185 \cdot 0.6 \cdot 40 = 10.04 \; kN$$

This results in an area pressure of:

$$q_w = \frac{F_w}{A_{ref}} = 0.251 \frac{kN}{m^2} = 0.00025 \; MPa$$
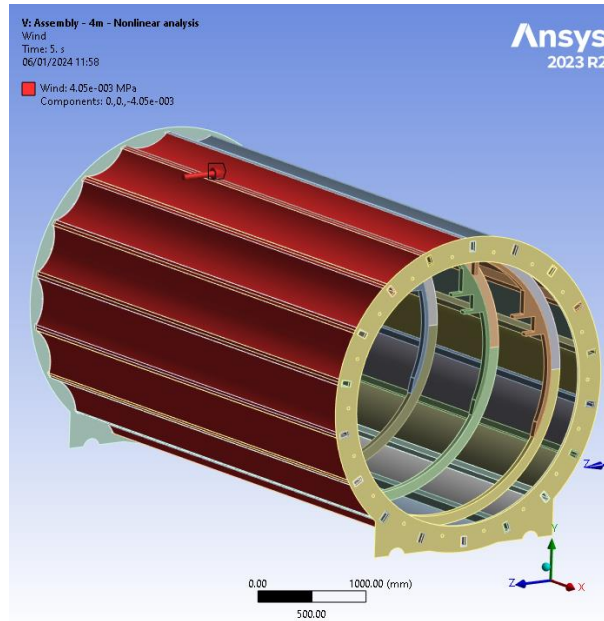
Figure 175: Wind load acting on the tube considering the design value of loads

Rails load

Rails are attached on the rail supports and introduce a dead load to the structure. Along the pod rails, the load consists of the levitation and propulsion rails. The load from the rails is concentrated at the points where they connect to the rail supports, meaning that the design of these supports affects how the load is distributed. By knowing the general location of the inner rails, the supports is designed (See chapter 4.6), and the loads are assigned as seen in Figure 176
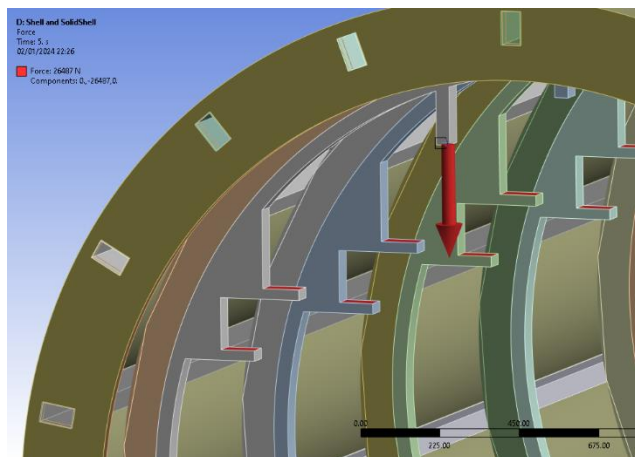
Figure 176: Rails load

Static load of the pod

Pod is attached to the rails and represent a vertical load to the rail supports. The magnitude depends on the size and length of the pod, as well as the weight of the cargo. In this study, it is assumed that the pod weight is 20 tons, with a length of 16 meters. Pod load is taken from the work of Muserues et al. [17], who investigated pod weights ranging from 10 to 20 tons and determined that fatigue is not a design concern for plain tube design. The assumption regarding length is made for the purpose of simplifying the application of load to the ring supports, ensuring even distribution among all rings in a single tube section. Therefore, the total pod weight is 196.2kN, which imposes a load of 12.26 kN per ring support.

Moving pod

Pod is attached to the rails, and rails are supported by the rail supports. As the pod moves along the rails, that imposes a moving load which is transferred through the rail supports to the structure. According to NEN EN1991-1-2 [29], dynamic effects should be taken into account. This consideration is due to several factors: rapid rate of loading due to the speed of the pod; the passage of successive loads with approximately uniform spacing which can excite the structure and under certain circumstances create resonance; and due to the potential wheel load variations resulting from either track or wheels [29].

Following the general design rules in NEN EN1991-1-2 [29], the results from static analysis should be multiplied by the dynamic factor Φ. An additional dynamic analysis is required if the criteria presented in Figure 177 are met.
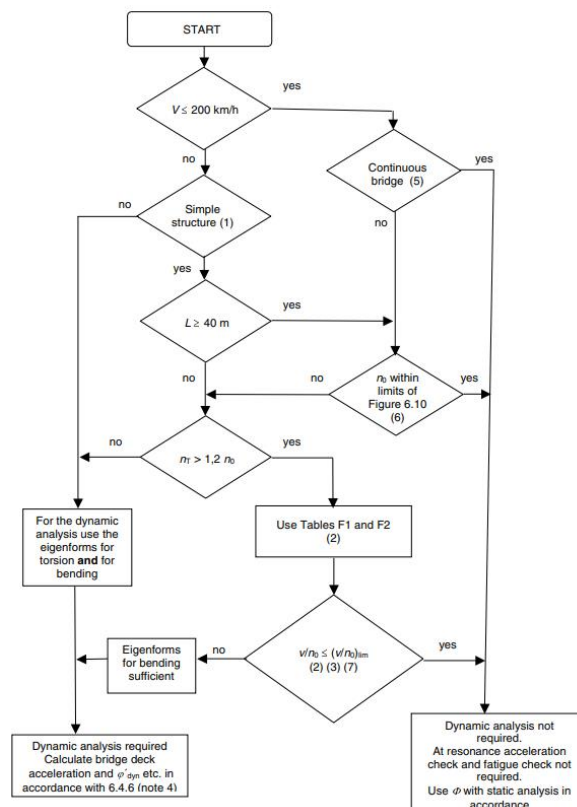
Figure 177: Flow chart for determining whether a dynamic analysis is required [29]

Where:

V is the Maximum Line Speed at the Site [km/h];

L is the span length [m];

n_0 is the first natural bending frequency of the bridge loaded by permanent actions [Hz]. For a simply supported bridge, subjected to bending only, the natural frequency can be estimated using the following formula:

$$n_0[Hz] = \frac{17.75}{\sqrt{\delta_0}}$$

Where:

δ_0 is the deflection at mid span due to permanent actions [mm] and is calculated, using a short term modulus for concrete bridges or composite steel and concrete bridges, in accordance with a loading period appropriate to the natural frequency of the bridge.

n_T is the first natural torsional frequency of the bridge loaded by permanent actions [Hz].

Looking at the flow chart conditions, the speed of the pod exceeds 200 km/h, and the tube is a simple structure, since the tube segments start and end at the flanges i.e., at the pylons. Natural frequencies were calculated in Ansys with Modal analysis of the model. Ansys outputs all natural frequencies, meaning that those frequencies can be related to both, bending or torsional vibrations. The first natural frequency is 22.69 Hz, also shown in Figure 178.
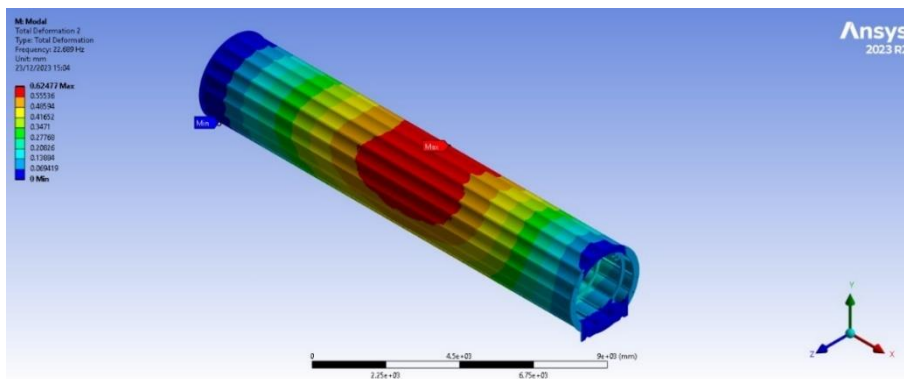
Figure 178: Modal analysis of 16m long model – Mode 1 [22.69 Hz]

Bending natural frequency can be estimated using the previously given equation:

$$n_0[Hz] = \frac{17.75}{\sqrt{\delta_0}} = \frac{17.75}{\sqrt{1.145}} = 16.58 \; Hz$$

Where the maximum vertical deflection is taken from the 16m model, as seen in **Error! Reference source not found.**.
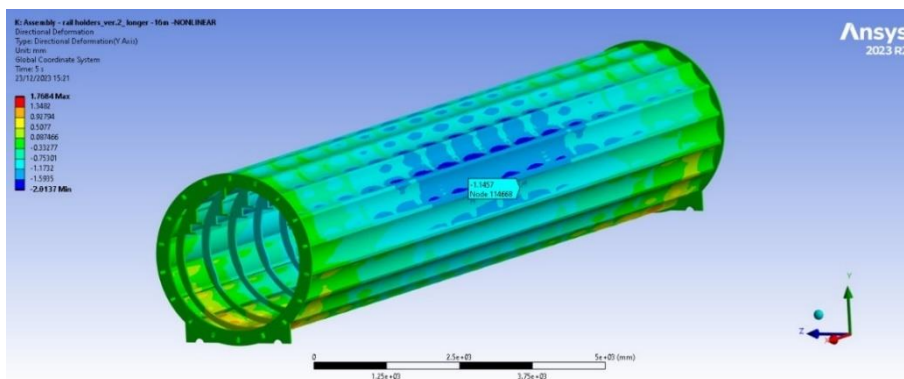
The probe for reading the vertical deformation can be taken from either 8th or 9th ring at the far right or far left side. This is due to the total deformation of the ring, which deforms in the shape of an ellipse due to the non-uniform loading, therefore the global vertical deformation can be accurately determined only at the left and right edges of the rings (Figure 180).
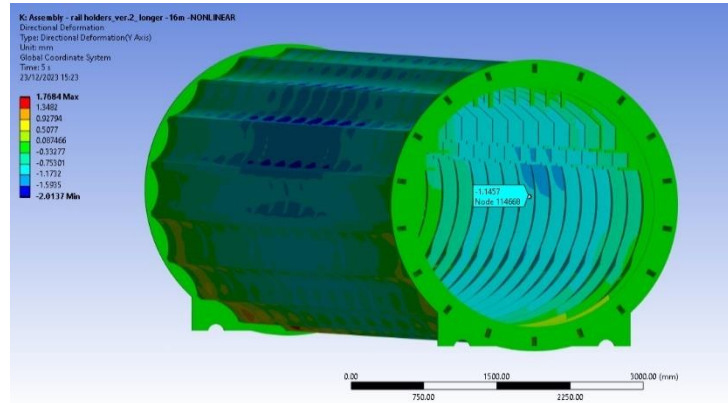
Figure 180: Probe location for reading the vertical deformation

It should be noted that the design of skeleton hyperloop tube and the way the load is applied does not entirely represent a bridge application. The most similar bridge cross-section in the standards is a closed box girder; therefore, those standards are only adapted due to structure similarities. This also justifies why the analytically calculated natural bending frequency is lower than the first natural frequency obtained from the Modal analysis in Ansys.

Following the flow chart, it is determined that the dynamic analysis is required for this structure. The results should thereafter be compared with the results of the static analysis multiplied by the dynamic factor Φ. But since dynamic analysis of the structure is outside the scope of his research, only the static analysis is performed with the use of dynamic factor.

Dynamic factor

Dynamic factor takes into account dynamic magnification of the stresses and vibration effects, but not the resonance effects [29]. Dynamic factor can be taken as either Φ_2 or Φ_3, which depends on the type of maintenance. Since the hyperloop technology is a high-risk application, carefully maintained track is a necessity, so Φ_2 is chosen:

$$\Phi_2 = \frac{1.44}{\sqrt{L_\Phi} - 0.2} + 0.82 \quad with\ 1.00 \leq \Phi_2 \leq 1.67$$

where:

L_Φ - 'Determinant' length (length associated with Φ)

Determinant length is calculated using a formula from DNV standards, Table 8.2 [7]. Case 5.3 is assumed, which is for main girders with closed frames or boxes. L_Φ is calculated as:

$$L_\Phi = k \cdot L_m$$

where:

$$L_m = \frac{1}{n} \cdot (L_1 + L_2 + .. + L_n)$$

And the structure should be considered as a three-span continuous beam, so n = 3 and k = 1.3.

So:

$$L_{\Phi} = 20.8 \ m$$

$$\Phi_2 = \frac{1.44}{\sqrt{20.8} - 0.2} + 0.82 = 1.15$$

The total pod load is therefore:

$$F_{pod} = 196.2kN \cdot \Phi_2 = 196.2kN \cdot 1.15 = 225.63 \ kN$$

And load per ring:

$$F_{ring} = \frac{F_{pod}}{16} = \frac{235.44kN}{16} = 14.1 \ kN$$

Breaking of the pod

Pod deceleration imposes a longitudinal force to the rails, and from the rails to the rail supports. This force can cause instability of the rings and stringers. In the model the longitudinal force is applied to the surfaces, to which the rails are attached.

A maximum suggested permissible acceleration for trains provided by J.P. Powell et. al. [30], is set at 2.45 m/s² for forward faced passengers, which is approximately a deceleration of 0.25g. Considering the pod weight to be 20000 kg, this imposes the following longitudinal breaking force:

$$F_b = m \cdot a = 20000 \cdot 0.25 \cdot 9.81 = 49 \ kN$$

The force is transferred from the rails to the ring supports. Since 16 ring supports are present per 16m tube segment, this imposes the following longitudinal load per ring support:

$$F_{l,ring} = \frac{F_b}{16} = 3062.5 \ N$$

Thermal expansion

The temperature of the hyperloop tube structure may increase due to environmental conditions, leading to the expansion of the material. Considering the potential extensive length of the hyperloop network, this thermal expansion could result in large stresses in the tube. Therefore, the temperature variation needs to be determined, after which an assessment can be done on the tube expansion. Currently, thermal expansion of the structure is mitigated with expansion joints. Thermal actions are determined based on NEN-EN 1991-1-5 [40]. Hyperloop tube is considered as a bridge with a steel box girder. Table 8.1 [40] provides the uniform bridge temperatures, where the steel box girder is considered as bridge deck type 1. Temperature deviation is based on extreme scenario, where the maximum temperature is taken as 70°C, and -30°C as the minimum temperature. This Temperature range is in line with the range, which was considered for the tube design currently used at European Hyperloop centre.

Settlement of Foundation

Foundation settlement is another concern, which needs to be addressed. Sudden settlement can cause loss of contact between tube and support, and consequently the tube stays elevated above the foundation. This doubles the bending length of the tube and could have adverse effects on the passing pod inside the tube. The tube would also have an increased compressive stress on the top, and tension stress on the bottom. This scenario could be checked by either doubling the length of the tube and assign the same loads; or by assigning displacement support, and allow initial displacement, that represents the

foundation settlement. To foresee such occurrences, a monitoring system could be implemented at the supports, detecting any settlements at any part of the infrastructure.

Accidental loads

Hyperloop structure should be checked for accidental loads, such as vehicle impact, hyperloop pod impact, explosion etc. Considering the pod velocity, and high safety measures required for the operation of hyperloop system, it is important that the structure can withstand loads by accidental occurrences. It is a low probability event, but the system needs to be well isolated from the external factors to operate without disturbances.

D. Combinations

Load combination is defined based on NEN-EN1990, Actions on Structures [26]. Structure consequence class 2 (CC2) is chosen in case if the hyperloop tube is to be used only for cargo transportation, and CC3 in case of the passenger transportation. Since this is still preliminary research of the design, an assumption is made that only cargo will be transported in the initial phases of hyperloop applications. Therefore, for this structure CC2 is determined, and the load factors are taken from Table NB.4 – A1.2 (B) from NEN-EN1990 [31], where an unfavorable condition was chosen for permanent actions.

Table 32: Load cases and load magnitudes

Load case	Load
q_{self} - Self-weight	/
q_{vac} - Vacuum pressure	0.1 MPa
q_r - Rails load	58.860 kN
q_w - Wind load	0.000375 MPa
q_s - Snow load	0.00056 MPa
$q_{s.pod}$ - Static pod load	196.2 kN
q_{br} - Breaking of the pod	3.0625 kN

Table 33: Table NB.4 – A1.2(B) – Design values of loads (STR/GEO) (group B) [31]

Blijvende en tijdelijke ontwerpsituaties	Blijvende belastingen		Overheersende veranderlijke belasting	Veranderlijke belastingen gelijktijdig met de overheersende	
	Ongunstig	Gunstig		Belangrijkste (indien aanwezig)	Andere
(Vgl. 6.10a)	$1,35\,G_{k,j,sup}$ [a]	$0,9\,G_{k,j,inf}$		$1,5\,\psi_{0,1}\,Q_{k,1}$	$1,5\,\psi_{0,i}\,Q_{k,i}$ $(i>1)$
(Vgl. 6.10b)	$1,2\,G_{k,j,sup}$ [b]	$0,9\,G_{k,j,inf}$	$1,5\,Q_{k,1}$		$1,5\,\psi_{0,i}\,Q_{k,i}$ $(i>1)$

[a] Bij vloeistofdrukken met een fysiek beperkte waarde mag zijn volstaan met $1,2\,G_{k,j,sup}$.

[b] Deze waarde is berekend met $\xi = 0,89$.

Table 34: Combinations of actions for ultimate limit states [31]

Action or effect	Design situation			
	Fundamental (persistent/ transient)	Accidental[a]	Seismic[b]	Fatigue[c]
General formula for effects of actions	(8.4)			
Formula for combination of actions	(8.12)	(8.15)	(8.16)	(8.17)
Permanent ($G_{d,i}$)	$\gamma_{G,i}G_{k,i}$	$G_{k,i}$	$G_{k,i}$	$G_{k,i}$
Leading variable ($Q_{d,1}$)	$\gamma_{Q,1}Q_{k,1}$	$\psi_{1,1}Q_{k,1}$ or $\psi_{2,1}Q_{k,1}$	$\psi_{2,j}Q_{k,j}$	$\psi_{2,j}Q_{k,j}$
Accompanying variable ($Q_{d,j}$)	$\gamma_{Q,j}\psi_{0,j}Q_{k,j}$	$\psi_{2,j}Q_{k,j}$		
Prestressing (P_d)	$\gamma_P P_k$	P_k	P_k	P_k
Accidental (A_d)		A_d	-	-
Seismic (A_{Ed})	-	-	$A_{Ed,ULS}$	-
Fatigue (Q_{fat})	-	-	-	Q_{fat}

[a] See A.2.6.8 for combinations of actions for accidental design situations.

[b] Depending on the magnitude of AEd,ULS, the seismic combination of actions covers both the near collapse (NC) and significant damage (SD) ultimate limit states defined in EN 1998 (all parts).

[c] See 8.3.4.5 for conditions of use for fatigue.

Table 35: Combinations of actions for serviceability limit states [31]

Action or effect	Combination			
	Characteristic	**Frequent**	**Quasi-permanent**	**Seismic**[a]
General formula for effects of actions	(8.28)			
Formula for combination of actions	(8.29)	(8.30)	(8.31)	(8.32)
Permanent ($G_{d,j}$)	$G_{k,i}$	$G_{k,i}$	$G_{k,i}$	$G_{k,i}$
Leading variable ($Q_{d,1}$)	$Q_{k,1}$	$\psi_{1,1}Q_{k,1}$	$\psi_{2,j}Q_{k,j}$	$\psi_{2,j}Q_{k,j}$
Accompanying variable ($Q_{d,i}$)	$\psi_{0,j}Q_{k,j}$	$\psi_{2,j}Q_{k,j}$		
Prestressing (P_d)	P_k	P_k	P_k	P_k
Seismic (A_{Ed})	-	-	-	$A_{Ed,SLS}$
[a] Depending on the magnitude of $A_{Ed,SLS}$, the seismic combination of actions covers both the damage limitation (DL) and fully operational (OP) serviceability limit states defined in EN 1998 (all parts).				

Table 36: Table A.2.7 (NDP) — Combination factors for railway bridges [31]

Action[p]			ψ_0	ψ_1	ψ_2 [a]
Individual components of traffic actions[d, e, g]	LM 71[o]		0,80	[b]	0
	SW/0[o]		0,80	[b]	0
	SW/2[h]		0	1,00	0
	Unloaded train[g]		1,00	–	–
	HSLM		1,00	1,00	0
	Traction and braking[o] Centrifugal force[o] Interaction forces due to deformation under vertical traffic loads		Individual components of traffic actions in design situations where the traffic loads are considered as a single (multi-directional) leading action and not as groups of loads should use the same values of ψ factors as those adopted for the associated vertical loads		
	Nosing forces		1,00	0,80	0
	Non-public footpaths loads		0,80	0,50	0
	Real trains		1,00	1,00	0
	Horizontal earth pressure due to traffic load surcharge				
	Aerodynamic effects		0,80	[b]	0
			0,80	0,50	0
Main traffic actions c, g, h (groups of loads)	gr11 (LM71 + SW/0)	Max. vertical 1 with max. longitudinal	0,80	0,80	0
	gr12 (LM71 + SW/0)	Max. vertical 2 with max. transverse			
	gr13 (Braking/traction)	Max. longitudinal			
	gr14 (Centrifugal/nosing)	Max. transverse			
	gr15 (Unloaded train)	Lateral stability with "unloaded train"			
	gr16 (SW/2)	SW/2 with max. longitudinal			
	gr17 (SW/2)	SW/2 with max. transverse			
	gr21 (LM71 + SW/0)	Max. vertical 1 with max. longitudinal			
	gr22 (LM71 + SW/0)	Max. vertical 2 with max transverse			

Action[p]			ψ_0	ψ_1	ψ_2 [a]
	gr23 (Braking/traction)	Max. longitudinal	0,80	0,70	0
	gr24 (Centrifugal/nosing)	Max. transverse			
	gr26 (SW/2)	SW/2 with max. longitudinal			
	gr27 (SW2)	SW/2 with max. transverse			
	gr31 (LM71 + SW/0)	Additional load cases	0,80	0,60	0
Other operating actions	Aerodynamic effects [i]		0,80	0,50	0
	General maintenance loading for non-public footpaths		0,80	0,50	0
Wind forces[f, g, h, i]	F_{Wk}		0,75	0,50	0
	F_W^{**}		1,00	0	0
Thermal actions	T_k		0,60[m, n]	0,60	0,50
Snow loads	$Q_{Sn,k}$ Persistent design situations[k] Execution[l]		0 0,8	0 -	0 -
Water actions			j	j	j
Construction actions[l]	Q_c		1,0	-	1,0

General combination formula:

$$1.2q_{self} + 1.2\psi_0 q_{vac} + 1.2\psi_0 q_r + 1.5\psi_0 q_w + 1.5\psi_0 q_{br} + 1.5\psi_0 q_s + 1.5\psi_0 q_{st.p.}$$

$\gamma_{G,i}$	q_{self}	q_{vac}	q_r	q_w	q_s	q_{st}	q_{br}
LC1	1.2	1.5	1.2	1.5	1.5	1.5	1.5
LC2	1.2	1.5	1.2	1.5	1.5	1.5	1.5
LC3	1.2	1.5	1.2	1.5	1.5	1.5	1.5
LC4	1.2	1.5	1.2	1.5	1.5	1.5	1.5
LC5	1.2	1.5	1.2	1.5	1.5	1.5	1.5
LC6	1.2	1.5	1.2	1.5	1.5	1.5	1.5
LC7	1.2	1.5	1.2	1.5	1.5	1.5	1.5
LC8	1.2	1.5	1.2	1.5	1.5	1.5	1.5
LC9	1.2	1.5	1.2	1.5	1.5	1.5	1.5
LC10	1.2	1.5	1.2	1.5	1.5	1.5	1.5

Ψ_0	q_{self}	q_{vac}	q_r	q_w	q_s	q_{st}	q_{br}
LC1	1	1	1	0	0	0	0
LC2	1	1	1	0	1	0	0
LC3	1	1	1	1	0	0	0
LC4	1	1	1	0.75	1	0	0
LC5	1	1	1	1	0.8	0	0
LC6	1	1	1	0.75	1	0.8	0
LC7	1	1	1	1	0.8	0.8	0
LC8	1	1	1	0.75	0.8	1	0
LC9	1	1	1	0.75	0.8	0	1
LC10	1	1	1	1	1	1	0

$G_{k,i}$	q_{self}	q_{vac}	q_r	q_w	q_s	q_{st}	q_{br}
LC1		0.1	58.86	0.000251	0.00056	196.2	3.0625
LC2		0.1	58.86	0.000251	0.00056	196.2	3.0625
LC3		0.1	58.86	0.000251	0.00056	196.2	3.0625
LC4		0.1	58.86	0.000251	0.00056	196.2	3.0625
LC5		0.1	58.86	0.000251	0.00056	196.2	3.0625
LC6		0.1	58.86	0.000251	0.00056	196.2	3.0625
LC7		0.1	58.86	0.000251	0.00056	196.2	3.0625
LC8		0.1	58.86	0.000251	0.00056	196.2	3.0625
LC9		0.1	58.86	0.000251	0.00056	196.2	3.0625
LC10		0.1	58.86	0.000251	0.00056	196.2	3.0625

F	q_{self}	q_{vac} [MPa]	q_r [kN]	q_w [MPa]	q_s [MPa]	q_{st} [kN]	q_{br} [kN]
LC1		0.12	70.632	0	0	0	0
LC2		0.12	70.632	0	0.00084	0	0
LC3		0.12	70.632	0.000375	0	0	0
LC4		0.12	70.632	0.00028	0.00084	0	0
LC5		0.12	70.632	0.000375	0.000672	0	0
LC6		0.12	70.632	0.0003	0.00084	235.44	0
LC7		0.12	70.632	0.000375	0.000672	235.44	0
LC8		0.12	70.632	0.00028	0.000672	294.3	0
LC9		0.12	70.632	0.00028	0.000672	0	4.6
LC10		0.12	70.632	0.000375	0.00084	294.3	0

SLS combinations

$\gamma_{G,i}$	q_{self}	q_{vac}	q_r	q_w	q_s	q_{st}	q_{br}
LC1	1	1	1	1	1	1	1
LC2	1	1	1	1	1	1	1
LC3	1	1	1	1	1	1	1
LC4	1	1	1	1	1	1	1
LC5	1	1	1	1	1	1	1
LC6	1	1	1	1	1	1	1
LC7	1	1	1	1	1	1	1
LC8	1	1	1	1	1	1	1
LC9	1	1	1	1	1	1	1
LC10	1	1	1	1	1	1	1

Ψ_0	q_{self}	q_{vac}	q_r	q_w	q_s	q_{st}	q_{br}
LC1	1	1	1	0	0	0	0
LC2	1	1	1	0	1	0	0
LC3	1	1	1	1	0	0	0
LC4	1	1	1	0.75	1	0	0
LC5	1	1	1	1	0.8	0	0
LC6	1	1	1	0.75	1	0.8	0
LC7	1	1	1	1	0.8	0.8	0
LC8	1	1	1	0.75	0.8	1	0
LC9	1	1	1	0.75	0.8	0	1
LC10	1	1	1	1	1	1	0

$G_{k,i}$	q_{self}	q_{vac}	q_r	q_w	q_s	q_{st}	q_{br}
LC1		0.1	58.86	0.000251	0.00056	196.2	3.0625
LC2		0.1	58.86	0.000251	0.00056	196.2	3.0625
LC3		0.1	58.86	0.000251	0.00056	196.2	3.0625
LC4		0.1	58.86	0.000251	0.00056	196.2	3.0625
LC5		0.1	58.86	0.000251	0.00056	196.2	3.0625
LC6		0.1	58.86	0.000251	0.00056	196.2	3.0625
LC7		0.1	58.86	0.000251	0.00056	196.2	3.0625
LC8		0.1	58.86	0.000251	0.00056	196.2	3.0625
LC9		0.1	58.86	0.000251	0.00056	196.2	3.0625
LC10		0.1	58.86	0.000251	0.00056	196.2	3.0625

F	q_{self}	q_{vac} [MPa]	q_r [kN]	q_w [MPa]	q_s [MPa]	q_{st} [kN]	q_{br} [kN]
LC1		0.1	58.86	0	0	0	0
LC2		0.1	58.86	0	0.00056	0	0
LC3		0.1	58.86	0.000251	0	0	0
LC4		0.1	58.86	0.0002	0.00056	0	0
LC5		0.1	58.86	0.00025	0.000448	0	0
LC6		0.1	58.86	0.0002	0.00056	156.96	0
LC7		0.1	58.86	0.00025	0.000448	156.96	0
LC8		0.1	58.86	0.0002	0.000448	196.2	0
LC9		0.1	58.86	0.0002	0.000448	0	3.0625
LC10		0.1	58.86	0.00025	0.00056	196.2	0

ULS combinations

LC1: Vacuum pressure only: $1.2q_{self} + 1.2\psi_0 q_{vac.} + 1.2\psi_0 q_r$

LC2: Snow: $1.2q_{self} + 1.2\psi_0 q_{vac} + 1.2\psi_0 q_r + 1.5\psi_0 q_s$

LC3: Wind: $1.2q_{self} + 1.2\psi_0 q_{vac} + 1.2\psi_0 q_r + 1.5\psi_0 q_w$

LC4: Snow leading: $1.2q_{self} + 1.2\psi_0 q_{vac} + 1.2\psi_0 q_r + 1.5\psi_0 q_w + 1.5\psi_0 q_s$

LC5: Wind leading: $1.2q_{self} + 1.2\psi_0 q_{vac} + 1.2\psi_0 q_r + 1.5\psi_0 q_w + 1.5\psi_0 q_s$

LC6: Snow leading with static pod: $1.2q_{self} + 1.2\psi_0 q_{vac} + 1.2\psi_0 q_r + 1.5\psi_0 q_w + 1.5\psi_0 q_s + 1.5\psi_0 q_{st.p.}$

LC7: Wind leading with static pod: $1.2q_{self} + 1.2\psi_0 q_{vac} + 1.2\psi_0 q_r + 1.5\psi_0 q_w + 1.5\psi_0 q_s + 1.5\psi_0 q_{st.p.}$

LC8: Static pod leading: $1.2q_{self} + 1.2\psi_0 q_{vac} + 1.2\psi_0 q_r + 1.5\psi_0 q_w + 1.5\psi_0 q_s + 1.5\psi_0 q_{st.p.}$

LC9: Breaking pod leading: $1.2q_{self} + 1.2\psi_0 q_{vac} + 1.2\psi_0 q_r + 1.5\psi_0 q_w + 1.5\psi_0 q_s + 1.5\psi_0 q_{br.p.}$

LC10: Critical combination: $1.2q_{self} + 1.2\psi_0 q_{vac} + 1.2\psi_0 q_r + 1.5\psi_0 q_w + 1.5\psi_0 q_s + 1.5\psi_0 q_{st.p.}$

SLS combinations

LC1: Vacuum pressure only: $q_{self} + \psi_0 q_{vac.} + \psi_0 q_r$

LC2: Snow: $q_{self} + \psi_0 q_{vac} + \psi_0 q_r + \psi_0 q_s$

LC3: Wind: $q_{self} + \psi_0 q_{vac} + \psi_0 q_r + \psi_0 q_w$

LC4: Snow leading: $q_{self} + \psi_0 q_{vac} + \psi_0 q_r + \psi_0 q_w + \psi_0 q_s$

LC5: Wind leading: $q_{self} + \psi_0 q_{vac} + \psi_0 q_r + \psi_0 q_w + \psi_0 q_s$

LC6: Snow leading with static pod: $q_{self} + \psi_0 q_{vac} + \psi_0 q_r + \psi_0 q_w + \psi_0 q_s + \psi_0 q_{st.p.}$

LC7: Wind leading with static pod: $q_{self} + \psi_0 q_{vac} + \psi_0 q_r + \psi_0 q_w + \psi_0 q_s + \psi_0 q_{st.p.}$

LC8: Static pod leading: $q_{self} + \psi_0 q_{vac} + \psi_0 q_r + \psi_0 q_w + \psi_0 q_s + \psi_0 q_{st.p.}$

LC9: Breaking pod leading: $q_{self} + \psi_0 q_{vac} + \psi_0 q_r + \psi_0 q_w + \psi_0 q_s + \psi_0 q_{br.p.}$

LC10: Critical combination: $q_{self} + \psi_0 q_{vac} + \psi_0 q_r + \psi_0 q_w + \psi_0 q_s + \psi_0 q_{st.p.}$

E. Analytical approach

Skeleton tube design

One of the known critical load cases on the tube is the vacuum pressure, which is the difference between the atmospheric pressure outside the tube and the pressure inside the tube.

$$q_{atm} = 101\ 325\ \text{Pa} - \text{atmospheric pressure}$$

$$q_{tube} = 100\ \text{Pa} - \text{tube pressure}$$

The imposed pressure on the plates is therefore:

$$Area\ load: q_{Ed} = q_{atm} - q_{tube} = 101.225\ kN/m^2$$

Considering the calculated area load all components were checked in regards to either their strength, stability or deflection. To obtain the load distribution, the model can be simplified as two simply supported beams offering support to a longitudinal plate.
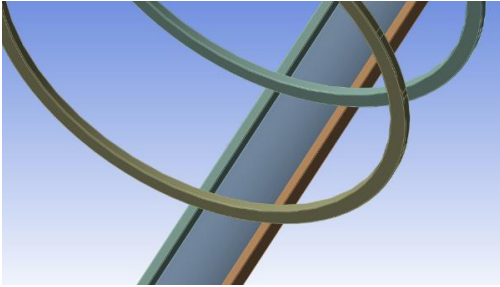
Figure 181: Isometric view of the components within the assembly
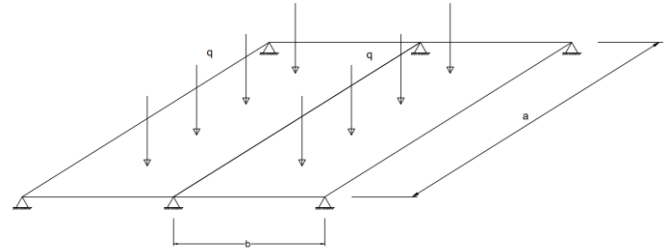
Figure 182: Simplification of the skeleton tube design

An assumption is made that the load is distributed as if the plates were flat, and not curved. The area load is evenly distributed across the plate, where each stringer takes half the area load per plate. Given the plate thickness, tube length, ring diameter and number of rings and stringers, the area load per plate can be estimated. A safety factor of k = 1.2 is used.

$$Area\ load: q_{Ed} = (q_{atm} - q_{tube}) \cdot k$$

$$Line\ load: q = q_{Ed} \cdot b$$

$$t = 1\ mm - plate\ thickness$$

$$L = 16\ m - tube\ length$$

$$d = 2.5\ m - ring\ diameter$$

$$n_{stringers} = 18 - number\ of\ stringers$$

$$n_{rings} = 16 - number\ of\ rings$$

$$k = 1.5 - Safety\ factor$$

$$b = \frac{\pi \cdot d}{n_{stringers}} \cong 0.44\ m$$

$$l = a = \frac{L}{n_{rings}} = 1\ m$$

$$Therefore:$$

$$Area\ load: q_{Ed} = (q_{atm} - q_{tube}) \cdot k = 121\ kN/m^2$$

$$Line\ load: q = q_{Ed} \cdot b = 53.4\ kN/m$$

Stringer verification

The stringers are simplified as the beams loaded by a uniformly distributed load along the length.
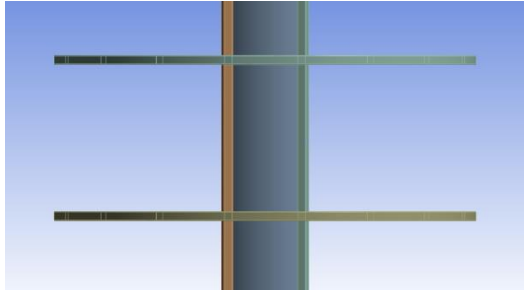
Figure 183: Top view of the stringers within the assembly
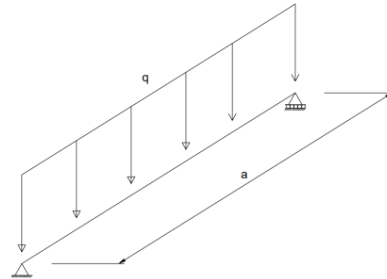
Figure 184: Stringer simplification

Bending moment resistance, shear force resistance and a combination of both have been verified. Lateral torsional buckling is not expected to take place, since a rectangular cross-section is assigned, and moreover, the length of the elements is short. Deflection does not play a vital role either when considering only a small segment of the stringer.

Resistance

$$V_{pl,Rd,y} = 89.72\ kN$$

$$M_{pl,Rd,y} = 13.60\ kNm$$

Strength checks

$$M_{Ed} = \frac{q \cdot l^2}{8} = 8.28\ kNm$$

$$V_{Ed} = \frac{q \cdot l}{2} = 33.125\ kN$$

$$UC = \frac{M_{Ed}}{M_{pl,Rd,pl}} = 0.6\ O.K.$$

$$UC = \frac{V_{Ed}}{V_{Rd,pl}} = 0.37\ O.K.$$

Bending and shear

$$\frac{V_{Ed}}{V_{Rd}} = 0.3 < 0.5\ \ Effect\ on\ the\ moment\ resistance\ is\ not\ present$$

Deflection

$$\delta = \frac{5L^4 q}{384EI_y} = 3.576\ mm$$

$$Where:$$

$$I_y = 1.206e6\ mm^4$$

$$E = 210\ 000\ MPa$$

Deflection limit:

$$\delta_{limit} = \frac{L}{250} = \frac{1000}{250} = 4\ mm$$

$$UC = \frac{\delta}{\delta_{limit}} = 0.89$$

Ring verification

The load path goes from the plates to the stringers, and from the stringers to the rings. Load on the ring can be expressed as point loads at the location of the stringers, as presented in the following figures.
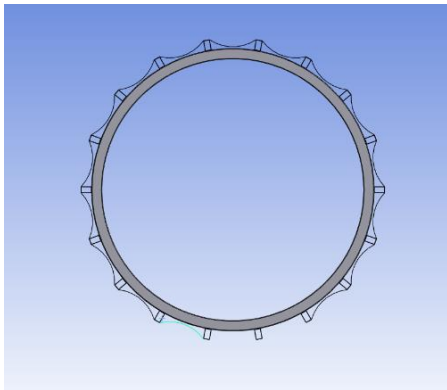
Figure 185: Cross-section of the Skeleton tube design
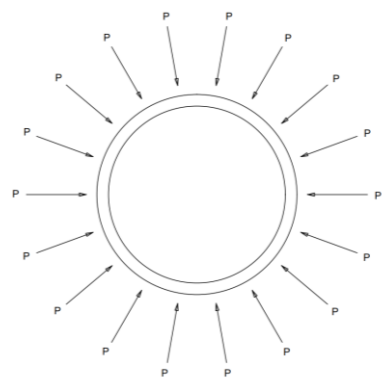
Figure 186: Simplification of the ring model

Point loads from the stringers represent the shear force to the rings, therefore the check is identical to the shear resistance check of the stringer. For the stability check, the ring is simplified as a column laterally supported on the location of the stringers. The applied load in this case is only from the vacuum pressure, but in a later stage, the critical load affecting the ring stability will be the non-uniform loading, such as wind or snow load. Critical buckling length is taken as the distance between two point supports, represented by stringers.

Shear

$$R_1 = R_2 = V_{Ed} = \frac{q \cdot l}{2} = 33.125\ kN$$

$$UC = \frac{V_{Ed}}{V_{Rd,pl,y}} = 0.37\ \ O.K.$$

Stability
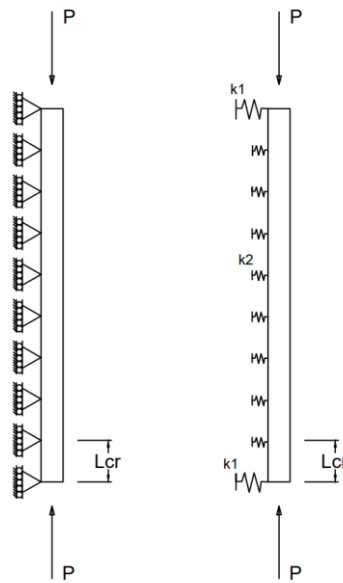
Figure 187: Simplification of the ring for the stability verification

For more realistic simplification of the model, the supports could be expressed as springs, since the tube itself experiences global buckling. But the instability of the rings is not significant, therefore the initial assumption can be used. To recreate a critical situation, an assumption is made that ring to stringer connections in the middle fail, so supports in the middle are removed. This increases the critical buckling length to 2.5m.

$$N_{cr} = \frac{\pi^2 \cdot E \cdot I}{L_{cr}^2}$$

Where:

$$E = 200 \text{ GPa} - \text{ Young's modulus}$$

$$I = 1.206\text{e}6 \ mm^4 - \text{ Second moment of inertia}$$

$$N_{cr} = \frac{\pi^2 \cdot E \cdot I}{L_{cr}^2} = 400 \ kN$$

$$P = 33.125 \ kN$$

$$UC = \frac{P}{N_{cr}} = 0.08 \ O.K.$$

Plate verification

Curved plate has been modelled as a cable structure with the uniform load along the cable.
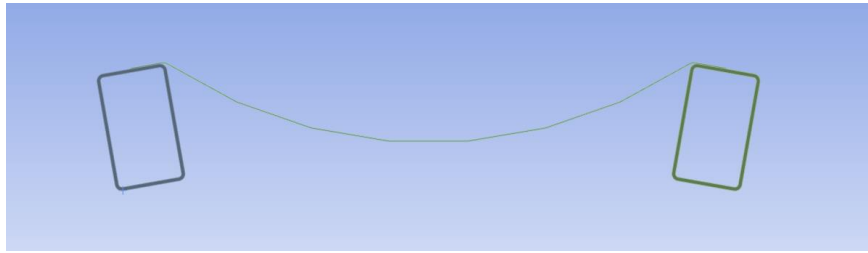
Figure 188: Plate cross-section
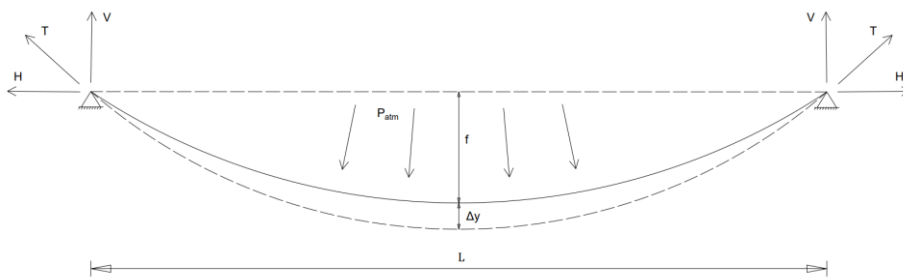
Figure 189: Plate simplification as a cable structure

In order to calculate the deflection of the plate, axial cable deformation (strain) needs to be calculated. This is done using the following relations: An assumption is made for the pinned supports, and in order to calculate the deflection of the plate, axial cable deformation had to be calculated.

$$\Delta l = \frac{Tl}{EA}$$

$$T = \sqrt{H^2 + V^2} = \sqrt{H^2 + H^2 \left(\frac{dz}{dx}\right)^2} = H\sqrt{1 + \left(\frac{dz}{dx}\right)^2}$$

$$ds = \sqrt{1 + \left(\frac{dz}{dx}\right)^2}\, dx$$

$$\Delta L = \int_{s=0}^{s=L} \frac{T\,ds}{EA} = \frac{H}{EA}\int_{x=0}^{x=l}\left[1 + \left(\frac{dz}{dx}\right)^2\right] dx = \frac{Hl}{EA} + \int_{x=0}^{x=l}\left(\frac{dz}{dx}\right)^2 dx$$

```
> restart;

> q:=151.84: L:=0.45: EA:=210000: (1/8)*q*L^2;
                                                                    3.842

> ODE:=-H*diff(z(x),x$2)=q;
                                                    ODE := -H( d²/dx² z(x) ) = 151.84

> z:=rhs(dsolve(ODE,z(x)));
                                                    z := - 1898 x²/(25 H) + _C1 x + _C2

> x:=0: eq1:=z=0: x:=L: eq2:=z=0;
                                                    eq2 := - 15.37/H + 0.45 _C1 + _C2 = 0

> sol:=solve({eq1,eq2},{_C1,_C2}); assign(sol): x:='x':
                                                    sol := { _C1 = 34.16/H, _C2 = 0. }

> z;
                                                    - 1898 x²/(25 H) + 34.16 x/H

> ds:=(1+(1/2)*diff(z,x)^2);
                                                    ds := 1 + ( - 3796 x/(25 H) + 34.16/H )² / 2

> LL:=int(ds,x=0..L);
                                                    LL := 87.54/H² + 0.4500

> dL:=H*L/EA;
                                                    dL := 2.143 × 10⁻⁶ H

> eq:=LL-dL=0.472;
                                                    eq := 87.54/H² + 0.4500 - 2.143 × 10⁻⁶ H = 0.472

> H:=fsolve(eq,H,0..10000);
                                                    H := 62.89  N/mm

> evalf(dL);
                                                    0.0001348

> x:=L/2; Dy:=((z-0.06)*1000);
                                                    x := 0.2250
                                                    Dy := 0.60  mm
```

Horizontal force: 62.89 N/mm

$$UC = \frac{F_H/t}{f_y} = \frac{62.89 \frac{N}{mm}/1mm}{355 \frac{N}{mm^2}} = 0.2 \ O.K.$$

Deflection: 0.6 mm

$$UC = \frac{P}{N_{cr}} = 0.08 \ O.K.$$

Ring to stringer connection

The spacing between stringers is 400mm, the width of the stringer flange is 60mm, and the spacing between rings is 1000mm. The load per ring is therefore calculated as follows:

$$A_{total} = (2 \cdot 200 + 60) \cdot 1000 = 460000 \ mm^2$$

$$F = p \cdot A = 0.12 \frac{N}{mm^2} \cdot 460000 \ mm^2 = 55.2 \ kN$$

Two strips are applicable if the stringer does not deform significantly, i.e., if the ring flanges do not buckle upwards once the load is applied. In case of a larger deformation, then the flanges are less utilised, and the load transfer into four smaller areas becomes more evident. The normal stress in the case of two strips is therefore calculated as:

$$A_{strip,2} = \ 3 \cdot 60 \ = 180 \ mm^2$$

$$\sigma = \frac{F}{2A} = 153.33 \frac{N}{mm^2}$$

$$\sigma < \ f_y = 355 \ MPa$$

In case of large deformation, the load would be distributed to four strips. In the analytical method, it is difficult to predict the length of a single strip since it depends on the steel grade, load magnitude and total deformation. An inverse engineering approach can be used to calculate the minimum required area strip for which the yield stress will not be reached. Therefore:

$$\sigma = \frac{F}{A} \quad \rightarrow \quad A = \frac{F}{\sigma} = \frac{55.2\ kN}{355\ N/mm^2} = 155.5\ mm^2$$

$$A_{strip} = \frac{A}{4} = 38.87\ mm^2$$

$$A_{strip} = w \cdot l \quad \rightarrow \quad l = \frac{A_{strip}}{w} = \frac{38.87\ mm^2}{3\ mm} = 13\ mm$$

The minimum length is, therefore, 13 mm. It should be noted that the analytical approach was performed considering vacuum pressure only under ideal conditions. Due to the slenderness of the structure, it is expected to be sensitive when exposed to non-uniform loadings, and its structural response might prove to be difficult to predict and verify analytically.

F. FEM results

Total deformation – Assembly without rails supports
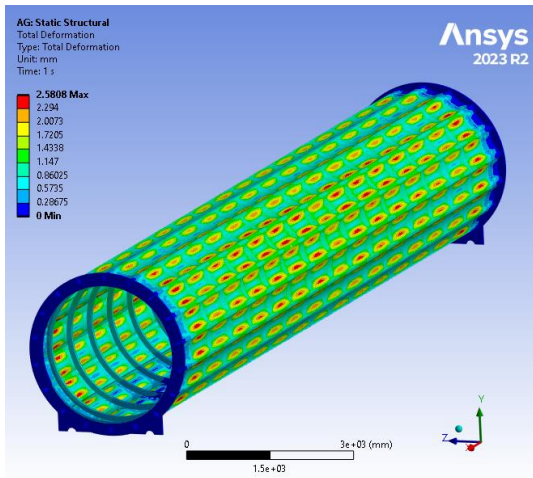
Figure 190: Total deformation [mm] of the 16m model without rails support due to LC1
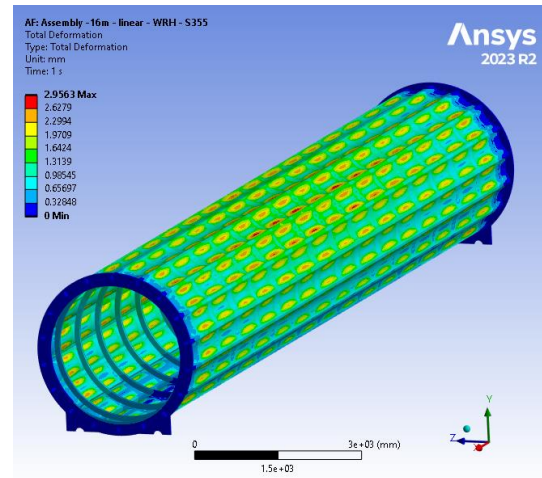
Figure 191: Total deformation [mm] of the 16m model without rails support due to LC10

Total deformation – Assembly with rails supports
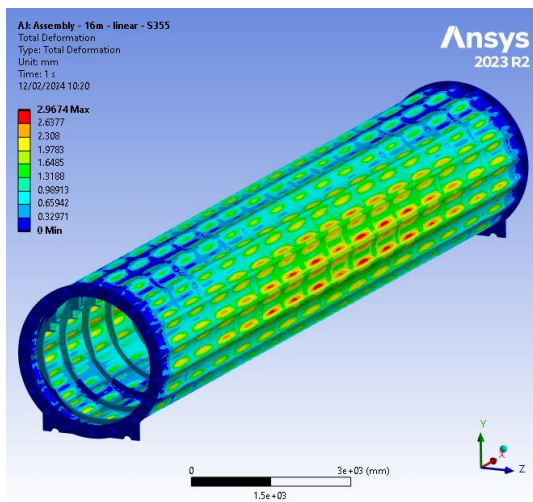
Figure 192: Total deformation [mm] of the 16m model with rails support due to LC1
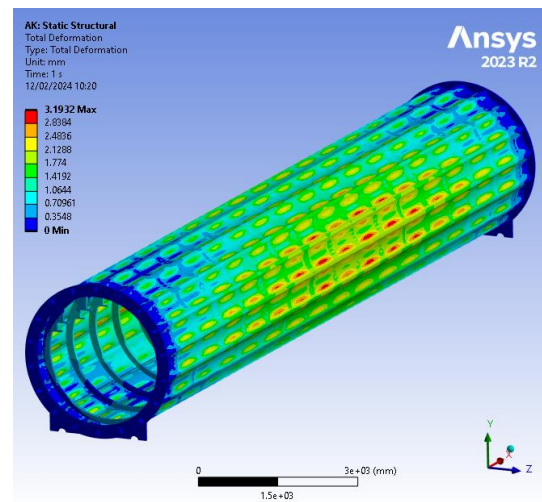
Figure 193: Total deformation [mm] of the 16m model with rails support due to LC2
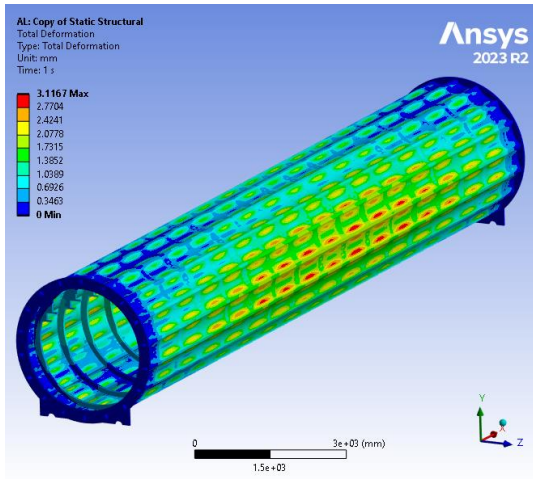
Figure 194: Total deformation [mm] of the 16m model with rails support due to LC3
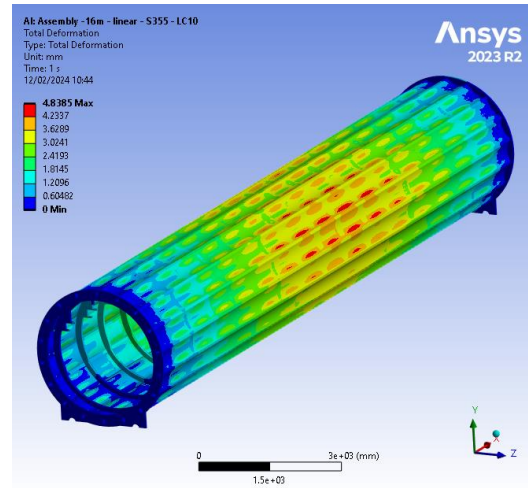
Figure 195: Total deformation [mm] of the 16m model with rails support due to LC10

Equivalent stress [MPa] – Assembly with rails supports
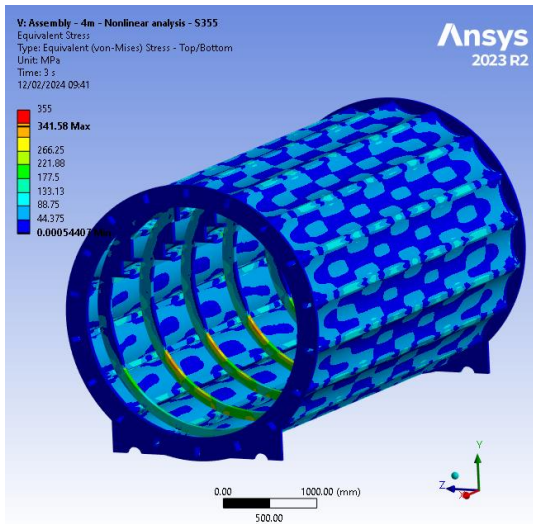
Figure 196: Equivalent Von Mises stress of the 5m model due to LC1
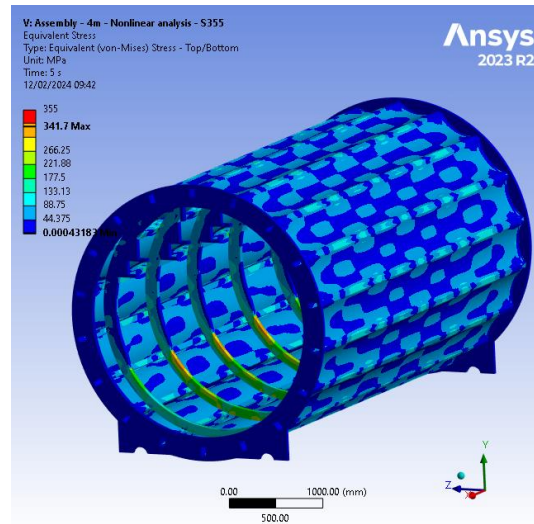
Figure 197: Equivalent Von Mises stress of the 5m model due to LC10

132

Equivalent stress [MPa] - Plates
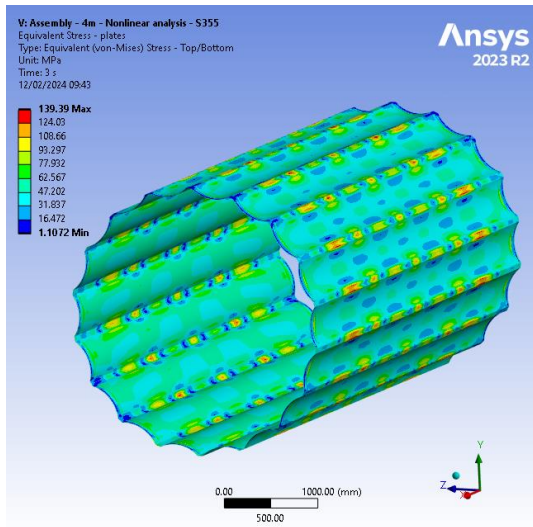
Figure 198: Equivalent Von Mises stress of the plates due to LC1
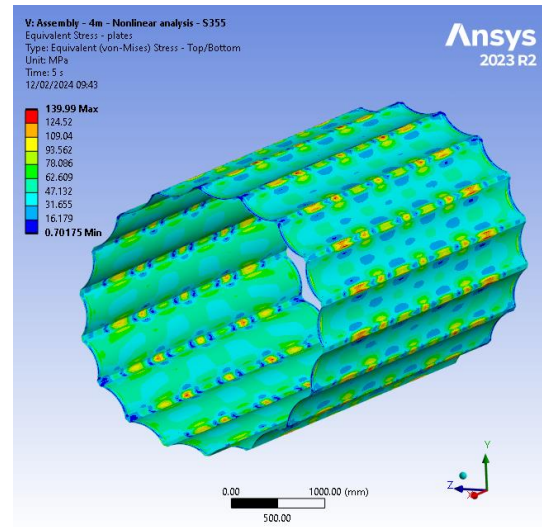
Figure 199: Equivalent Von Mises stress of the plates due to LC10

Equivalent stress [MPa] - Side plate (critical)
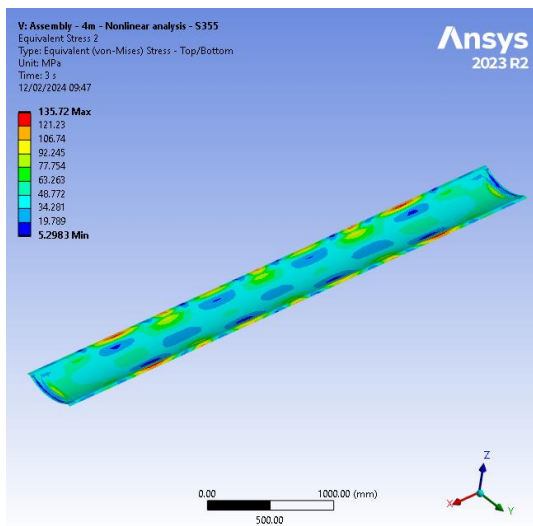
Figure 200: Equivalent Von Mises stress of the critical plate due to LC1
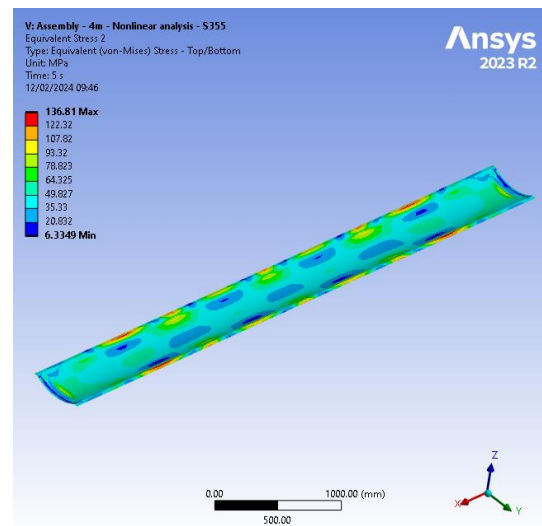
Figure 201: Equivalent Von Mises stress of the critical plate due to LC10

Equivalent stress [MPa] - Middle ring
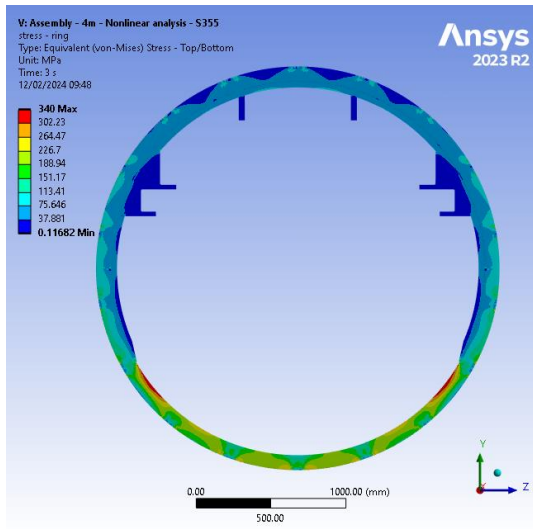
Figure 202: Equivalent Von Mises stress of the ring due to LC1
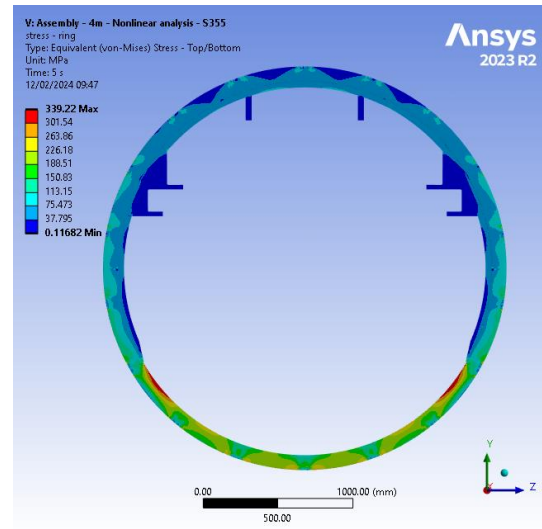
Figure 203: Equivalent Von Mises stress of the ring due to LC10

Equivalent stress [MPa] - Stringer
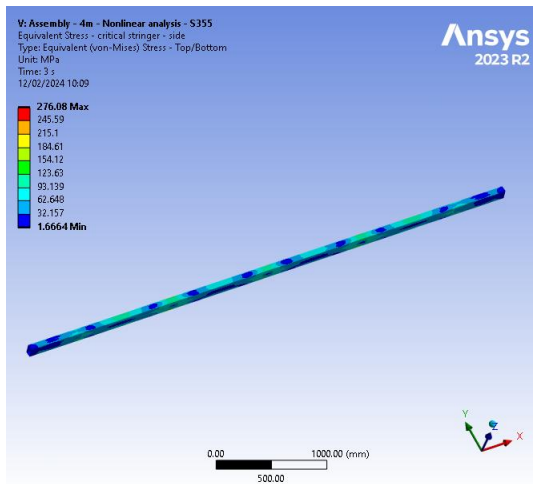
Figure 204: Equivalent Von Mises stress of the stringer due to LC1
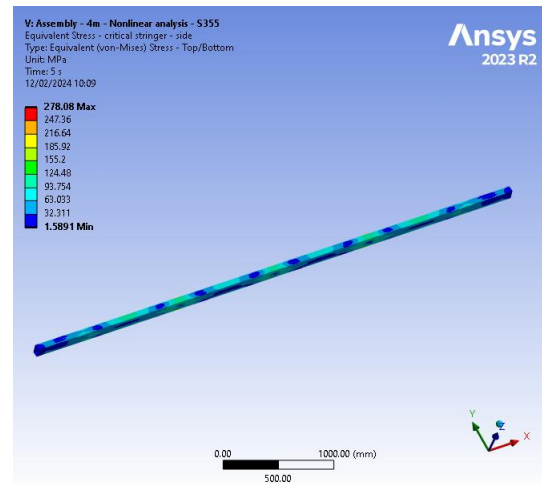
Figure 205: Equivalent Von Mises stress of the stringer due to LC10

Total deformation [mm] - Assembly
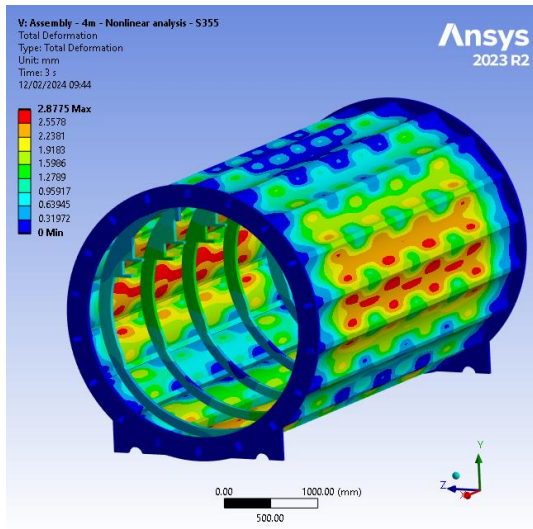
Figure 206: Total deformation of the Assembly due to LC1
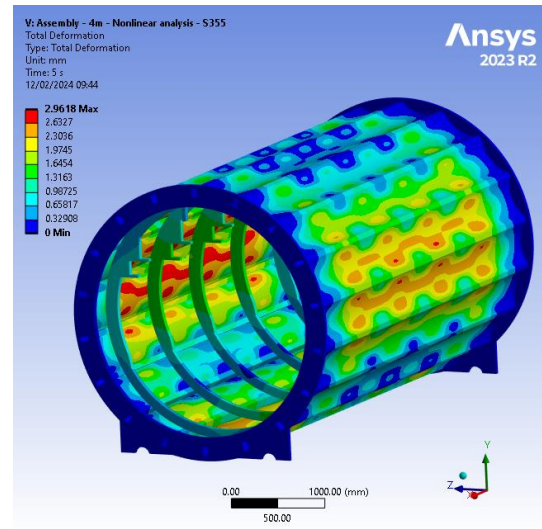
Figure 207: Total deformation of the Assembly due to LC10

Total deformation [mm] - Plates
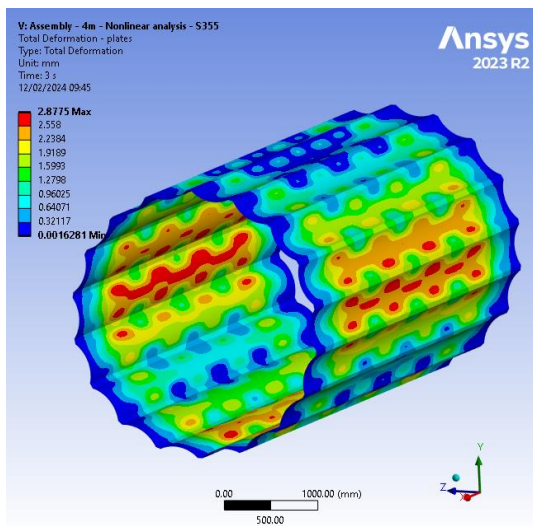
Figure 208: Total deformation of the plates due to LC1
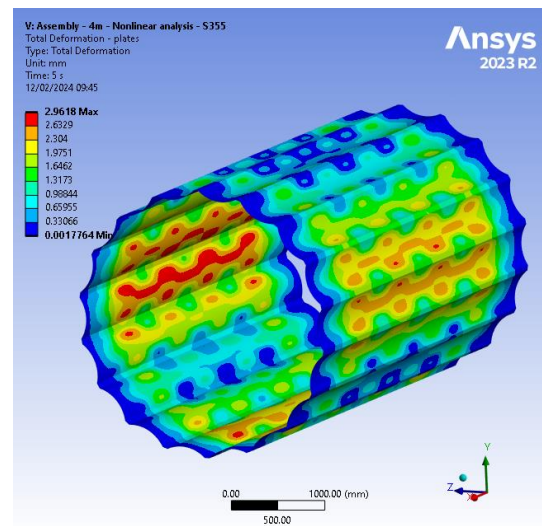
Figure 209: Total deformation of the plates due to LC10

Total deformation [mm] - Side plate (critical)
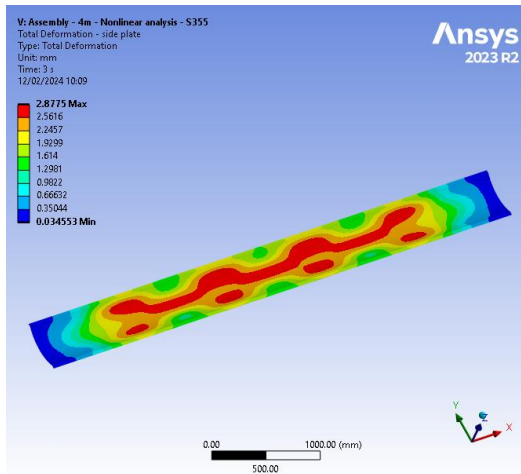
Figure 210: Total deformation of the critical plate due to LC1
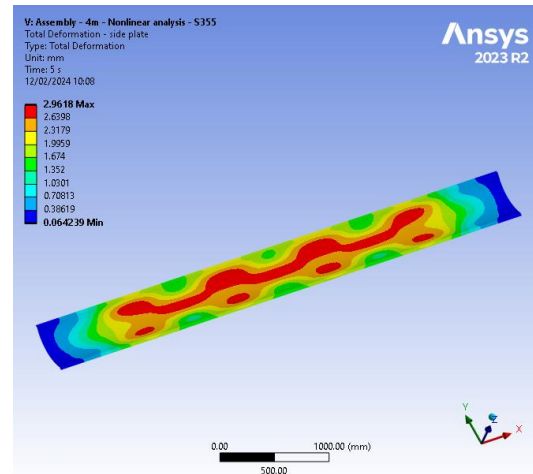
Figure 211: Total deformation of the critical plate due to LC10

Total deformation [mm] - Middle ring
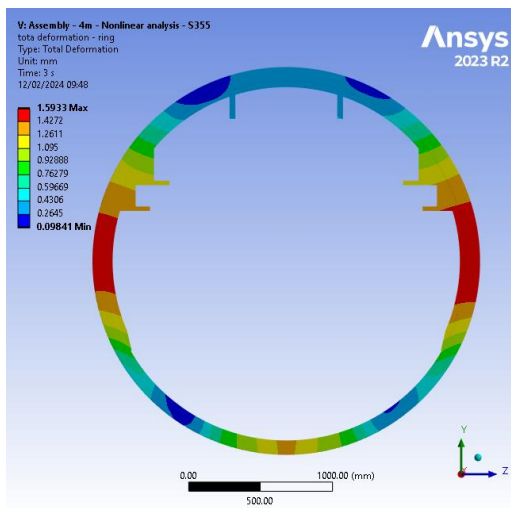
Figure 212: Total deformation of the ring due to LC1
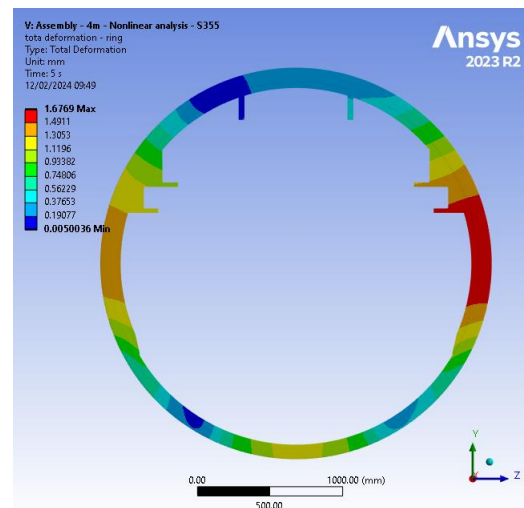
Figure 213: Total deformation of the ring due to LC10

Total deformation [mm] – Stringer (critical)
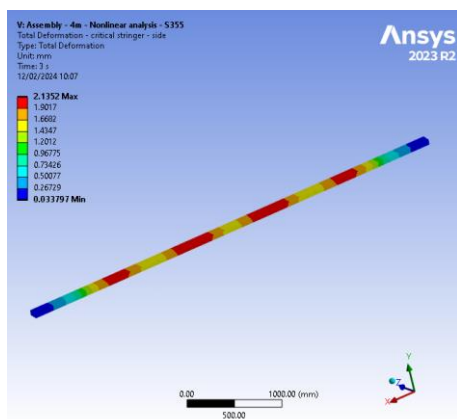
Figure 214: Total deformation of the stringer due to LC1
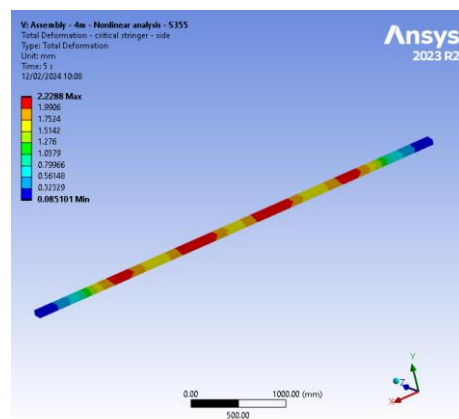
Figure 215: Total deformation of the stringer due to LC10

136

Total strain - Assembly
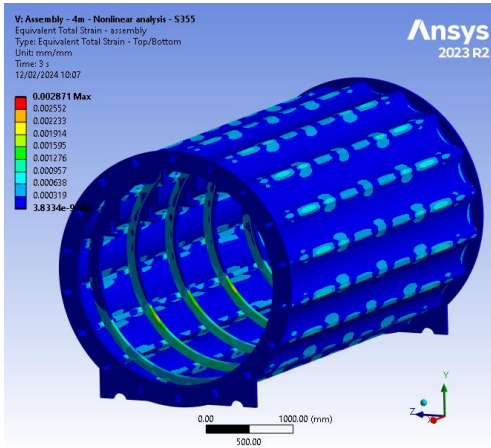
Figure 216: Equivalent Total Strain of the Assembly due to LC1
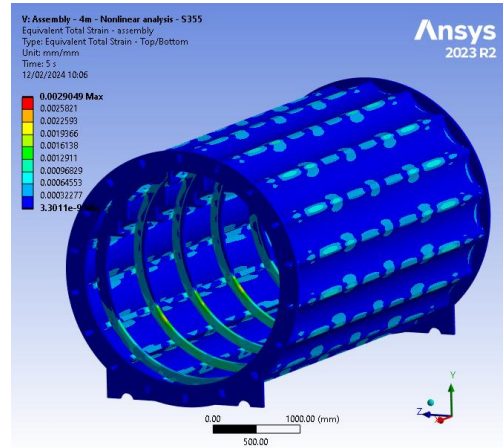
Figure 217: Equivalent Total Strain of the Assembly due to LC10

Total strain - Middle ring
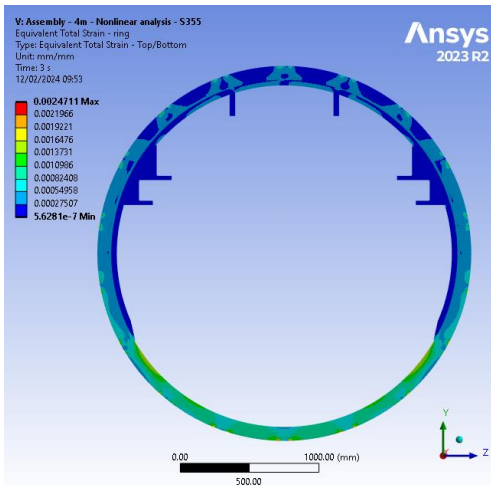
Figure 218: Equivalent Total Strain of the ring due to LC1
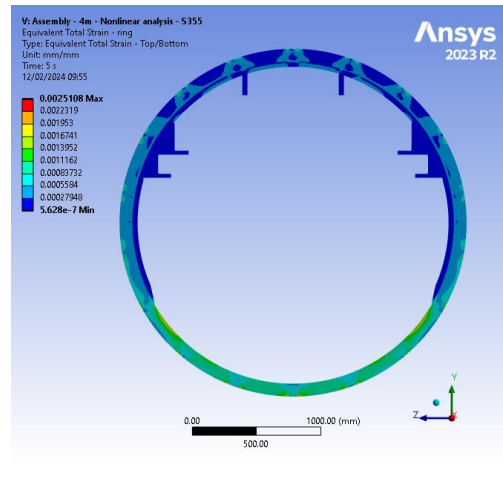
Figure 219: Equivalent Total Strain of the ring due to LC10

Eigenvalue buckling – Skeleton tube design

Model with rail supports
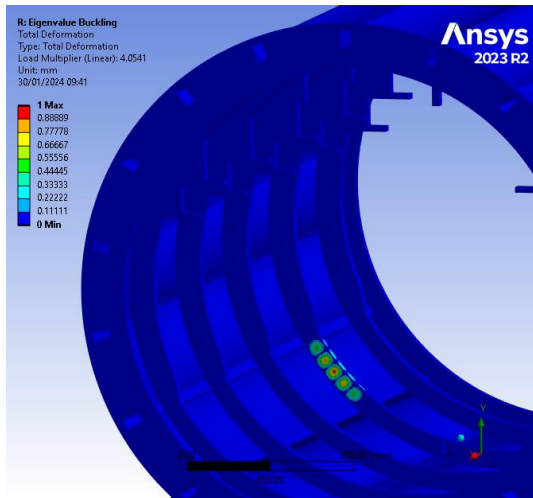
Figure 220: Buckling mode 1 [λ = 4.054]
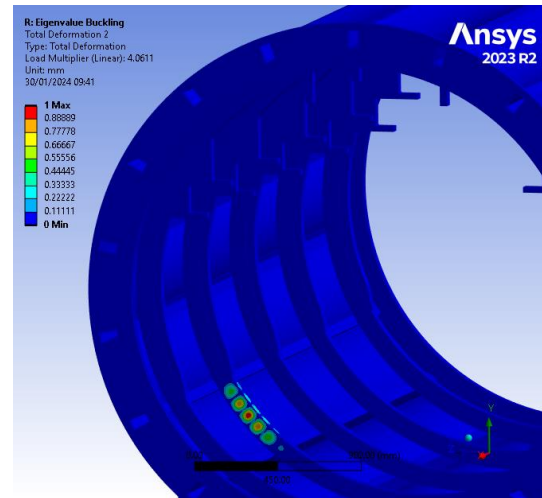
Figure 221: Buckling mode 2 [λ = 4.061]
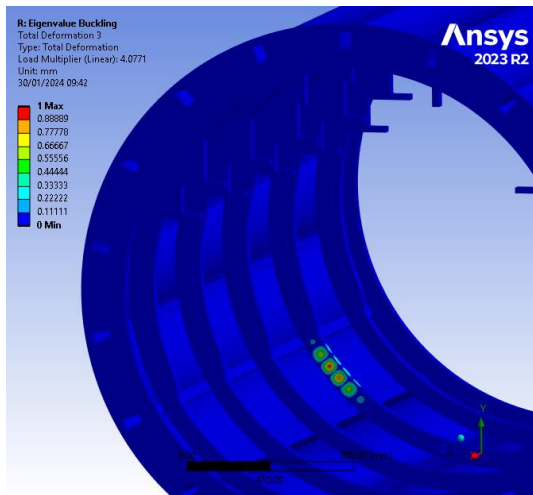
Figure 222: Buckling mode 3 [λ = 4.077]
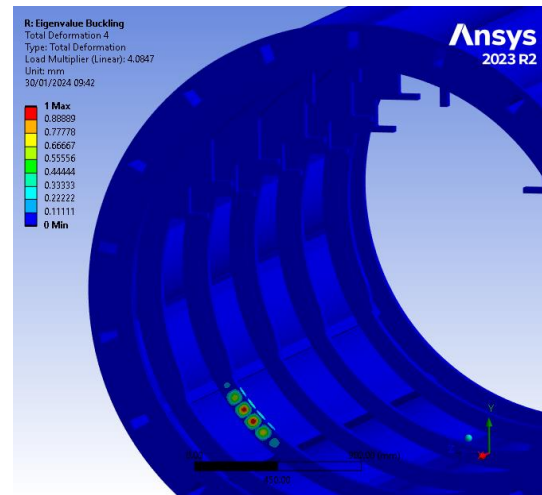
Figure 223: Buckling mode 4 [λ = 4.085]
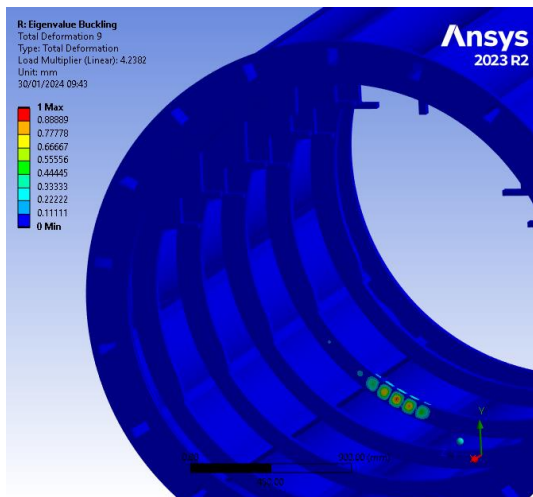
Figure 224: Buckling mode 5 [λ = 4.196]
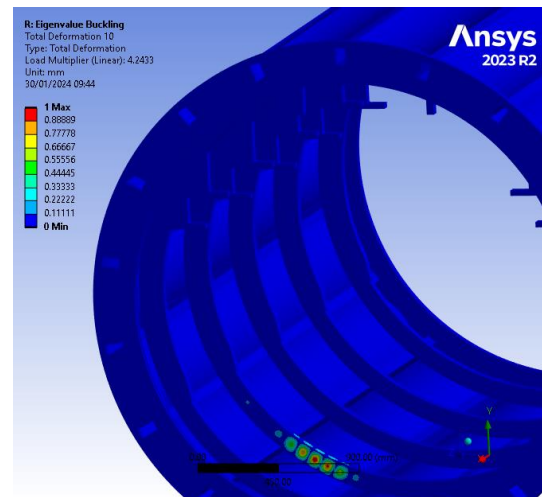
Figure 225: Buckling mode 6 [λ = 4.2]
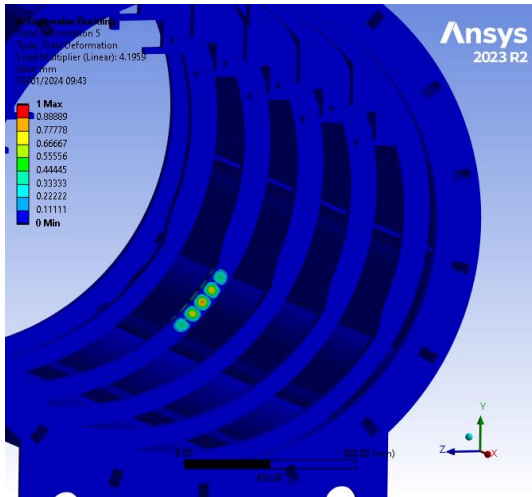
Figure 226: Buckling mode 7 [λ = 4.22]
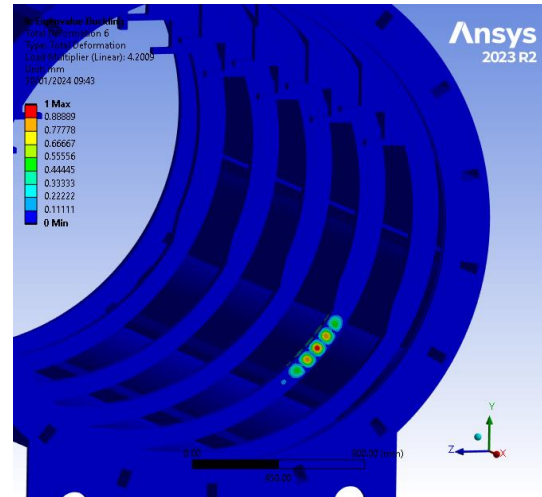
Figure 227: Buckling mode 8 [λ = 4.224]
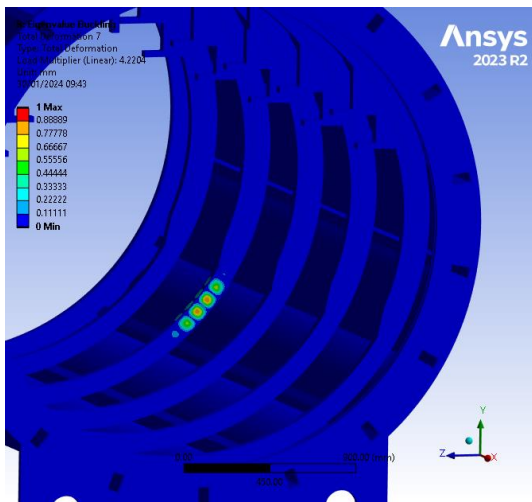
Figure 228: Buckling mode 9 [λ = 4.238]
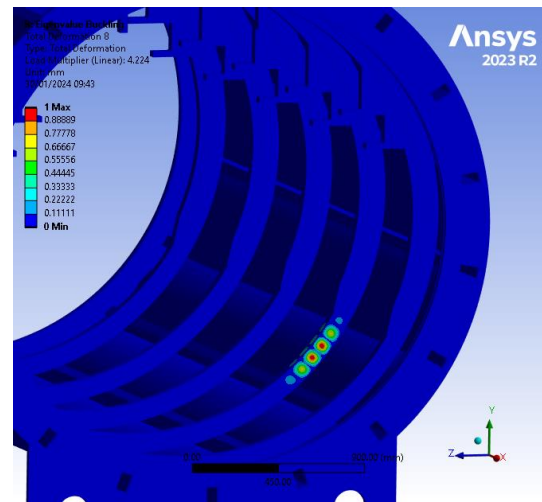
Figure 229: Buckling mode 10 [λ = 4.243]

G. Steel bracket with a slotted hole in the stringer
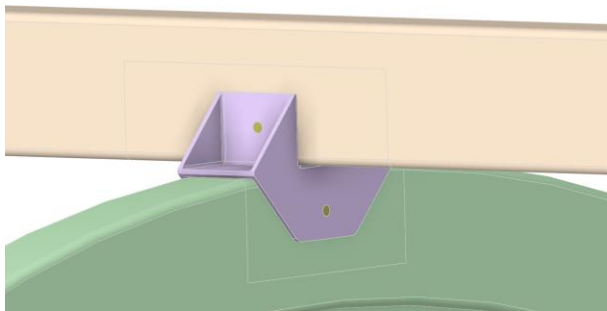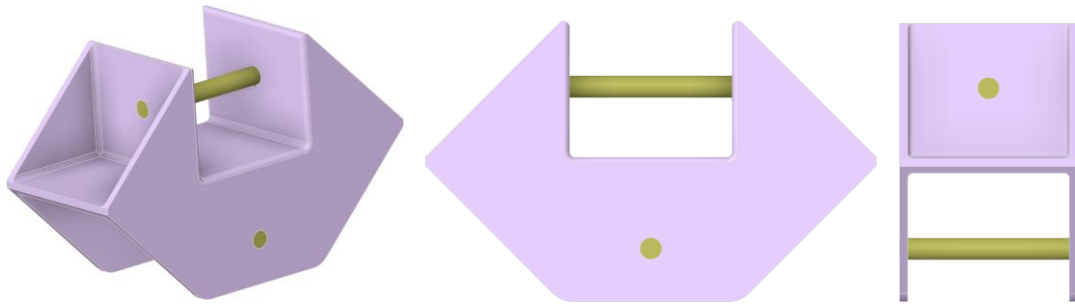
Figure 230: Ring – Stringer connection
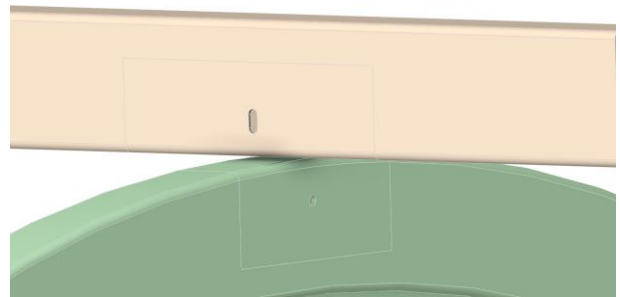
Figure 231: Visualisation of a slotted hole
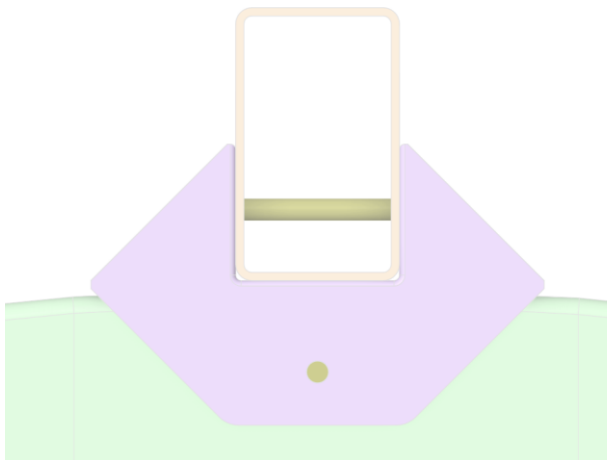
Figure 232: Front view of the assembly
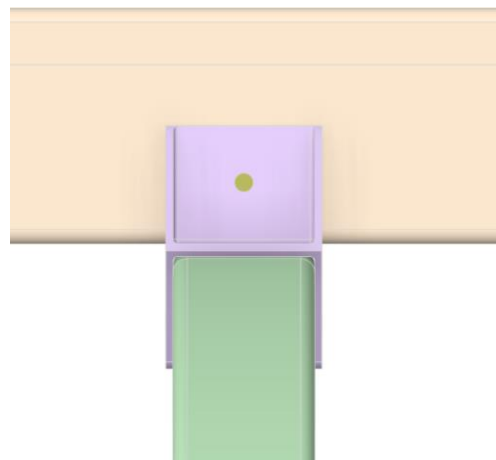
Figure 233: Side view of the assembly

H. Impact load analysis recommendation

This section provides a recommendation on the impact load analysis. The FE analysis was performed using an explicit dynamics analysis in Ansys [24].

Special attention must be given to the selection of boundary conditions. In the models used in this section, fully fixed boundary conditions were applied along the edges of the plate sections. This resulted in unreliable energy results, since the energy wave deflected from the fixed edge and disturbed energy data. This can be mitigated in the future by assigning dampers (springs) along the boundaries, or by simply modelling a larger segment of the tube for this analysis.

Since the energy results are invalid and inconclusive, only the stresses and deformations are provided. In this preliminary research, the projectile velocity is determined for which the yield and ultimate strength of the plate is reached.

Skeleton tube design

A sphere with a 50mm diameter made out of S355 steel and weighing approximately 5kg, is used as a projectile. The projectile's dimensions and mass are determined on the hypothesis that it could either me thrown by an individual or become airborne and impact the structure as a result of wind action.

Different velocities were assigned to the projectile, with the aim to find the maximum velocity of the sphere, at which the plate reaches yield point and failure. This analysis was conducted in an explicit dynamics analysis.
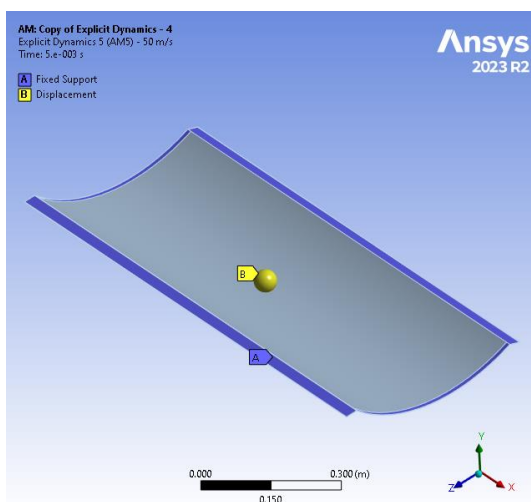
Figure 234: Setup of the impact load analysis
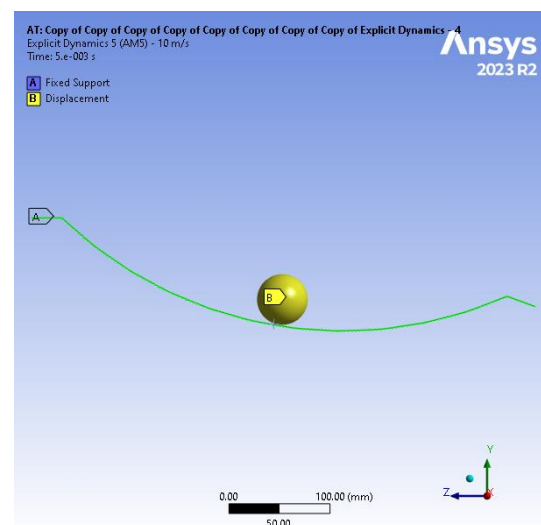
Figure 235: Setup – side view

Initially, the projectile velocity was found for which the stress in the plate reaches yield point. Figure 236 shows the stress in case of projectile velocity of 25km/h, and the plate deforms by 5.85mm at the location of an impact. Due to an impact load, the plate transversely tensions and experiences a vertical deformation adjacent to the impact, as showcased in Figure 237.
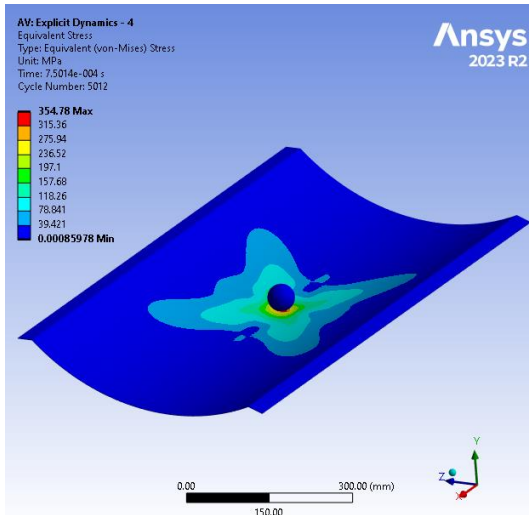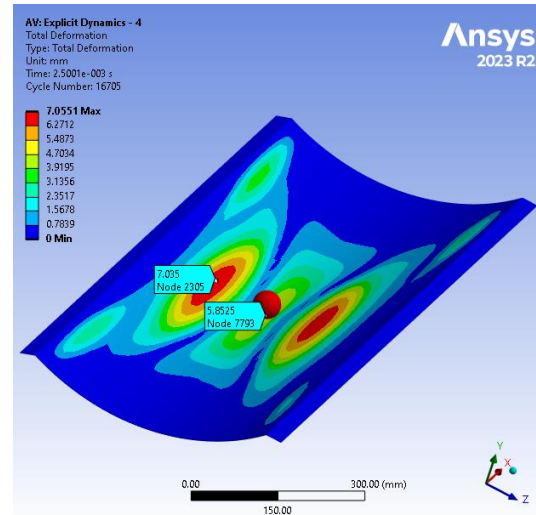
Figure 236: Stress [MPa] at v = 25km/h – S355

Figure 237: Total deformation [mm] at v = 22km/h – S355

After that, an iterative process was performed to identify the projectile velocity at which the ultimate strength is reached. A projectile velocity of 115km/h proved to be critical for plate failure. This resulted in plastic deformation of the plate, with stress levels peaking at 544MPa, as seen in Figure 238. The plate deformed locally by 19.9mm (Figure 239), which means that if the projectile had struck the plate at the location of the ring, it would likely have caused damage to the ring as well. In this case, a rupture of the plate is anticipated. The strongest wing gust ever recorded in the Netherlands [41] is 145km/h; therefore, a failure is expected if the projectile would have hit the plate at that velocity.
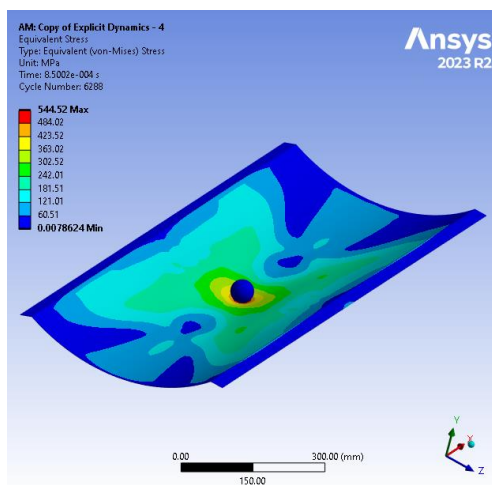
Figure 238: Ultimate strength reached at v = 115km/h – S355
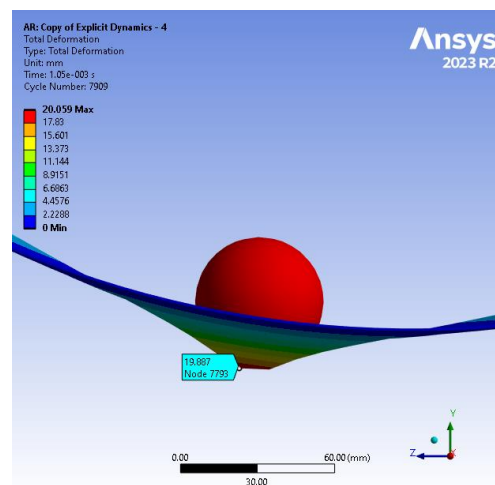
Figure 239: Total deformation [mm] at v = 115km/h

The aim of the last assessment was to observe the plate behaviour at failure. A projectile velocity of 250km/h was chosen, at which the plate gets fully penetrated. It can be seen that the plate does not deform significantly in the area surrounding the impact location. This indicates that the velocity was sufficiently high to prevent the plate to undergo gradual elastic and plastic deformation, leading instead to an almost instant rupture.
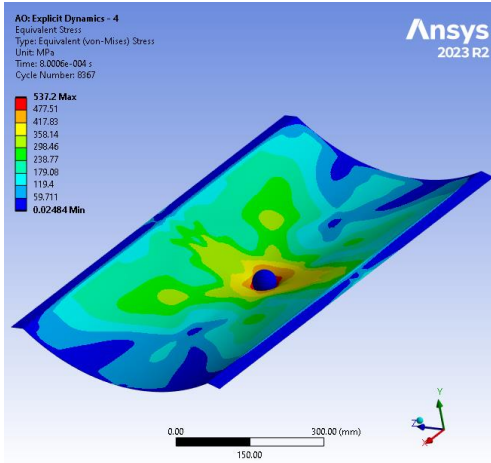
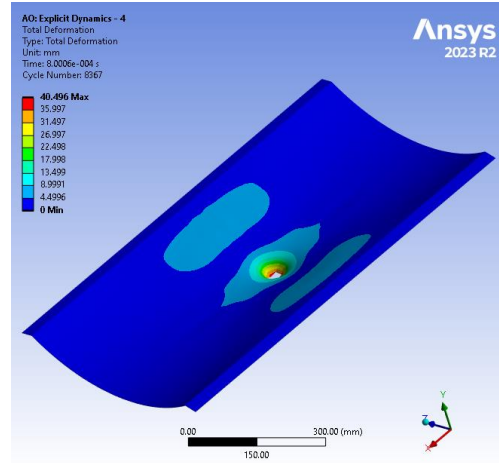Figure 240: Stress [MPa] at v = 250km/h

Figure 241: Total deformation at v = 250km/h

The following figures show the penetration in four steps.
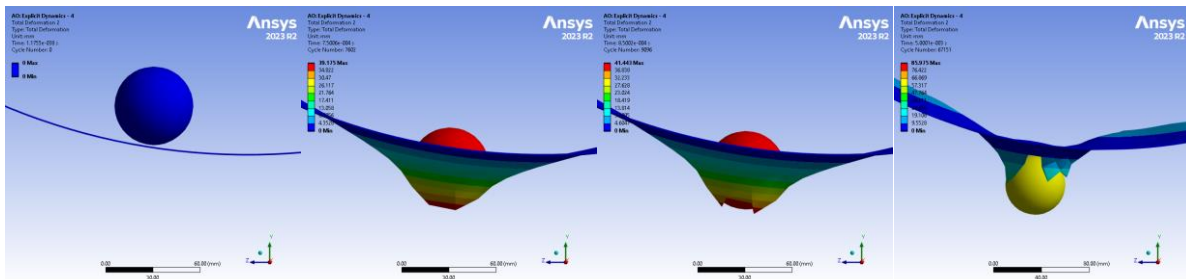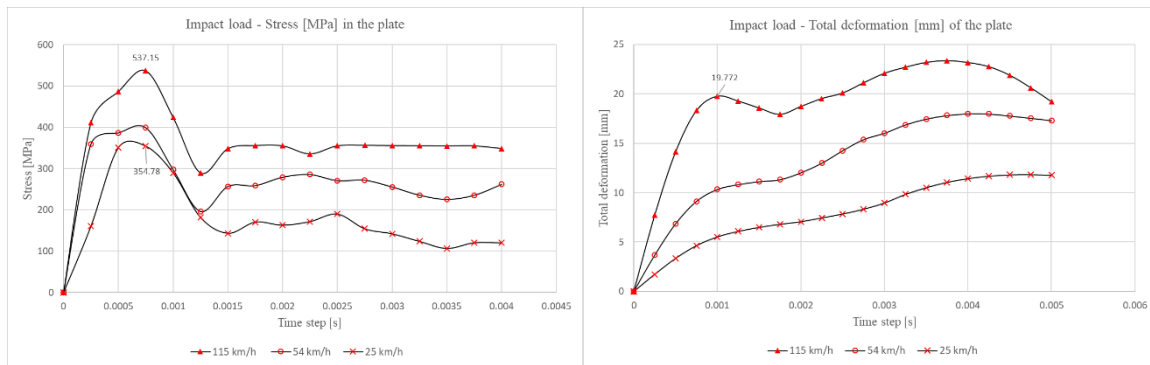

Figure 242: Full penetration of the plate by the projectile

The following two graphs represent the stress and deformation of the plate for different projectile velocities. The highlight are 25km/h and 115km/h projectile velocities, which showcase yield limit and ultimate strength limit.

Graph 12: Stress and deformation of the plate due to an impact by a spheric projectile.

Once the projectile hits the plate, if it does not penetrate the surface, it gets deflected. Due to the slenderness of the plate, a deformation wave is generated, that travels to the plate edges and deflects back. In the graphs, the second peak in stress and deformation is attributed to that plate's wave effect. This response is even more evident, once the vacuum pressure is assigned, meaning that the projectile hits the tube while the plates are tensioned. Plate's prestress affects the resistance to the impact load as well, as it can be seen in Graph 13, where a response comparison is made between unloaded and prestressed plate. An observation is made, that when vacuum pressure is present, the projectile hitting the plate at 25km/h causes plastic deformation.

143
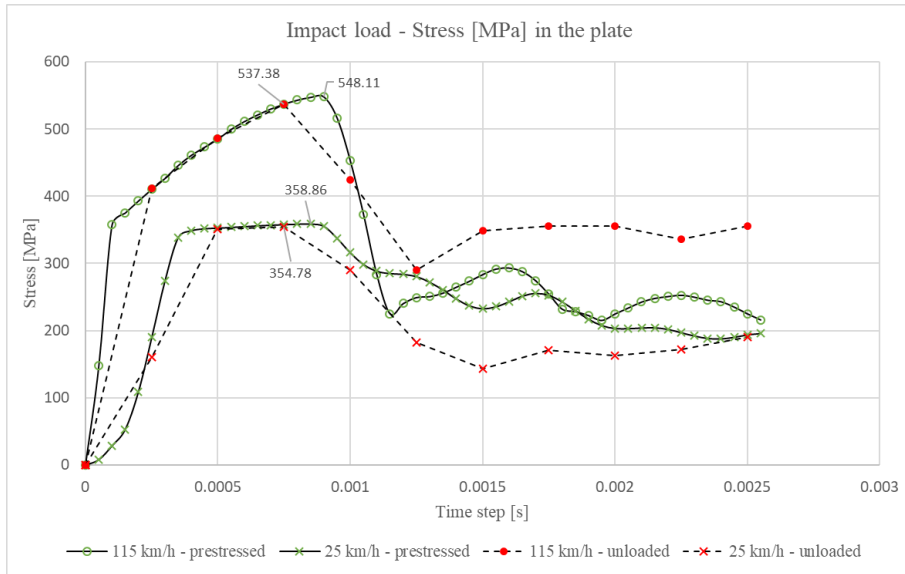
Graph 13: Impact load response comparison between unloaded and prestressed plate.

This analysis showed that the plate could resist a 5kg heavy projectile with a velocity of up to 115km/h. However, if the projectile hits the area where the ring is located, it will strike at the ring as well and potentially weaken the whole structure.

Plain tube design

This chapter presents the resistance to the impacts of the plain tube. The projectile is a sphere made out of S355 structural steel with a diameter of 50mm and a mass of 5kg**Error! Reference source not found.**.
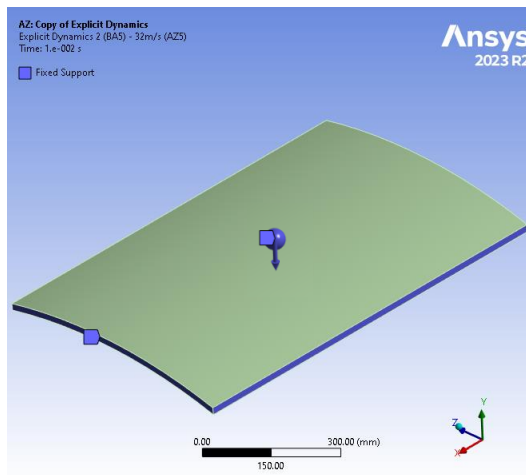
Figure 243: Setup of the impact load analysis

The yield strength of the skeleton tube plate was reached at the projectile velocity of 25 km/h and ultimate strength at 115 km/h. Since the wall thickness of the plain tube is 16 times thicker, it exhibits no stress increase at 25 km/h, while at 115 km/h, the stress increased up to 326.6MPa at the location of an impact (Figure 244). Using an iterative approach, the yield strength was achieved at the projectile velocity of 165.2km/h, as seen in Figure 245.
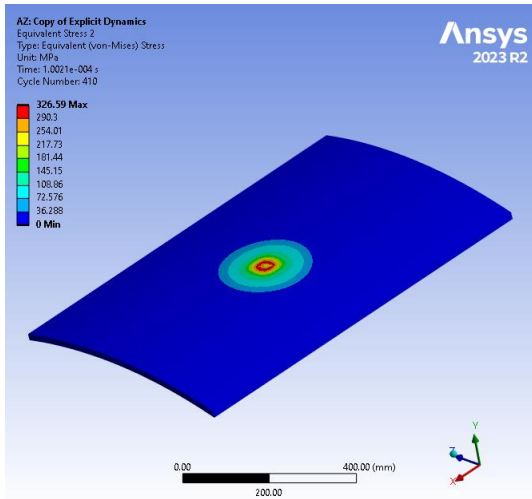
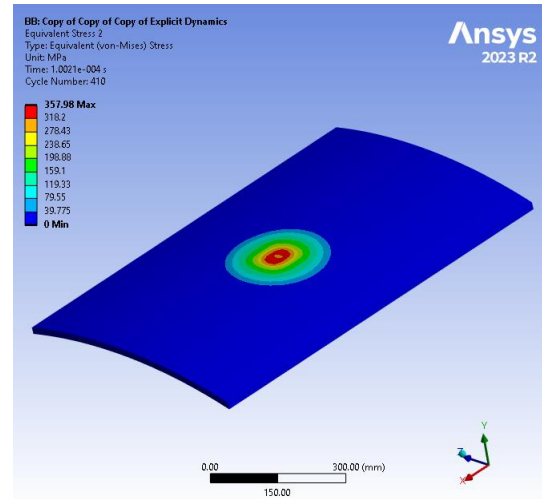*Figure 244: Stress [MPa] at v = 115km/h (the projectile velocity, at which the skeleton tube plate ruptures).*

Figure 245: Yield strength reached at v = 165.6km/h – S355

Lastly, the ultimate strength of the plate was reached at the projectile velocity of 648 km/h, as showcased in Figure 246. The total deformation at ultimate strength is presented in Figure 247, where the plate bends locally by 16.6mm before failure.
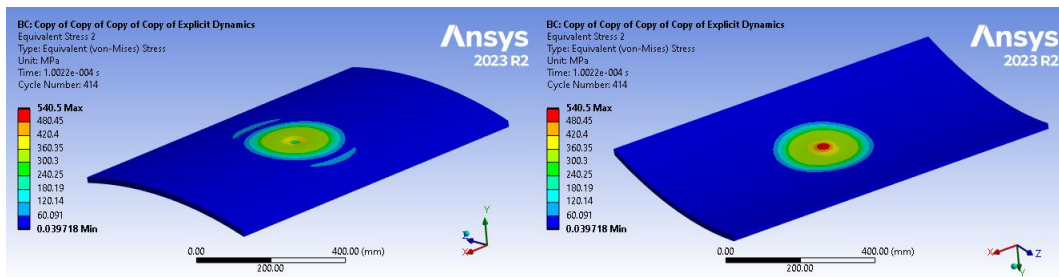

Figure 246: Ultimate strength reached at v = 648km/h – S355

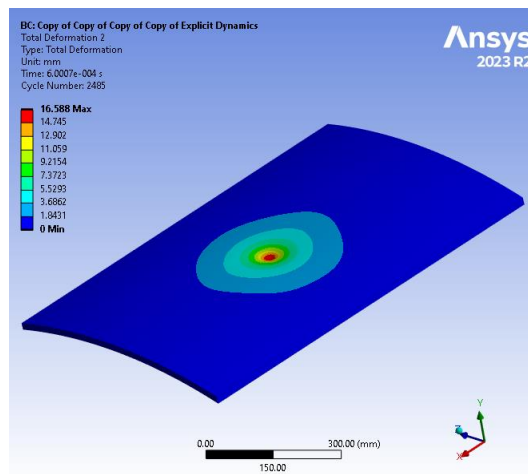*Figure 247: Total deformation [mm] at ultimate strength (v = 648km/h)*